Mock Observations of the Sunyaev-Zel'dovich Effect in Massive Galaxy Clusters and a Six-Layer Integral Antireflective Structure for Silicon Optics

Thesis by

Theodore Kenneth Macioce

In Partial Fulfillment of the Requirements for the
Degree of
Doctor of Philosophy

Caltech

CALIFORNIA INSTITUTE OF TECHNOLOGY
Pasadena, California

2023
Defended February 13, 2023

ACKNOWLEDGEMENTS

Mom and Dad, as always, thank you for your support. Thank you also for encouraging me to pursue my interests from a young age and to stick with this project until the end.

Sunil, you have been more than generous with your time and your guidance on both this project and my career. Thank you for your immense patience during this whole process.

Jack, thank you for your repeated willingness to help me through this project, especially during crunch time. Your training has shaped how I approach problems, probably for years to come.

Thanks to numerous others for your help and contributions to this project, especially Massimo, Junhan, Emily, Ouns, Sophia, Britney, Giselle, and Isaac.

Fabien, Cécile, and John, thanks for giving me a glimpse into the world of hardware during my brief but eye-opening stints in the Cahill lab and at MDL. Thanks also to the GBT staff, especially Wilson Skipper, for letting me have some exposure to real-life observing.

Thanks to Nancy, Sheri, and Kathy for your hard work in enabling the logistics of my degree.

Emily, I'm not going to acknowledge Xena, the turtles, Donut, the parrots, the peacocks, or any of the other fauna I encountered during my time at Caltech. However, I will thank you especially for your emotional support, which was badly needed to finish this document.

This work has been supported by a NASA Space Technology Research Fellowship Fellowship and by an NSF research grant.

ABSTRACT

Part 1: Measuring the kinematic Sunyaev-Zel'dovich (kSZ) effect is a promising observational tool to constrain both cosmic growth and galaxy cluster formation. As millimeter-wave telescopes gain sensitivity and angular resolution over multiple frequency bands, high signal-to-noise imaging of the kSZ effect in large samples of galaxy clusters will become increasingly feasible. However, maximizing the science reach of these upcoming data will require more sophisticated analysis methods to characterize and remove contamination from a range of unwanted signals, such as the emission from dusty star forming galaxies. Current predictions of kSZ-derived constraints do not account for these effects in sufficient detail. Moreover, they typically rely on Fisher matrix analyses, which cannot fully capture the degeneracies among the physical parameters describing the cluster. We present a mock observation and analysis pipeline to determine the science reach of kSZ galaxy cluster observations that employs more detailed noise models and more sophisticated analysis methods. From our mock observations, we derive new forecasts of the constraining power of next-generation telescopes on cluster peculiar velocities for several instrument configurations from the 10-m, 30-m, and 50-m classes. These forecasts will inform the designs of next-generation telescopes targeting kSZ observations and will indicate the optimal instrumentation for both cosmological and cluster-scale constraints. The software pipeline we develop will also be directly usable as an analysis tool once observations from such telescopes become available.

Part 2: Silicon optics can greatly benefit future millimeter and submillimeter astronomical instruments thanks to silicon's useful properties such as low loss, high refractive index, and high strength. However, silicon's high index (n = 3.4) necessitates antireflection (AR) treatment, which has proven a major challenge, especially for the multilayer treatments required for wide spectral bandwidths. We present our approach to this challenge, in which we develop a wide-bandwidth integral AR structure for silicon optics that uses a novel fabrication technique that combines deep reactive ion etching (DRIE) and wafer bonding. We have previously demonstrated a two-layer AR structure for windows over a 1.6:1 bandwidth and are currently fabricating a four-layer coating for a 4:1 bandwidth. Here, we focus on a design for a six-layer structure optimized to give -20 dB reflection between 80 and 420 GHz (5.25:1 bandwidth), which will be useful for future multicolor SZ observations.

PUBLISHED CONTENT AND CONTRIBUTIONS

Macioce, T. et al. (Dec. 14, 2019). "Multilayer Etched Antireflective Structures for Silicon Vacuum Windows". In: *Journal of Low Temperature Physics*. ISSN: 0022-2291, 1573-7357. DOI: `10.1007/s10909-019-02294-4`.

T.M. created and simulated the design, participated in the testing, created some of the figures, and was the primary author of the manuscript.

TABLE OF CONTENTS

LIST OF ILLUSTRATIONS

LIST OF TABLES

Part I

Mock Observations of the Sunyaev-Zel'dovich Effect in Massive Galaxy Clusters

Chapter 1

INTRODUCTION

The cosmic velocity field is one of the most important observables in modern cosmology. It encodes information relevant to some of the most fundamental questions in physics: Does the dark energy equation of state evolve with time? Is Einstein's General Relativity (GR) valid on large scales? What is the sum of neutrino masses? Several authors (e.g., Mueller et al., 2015a; Gil-Marín et al., 2016; Mueller et al., 2015b) have predicted that a variety of cosmic velocity field measurements can provide strong constraints on these physical properties of the universe.

There are several types of measurements that can constrain the cosmic velocity field. Some of the most competitive options are optical surveys of large-scale structure (LSS) that measure the apparent 3D clustering of galaxies, including surveys of redshift-space distortions (RSD).[1] As one example, the Sloan Digital Sky Survey's extended Baryon Oscillation Spectroscopic Survey (SDSS/eBOSS) already provides velocity measurements with sufficient precision to rule out an expansion-free universe (e.g., Zhao et al., 2021). In addition, RSD measurements can test whether GR correctly describes gravity on large scales. They can do this by constraining the cosmic growth rate index γ, which has a value of 0.54 for GR and different values for other gravity models (e.g., Gil-Marín et al., 2016). Currently, measurements by, e.g., SDSS constrain this value at the level of $\sigma(\gamma) \approx 0.1$ (Beutler et al., 2014). In the coming years, the so-called "Stage IV" clustering surveys such as the Dark Energy Spectroscopic Instrument (DESI; Levi et al. (2013)) will leverage increased sensitivity to further improve this constraint; DESI is projected to achieve a γ constraint at the level of $\sigma(\gamma) = 0.02 - 0.04$ (A. G. Kim et al., 2020; DESI Collaboration et al., 2016).

Another potentially powerful way to constrain the cosmic velocity field is to measure the velocities of many individual, massive galaxy clusters. As the largest structures to have formed in the universe, with masses of order $10^{15} M_\odot$, galaxy clusters are important tracers of cosmic evolution from redshifts $0 < z \lesssim 2$. Bhattacharya et al. (2008) and Kosowsky et al. (2009) first explored the possibility of

---

[1] RSD refers to fluctuations in the apparent line-of-sight clustering of galaxies due to their peculiar velocities, which arise from their gravitational attraction to matter overdensities in the large-scale structure.

applying measurements of clusters' velocities to constrain the cosmic velocity field, predicting constraints that complement those from LSS measurements, which probe lower mass scales. We shall explore this possibility in more detail in this work.

In addition, measurements of the internal velocity field within galaxy clusters, especially of the intracluster medium (ICM), can aid in understanding the details of large-scale structure formation. Several aspects of this process are not yet well understood. As one example, hydrodynamical simulations predict that accreting matter is not completely virialized during cluster formation (e.g., Lau et al., 2009; Morandi et al., 2012; K. Nelson et al., 2014; Siegel et al., 2018), but there is not yet a wealth of observational evidence to support these predictions. Indeed, there is some evidence that these simulations may underpredict the level of virialization, or conversely, that they overpredict the nonthermal pressure support, i.e., the extent to which nonthermal processes such as bulk motion and turbulence provide support against the ICM collapsing under gravity (Eckert et al., 2019).

Hydrostatic mass measurements, which are useful for cluster cosmology, also depend on a better understanding of the ICM velocity structure to calibrate out biases, although mass estimates using gravitational lensing, which are not subject to this bias, are more common in recent cosmological measurements. Other poorly understood ICM properties include viscosity and response to plasma instabilities; these too can be investigated by imaging the ICM velocity (Lau et al., 2009; Nagai et al., 2013; Parrish et al., 2012; ZuHone et al., 2018; Vazza et al., 2017). Clarifying these points will require velocity reconstruction with precision at the level of $\sigma_v \lesssim 100$ km/s (Nagai et al., 2013).

Measuring the ICM motions is becoming increasingly feasible thanks to improving instrumentation on spectroscopic X-ray satellites, which can measure line emission to trace gas velocity. Gas motions in the Perseus cluster have already been measured by the Hitomi satellite (Hitomi Collaboration, 2016; Hitomi Collaboration et al., 2018), which measured velocity dispersions with a precision of $\lesssim 10$ km s^{-1}. Future missions planned for launch (XRISM (XRISM Science Team, 2020)) or under development (*Athena* (Barret et al., 2020), *Lynx* (Gaskin et al., 2018)) will be able to map the velocity of more low-redshift clusters with precision ranging from 10–100km s^{-1} out to roughly r_{500}, meeting the criterion of Nagai et al. (2013). The later observatories will likely have some sensitivity to higher-redshift clusters, though the sensitivity degrades, by a factor of $(1+z)^4$ at worst, due to cosmological dimming.

The kinematic Sunyaev-Zel'dovich (kSZ) effect (Sunyaev et al., 1972) provides an alternative way to measure cluster peculiar velocities that complements optical large-scale structure measurements. It also complements X-ray ICM measurements in measuring internal cluster velocities. The kSZ effect is one of a few Sunyaev-Zel'dovich (SZ) effects, the others being the thermal (tSZ), relativistic (rSZ), and nonthermal (ntSZ) effects. All these SZ effects are caused by the scattering of cosmic microwave background (CMB) photons off the electrons of the ionized ICM. The kSZ effect is proportional to the line-of-sight velocity of the ICM; we discuss the other SZ effects in more detail in Section 2.2.

The kSZ effect has distinct advantages for velocity field imaging. For one, its magnitude is linear in ICM density, so it is sensitive to velocities even in the relatively low-density cluster outskirts. This behavior complements X-ray ICM measurements, as the X-ray surface brightness scales as the square of the ICM density. In addition, the kSZ effect is independent of redshift, while X-ray observations are most sensitive at low redshifts, since the X-ray flux density falls off with the distance to the cluster.

Observations of the kSZ effect can also complement optical large-scale structure (LSS) surveys in statistical measurements. Both kSZ and optical LSS measurements can constrain the cosmic growth index γ and the dark energy equation of state parameter w_0, but the kSZ-derived constraints are subject to different degeneracy curves, so they can help break the degeneracies in purely optically derived constraints: see, e.g., Mueller et al. (2015a). In addition, kSZ observations can provide a cross-check of such optical LSS constraints. In particular, kSZ observations can probe the mass scale of a full galaxy cluster ($> 10^{14} M_\odot$), whereas optical LSS measurements are most sensitive to galaxy- and group-scale objects ($\lesssim 10^{13} M_\odot$).

The kSZ effect is difficult to detect, however, and there have been few significant kSZ detections in individual clusters. The kSZ effect competes with the dominant tSZ effect, which is typically brighter by a factor of ~ 10, and contaminants such as dusty star-forming galaxies (DSFGs) and primary anisotropies of the CMB. As a result, the previous detections of the kSZ effect in individual clusters have been (a) in particularly energetic mergers and (b) only modestly significant, with velocities differing from 0 with significance levels of 4.2 σ (Sayers et al., 2013), 5.3σ (Adam et al., 2017), 2.8 σ (Planck Collaboration et al., 2018), and 4 σ (Sayers et al., 2019).

Studies such as Hand et al. (2012) have demonstrated that it is possible to improve the sensitivity of statistical velocity field measurements with a technique known as "pairwise kSZ." The pairwise technique seeks to measure line-of-sight velocity *differences* rather than velocities. The statistical measurement is sensitive mainly to $10^{13} M_\odot$ objects currently, which is a higher mass scale than that of RSD but lower than that of cluster peculiar velocities. The technique involves CMB maps constructed to enhance the kSZ signal on the positions of optically detected galaxies. This enhancement is accomplished by taking the difference in the CMB maps between pairs of nearby objects and stacking on many such pairs.[2] This pairwise differencing scheme is effective because features intrinsic to the individual objects, such as the tSZ signal, are the same on average, so they vanish in the stacks, unlike the pairwise kSZ signal. Several groups have made kSZ measurements in this way: see Hand et al. (2012), Soergel et al. (2016), Planck Collaboration et al. (2016b), Schaan et al. (2016), De Bernardis et al. (2017), Li et al. (2018), and Sugiyama et al. (2018). While the pairwise technique is effective for statistical cosmic velocity measurements, it cannot be used to image the ICM velocity in individual clusters. Moreover, it remains useful to develop a technique for analyzing individual cluster observations to probe higher mass scales with different systematics. In this work, therefore, we consider only the case of single-cluster detection.

To advance beyond the existing low-significance kSZ detections in major mergers to high-fidelity imaging of the ICM velocity structure, instruments with improved sensitivity and angular resolution are needed. Several collaborations are planning instruments to satisfy these criteria, including CMB-S4 (K. N. Abazajian et al., 2016; Abitbol et al., 2017; K. Abazajian et al., 2019), CMB-HD (Sehgal et al., 2019), and AtLAST (Klaassen et al., 2019). As these instruments' designs have not yet been finalized, there is a need to tune them based on our anticipation of the details of the observations. In particular, designs with larger apertures and more observing bands may have better ability to remove contamination, but there is a trade-off in construction and development cost. Thus, it is desirable to know in advance exactly how powerful the instruments must be.

To this end, several authors have made progress in developing techniques and forecasts for next-generation instruments to maximize the science reach of kSZ observations (e.g., Morandi et al., 2013; Mittal et al., 2018). However, these studies do not fully encapsulate the complexity of the observational effects that will be present in the deeper maps, as their modeling and analysis are based on simplifying assumptions that are inadequate even for existing data from previous-generation

---

[2] Calculating this difference in a consistent way depends on knowledge of the distances to the two objects, which can be estimated from the optical redshifts; in general, the bias due to the peculiar velocities is small.

facilities. Thus, our work provides more sophisticated mock observations to guide design choices for next-generation mm/submm telescopes so they may detect and measure the kSZ signal in massive galaxy clusters. Going forward, the software pipeline in this project will also enable analysis of the next-generation telescope data once it becomes available.

The specific advantages of this work over similar previous forecasting studies are more detailed treatments of the contaminants of the kSZ signal, whose characteristic spectra are shown in Figure 3.1. For one, we treat contamination from dusty star-forming galaxies (DSFGs, discussed in Section 2.3.1) in a more detailed way by modeling it as a collection of point sources. A common approach used by large-scale analyses is to model DSFG contamination as a power spectrum like that of the CMB and remove it by matching the various components in harmonic space using a technique such as SMICA (e.g., Delabrouille et al., 2003). While this approach is effective for, e.g., CMB power spectrum measurements, it misses the non-Gaussianity of the residual contamination. We expect these residuals to become significant at the smaller angular scales relevant for detailed cluster measurements: see, e.g., Figure 3.3c. Thus, we use the approach of treating DSFGs as individual sources in the modeling and subtracting each resolved source individually, as described in Section 3.1. Existing analyses of observational data (Zemcov et al., 2003; Zemcov et al., 2007; Lindner et al., 2015; Adam et al., 2017; Sayers et al., 2013; Sayers et al., 2019; Butler et al., 2022) have demonstrated that this kind of careful treatment of CIB removal is necessary for proper kSZ reconstruction, but existing forecasts have not included it.

In addition, we take a more thorough approach to forecasting constraints on cluster peculiar velocities. Forecasters, including Mittal et al. (2018), typically use Fisher matrix analyses to predict constraining power. These analyses are expedient, but they assume that the uncertainties on cluster velocity and other observables (described in Section 2.2) are Gaussian and thus well-described by a covariance matrix. This assumption can fail to hold when the observables suffer complicated degeneracies that are not accurately described by Gaussians, which can lead to biased velocity estimates. We solve the problem of capturing any such nontrivial degeneracies among the cluster parameters by using an iterative, bootstrap-like noise resampling method. This method enables us to robustly predict SZ parameter constraints, in the presence of both instrument noise and astrophysical contaminants.

In this work, we apply the methods described above to predict constraints on kSZ-derived velocities and other galaxy cluster parameters such as temperature and optical depth. We derive the SZ parameter constraints for a range of galaxy cluster masses and redshifts. In addition, we explore the impact of telescope diameter on such measurements. A number of additional aspects could be explored with the existing pipeline, and some others, particularly instrumental effects, could be added relatively straightforwardly; these are discussed in Section 6.2.

The remaining chapters of Part 1 are organized as follows. Chapter 2 describes the pipeline used to generate the mock cluster observations. Chapters 3 and 4 describe the map cleaning and parameter extraction stages of the analysis pipeline, respectively. In Chapter 5 we present cluster-level results derived from running the full observation and analysis pipeline with several representative instrument configurations. Finally, we discuss the results, applications, and future work in Chapter 6.

Chapter 2

MOCK OBSERVATION PIPELINE

In this work, we use a two-stage pipeline to calculate constraints on the velocity of each galaxy cluster. The first of these stages is to generate realistic mock observations for each cluster; the second stage is to analyze these observations to recover the cluster parameters and estimate constraints on their values. This chapter describes the model for the first stage.

We generate the mock observations by combining the signal from the galaxy cluster with other contaminating astrophysical signals. We first present the model of the cluster itself (Section 2.1) and describe the calculation of the SZ signals from that cluster model 2.2. We then discuss the models for the contaminants in Section 2.3, which include dusty star-forming galaxies (Section 2.3.1) and CMB (Section 2.3.2). We also model the gravitational lensing of the contaminant signals (Section 2.4). Finally, we describe our model for the other observational effects to generate the images in Section 2.5.

2.1 Galaxy Cluster Model

When generating mock observations, we use one of two options to describe a galaxy cluster's physical properties: an analytical model based on a generalized Navarro-Frenk-White (GNFW) profile (Nagai et al., 2007), or a more realistic model based on the publicly available IllustrisTNG simulations (D. Nelson et al., 2019; D. Nelson et al., 2018; Marinacci et al., 2018; Naiman et al., 2018; Pillepich et al., 2018a; Springel et al., 2018). Both models give the spatial distributions of the SZ-relevant properties of ICM temperature, velocity, and number density. In addition, both models describe the mass distribution, which is relevant for gravitational lensing (Section 2.4).

In the analytical model, the GNFW profile gives the ICM pressure as a function of radius:

$$P(r) = \frac{P_0}{(r/r_s)^{\gamma}[1 + (r/r_s)]^{(\beta-\gamma)/\alpha}}, \tag{2.1}$$

where r_s is the scale radius, P_0 is the normalization, and the slope parameters α, β, and γ are taken to be the best-fitting values from Arnaud et al. (2010). We model the ICM temperature distribution $T(r)$ as in Vikhlinin et al. (2006) (corrected values are given in an erratum: Vikhlinin et al. 2015). In this case, we assume uniform motion of the ICM along the line of sight. Finally, we model the total mass distribution for lensing by matching an NFW profile to the GNFW model with a correction for hydrostatic mass bias as described in Section 2.4. Overall, the analytical model is useful as a starting point for developing the pipeline, since it is straightforward to implement and test; we rely on the simulated clusters for a more realistic description of the parameters' spatial variation, including nontrivial velocity structures.

The IllustrisTNG simulations are hydrodynamical simulations that evolve galaxy clusters in their cosmological context, accounting for both large- and small-scale effects. The simulations are based on the quasi-Lagrangian AREPO code (Springel, 2010), which uses a moving Voronoi mesh for spatial discretization. They assume a cosmological model based on Planck Collaboration et al. (2016a); in particular, they assume $\Omega_{\Lambda,0} = 0.6911$, $\Omega_{m,0} = 0.3089$, $\Omega_{b,0} = 0.0486$, $\sigma_8 = 0.8159$, $n_s = 0.9667$, and $h = 0.6774$ (D. Nelson et al., 2018). The simulations also contain a variety of baryonic effects, including: radiative cooling; ISM pressurization due to unresolved supernovae; star formation, evolution, and feedback; and supermassive black hole growth and feedback. The simulation parameters have been tuned to match a handful of observed properties and statistics of $z = 0$ galaxies, including the stellar mass function, the stellar-to-halo mass relation, the total gas masses within r_{500}, the stellar mass – stellar size relation, and the black-hole–galaxy mass relation, as well as the cosmic star formation rate density as a function of z for $z \lesssim 10$ (Pillepich et al., 2018b).

For our cluster sample, we use the largest simulation volume, TNG300, which has a side length of $205h^{-1}$ Mpc; mass resolutions of $m_{\mathrm{DM}} = 7.5 \times 10^6\ M_\odot$ and $m_{\mathrm{baryon}} = 1.1 \times 10^7\ M_\odot$ for dark matter particles and baryons, respectively; and a minimum spatial resolution of $0.25h^{-1}$ kpc (comoving) set by the adaptive gas gravitational softening. We select massive halos from the simulation's existing group catalog, which was generated with a friends-of-friends criterion (FoF; Huchra et al., 1982; Davis et al., 1985). For the SZ effect calculations, we use the simulation's data on temperature, velocity, and electron number density, which are specified for each Voronoi cell in the mesh at each simulation snapshot; we obtain total mass data for the lensing calculation in an analogous way. We approximate a line-of-sight projection of these quantities and their dispersions using `Py-SPHViewer` (Benitez-Llambay, 2015).

2.2 Intracluster Medium Observables

Given a model of the ICM from Section 2.1, the first goal of our pipeline is to produce a map of the relevant SZ observables: a thermal (tSZ) component, a kinematic (kSZ) component, and the corrections to both components due to their relativistic thermal and bulk motion, which are sometimes considered as a separate rSZ component. There is also a nonthermal (ntSZ) component, discussed below, which we do not model in this work. The kSZ component is the most relevant in this work, as it contains cluster velocity information, but we also model the other components because they affect our ability to recover the velocities. We describe the components in detail below.

The tSZ component is due to the inverse Compton scattering of CMB photons by electrons of the hot ICM (e.g., Sunyaev et al., 1972; Rephaeli, 1995a; Birkinshaw, 1999; Carlstrom et al., 2002). It manifests as a change in the surface brightness of the CMB (B_ν), and its magnitude can be expressed in terms of the Compton y parameter, which is proportional to the electron thermal pressure integrated along the line of sight:

$$y = \int n_e \sigma_T \frac{k_B T_e}{m_e c^2} dl, \tag{2.2}$$

where n_e, σ_T, k_B, T_e, and m_e are the electron number density, Thomson scattering cross section, Boltzmann constant, and electron temperature, respectively. The tSZ signal's spectral dependence can be encoded as a factor $f(\nu, T_e)$:

$$\frac{\Delta B_\nu}{B_\nu} = y f(\nu, T_e). \tag{2.3}$$

In the nonrelativistic limit (i.e., the limit of low ICM temperature), this spectral dependence is purely a function of frequency:

$$\frac{\Delta B_\nu}{B_\nu} = y \frac{x e^x}{e^x - 1} \left[x \frac{e^x + 1}{e^x - 1} - 4 \right], \tag{2.4}$$

where the dimensionless frequency parameter x is given in terms of the CMB temperature by $x = \frac{h\nu}{k_B T_{\text{CMB}}}$. As the ICM temperature becomes high ($k_B T_e / m_e c^2 \gtrsim 0.01$), relativistic corrections to the tSZ effect become important (e.g., Rephaeli, 1995b; Itoh et al., 1998; Nozawa et al., 1998b; Itoh et al., 2004). These relativistic corrections, part of the rSZ component, have the effect of shifting the spectrum toward higher frequencies; the magnitude of this effect increases with increasing T_e. In effect, the spectral shape of the SZ signal becomes dependent on T_e.

The kSZ component is simply a Doppler shift of the CMB spectrum due to the bulk motion of the ICM relative to the CMB rest frame (e.g., Sunyaev et al., 1972;

Sunyaev et al., 1980; Birkinshaw, 1999; Carlstrom et al., 2002). Its magnitude is proportional to the product τv_z, where v_z is the line-of-sight velocity of the ICM, and the optical depth for Compton scattering τ is given by

$$\tau = \int n_e \sigma_T dl. \tag{2.5}$$

τ is also proportional to y, and therefore also the tSZ signal, through the density-weighted line-of-sight average of the gas temperature:

$$y = \tau \left\langle \frac{k_B T_e}{m_e c^2} \right\rangle_\rho, \tag{2.6}$$

where the subscript ρ indicates a density-weighted average. In the nonrelativistic limit, the kSZ signal can be expressed as a frequency-independent change in the CMB temperature:

$$\frac{\Delta T_{\mathrm{CMB}}}{T_{\mathrm{CMB}}} = -\frac{v_z \tau}{c}, \tag{2.7}$$

where positive v_z indicates motion away from the observer. Note that this implies that the kSZ signal is spectrally degenerate with the primary CMB fluctuations. The fractional change in CMB temperature can be converted to surface brightness in the standard way:

$$\frac{\Delta B_\nu}{B_\nu} = \frac{x e^x}{e^x - 1} \frac{\Delta T_{\mathrm{CMB}}}{T_{\mathrm{CMB}}}, \tag{2.8}$$

where $x = h\nu / k_B T_{CMB}$ is the dimensionless frequency. There are also relativistic corrections to the kSZ effect (e.g., Nozawa et al., 1998a; Sazonov et al., 1998); while these do give the kSZ effect a distinct spectral signal, their magnitude is quite small compared to the typically-dominant nonrelativistic tSZ and kSZ effects, and so they do not offer much help in separating the kSZ signal from primary CMB fluctuations.

Finally, there is another version of the SZ effect that may be relevant in certain clusters, namely the nonthermal or ntSZ effect (e.g., Mroczkowski et al., 2019). The ntSZ effect is analogous to the tSZ effect, except the ntSZ effect is caused by the highly relativistic, nonthermal component of the ICM's electron distribution. The ntSZ effect is difficult to model because the electron momenta can be distributed in a complicated way. Fortunately, it is a small effect, typically around 1% of the tSZ surface brightness (CCAT-Prime Collaboration et al., 2022). Thus, we do not model the ntSZ component in this work.

In the software pipeline, we model these effects, including relativistic corrections, using the `SZpack` package of Chluba et al. (2012). Here, we note several simplifying assumptions made by the code, both within `SZpack` itself and as modifications of the output. For one, `SZpack` is based on the single scattering approximation, which is the assumption that each CMB photon will interact with at most one electron on its path to the observer. A correction for multiple scattering only affects the SZ signal at the 0.1% level (Chluba et al., 2014), so it is safe to ignore for near-term observations. In addition, `SZpack` offers several modes of calculation that enable trading off accuracy for computational efficiency. The various modes have different limitations that are discussed in Chluba et al. (2012), but the assumptions common to all of them—$T_e < 75$ keV, $v_z/c < 0.01$, and $\tau \lesssim 0.01$—are valid for the clusters we consider. We have chosen to use the mode that calculates line-of-sight projections of the SZ effects using projections of v_z, T_e, τ, and their higher-order moments; for additional speed, we keep only the first-order terms. With this approximation, we avoid peforming a per-pixel, per-frequency line-of-sight integral with an expensive SZ effect calculation in its integrand. However, we must still calculate the projection of τ numerically, which is also computationally expensive, as Equation 2.5 does not have an analytical solution for our ICM model. Thus, we optimize this calculation by using an adaptive quadrature routine and interpolating the value of the τ integral from a 1D profile onto the 2D map. These efficiency gains are not crucial for mock image creation but are important for the analysis phase, where we reuse parts of the mock image generation code; see Section 4.1 for details.

2.3 Contaminants

With increasingly sensitive instrumentation becoming available, SZ observations will become a more powerful tool to constrain cosmic growth and cluster astrophysics. However, this increase in sensitivity also implies that astrophysical backgrounds and foregrounds will engender systematic uncertainties comparable to or greater than instrument noise. Indeed, the various contaminants are already the dominant source of uncertainty in SZ parameter recovery (e.g., Butler et al., 2022).

To accurately characterize the capabilities of next-generation instruments, we include a realistic suite of contaminants in our mock observation pipeline, prioritizing those that are most likely to bias SZ reconstruction in clusters. We model emission from dusty star-forming galaxies (2.3.1), both in the field and within the cluster, as the most prominent component of the contamination. We also consider fluctuations in both the primary CMB and secondary kSZ signals (2.3.2), which present a significant challenge in separation due to their spectral degeneracy with cluster's kSZ signal. Finally, we note our instrument noise model (2.3.3). Other contaminants are the subject of future work—see Chapter 6 for details.

2.3.1 Dusty Star-Forming Galaxies

The first source of contamination we consider is emission from dusty star-forming galaxies (DSFGs). DSFGs are defined by their emission at infrared and submillimeter wavelengths, where the original examples of DSFGs were selected, but they can belong to any of a few galaxy types, including gas-rich disks and mergers of starbursting galaxies (Casey et al., 2014). As their name implies, DSFGs tend to have very high star formation rates (SFR), on the order of thousands of $M_\odot$ yr^{-1} (Robitaille et al., 2010), compared to $\sim 2 M_\odot$ yr^{-1} for the Milky Way. In some cases, DSFGs are completely obscured by dust and thus are not visible at optical wavelengths.[1] Compared to the late-type galaxies that are common today, the DSFGs we observe are often younger and at higher redshifts.

DSFGs are a significant SZ contaminant because they are generally brighter than the SZ signal at $\nu \gtrsim 250$GHz. DSFGs are bright at these frequencies because of their combination of high star formation rates and dust. Specifically, the high star formation rates of DSFGs imply that they have high UV luminosity (Kennicutt, 1998). The abundance of UV starlight is absorbed by dust grains along the line of sight, which are heated to an average temperature T_{dust}, typically in the range of 30 to 40 K. The heated dust grains then reemit in the infrared, while the UV absorption suppresses their optical and UV brightness.

The infrared spectral energy distribution (SED) of a DSFG is best modeled as a blackbody $B_\nu(T_{\text{dust}})$ modified by a number of properties of the interstellar medium (ISM). These include temperature nonuniformity, source emissivity, and partial opacity of the dust grains (Casey et al., 2014). These effects are encoded in the optical depth τ_ν, which has been empirically found to scale as $\left(\frac{\nu}{\nu_0}\right)^\beta$, where β is the spectral index of emissivity and ν_0 is the frequency at which the dust becomes optically thick. Using the radiative transfer equation (Rybicki et al., 1986), we can solve for the observed SED as

$$S(\nu, T) \propto B_\nu(T)(1 - e^{-\tau(\nu)}) = \frac{(1 - e^{-\tau(\nu)})\nu^3}{e^{h\nu/kT} - 1}. \tag{2.9}$$

In the optically thin limit, which is valid for wavelengths $\gtrsim 450$ μm (Casey et al., 2014) as in our case, (2.9) reduces to:

$$S(\nu, T) \propto \frac{\nu^{3+\beta}}{e^{h\nu/kT} - 1}. \tag{2.10}$$

---

[1] This is particularly true for the earliest detected sources, known as starbursts.

Beyond frequency-dependent dust emissivity, additional effects include multiple temperature components and levels of dust obscuration.

The emission of the modified blackbody SED typically peaks around 100μm (e.g., Magdis et al., 2012) in the rest frame. However, the galaxies are bright even in the submillimeter band, as the SED has a long Rayleigh-Jeans tail, and the galaxies have a typical redshift z obeying $1 < z < 3$.

The other factor in DSFGs' significance as a contaminant is that they are dense in submm fields. This occurs because of the DSFGs' strongly negative K-correction, which is the factor used to convert a redshifted source's flux density from the observed frame to the rest frame; see, e.g., Casey et al. (2014) for details. The negative K-correction is caused by the shape of the source SED (2.9): the sources' steeply rising spectrum (up to $\sim$ 100 μm in the rest frame) implies that, as the DSFG spectrum is redshifted, the flux near 1 mm stays roughly constant. Thus, we are equally sensitive to a given source regardless of its redshift, which results in a high density of sources in an image with similar brightness values. As a result, a given resolution element can often contain multiple bright sources, which makes it difficult to fully remove DSFG emission from the SZ maps. This is exacerbated by the relatively poor angular resolution near 1 mm.

We consider DSFGs separately in the cases that they are field galaxies or cluster members. We model the population of field DSFGs, known as the cosmic infrared background (CIB or CIRB), using the SIDES simulated catalog (Béthermin et al., 2017). SIDES is built on a halo distribution from the Bolshoi-Planck dark matter simulation (Rodríguez-Puebla et al., 2016). It uses an abundance-matching procedure to populate the halos according to stellar mass function measurements for $0 \leq z \leq 7.5$ (Kelvin et al., 2014; Moutard et al., 2016; Davidzon et al., 2017; Grazian et al., 2015). These features make SIDES the first simulation of its kind to correctly account for the spatial correlations and redshift distributions of DSFGs.

In addition to the field galaxies, we model a population of member galaxies for each cluster, many of which may also be considered DSFGs. These cluster member galaxies are particularly important to include because their emission tends to be spatially correlated with the SZ signal. However, these galaxies have not been studied as well as field galaxies, so we cannot simply model them with a mock source catalog such as SIDES. Instead, we begin with the procedure of Melin et al. (2018) to model the galaxies' luminosity functions and SEDs based on a field galaxy model (Cai et al., 2013). We then adjust the number counts according to *Herschel* and *Spitzer* observations in galaxy clusters using the work of Alberts et al. (2016). We describe the cluster member dust model in more detail in Appendix A.1.3.

The central galaxy in a dynamically relaxed cluster, known as the brightest cluster galaxy (BCG), deserves special consideration. There is a strong feedback loop between the central galaxy and the ICM (e.g., Voit, 2005). This results in significant AGN activity within that galaxy, including strong synchrotron emission from the AGN core. This emission can be a significant fraction of the SZ signal, 10% or more (e.g., Sayers et al., 2013; Coble et al., 2007; Cooray et al., 1998; Romero et al., 2017). In practice, it would be ideal to jointly fit for the BCG emission and the SZ signal; the synchrotron emission could be modeled as a simple powerlaw. Alternatively, to avoid the complications related to the BCG's size and systematic errors in the fitting, it may be best to simply excise a beam-sized region around the BCG from the map. We did not have time to develop and test either of these alternatives in our pipeline, so we did not model the BCG emission in this work.

In addition, there may be a diffuse component of dust emission in galaxy clusters. The evidence for this component is a Planck detection of cluster-coincident dust (Erler et al., 2018). However, the origin of this dust emission is unclear, and it may be due entirely to cluster member galaxies. Thus, without a well-constrained model, we do not attempt to include this emission in our mock observations.

A final potential source of dust contamination in SZ signals is far-IR emission from the Milky Way. This component is known as the Galactic cirrus due to its spatial structure. The cirrus emission is strongest at large angular scales, with a power spectrum that scales with the angular wavenumber k as $k^{-2.6}$ from $1'$ to $200'$ (Bracco et al., 2011). However, because this emission comes from the local universe, it is not redshifted from its FIR peak, so it is less significant in the submm band. Based on SPT observations, Reichardt et al. (2021) inferred that, even for relatively large angular scales of $\ell \sim 2000$, the Galactic cirrus component was an order of magnitude below DSFG emission at 220 GHz. In the context of SZ observations, Butler et al. (2022) found that the uncertainty on SZ reconstruction due to cirrus was 20% of the uncertainty due to DSFG emission in the 600 GHz and 850 GHz bands of *Herschel*/SPIRE. Extrapolating their findings down to our bands,[2] which are at lower frequencies, we find that the uncertainty due to cirrus remains at roughly 20% of that due to DSFGs. We hope that similar fractional uncertainties will be

---

[2] For this extrapolation, we assume an SED (Equation 2.9) with $T = 10$ K and $\beta = 1.8$ for the DSFGs and $T = 20.1$ K and $\beta = 1.3$ for the cirrus (Bracco et al., 2011).

achievable in the future with improved instrumentation, but we have not investigated this fully.

We note our assumption about source morphology, which is relevant to our modeling of lensing (Section 2.4) and to our source subtraction procedure (Section 3.1). All the sources we include are assumed to be pointlike: that is, the angular size of each source is less than that of the PSF. This assumption is justified in the regime we consider: our highest-resolution instrument configuration, which uses a 50m telescope, has a minimum beam FWHM of $4.5''$, while most DSFGs have structure on the scale of $< 1''$ (e.g., Casey et al., 2014). Thus, the full rasterized CIB map consists of many scaled copies of the PSF.

We use two algorithms to generate these CIB maps: a fast, FFT-based version and a slower but more accurate version that adds shifted PSF copies to the map. The FFT-based version, which discretizes the source positions to a fraction of the pixel size and convolves with the PSF, is used for map generation in the main simulation loop, where efficiency is important due to the many sources included. The slower version, which avoids the positional error from discretization, is used for the reconstruction of resolved sources, as described in Section 3.1.

2.3.2 Primary CMB Anisotropies

The CMB temperature power spectrum peaks at an angular scale of approximately one degree (e.g., Planck Collaboration et al., 2020), so it is possible for the primary CMB power to leak into SZ signal measurements. This is especially true for local clusters, which can have virial diameters $\gtrsim 1$ degree, while moderate redshift clusters at $z \sim 0.5$ are closer to $10'$ in diameter. Moreover, the primary CMB and kSZ signals are spectrally degenerate, so disentangling the two can be difficult. To calculate the CMB power spectrum $D_\ell = \frac{\ell(\ell+1)}{2\pi} C_\ell$, we use the CAMB code of Lewis et al. (2000). Since the CAMB output stops at $\ell = 4000$, we extrapolate to higher ℓ by fitting an exponential decay model above $\ell = 3000$ to trace the Silk damping tail of the CMB spectrum. Finally, using the flat sky approximation, we apply a Fourier transform to the power spectrum to generate map-space CMB realizations.

The CMB also contains additional secondary anisotropies apart from the SZ signal of the galaxy cluster in question. These include the tSZ and kSZ signals of other large-scale structure in the universe, in addition to the inhomogeneous distribution of gas during the epoch of reionization (Gruzinov et al., 1998; Knox et al., 1998). At angular scales $\ell \gtrsim 2000$ or $\theta \lesssim 6'$, the secondary kSZ and tSZ signals are predicted to have relatively flat power spectra in D_ℓ, where the combined value of D_ℓ is of order unity in units of μK^2 (Battaglia et al., 2013; Calabrese et al., 2014). Existing measurements are consistent with these predictions (Reichardt et al., 2021). Thus, these background SZ signals are expected to dominate over the primary CMB signal at small angular scales, $\ell \gtrsim 4000$ or $\theta \lesssim 3'$, and so they may be a significant contaminant to our images.

The background kSZ and tSZ anisotropies can be modeled by using the power spectra of Reichardt et al. (2021). These power spectra can be converted to map space realizations in a manner analogous to the method for the primary CMB. They can then be scaled by the known tSZ and kSZ spectra. However, modeling the gravitational lensing of these components (see Section 2.4) is a challenge, as they exist at multiple redshifts that are not precisely constrained. Thus, we have not included either these background models or the perturbations on them due to lensing in this work.

2.3.3 Instrument Noise

Finally, we include instrument noise as an independent Gaussian white noise term in each frequency channel. For each instrument configuration we consider, we use the confusion noise level as a reference in each observing band. The confusion noise level is equal to the RMS fluctuation per beam due to DSFGs after removing the ones that are bright enough to be individually detected;[3] confusion limits used in this work are shown in Table 5.1, along with the expected integration times required to reach these limits in practice. In the simple case of beam-sized pixels, this means the RMS fluctuation in each map pixel is taken to be equal to the RMS fluctuation in the confusion noise per beam:

$$\sigma_{\text{beam}} = \frac{\sigma_{\text{confusion}}}{\Omega_{\text{beam}}}, \tag{2.11}$$

where $\sigma_{\text{confusion}}$ has flux density units (as it is the 1σ uncertainty on each source), and σ_{beam} has surface brightness units for consistency with the SZ signal. In our case, however, the beam spans multiple pixels, so it is necessary to convert σ_{beam} to a per-pixel RMS σ_{pixel}. The conversion factor depends on the exact shape of the beam; for a Gaussian beam, it implies the following expression for the per-pixel

---

[3] In particular, in this work, we calculate the confusion limit directly from SIDES by selecting the 5σ flux density threshold S_{lim} such that the collection of sources below this threshold have a per-beam RMS fluctuation equal to $\frac{1}{5}S_{\text{lim}}$.

RMS:

$$\sigma_{\text{pixel}} = \sqrt{\frac{2\Omega_{\text{beam}}}{\Omega_{\text{pixel}}}} \frac{\sigma_{\text{confusion}}}{\Omega_{\text{beam}}}. \tag{2.12}$$

In other words, it can be shown that Gaussian white noise with a per-pixel RMS following (2.12) leads to the same 1σ uncertainty on the source's flux density as a background of sources with confusion RMS $\sigma_{\text{confusion}}$.

2.4 Gravitational Lensing by the Cluster

2.4.1 Lensing of Pointlike Backgrounds

Gravitational lensing of background DSFGs by the cluster significantly affects their observed properties (Zemcov et al., 2013; Sayers et al., 2019). In particular, lensing of the CIB towards a massive cluster results in a deficit in the residual CIB surface brightness after removing individual bright sources. Zemcov et al. (2013) were the first to measure this effect at the centers of four massive clusters. Lima et al. (2010) also find that lensing is a significant SZ contaminant based on BLAST data. The findings of Sayers et al. (2019) are perhaps the best precedent for our work in the context of SZ reconstruction. Using 10 clusters with mass models constructed from HST data, they calculated the change in CIB surface brightness in randomly generated lensed CIB realizations after removing bright sources. They found that that this change amounted to an average reduction of 15% in the SZ surface brightness at 270 GHz.

However, this effect has not always been addressed in prior SZ forecasts. We include it in this work to determine the extent to which it can bias kSZ peculiar velocity measurements in individual clusters. Our testing has determined that the deficit can lead to a 1σ to 2σ bias in the kSZ velocity if it is neglected in the analysis; see Section 3.3.

It is important to precisely state the scope and mechanics of this effect, hereafter called the "lensing deficit," in order to understand its relevance to our observational scenario. A lensing deficit can arise in the presence of a magnification bias, which is described by Turner (1980). The magnification bias can be positive or negative depending on the background source counts dN/dS. In the submillimeter band, in which we detect DSFGs, dN/dS is a steep function of S, so the magnification bias is positive (A. W. Blain, 1997; A. Blain, 2002). This positive magnification bias implies an increase in the flux density of each detected source, so it becomes possible to detect more sources that are intrinsically dimmer. In addition, these intrinsically dimmer sources reside on a flatter portion of the dN/dS curve, so there are fewer sources remaining below the detection threshold. Thus, there is a net deficit of the residual CIB after subtraction of all detectable sources. Given that the residual CIB contaminates the SZ effect, we have therefore chosen to model the lensing deficit to account for its local bias to the CIB. It must be emphasized that the action of source removal is key to this effect: the lensing deficit manifests even though lensing conserves the mean surface brightness in the map before source removal.

To model the effect of gravitational lensing in our mock observations, we must first calculate maps of the deflection angles $\boldsymbol{\alpha}(\boldsymbol{\theta})$, which are the input to the lens equation (e.g., Blandford et al., 1992):

$$\boldsymbol{\beta} = \boldsymbol{\theta} - \boldsymbol{\alpha}(\boldsymbol{\theta}), \tag{2.13}$$

where $\boldsymbol{\alpha}(\boldsymbol{\theta})$ is the reduced deflection angle[4] at position $\boldsymbol{\theta}$ and $\boldsymbol{\beta}$ is the unlensed source position on the sky. Calculating these deflection angles requires an assumption about the total mass distribution in the fiducial cluster, which we separate into the cases of an analytical cluster model and a map based on hydrodynamical simulations.

We address the analytical case first. One can calculate maps of $\boldsymbol{\alpha}$ with a surface mass density profile $\Sigma(r)$ by using the analytical lensing formalism of, e.g. Bartelmann (1996). For the assumed $\Sigma(r)$ profile, it is desirable to be as consistent as possible with the GNFW profile we assume for the ICM density in modeling the SZ component. However, the GNFW model has a non-analytical projected mass density, and moreover, it contains no information about the dark matter distribution within the cluster. Therefore, for simplicity, we assume that the total mass profile, including both ICM and dark matter, is well-described by a pure NFW model (Navarro et al., 1996; Navarro et al., 1997), which enables using the analytical lensing formalism directly. To convert the GNFW ICM model to an NFW mass profile, we assume hydrostatic equilibrium of the ICM with a correction for the hydrostatic mass bias $b = 0.15$ based on the review given in Gianfagna et al. (2021):

$$M_{\text{enc}}(r) = -\frac{1}{1-b}\frac{r^2}{G\rho_{\text{gas}}}\frac{dP}{dr}, \tag{2.14}$$

where $M_{\text{enc}}(r)$ is the total mass enclosed in a sphere of radius r, and the gas pressure and density profiles $P(r)$ and $\rho_{\text{gas}}(r)$ are given by the GNFW model, with a mean

---

[4] The reduced deflection angle is the change of position on the sky, in contrast to the unreduced deflection angle, which is the angle by which the light ray itself changes direction. We revisit the distinction below.

molecular weight of $\mu = 0.59$ assumed for the ICM. We then fit for the NFW normalization ρ_0 and scale radius r_s that optimize the agreement with (2.14) by minimizing the mean squared error in $M_{\rm enc}(r)$ over the range $0.03 < r/R_{500} < 3$. Given the best-fitting NFW parameters, it is straightforward to project the NFW mass density and calculate the deflection angles using, e.g., Equation 6 of Golse et al. (2002). The angles can be expressed in terms of the total mass $m(r)$ within a cylinder of radius r:

$$\boldsymbol{\alpha} = \frac{m(r)\boldsymbol{r}}{r^2}, \tag{2.15}$$

where $m(x)$ is given in, e.g., Bartelmann (1996).

There is a difference between the reduced and unreduced deflection angles. The reduced angles, usually written as $\boldsymbol{\alpha}$, are used in the lens equation to describe the difference between the "true" and apparent position angles of the source as viewed by the observer, while the unreduced angles $\hat{\boldsymbol{\alpha}}$ describe the effective angle by which a ray is deflected by the lens on its path to the observer. See Figure 5 of Blandford et al. (1992) for an explanation.

The case of simulated cluster maps differs in its derivation of $\boldsymbol{\alpha}$, which cannot be expressed analytically without spherical symmetry. Instead, one must solve the Poisson equation for the 2D lensing potential (e.g., Blandford et al., 1992):

$$\nabla^2\psi(\boldsymbol{\theta}) = 8\pi G\Sigma(\boldsymbol{\theta}), \tag{2.16}$$

where $\psi(\boldsymbol{\theta})$ is the 2D lensing potential and $\Sigma(\boldsymbol{\theta})$ is the 2D projected mass density of the cluster. We obtain maps of the 2D mass density by projecting the total mass data from the simulations in the same way as for the gas properties. The unreduced deflection angles $\hat{\boldsymbol{\alpha}}$ are then obtained as the gradient of ψ, or more precisely,

$$\hat{\boldsymbol{\alpha}} = \nabla\psi/c^2. \tag{2.17}$$

We use code provided by M. Meneghetti to solve (2.16) numerically by Fourier transformation and computing the gradient of ψ to obtain maps of $\hat{\boldsymbol{\alpha}}$. Finally, we convert the unreduced deflection angles $\hat{\boldsymbol{\alpha}}$ to the reduced angles $\boldsymbol{\alpha}$ by rescaling according to the source-observer and lens-source angular diameter distances $D_{\rm s}$ and $D_{\rm ls}$ (e.g., Blandford et al., 1992):

$$\boldsymbol{\alpha} = \frac{D_{\rm ls}}{D_{\rm s}}\hat{\boldsymbol{\alpha}}. \tag{2.18}$$

With deflection angle maps in hand, it is possible to proceed with the lensing calculation. For implementing lensing of pointlike background sources, we separately consider the regimes of the strongly-lensed core and the weakly-lensed cluster outskirts. In the cluster core, we rely on a ray tracing calculation, which is performed using the SKYLENS code (Plazas et al., 2019; Meneghetti et al., 2020) The code selectively samples the background at a higher resolution than the nominal pixelization under the assumption that the galaxies are described by a Sersic model. Using this high-resolution ray trace, we can capture strong lensing effects such as arcs, distortion, and multiple images.

However, the ray trace is computationally expensive given the requirements of our pipeline. In part, this is due to the aforementioned requirement of high-resolution sampling for sources that may be strongly lensed. In addition, the ray trace calculation must be performed separately for each observing band: while the deflection angle maps themselves are independent of observing frequency, we do not assume the source SEDs are identical, and so the "preimage" of the ray trace is frequency-dependent.

Thus, we have developed an alternative mode for the cluster outskirts for improved performance. This alternative mode is based on the assumption that each source remains pointlike after lensing. We consider the sources to have modified positions and flux densities according to the reduced deflection angles $\boldsymbol{\alpha}$ and magnifications μ. The magnification is calculated from the determinant of the lensing Jacobian $\mathcal{A}$, also known as the inverse magnification tensor:

$$\mu = [\det \mathcal{A}]^{-1} = \left[\det \frac{\partial \boldsymbol{\theta}}{\partial \boldsymbol{\beta}}\right]^{-1} . \tag{2.19}$$

Under this assumption, the code's performance does not scale as steeply with source count, as there is no need to sample the map at higher than nominal resolution. This approximation also mitigates the penalty of scaling with the number of observing bands, as the deflection and magnification can be calculated just once per source. Consequently, we can reuse the fast rasterization code of Section 2.3.1 with the source positions adjusted and the SEDs uniformly rescaled by the μ.

To calculate the modified source properties in the weak lensing regime, we again use the code of M. Meneghetti, with some modifications for additional performance gain. The original code uses a nominal-resolution ray trace to locate the images of each source. This is necessary in the general case, which includes the strong lensing regime, but the calculation is somewhat computationally expensive. We avoid this ray trace by assuming that each source has only a single image, whose location we approximate by mapping the deflection angles $\boldsymbol{\alpha}(\boldsymbol{\theta})$ back to the source plane using the implicit equation

$$\boldsymbol{\alpha}_{\rm src}(\boldsymbol{\beta}) = \boldsymbol{\alpha}_{\rm img}(\boldsymbol{\theta} - \boldsymbol{\alpha}_{\rm img}(\boldsymbol{\theta})). \tag{2.20}$$

We calculate the source-plane deflection angles $\boldsymbol{\alpha}_{\rm src}(\boldsymbol{\beta})$ on a grid to enable partitioning the sources into redshift bins, which reduces the number of times the deflection angles must be rescaled from $\hat{\boldsymbol{\alpha}}$ and remapped to source-plane coordinates. In addition, we sample $\boldsymbol{\alpha}_{\rm src}(\boldsymbol{\beta})$ on a coarse grid relative to the nominal resolution to take advantage of the angles' slow variation with radius in the weak lensing regime. We then calculate the lensed source positions $\boldsymbol{\theta}_i$ from the unlensed positions $\boldsymbol{\beta}_i$:

$$\boldsymbol{\theta}_i = \boldsymbol{\beta}_i + \boldsymbol{\alpha}_{\rm src}(\boldsymbol{\beta}_i). \tag{2.21}$$

Finally, we calculate each source's magnification μ_i by sampling the Jacobian determinant $\det \mathcal{A}$, as calculated with the original code, at the lensed positions $\boldsymbol{\theta}_i$.

Ultimately, however, we have not used these optimizations to generate our results, as the performance of SKYLENS has been sufficent for the small sample size. We generated lensed maps of CIB realizations for each of the clusters in our sample using high-performance computing infrastructure. For analyzing a larger cluster sample or when sampling a continuum of cluster parameters, it may be worthwhile to include these optimizations. It is a subject for future work to set sensible boundary conditions in map space between the strong and weak lensing regimes.

2.4.2 Lensing of Smooth Backgrounds

Primary CMB fluctuations are also affected by gravitational lensing, so we also model this in our pipeline. Since the CMB does not have significant structure below the angular scale of the beam, and since it exists at a single redshift, the ray tracing calculation is straightforward and efficient given deflection angle maps: it suffices to sample the map of $\Delta T_{\rm CMB}$ at each pixel position $\boldsymbol{\theta}$ offset by the deflection angles $\boldsymbol{\alpha}(\boldsymbol{\theta})$ according to the lens equation (2.13). We use bilinear interpolation to sample at non-integer pixel positions.

2.4.3 Demonstration

We include a demonstration of the lensing pipeline in Figure 2.1, which shows example realizations of lensed CIB and CMB. To highlight the deflection effect, we show the maps as differences between lensed and unlensed realizations. The deflection of the sources in (a) can be clearly seen as dipoles in the residual. The lensing has a subtler effect on the CMB temperature, but it is still visible in the difference map.

2.5 Observational Effects

The last ingredient in the mock observation pipeline is the instrument itself. Imaging instruments have several nonidealities in practice, but we model only the nonidealities that are most likely to interfere with the analysis and are common to all observational scenarios. In particular, the effects we model are the point spread function (PSF), spatial filtering, and finite spectral bandwidth. We describe our treatment of these effects below.

2.5.1 Point Spread Function Model

The PSF is important to model in SZ observations chiefly because it limits our ability to remove point source contamination and resolve cluster substructure. There are two aspects of PSF modeling to consider: width (FWHM) and shape. Most of the instrument configurations in Chapter 5 have published reference values for the FWHM; we use these reference values where available but use default values in Table 2.1 in all other cases. For the shape of the PSF, we assume a circular Gaussian, which is simple to calculate and approximately accurate for a wide range of telescopes.

Real PSFs, however, can have non-negligible non-Gaussian side lobes. These side lobes may cause leakage of the SZ signal from the central region of the cluster to the outskirts, which can impact the SZ constraints if the PSF shape is characterized imperfectly. However, if the PSF shape can be characterized accurately enough that it has a negligible effect on the SZ constraints, then it is reasonable to assume, as we do, that the PSF is a perfectly-characterized Gaussian. In addition, the strength of the side lobe contamination depends strongly on the properties of a given instrument. Thus, we leave treatment of non-Gaussian PSFs to instrument-specific analyses, although our formalism is fully capable of incorporating non-Gaussian beams because no aspect of the analysis requires beam Gaussianity.

2.5.2 Signal Transfer Function

Next we consider the effect of the signal transfer function, which is a result of the sky subtraction needed to mitigate contamination from the Earth's atmosphere. Emission from the atmosphere is brighter than the largest expected SZ signal by a factor of $\sim 10^4$, and it varies with an angular power spectrum that follows a powerlaw

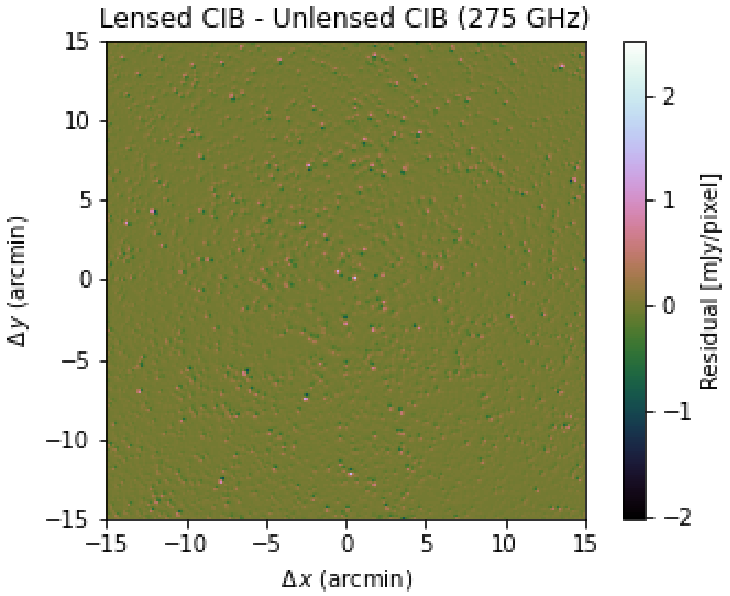

(a) CIB

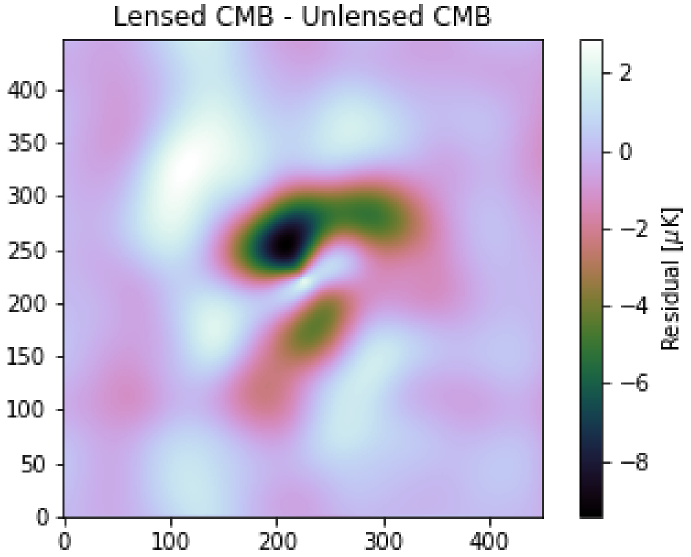

(b) CMB

Figure 2.1: Examples of the lensing calculation applied to point-like (a) and smooth (b) backgrounds. Both images show the difference between the lensed background and the unlensed background.

Band Frequency (GHz)	10 m FWHM (arcsec)	30 m FWHM (arcsec)	50 m FWHM (arcsec)
90	87.4	31.7	19.0
150	52.4	17.7	10.6
220	35.8	12.1	7.3
270	28.6	9.9	6.0
350	22.5	8.2	4.9
400	19.7	7.4	4.4

Table 2.1: Assumed FWHM values for PSFs in baseline 10m, 30m, and 50m instrument configurations.

with an exponent of $-11/3$. Thus, some form of spatial high-pass filtering is required to remove these fluctuations (e.g., Sayers et al., 2011; Bender, 2011; Romero et al., 2020; Ruppin et al., 2018; Schaffer et al., 2011); in practice, this filtering is implemented as a combination of common-mode subtraction among detectors and explicit high-pass filtering of the timestream.

We base our transfer function model on an 8 arcminute FoV and increased scan speed relative to the Bolocam instrument (e.g., Sayers et al., 2011). These assumptions have the effect of moving the high-pass filter cutoff frequency down by a factor of 5 in wavenumber. To calculate our transfer function model, we fit a 2-pole filter model to the Bolocam filter profile given in Sayers et al. (2011):

$$T(u) = \frac{u^2}{u_{\text{cutoff}}^2 + u^2}, \tag{2.22}$$

where u is the angular wavenumber and u_{cutoff} is the cutoff wavenumber; modes with $u < u_{\text{cutoff}}$ are attenuated by the filter. We found that a value of $u_{\text{cutoff}} = 0.0945\ \text{arcmin}^{-1}$ produced a good fit to the Bolocam transfer function, so for our model we use a cutoff of $\frac{1}{5}u_{\text{cutoff}} = 0.0189\ \text{arcmin}^{-1}$.

2.5.3 Finite Bandwidth Effects

Finally, we consider how finite bandwidth can affect the SZ observations. All the instruments we consider in this work will perform photometric (i.e., non-spectroscopic) measurements, so the signals we consider are band-integrated. Because the SZ effect and the contaminants have spectra that are nonlinear functions of frequency, it is important in practice to model both the frequency response of the instrument and the how the signals vary with frequency within each band.

Modeling this frequency dependence is computationally costly for the relativistic SZ corrections, however, especially in the inner loop of our reconstruction procedure

(Section 4.1). Thus, in our pipeline, we calculate single-frequency approximations to the band-integrated SZ signals, which require only one call to SZpack per band. Assuming top-hat instrument response functions, we found that the bias in this approximation is typically $\lesssim 1\%$ in the kSZ signal and $\lesssim 0.1\%$ in the tSZ signal. Refer to Appendix A.1.4 for details. The bias can be further reduced to below 0.1% by calculating the SZ signal at 4 frequencies per band; adding this capability to the pipeline is the subject of future work.

An additional complication in practice is uncertainty in the calibration of these bandpasses. Given that this effect is strongly instrument-dependent, we leave the task of modeling these calibration uncertainties to future studies.

Chapter 3

MAP CLEANING

Given the spectral overlap of the SZ signals with the primary CMB temperature anisotropies and emissions from radio galaxies and dusty star-forming galaxies (Figure 3.1), it is necessary in practice to consider these contaminants and remove them from SZ observations. The tSZ signal can be recovered to roughly 10% accuracy without map cleaning, but better accuracy is needed to constrain the weaker rSZ and kSZ signals.

Prior forecasting by Mittal et al. (2018) considered contamination by DSFGs and used high-frequency data to clean it, but the contamination was included as a Gaussian noise term. In contrast, we consider DSFG contamination as a collection of point sources, as described in Section 2.3.1. Accordingly, to clean this contamination, we use an algorithm that accounts for the DSFGs' point-like nature and their correlation among bands. We describe our cleaning algorithm in detail below.

Mittal et al. (2018) also included primary CMB anisotropies in their maps but did not attempt to subtract or filter them. Given the faintness of the signals we are reconstructing, it is appropriate to model these effects more fully. In modeling the map cleaning process, we reconstruct the signals and estimate biases and uncertainties as similarly as possible to the process for real data in order to obtain maximally realistic values for the precision on the reconstruction of SZ parameters.

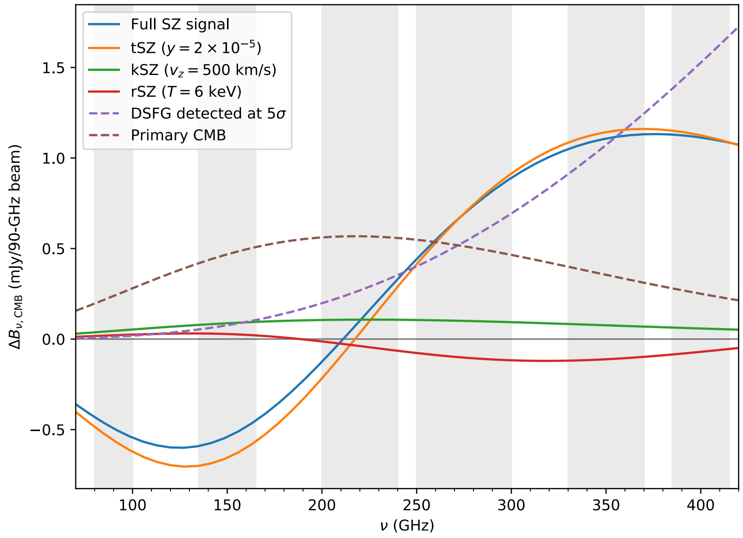

(a) Component spectra normalized to a 90-GHz beam

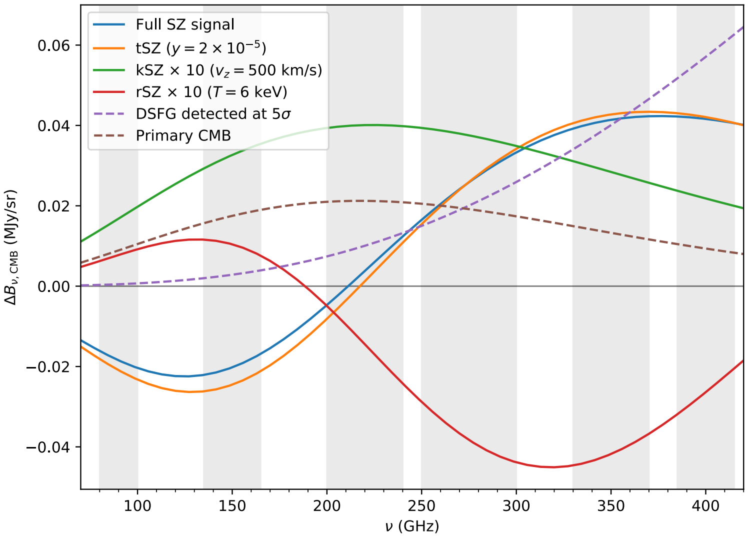

(b) Component spectra rescaled to have similar magnitudes

Figure 3.1: Example spectra of the relevant SZ components with contaminant spectra. The SZ signals, which include the total SZ (solid blue), tSZ (solid orange), kSZ (solid green), and rSZ (solid red), are shown for a cluster with $y = 3 \times 10^{-4}$, $T_e = 6.3$ keV, and $v_{\mathrm{pec}} = 500$ km/s and are evaluated at a radius of r_{500}. The contaminant spectra are those of a DSFG (dashed purple) and the primary CMB fluctuations (dashed brown); the DSFG spectrum matches the confusion limit at 400 GHz for a 30m telescope. The gray bars indicate six observing bands at the atmospheric windows centered on 90, 150, 220, 270, 350, and 400 GHz.

3.1 Point Source Removal

We have developed a procedure to remove point sources from the CIB maps, which we generate as described in Section 2.3. We perform source detection using the StarFinder IDL code (Diolaiti et al., 2000), which is tuned to detect sources effectively in a crowded field.

By default, StarFinder works in three phases. In the first phase, it searches for local peaks in the contaminated map that fall above a spatially varying background estimate plus a detection threshold; the threshold is specified as a fraction of the per-pixel noise RMS $\sigma_{\rm pixel}$.[1] In the second phase, it discards any peaks at which the local correlation of the map with the PSF falls below a specified value.[2] Finally, it refits a model of the PSF shape at each peak to improve the accuracy of the estimates of the source locations and flux densities (i.e., the astrometry and photometry). This full process is iterated multiple times with decreasing noise thresholds, and including previous detections in the background estimate, to better account for any blended sources and remove spurious detections. StarFinder outputs a catalog of the sources detected in the map, which contains each source's position and flux density along with uncertainties on both.

In principle, such a catalog is sufficient to reconstruct the CIB and remove it from the map. However, StarFinder's algorithm has two key limitations: it does not account for the effect of flux boosting (described in, e.g., Crawford et al. (2010)), and it can only detect sources in a single frequency band at a time. We have developed machinery to apply StarFinder to our situation, where we have maps in multiple bands and flux boosting may be a concern.

3.1.1 Accounting for Flux Boosting

The effect of flux boosting arises in the regime where the differential source counts dN/dS are a steep function of flux density. Because of the steeply rising dN/dS, a source with an observed flux density S_ν is more likely to be a dimmer source that has fluctuated upward in flux due to noise than a brighter source that has fluctuated downward. In effect, the posterior distribution of true flux for a given observed flux S_ν is biased to lower fluxes than S_ν, or, more simply put, observed fluxes are biased high on average. Failing to account for flux boosting

---

[1] This convention for the threshold is not equal to the signal-to-noise ratio (SNR) of the detected source when the PSF is multiple pixels wide. We apply an aggressive detection threshold of $1\sigma_{\rm pixel}$ and rely on a manual cut at the end to discard sources with SNR < 4.

[2] We use a value of 0.4 in this work.

leads to the subtraction of too large a flux on a source-by-source basis, which causes negative pointlike artifacts to appear in the source-subtracted map. StarFinder does not perform a correction ("deboosting") for this effect on the flux densities of the sources it detects, so we manually implemented this functionality into our pipeline.

We considered two methods for accounting for flux boosting. The first of these is the Bayesian formalism of Crawford et al. (2010), which gives the posterior probability distribution of the flux density of the brightest source within a pixel S_{max} given the detected flux density of the source $S_{p,m}$ and the prior probability distribution $P(S_{\mathrm{max}})$ derived from the source counts. For the sake of computational tractability, our implementation of the formalism makes the approximation (also described in Crawford et al. (2010)) that the likelihood $P(S_{p,m}|S_{\mathrm{max}})$ is Gaussian, which greatly simplifies the calculation at the cost of some accuracy. From the posterior probability density function (PDF) $P(S_{\mathrm{max}}|S_{\mathrm{p,m}})$, this method chooses a single representative value of S_{max} to be the true flux density for CIB reconstruction; in practice, we use the median value of the posterior as a representative.

The second method we considered is to calibrate an empirical relation between the known true flux density of a source S_{true} and the flux density of the detection S_{detected}. There is some ambiguity inherent in the definition of S_{true}, as a detected source does not necessarily correspond exactly to a single true source in the CIB realization, either in position or in flux density, due to the contributions of nearby sources. Based on our testing, we have found that the most useful way to define S_{true} given a detection is as the amplitude of a fit of the PSF to the noiseless input CIB map at the detected source position. Furthermore, we remove all contributions to S_{true} from sources above a 4σ detection threshold that are outside StarFinder's minimum source separation of 1 FWHM. The calibration is performed on a noisy map of the full field of the SIDES catalog; it consists of fitting a curve to S_{true} vs. S_{detected} (Figure 3.2). We chose the form of a piecewise linear function for this fitting curve as a compromise between the robustness of the fitting behavior and the flexibility to deviate from linearity. Finally, the true flux density of an unknown source can be estimated by evaluating the piecewise calibration function at S_{detected}.

Figures of Merit

In tuning the parameters of the source removal algorithm, we have used several figures of merit (FoM) to evaluate its performance. The simplest of these is the

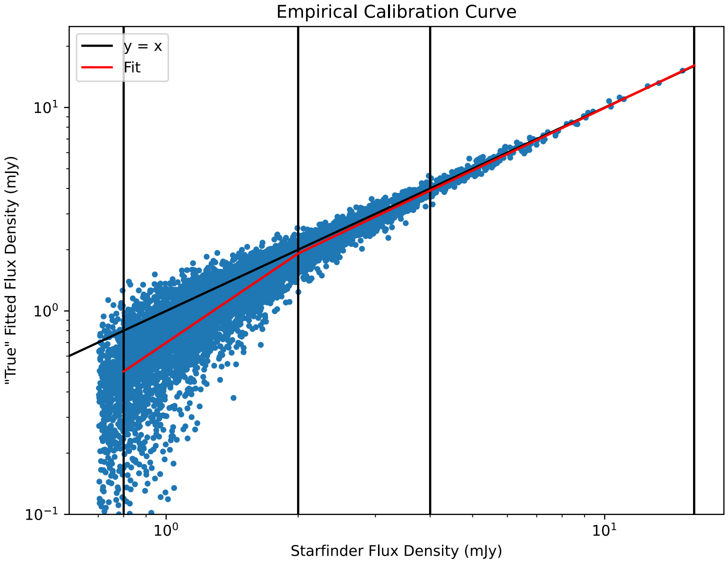

Figure 3.2: Empirical calibration of StarFinder's flux estimate for all sources detected in a large (2 deg^2) map. For each detected source (blue), StarFinder's estimate S_{detected} is compared to a fit to the true flux density S_{true} within a beam of the detected position in the noiseless map. The red curve shows the piecewise linear fit to the calibration data, while the black line shows $S_{\text{true}} = S_{\text{detected}}$ for comparison. (The vertical black lines indicate boundaries of the piecewise linear fitting regions.) It can be seen that, on average, S_{detected} only exceeds S_{true} in dim sources.

residual map-space RMS, calculated as the RMS of the difference between the input map of source fluctuations M_{in} and the map of reconstructed sources M_{out}, where both maps have been convolved with the beam and M_{in} has been calculated before the addition of instrument noise:

$$\text{FoM} = \text{RMS}(M_{\text{in}} - M_{\text{out}}). \tag{3.1}$$

A more informative figure of merit is the histogram of all the pixels of the residual map $M_{\text{in}} - M_{\text{out}}$, which can be used to see deviations in the residual from a Gaussian noise distribution. Another option is to consider the angular power spectrum of residual map pixels. We use these FoM to compare the two techniques for boost corrections, as shown in Figure 3.3.

The postage stamps stacked on source positions (Figure 3.3a) are the most transparent way to visualize how each method affects the residual in the map. Applying no correction results in a clear over-subtraction on average, while there is apparently a trade-off between the two correction methods. The empirical method

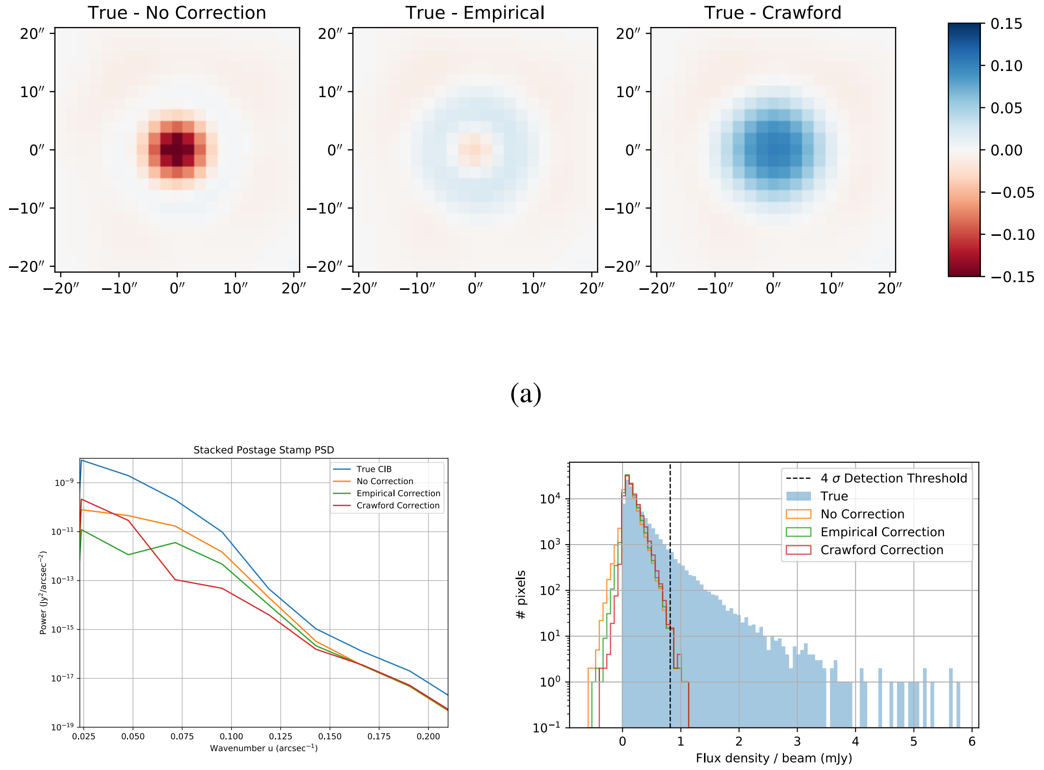

(a)

(b)

(c)

Figure 3.3: Demonstrations of the performance of the boosting correction algorithm in the case of a 30m telescope with confusion-limited noise at 270 GHz. a Postage stamps of residual CIB maps ($M_{\text{in}} - M_{\text{out}}$) stacked on detected source positions, where M_{out} is uncorrected, corrected empirically, and corrected with the Bayesian method of Crawford et al. (2010), respectively. The postage stamps are normalized relative to the peak of the stack on the true CIB map. b Residual CIB power spectra within postage stamps stacked on detected source positions, where the wavenumber u is defined in the flat sky approximation such that when u has units of rad^{-1}, $2\pi u = \ell$, where ℓ is the angular multipole. Power spectra are given for both the residual CIB maps—with the Crawford et al. (2010) boost correction (blue), the empirical correction (orange), and no correction (red)—and the true CIB map M_{in} (green). c Histograms of flux density values in each pixel within a postage stamp of the source in the true CIB map (blue), the uncorrected residual map (orange), and the empirically corrected residual map (green). Compare the performance to the 4σ detection threshold (dashed line). The map pixels have been rebinned by a factor of 5 to match the FWHM of the beam.

reduces the over-subtraction but suffers from an annular feature in the stack at a radius of slightly less than one FWHM of the beam (in this case, $10''$). This suggests that the source positions are being slightly misestimated due to other nearby dim sources. It is interesting to note that the annulus does not disappear in the case where the sources in the map follow a uniform distribution in space (unlike SIDES, where clustering is taken into account); hence, it seems that source clustering does not cause the feature. The Crawford et al. (2010) method, on the other hand, lacks the annular feature but tends to under-subtract sources, likely because it yields the posterior PDF of only the brightest source within a beam without including contributions from dimmer sources.

These characteristics can also be seen in the postage stamps' power spectra (Figure 3.3b): the Crawford et al. (2010) technique performs better at small angular scales, while the empirical correction performs better on scales of the beam size and larger. Since the SZ signal we seek occurs mostly at angular scales larger than that of the beam, the SZ signal recovery is presumably less sensitive to sub-beam-scale residuals; hence, we choose the empirical correction technique to apply to the main analysis.

The histograms of Figure 3.3c illustrate how the algorithms' performance affects the entire recovered map. The histogram bins count residuals per beam by binning the FoM map (Equation 3.1) into beam-sized pixels and only considers pixels located at detected source positions. This procedure roughly corresponds to counting the residual per source detection while avoiding the ambiguity in pairing detected sources with one or more sources in the ground truth catalog. As these histograms illustrate, any of the source subtraction methods (with or without boost correction) modify the map histogram by removing the long positive tail of bright sources and leaving a distribution resembling Gaussian noise. The effect of the boost corrections is to reduce the negative tail where oversubtraction is occurring. The Crawford et al. (2010) is arguably more effective in this regard, although perhaps at the expense of undersubtraction for some sources.

3.1.2 Multiband Source Removal

The procedure described above applies to removing point sources from a single-band map. However, given our multifrequency analysis, we must extend the procedure to make use of multiband data. It is possible to detect sources in multiple channels independently, as done by past multiband SZ analyses (e.g., Sayers et al., 2013). However, we can improve the signal-to-noise ratio of the detections by using a weighted multiband combination of single-channel maps. We implement this source removal procedure in two steps—detection and refitting—which we describe in detail below. The entire multiband source detection and refitting algorithm is depicted in the diagram in Figure 3.6. We assume a 6-band instrument for the procedure described in this section.

Our goal in the detection step is to obtain a maximally complete and accurate catalog of source positions as an input to the multiband refitter. To combine the single-channel maps into one, we must first rescale them by factors $r_\nu = S_{\text{ref}}/S_\nu$, where S_ν is the source SED, with the highest-frequency flux density S_{ref} as a reference point. For this step, we assume that all sources obey an identical modified blackbody SED (2.10), which depends on two parameters: the observed temperature T and spectral index β. After rescaling the maps by the SED, we form an optimal combination map using an inverse-variance-weighted average of the single-channel maps. That is, we can express the map as a combination

$$M_{\text{combined}} = \sum_\nu \frac{r_\nu w_\nu M_\nu}{\sum_\nu w_\nu}, \tag{3.2}$$

where M_ν are the single-band maps and w_ν are the weight factors that maximize the combined signal-to-noise ratio. See Appendix A.3.1 for a derivation of these optimal weight factors. Finally, we use StarFinder to extract the source positions from the combined map, setting the detection threshold at 4σ relative to the noise level, which we calculate from the noise levels of the individual maps.

There is an important detail in the choice of the source SED: since the sources in SIDES have a range of SEDs, there is no single natural choice of the parameters T and β. To find optimal values of T and β, we fitted the modified blackbody template to the observer-frame SEDs S_ν of the SIDES sources. We found that $\beta = 1.8$ is a good match for most of the sources, but the best-fitting value of T ranges from ~ 5 K $-$ 80 K. When forming the multiband combinations as described above, we found that lower values of T tend to detect more sources than high values, with a 3% increase in detected source count from $T = 10$ K to $T = 5$ K. Employing the multiband map with any value of T yielded a 40% gain in the number of detected sources over simply using the 400 GHz band [3].

By one metric, however, we found that using the 10 K SED slightly improved the positional accuracy of source detections compared to the 5 K SED. Specifically,

---

[3] These tests assumed a 30m telescope integrating to the confusion limit.

we found that the RMS spread of deviations relative to the estimated uncertainty of the centroid position—rms $\left(\frac{\Delta_x}{\sigma_x}\right)$—decreased from 1.6 with 5 K to 1.5 with 10 K. To attempt to minimize such astrometry errors, we use a compromise in our algorithm: we perform two detection passes, first fitting with $T = 5$ K and refitting with $T = 10$ K. However, there is a significant runtime penalty for performing this extra fitting pass, typically $\sim 25\%$ of the computational cost of the full multiband fitting algorithm. We do not expect that the additional fitting pass significantly affects the SZ reconstruction, particularly considering that another metric of the spread—the median of $\left|\frac{\Delta_x}{\sigma_x}\right|$—does not improve with the warmer SED. For future work, if computation time is an important consideration, one should investigate whether this additional step adds significant benefit in constraining the SZ signal.

With the source positions in hand, we proceed to fit an SED at each source position. The first step is to repeat PSF photometry at each source position in each single-band map. We perform this PSF photometry by simultaneously fitting an image of the PSF and a sloped background component at each source position. We also subtract initial estimates of the fluxes of the known nearby sources, as determined by StarFinder from M_{combined} and rescaled by the 10 K SED. We perform two passes of this PSF fitting for all the sources to better account for overlapping sources. Next, we correct for the boosting effect at each frequency as described in Section 3.1.1. Finally, we fit a modified blackbody SED template (2.10) to the deboosted flux densities, fixing $\beta = 1.8$ but varying both T and the amplitude. To check that this SED model is valid for SIDES sources, we performed a collection of fits of the SED to SIDES photometry, which we report in Appendix A.1.2. However, there are a few important complications in this photometry and SED refitting process that we note below.

The first complication occurs when a bright source subsumes a nearby dim source in the low-frequency channels. That is, the PSF photometry incorrectly attributes the dim source's flux density to the bright source, even when the dim source is detected at high significance in the higher-frequency bands. Iterating PSF photometry steps alone is not sufficient to solve this problem. Instead, we leverage information from the higher-frequency bands to provide a first estimate of the dim sources' flux densities. To do this, we perform PSF photometry and SED fitting with the three highest-frequency bands alone. We then extrapolate the SED to the low-frequency bands and then repeat the photometry and SED fitting with all frequency channels. To validate the SED fitting procedure, we checked that the distribution

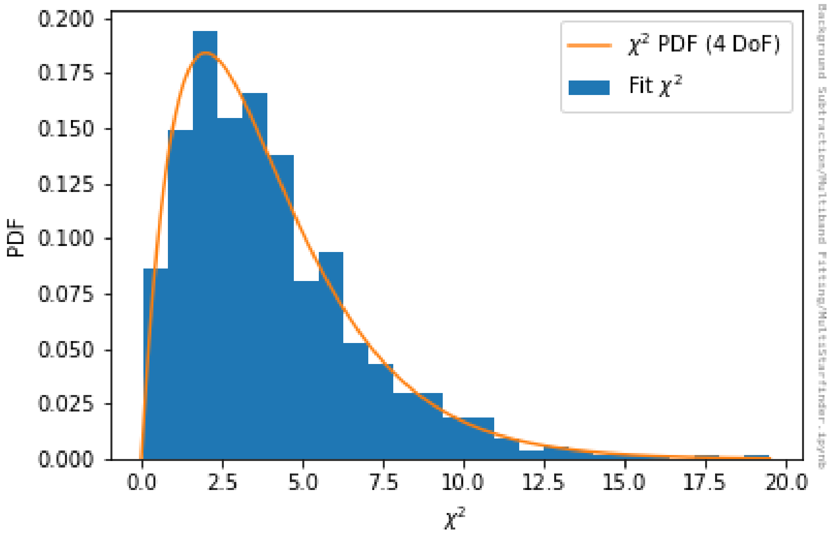

(a) χ^2, linear scale

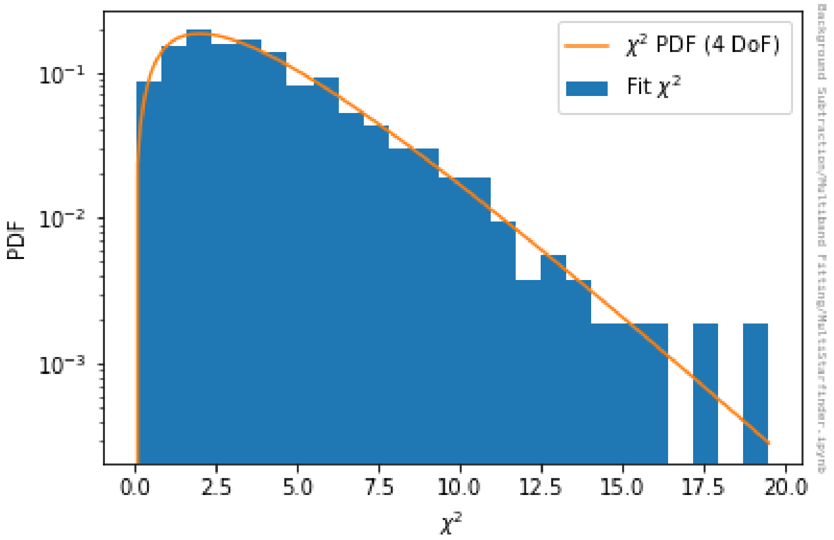

(b) χ^2, logarithmic scale

Figure 3.4: χ^2 histogram for modified-blackbody SED fits (blue) compared to the expected χ^2 distribution with 4 degrees of freedom (orange). We show both linear (a) and logarithmic (b) scales to demonstrate the absence of extreme outliers.

of the χ^2 values from the SED fits matches the expected χ^2 distribution with the correct number of degrees of freedom; see Figure 3.4.

An additional complication is incorporating a boost correction in the regime of multiband detection. The boosts can be computed in the empirical mode of the single-band case described above (Section 3.1.1) by simply treating the combined map M_{combined} (Equation 3.2) as a single-frequency map. As before, S_{detected} is the StarFinder output flux, and S_{true} is a proxy for the input flux density that is calculated in map space. $S_{\text{detected}} - S_{\text{true}}$ gives the level of boosting.

Figure 3.5 shows boosts calculated in the 10m and 30m cases, under the assumption that the sources obey a 10 K modified blackbody SED. The 10m case (Figure 3.5a) shows boosting in the dim sources as before. However, the 30m case (Figure 3.5b) apparently no longer has any noticeable boosting, even for dim sources. It is surprising that the 30m boost vanishes, but previous works have found substantial variations in the level of boosting depending on the observational scenario and details of the method. For example, Zavala et al. (2017) found a fractional boost of only 10% at low measured flux densities, which quickly fell to zero for higher measured flux densities, while Wang et al. (2017) found a boost of 30% for the lowest measured flux densities that gradually approached zero. Thus, it does not seem unreasonable that the 30m boost is apparently insignificant.

Integrating the boost correction into the pipeline requires a final step of redistributing the boost among the observing bands. The optimal way to perform this redistribution is not perfectly clear, and so it remains a subject for future work. One possibility may be to distribute the combined boost $\Delta S_{\text{combined}}$ proportionally to the weight factors w_ν. However, a few factors lead us to believe that it is not critical to develop machinery for the multband boost correction. For one, as shown above, the 30m case has an apparently negligible boost. In addition, we have not found evidence that the residual source boosting leads to a bias in the SZ signal in the multiband regime: see, e.g., Figure 5.1. Finally, we expect the bias to be subdominant to the lensing deficit of Section 2.4, and so any bias due to boosting could be characterized in map space in an analogous way to the lensing deficit correction; see Section 3.3.

As a final detail of the multiband source fitting procedure, we note that the presence of the SZ signal may bias the recovered flux densities of the point sources (and vice versa). To mitigate this effect, it is necessary to jointly fit for the source fluxes and the SZ signal. We implement this joint fitting by an iteration cycle in

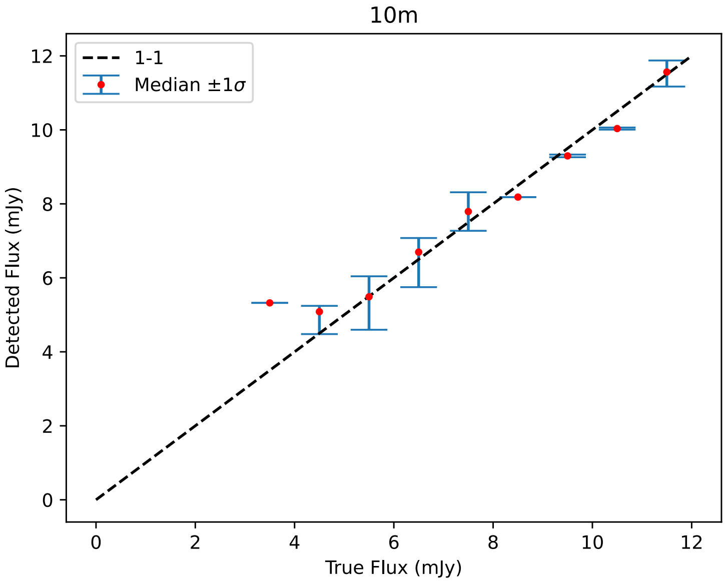

(a) Combined 10m boosts

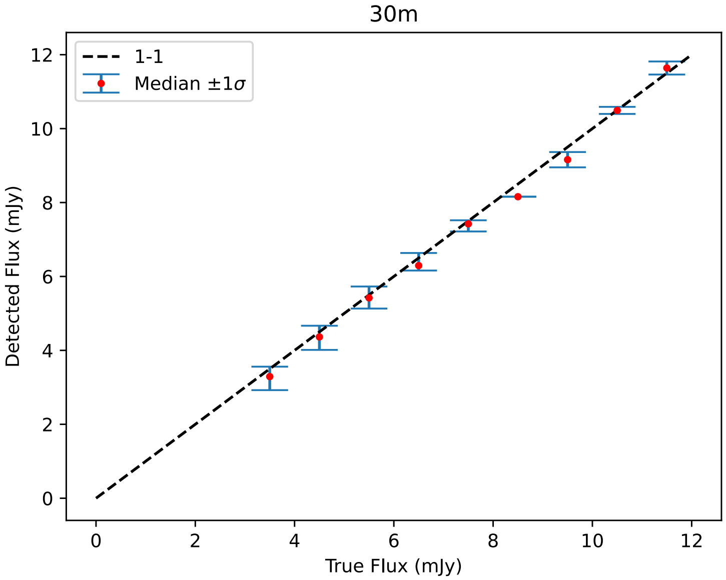

(b) Combined 30m boosts

Figure 3.5: Demonstration of boosting in multiband detections, showing detected flux density as a function of true flux density for 10m (a) and 30m (b) telescope diameters. Detections are binned by true flux density; within each bin, the distribution of detected flux densities is indicated by the median (red dots), and 16% 84% levels (blue bars). The dashed line represents equality between the detected and true flux densities.

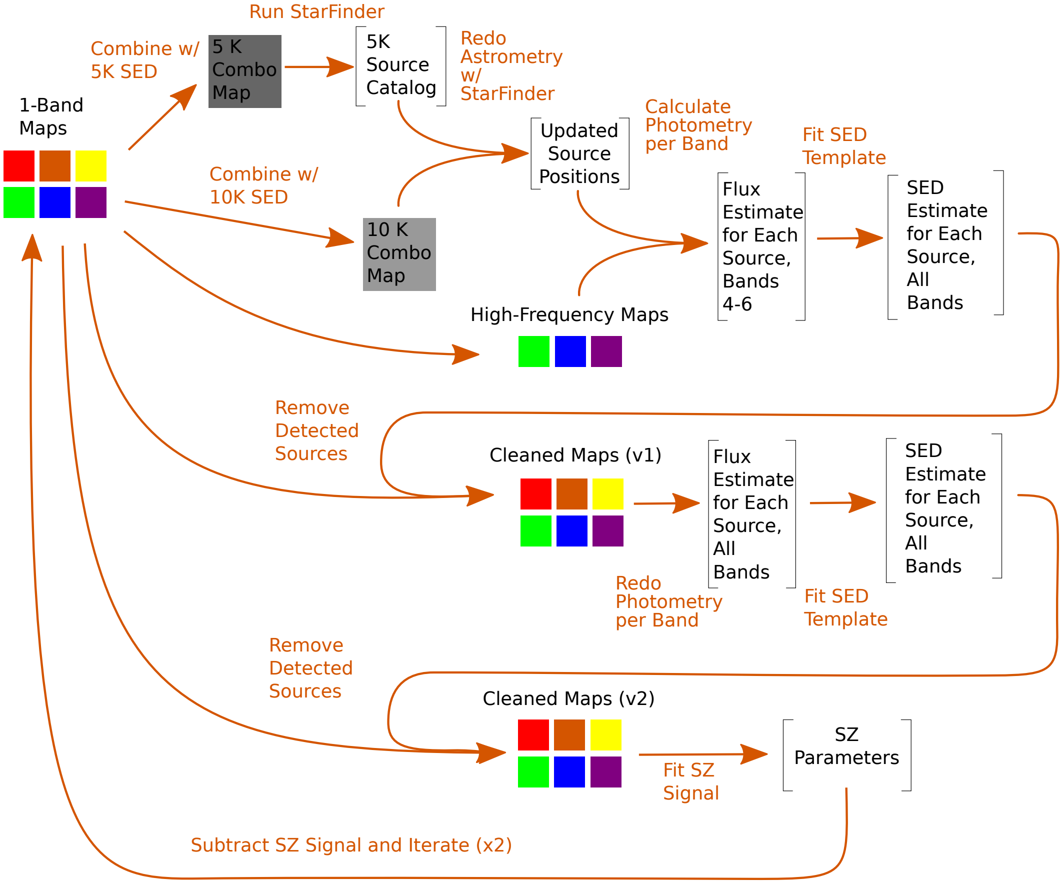

Figure 3.6: Detailed diagram describing the steps of the multiband source removal algorithm, beginning from the raw input maps (labeled “1-Band Maps”).

which we alternate between fitting for CIB sources and SZ signal, as illustrated in the diagram in Figure 3.6.

3.2 CMB Removal

As described in Section 2.3.2, the mock observations include a model of the primary CMB anisotropies. The primary CMB anisotropies follow the same frequency spectrum as the non-relativistic kSZ signal. In particular, in units of CMB temperature, both of these components are independent of frequency. Thus, to recover the kSZ signal without bias, it is important to remove the primary CMB anisotropies from the maps as well as possible.

In our observational scenario, the relevant components are the primary CMB, the tSZ signal, and the kSZ signal. The literature contains numerous examples of CMB component separation methods; see, e.g., Leach et al. (2008) and Delabrouille et al. (2009b) for a review.[4] We use a combination of two techniques to separate these components. To separate the tSZ signal out from the other two components, we use the well-known internal linear combination technique (ILC; e.g., Remazeilles et al. (2011)). From the output of the ILC procedure, we use a technique known as inpainting to separate the kSZ and CMB signals. At the end, we can recombine the tSZ and kSZ signals as the input to the fitting technique described in Chapter 4. We describe the component separation techniques in more detail below.

We note that our final set of mock observations and analyses in Chapter 5 does not include any CMB anisotropies. This is because we have not had time to fully incorporate the removal algorithms described below into our pipeline. However, we have implemented them and tested them in isolation, and they give unbiased results in these simplified scenarios. A future publication will show updated versions of these simulations with the primary CMB component included and treated fully in the analysis.

3.2.1 tSZ Separation by Internal Linear Combination

Our task is to separate the tSZ signal from the CMB and non-relativistic kSZ signal in a multifrequency map. The ILC algorithm performs this separation based on the known frequency dependences of the components. ILC is a good choice because it is fast and easy to implement, and it only requires some conservative assumptions about the data, although it can be biased if any of the unmodeled components are correlated with the CMB (Delabrouille et al., 2009a).

To describe the ILC procedure, we follow the nomenclature of Remazeilles et al. (2011), except that we work with quantities in 2D Fourier space as a function of $\boldsymbol{\ell}$ instead of map pixels.[5] We can first write the data map $x_i(\boldsymbol{\ell})$ at each frequency i as the sum of its components:

$$x_i(\boldsymbol{\ell}) = a_i s(\boldsymbol{\ell}) + b_i y(\boldsymbol{\ell}) + n_i(\boldsymbol{\ell}), \tag{3.3}$$

where the a_i is the (constant) known frequency dependence of the CMB, $s(\boldsymbol{\ell})$ is the spatial dependance of the CMB plus the kSZ signal, b_i is the known frequency dependence of the tSZ signal, $y(\boldsymbol{\ell})$ is the spatial dependence of the tSZ signal, and $n_i(\boldsymbol{\ell})$ is the noise in the map. The noise term $n_i(\boldsymbol{\ell})$ includes instrument noise as well as any residual contamination from the point-source removal step described

---

[4] NASA Legacy Archive for Microwave Background Data Analysis (LAMBDA) provides a list of techniques for CMB analysis: http://lambda.gsfc.nasa.gov/toolbox/tb_comp_separation.cfm.

[5] Under the flat sky approximation, $\boldsymbol{\ell}$ is related to the angular multipole ℓ as $|\boldsymbol{\ell}| = \ell$.

in Section 3.1. Rewriting in vector form, where the components of the vectors correspond to the frequencies i, this becomes:

$$\boldsymbol{x}(\boldsymbol{\ell}) = \boldsymbol{a}s(\boldsymbol{\ell}) + \boldsymbol{b}y(\boldsymbol{\ell}) + \boldsymbol{n}(\boldsymbol{\ell}). \tag{3.4}$$

In terms of this nomenclature, the goal of the ILC procedure is to obtain a minimum-variance estimate the combined CMB and kSZ signal $s(\boldsymbol{\ell})$ given the frequency dependences $\boldsymbol{a}$ and $\boldsymbol{b}$. We want to estimate $s(\boldsymbol{\ell})$ by forming a linear combination of the frequency channels of the data map, that is:

$$\widehat{s} = \boldsymbol{w}^t \boldsymbol{x}, \tag{3.5}$$

where $\boldsymbol{w}$ is a vector of weights.

The ILC formalism comes in two flavors, which have different criteria for the optimal $\boldsymbol{w}$ besides minimum variance of s. The first of these is the standard version of ILC, in which $\boldsymbol{w}$ is subject to the constraint of preserving the CMB spectrum:

$$\boldsymbol{w}^t \boldsymbol{a} = 1, \tag{3.6}$$

which is to say $\widehat{s}(\boldsymbol{\ell})$ will perfectly match $s(\boldsymbol{\ell})$ in the case that the other components are zero. The standard ILC yields the following weights:

$$\boldsymbol{w} = \frac{a^t \widehat{\boldsymbol{R}}^{-1}}{a^t \widehat{\boldsymbol{R}}^{-1} a} \boldsymbol{x}, \tag{3.7}$$

where $\widehat{\boldsymbol{R}}$ is the empirical covariance matrix among frequencies of the map $\boldsymbol{x}$, calculated by averaging over realizations (index k) of the noise and CMB as follows:

$$\widehat{\boldsymbol{R}} = \sum_k \sum_{i,j} \boldsymbol{x}_{i,k}(\boldsymbol{\ell}) \boldsymbol{x}_{j,k}(\boldsymbol{\ell}), \tag{3.8}$$

where i and j run over the frequency bands.[6] However, these weights do not account for the presence of the tSZ signal, so the standard ILC estimate $\widehat{s}$ is contaminated by the tSZ signal. Such contamination is a problem when trying to recover the kSZ signal from the CMB + kSZ map.

The other version, known as constrained ILC, imposes an additional constraint on the weights, which is that they must zero out the tSZ signal:

$$\boldsymbol{w}^t \boldsymbol{b} = 0. \tag{3.9}$$

---

[6] The covariance matrix can also be computed by averaging over bins of ℓ. However, we have found that this leads to a small bias in the recovered signals $\widehat{s}$ and $\widehat{y}$ in some cases.

Optimizing again for minimum variance subject to both Equations 3.6 and 3.9, one finds

$$\boldsymbol{w}^t = \frac{\boldsymbol{a}^t \widehat{\boldsymbol{R}}^{-1} - \frac{(\boldsymbol{a}^t \widehat{\boldsymbol{R}}^{-1} \boldsymbol{b}) \boldsymbol{b}^t \widehat{\boldsymbol{R}}^{-1}}{\boldsymbol{b}^t \widehat{\boldsymbol{R}}^{-1} \boldsymbol{b}}}{\boldsymbol{a}^t \widehat{\boldsymbol{R}}^{-1} \boldsymbol{a} - \frac{(\boldsymbol{a}^t \widehat{\boldsymbol{R}}^{-1} \boldsymbol{b})^2}{\boldsymbol{b}^t \widehat{\boldsymbol{R}}^{-1} \boldsymbol{b}}}. \tag{3.10}$$

As an simple explanation of the behavior of Equation 3.10, we note that the first term in the numerator estimates the CMB in a manner similar to Equation 3.7, while the second term in the numerator removes any correlation between the tSZ template and the map. The second term of the denominator is needed to adjust the normalization to preserve the CMB and satisfy Equation 3.6, as the tSZ removal from the numerator also subtracts some of the CMB on average due to its correlation with tSZ.

With this result, the CMB + kSZ component can be estimated efficiently without contamination from tSZ. The tSZ component can also be estimated by swapping each instance of $\boldsymbol{a}$ and $\boldsymbol{b}$. Given that we know the spectrum $\boldsymbol{b}$ of the tSZ signal, there is no reason to prefer standard ILC over constrained ILC in our scenario. See Eriksen et al. (2004) for a derivation of this result that uses the method of Lagrange multipliers.

An important difference between our version of algorithm and the Remazeilles et al. (2011) original is that we consider relativistic corrections to the SZ signal. To do this, we reinterpret Equation 3.4 such that the $\boldsymbol{b}y(\boldsymbol{\ell})$ term includes the relativistic SZ corrections. The relativistic corrections include both relativistic tSZ and relativistic kSZ, which depend on the cluster's temperature T_e and velocity v_z (Section 2.2). Thus, if the T_e and v_z are known, then the frequency dependence $\boldsymbol{b}$ is known, and so the ILC weights of Equation 3.10 can recover the CMB + nonrelativistic kSZ component without bias. Figure 3.7 demonstrates this fact.

However, in practice, we do not have perfect knowledge of T_e and v_z. We may improve the reconstruction of the relativistic tSZ corrections through a prior on T_e, which we shall motivate later in Section 4.1.2. With a 10% prior, we expect the error in the rSZ reconstruction to be a modest perturbation on the CMB reconstruction. Moreover, the relativistic kSZ signal is small to begin with, so it may be safe to neglect, or it may be reconstructed iteratively with information on v_z from prior fitting of the SZ signal. Ultimately, one must characterize the bias on velocity reconstruction due to these effects.

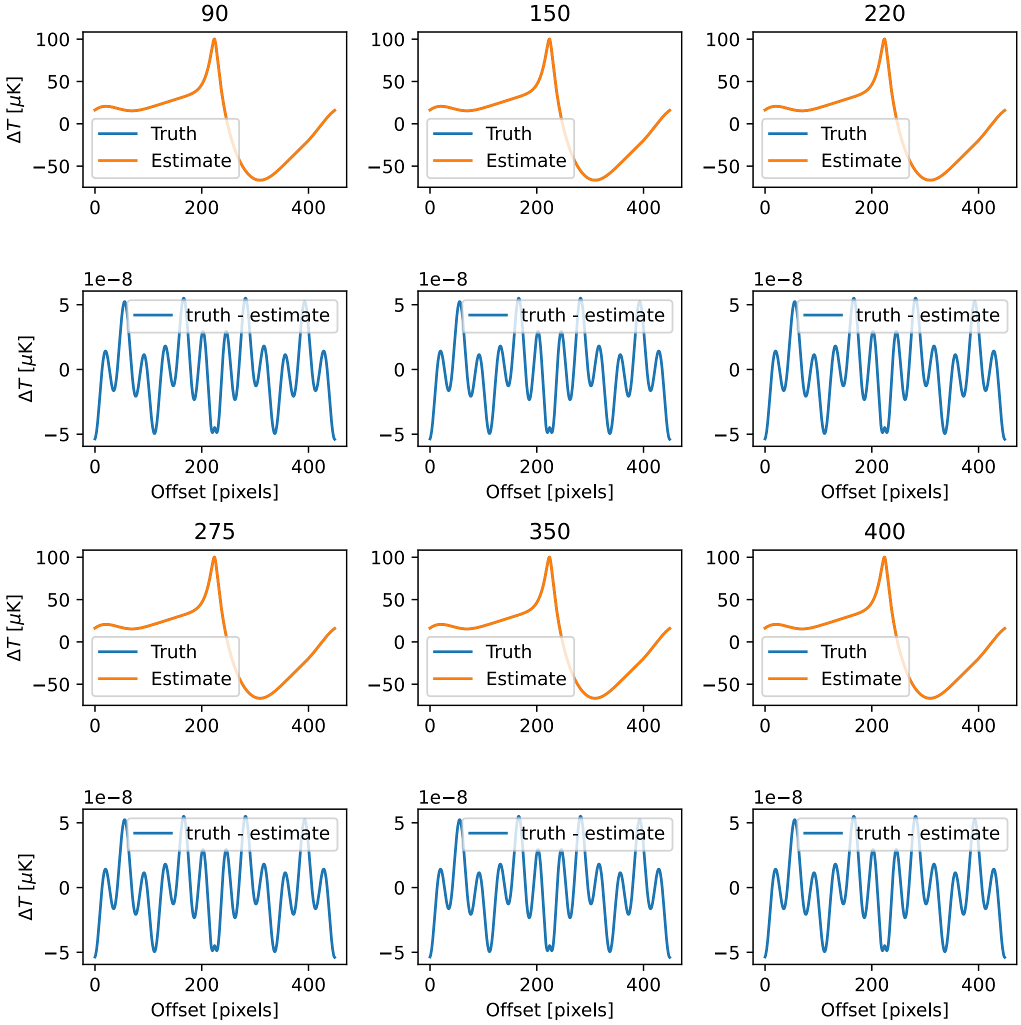

Figure 3.7: Demonstration of ILC performance in an ideal scenario. The top two rows show 90-220 GHz, while the bottom two rows show 270-400 GHz. The top panels (first and third rows) show the ground truth value of the CMB + kSZ component compared to the ILC estimate, and the bottom panels (second and fourth rows) show the residual at a fractional level of 10^{-9}. In this test, the mock observation contains the CMB anisotropies and the full relativistic SZ signal but no noise, and the ILC weights are calculated with the exact value of the relativistically correct SZ spectrum. The residuals contain oscillatory artifacts, which are due to the Fourier-space reconstruction.

3.2.2 kSZ Separation by Inpainting

Removing the tSZ signal as described in Section 3.2.1 yields an estimate of the frequency-independent map $s(p)$,[7] which contains the primary CMB and the nonrelativistic kSZ signal. The remaining problem is to separate these two signals using spatial information alone. The CMB power spectrum peaks at large angular scales (1°; $\ell \sim 200$) and is exponentially damped at increasing ℓ, while the kSZ signal of a galaxy cluster tends to peak at scales of a few arcminutes, or $\ell \gtrsim 3000$ (Alonso et al., 2016). We can improve the estimate of the spatial scale of the kSZ signal if the tSZ signal is known, since the two SZ signals are spatially correlated. Using this prior knowledge of the kSZ and CMB power spectra, it is possible to separate the two signals in the map.

There are several practical ways to apply this prior knowledge to reconstruct the kSZ signal. The simplest approach is to use aperture photometry with a radius set to include the cluster signal (Alonso et al., 2016). However, this approach yields relatively low S/N on the kSZ signal. Two other classes of techniques can improve on aperture photometry: namely, matched filters and inpainting. A matched filter can be constructed with knowledge of the CMB angular power spectrum and an estimate of the SZ profile. We describe inpainting in more detail below. Both techniques are useful in different cases, but, in this work, we use a technique based on inpainting because it can effectively separate non-CMB signals without precise knowledge of their power spectra.

Inpainting algorithms work based on the fact that the central part of the constrained ILC map is dominated by kSZ but has CMB contamination, while the outer part is dominated by CMB. We use the outer parts of the map to make an estimate of the CMB in the inner part, which we subtract to recover kSZ. Several authors have developed methods for estimating the CMB component in the inner region of the map. As one early example, (Forni et al., 2005) estimated the CMB in the inner region by fitting a 2D spline to the outer region. One can improve on the spline fits, however, by constructing CMB realizations that have the known correct power spectrum. The realization must then be constrained to match the outer region of the map. This is known as the method of constrained Gaussian realizations (Hoffman et al., 1991). Several CMB lensing studies have used this latter variant of inpainting to remove kSZ contamination (Benoit-Lévy et al., 2013; Raghunathan et al., 2019).

---

[7] p refers to the pixel in map space; $s(p)$ is the inverse Fourier transform of $s(\boldsymbol{\ell})$ from the prior section.

In addition, several analyses of Planck data (e.g., Planck Collaboration et al., 2018) have used inpainting with constrained realizations to recover kSZ from CMB maps.

In this work, we use an inpainting algorithm based on the constrained realization method of Raghunathan et al. (2019). The reference uses the variable T for the true CMB temperature field in the map— $s(p)$ from the previous section is the sum of T and the kSZ signal—but we note that this field is represented as a vector over map pixels, so here we denote it with the bold symbol $\boldsymbol{T}$. The algorithm begins by defining a mask that separates $\boldsymbol{T}$ into an inner region (region 1), which is a circle of radius R_1, and an annular outer region (region 2) with outer radius R_2. Both regions are concentric with the centroid of the tSZ signal. The goal of the algorithm is to find the most likely CMB signal $\hat{\boldsymbol{T}}_1$ in region 1 given the signal $\boldsymbol{T}_2$ in region 2 and the CMB covariance matrix $\hat{\mathbf{C}}$.

To estimate $\hat{\mathbf{C}}$ for the region of our map, we generate random Gaussian realizations of the CMB in the same manner as in Section 2.3.2, using CAMB as the source of the CMB power spectrum. We may then calculate $\hat{\mathbf{C}}$ in the usual manner for each Gaussian realization $\boldsymbol{G}_i$; we average over n such realizations as follows:

$$\hat{\mathbf{C}} = \frac{1}{n-1}\sum_{i=0}^{n}(\mathbf{G} - \langle\mathbf{G}\rangle)(\mathbf{G} - \langle\mathbf{G}\rangle)^T. \tag{3.11}$$

We follow Raghunathan et al. (2019) in choosing $n = 50000$ to produce a satisfactory estimate. $\hat{\mathbf{C}}$ can then be separated into parts with pixel indices corresponding to regions 1 and 2:

$$\hat{\mathbf{C}} = \begin{pmatrix} \hat{\mathbf{C}}_{11} & \hat{\mathbf{C}}_{12} \\ \hat{\mathbf{C}}_{21} & \hat{\mathbf{C}}_{22} \end{pmatrix}. \tag{3.12}$$

With an estimate of the full covariance matrix, we can proceed to estimate $\hat{\boldsymbol{T}}_1$. Given $\boldsymbol{T}_2$, $\boldsymbol{T}_1$ follows a Gaussian probability distribution with a mean of

$$\overline{\boldsymbol{T}}_1 = \hat{\mathbf{C}}_{12}\hat{\mathbf{C}}_{22}^{-1}\boldsymbol{T}_2 \tag{3.13}$$

and a covariance of

$$\boldsymbol{\sigma} = \hat{\mathbf{C}}_{11} - \hat{\mathbf{C}}_{12}\hat{\mathbf{C}}_{22}^{-1}\hat{\mathbf{C}}_{21} \tag{3.14}$$

(Benoit-Lévy et al., 2013). The most likely $\hat{\boldsymbol{T}}_1$, then, is simply given by Equation 3.13. Benoit-Lévy et al. (2013) argue for using an additional random realization $\tilde{\boldsymbol{T}}$ (which is $\tilde{\boldsymbol{T}}_1$ in region 1 and $\tilde{\boldsymbol{T}}_2$ in region 2) to match the covariance σ. When one requires the mean of this realization to satisfy Equation 3.13, one obtains a corrected estimator for $\boldsymbol{T}_1$:

$$\hat{\boldsymbol{T}}_1 = \tilde{\boldsymbol{T}}_1 + \hat{\mathbf{C}}_{12}\hat{\mathbf{C}}_{22}^{-1}(\boldsymbol{T}_2 - \tilde{\boldsymbol{T}}_2). \tag{3.15}$$

Raghunathan et al. (2019) follow this approach. However, in our tests, we have found that Equation 3.13 is sufficent to reconstruct the kSZ signal.

As a caveat to the above, we note that $\boldsymbol{T}_2$ contains noisy small-scale modes, whereas for reconstructing the CMB, we are only interested in preserving the large-scale modes. These small-scale modes appear in $\boldsymbol{T}_2$ because the window function—the outer region as defined above—has a hard cutoff in map space, which amounts to a convolution in frequency space, i.e., mode mixing. To mitigate this mode mixing, we apply a spatial low-pass filter to the input map before applying Equation 3.13 or 3.15 to estimate $\boldsymbol{T}_1$ (J. Kim, 2020, private communication). The filter is set to remove modes above $\ell = \ell_{\mathrm{LPF}}$, which corresponds to the inner radius R_1 of the mask.

We take a moment to indicate our preferred values for the mask parameters. While R_1 could be optimized for the particular cluster being considered, we have chosen the generally applicable value of $R_1 = 5'$ based on our testing. We use $\ell_{\mathrm{LPF}} = 2160$ for the filter to match this value of R_1. In addition, prior testing by Benoit-Lévy et al. (2013) and Raghunathan et al. (2019) suggests that a small annulus is sufficient (and desirable, for computational efficiency); we use $R_2 = 20'$.

We note that a potential shortcoming of the above approach is the way in which it assumes there is no CMB information in region 1 and there is only CMB information in region 2. A smoother weighting scheme is probably closer to optimal and less subject to bias. In the future, we plan to publish an updated version of the Raghunathan et al. (2019) algorithm that uses such a smooth weighting scheme.

3.3 Lensing Bias Correction

As we described in Section 2.4, previous works have found that gravitationally lensed CIB sources can lead to a bias in the SZ signal recovery. Indeed, in our tests, we found a 1–2σ bias in the cluster velocity estimate in maps that included lensed CIB. In particular, to clarify the sign convention, we found

$$v_{z,\mathrm{estimate}} - v_{z,\mathrm{true}} \lesssim -\sigma_v \tag{3.16}$$

for the cluster we tested, which had properties close to those of the real cluster MACS J0329.6-0211. This bias remained after two iterations of CIB cleaning (Section 3.1) and SZ fitting. Thus, we determined that there was a need to correct for the effect of lensing to reduce the bias in the velocity estimate.

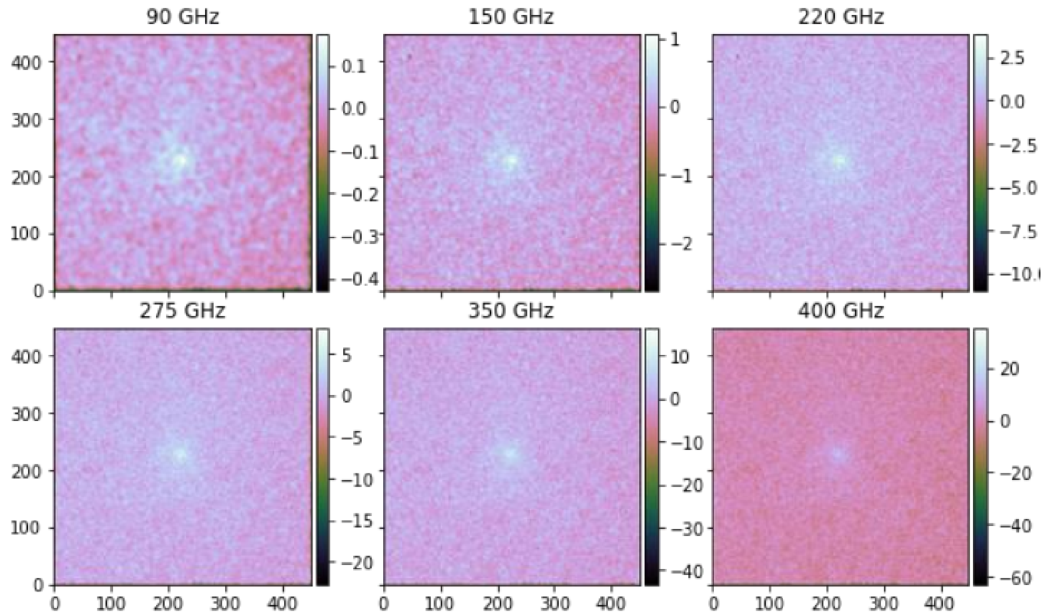

Figure 3.8: Example maps of the mean lensing bias correction for 100 CIB realizations. A positive value in the map indicates that the source removal algorithm overestimates the CIB (and thus underestimates the residual) on average. In the final calculation, these maps are cropped by 5σ of the lowest-frequency Gaussian beam to remove edge effects. Units of the color scale are μJy/pixel for a pixel size of 4 arcseconds.

To better characterize the lensing bias, we wish to understand how lensing affects the CIB reconstruction independently of the SZ signal. To this end, we generate an ensemble of 200 lensed CIB realizations using the mass model of the cluster we wish to analyze.[8] These realizations also include instrument noise, although we have found that it affects the calculation only modestly. With each realization, we identify and fit for sources using the multiband removal procedure of Section 3.1. We then calculate the average (over realizations) residual map in each frequency band. To minimize effects from strongly-lensed sources, we calculate this combination as the mean over all realizations of each pixel after clipping outliers with a 5σ threshold. The result is that, for a pixel with coordinates (x, y) and frequency ν, we can express the bias correction $b_\nu(x, y)$ as follows:

$$b_\nu(x, y) = \frac{1}{n(x, y)} \sum_i r_{\nu,i}(x, y), \tag{3.17}$$

where the $r_{\nu,i}(x, y)$ are the pixels of the $n(x, y)$ residuals i that fall within the 5σ

---

[8] In a real-world analysis, it would be necessary to estimate the cluster mass model either by iteration or using an external data source.

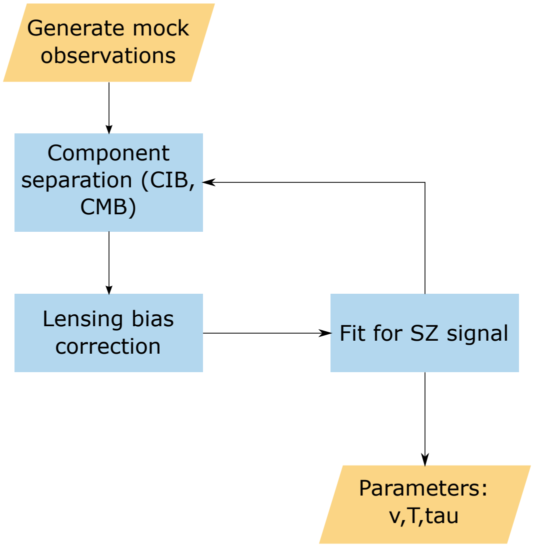

Figure 3.9: Flow chart illustrating the SZ reconstruction process with the lensing bias correction included.

threshold. See Figure 3.8 for example maps of the bias correction.

Figure 3.9 illustrates how the lensing bias correction is integrated into the analysis pipeline. On each pass of CIB removal, which is slightly over-subtracted due to lensing bias, we add back the CIB lensing bias determined in the above manner, prior to the SZ fitting for that pass. Some iteration is still necessary to recover the SZ signal in an unbiased way. In practice, we have found that two iterations of this procedure are generally sufficient.

We have confirmed that applying the lensing bias correction reduces the bias in our estimate of v_z to well below 1σ. However, we have not had time to fully incorporate the correction into our pipeline, so we have not included SZ constraints with lensing in our results.

Chapter 4

EXTRACTING CLUSTER PHYSICAL PROPERTIES FROM RECONSTRUCTED SZ MAPS

After the mock images have been cleaned of the relevant contaminants, we wish to infer the cluster properties from the map-space data. In this chapter, we describe the procedure used to analyze the cleaned maps and extract relevant cluster parameters along with their uncertainties. Section 4.1 discusses the extraction of properties defined as a scalar value for the entire cluster (e.g., the bulk velocity and mass-weighted mean temperature), while section 4.2 describes a simple way to map out constraints on internal cluster properties.

4.1 Bulk Cluster Properties

Our goal is to simultaneously constrain the bulk properties of the intracluster medium—peculiar velocity (v_z), ICM electron temperature (T_e), and optical depth (τ, Equation 2.5)—given mock observational map data. Extracting these bulk parameters provides the necessary inputs to several types of cosmological analyses. The cluster peculiar velocity v_z, which can be used to constrain the behavior of dark energy and gravity on large scales as in Bhattacharya et al. (2008) and Kosowsky et al. (2009), is of primary interest in this work. The other parameters T_e and τ, which are degenerate with v_z in their effect on the total SZ signal, must be constrained simultaneously as nuisance parameters.

The choice of parameterization in terms of v_z, T_e, and τ is not unique. One may, for example, use the Compton y parameter (Equation 2.2) instead of τ. This choice is somewhat arbitrary, but we use τ for the convenient fact that both the kSZ and tSZ signals scale with it, so it is natural to calculate it as an intermediate component of the cluster model.

4.1.1 Least-Squares Fitting

We constrain the ICM properties of our mock observations by fitting a noiseless analytical model analogous to the one used to generate the mock observations as described in Chapter 2. This model is composed of the ICM model of Section 2.1 and a description of the telescope's beam and the signal transfer function as in Section 2.5. The free parameters of this model include the GNFW pressure normalization P_0, an isothermal temperature component T_e, a single bulk velocity component v_z, the scale radius r_s, an x, y position on the sky, and, in certain cases, the GFNW slope parameters α, β, and γ. We assume the clusters are spherical for simplicity. In addition, we assume that the beam and transfer function have been fully characterized in advance, so we do not parameterize them in the fitting process. The reported value of τ is the average optical depth within a $1'$ radius.

We chose this model because it is straightforward to implement and fit. Moreover, fitting a model in this way enables us to robustly characterize non-Gaussian uncertainties, in contrast to Fisher matrix methods; see Section 4.1.2 below for details. In addition, the form of the ICM model is a good match to the average shape of hydrodynamically simulated clusters. While this approach does ignore deviations from smooth radial profiles, we will show using simulated clusters that this approach does not create significant biases.

We consider two different types of mock observations, each of which uses a different description of the cluster: (a) a smooth, analytical, radial profile, referred to as the "analytical case," and (b) a map of a hydrodynamically simulated cluster lacking azimuthal symmetry. The analytical case serves as a useful starting point for which the computational machinery has already been implemented. The second case, the "simulation-based case," which can be viewed as a generalization of the first, will be necessary for process validation and for application to real observations. It is natural to discuss the analytical case first, as the machinery for fitting in the simulation-based case builds upon that for the analytical case.

In the analytical case, it suffices to perform a least squares fit using the analytical model described above. The goal of the fitter is to minimize the value of the χ^2:

$$\chi^2 = \sum_i \frac{(D_i - M_i)^2}{\epsilon_i^2}, \tag{4.1}$$

where D_i is the data vector, M_i is the model vector, and ϵ_i is the noise RMS per pixel; the index i runs over all map pixels in all frequency channels. The data vector D_i is the output of the mock observation pipeline, including noise and all contaminants, while the model vector M_i consists of the projected SZ signal of the cluster alone. While it is necessary in real observations to allow the noise rms ϵ_i to vary from pixel to pixel, we assume for simplicity in this work that ϵ_i is a constant function of position on the sky and varies only with observing frequency.

We explored two choices for the fitting algorithm, namely, the Levenberg-Marquardt (Levenberg, 1944; Marquardt, 1963) and Nelder-Mead (Nelder et al.,

1965) algorithms. The Levenberg-Marquardt (L-M) algorithm works by estimating the gradient of the χ^2, while the Nelder-Mead algorithm uses the values of the χ^2 directly.[1] The L-M algorithm is a popular choice because it converges quickly and fitters generally provide uncertainty estimates. The Nelder-Mead algorithm is more robust, but it tends to converge more slowly and, since it does not calculate derivatives, does not automatically give uncertainty estimates.

In the end, we chose to use the Nelder-Mead algorithm for its added robustness. The L-M algorithm failed to converge in enough cases that it impacted our constraints derived from bootstrapping over many noise realizations as described in Section 4.1.2. The downside of slower convergence was mitigated by using high-performance computing (HPC) resources, and, in any case, the least-squares fit was not the computational bottleneck in the analysis pipeline.[2] In addition, we relied on noise resampling to determine the uncertainties (see Section 4.1.2), so we did not need uncertainty estimates based on derivatives.

We have made some effort to adapt the least-squares fitter to work well in the simulation-based case, that is, when the mock data map is more complicated than a simple radial profile. Our tests of this regime have used SZ effect maps derived from the IllustrisTNG simulations (D. Nelson et al., 2019). Although the GNFW model was designed to agree well with hydrodynamical cluster simulations (Nagai et al., 2007), achieving convergence has proven to be somewhat nontrival without manually guiding the fitter, which would be intractable when analyzing a large number of clusters, particularly when using bootstrap resampling as described in the following section. This difficulty appears to be due to the behavior of the fitting algorithm and not a deficiency in the freedom of the GNFW parameterization.

To help automate convergence, we considered (but have not tested) the approach of fitting a one-dimensional profile to determine the shape parameters of the cluster's ICM before attempting to fit the full multiband map, in the hope that the reduced degrees of freedom will improve the convergence of the fit. Here, we describe the proposed steps in detail. First, locate the cluster center in a map by fitting a cluster model using GNFW slope parameters α, β, and γ fixed to the values given in Arnaud et al. (2010), which should be a good match to the general case on average. For simplicity, it should suffice to pick a single frequency band for the fit. Next, calculate an approximate profile by averaging the map in single-pixel-wide

---

[1] Nelder-Mead is also known as the amoeba method. IDL, for example, uses this nomenclature.

[2] The bottleneck was generally the source cleaning algorithm (Section 3.1).

annular bins. Fit this profile with a projected cluster model to obtain estimates of the slope parameters along with the scale radius r_s and the amplitude. There is some degeneracy among these parameters, so it may be necessary to fix one or more of them for the fit to converge. Allowing ellipticity in the GNFW model may also be necessary for certain clusters in practice; one could calculate a profile by averaging the map on ellipses instead of circles, and the ellipses' axis ratios could be determined by alternating with a 2D map fit. Finally, with this estimate of the cluster shape, one may reattempt fitting the cluster model, with its shape parameters fixed, to the full multiband map as described above. The full process—fitting the profile, then fitting the full map—may be iterated to improve the fit.

4.1.2 Characterizing Parameter Uncertainties from Least-Squares Fits

The uncertainty estimates for the fit parameters are most simply described in terms of the covariance matrix, which can be provided by an L-M fitter. However, the use of a covariance matrix depends on the assumption that the uncertainties are Gaussian, which is invalid when the fit parameters have complicated degeneracies. Instead, we use a bootstrapping approach over multiple noise realizations to map out the degeneracy contours. We consider the "degeneracy contours" to be the contours of the 68% and 95% confidence regions in the two-dimensional spaces between pairs of parameters, e.g., the v_z-τ plane. It is important to consider the degeneracy contours because they provide a more complete description of the uncertainty on the value of a parameter than, e.g., 1-dimensional confidence intervals. In addition, approximating the uncertainties as Gaussian can lead to biased estimates of their values.

We note that the three parameters v_z, T, and τ occupy a three-dimensional space, so describing the constraints in terms of 2D regions is an approximation. We have produced an animated visualization (not shown in this thesis) that suggests that the parameters lie on a 2D surface within the 3D parameter space. However, we use the projected 2D contours for ease of visualization and relative simplicity of parameterization.

The bootstrapping procedure begins with a complete fixed set of assumptions about the galaxy cluster being analyzed, the instrument configuration, and the levels of the relevant contaminants. These assumptions are sufficient to generate a mock observation of the cluster up to the specific realizations of the contaminants. To characterize how accurately the cluster properties can be recovered in practice, one may generate multiple noise realizations and then fit these realizations without assuming foreknowledge of the cluster properties. Each realization allows all the relevant noise sources to fluctuate: the instrument noise is realized as Gaussian white noise with the given RMS; the CIB galaxies are drawn from a random field of view within the SIDES catalog; and the CMB realization is generated with the CAMB power spectrum as in Section 2.3. Each realization also accounts for the effect of gravitational lensing of the CMB and CIB by the cluster. Coadding these noise realizations with the mock cluster observation yields a full mock observation.

For each full mock observation, we then deduce the best-fitting set of cluster parameters using a least-squares fit as described above. Finally, we consider the locus of points given by the set of best-fitting parameters from all noise realizations as the basis for constructing confidence regions. Since each set of full mock observations is computationally expensive to generate, we have developed an algorithm to robustly derive degeneracy contours from a relatively small sampling of points. This algorithm and the nature of these degeneracies are described in detail in Appendix A.3.2.

However, even when properly accounting for the curvature of the degeneracies, we find that the 1D parameter estimates are poorly constrained in our nominal observing configuration (see Figure 4.2), which warrants improvement. To help break the degeneracies, one can simulate adding information from a separate T_e measurement by adding a prior. We use a Gaussian prior with a 10% rms.

We considered two ways to obtain such a temperature prior in practice. One possibility is through spectroscopic X-ray observations of the ICM. Current X-ray temperature constraints are limited by calibration uncertainties of Chandra and XMM-Newton, which are discrepant at a typical level of $\sim$ 10%, though this value worsens with increasing temperature (Schellenberger et al., 2015). In addition, the spectroscopic temperature measure T_X provided by X-ray observations is distinct from the temperature T_{SZ} (or T_y) that determines the observed rSZ effect,[3] and so using T_X may introduce both bias and scatter, which must be estimated. Studies of simulated clusters (Biffi et al., 2014; Lee et al., 2022) find that T_X and T_{SZ} are related to the mass-weighted temperature T_m by scaling relations with a scatter of $\sim$ 10%; at worst, these scatters would add in quadrature for an additional factor of $\sqrt{2}$ in the T_X–T_{SZ} relation, though this value would be lower if the individual scatters were

---

[3] The difference arises due to how T_X and T_{SZ} are measured: T_X is weighted by the X-ray luminosity, which scales as n_e^2, while T_{SZ} is weighted by τ, which scales as n_e.

correlated. We optimistically assume that calibration uncertainties will improve in the coming years such that the total uncertainty on T_{SZ} approaches 10%.

An X-ray temperature prior is a good choice for detailed studies of individual clusters. However, it will not soon be feasible to obtain such complementary X-ray observations for the large sample sizes required to constrain cosmology. Thus, one can alternatively obtain a temperature prior using scaling relations. For example, the integrated Compton parameter Y_{SZ} [4] is correlated with the SZ temperature through the Y_{SZ}–T_{SZ} scaling relation. One could obtain an initial estimate of Y_{SZ} by fitting the map with $v_z = 0$ and an assumed T_{SZ}, applying the scaling relation to estimate T_{SZ}, and then iterating and recalculating Y_{SZ} on each pass. However, the efficacy of this process is limited by the Y_{SZ}–T_{SZ} scatter. Figure 5 of Lee et al. (2022) shows the Y_{SZ}–T_{SZ} relation for a collection of simulations; the scatter is dominated by the differences between simulations, but one can infer a $\sim$ 10% scatter by using only the massive clusters within a single simulation.

In a Bayesian approach, as described in Section 4.1.3, it is straightforward to include a prior on temperature or other fitted parameters as a multiplicative factor in the posterior PDF. In our frequentist bootstrapping approach, however, we must use a different method. Since each term of the χ^2 (4.1) corresponds to a single pixel, our approach is to add an artificial pixel D_n to our maps; its value in each noise realization is equal to the known temperature of the cluster plus a Gaussian fluctuation of the specified width. That is, $D_n = M_n + N_n$, where M_n is the model value of T_e and N_n is the specified Gaussian fluctuation with $\sigma = \epsilon_n$. We have verified that this approach gives correct results in the limit that T_e is unconstrained by the data, i.e. the constraint is fully driven by the prior: see, e.g., Figure 4.2.

Figure 4.1 shows how adding a temperature prior affects the degeneracies. It can be seen that having external constraining power on a cluster's T_e can significantly reduce the uncertainty on v_z and τ by cutting across the degeneracy contours. In this example, a 6 keV cluster with a 10% T_e prior yields an 80 km/s constraint on v_z. A 5% prior, which may be achievable in the longer term, can reduce uncertainties even further, yielding a 40 km/s constraint on v_z.

---

[4] Calculating Y_{SZ} requires an aperture size, usually given as a characteristic overdensity radius, e.g. R_{500}. Such an aperture size can be obtained using either a $Y - M$ scaling relation or by using a physical aperture size.

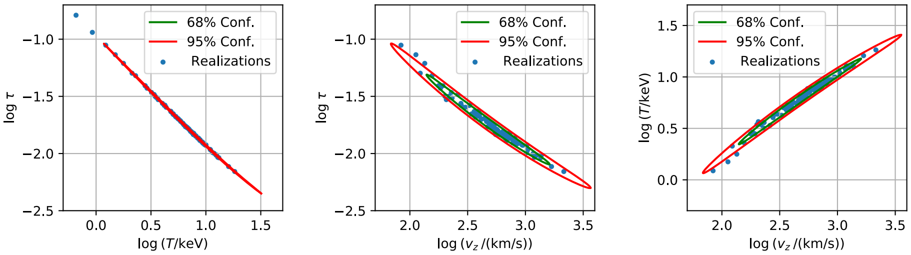

(a) Parameter degeneracies with no prior on T_e

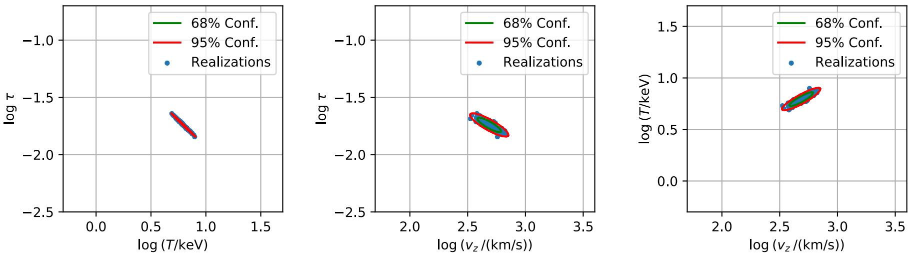

(b) Parameter degeneracies with a 10% prior on T_e

Figure 4.1: Comparison of recovered parameter uncertainties with (a) and without (b) a prior on the gas temperature for an example cluster with $T_e \approx 6$ keV, $v_z \approx 500$ km/s and $\tau \approx 0.02$. The extreme degeneracies among the model parameters are apparent in (a); adding a 10% prior on T_e largely breaks these degeneracies (b), significantly improving the constraints on v_z ($\sim$ 15%) and τ ($\sim$ 10%). See Figure 4.2 for marginalized 1D constraints.

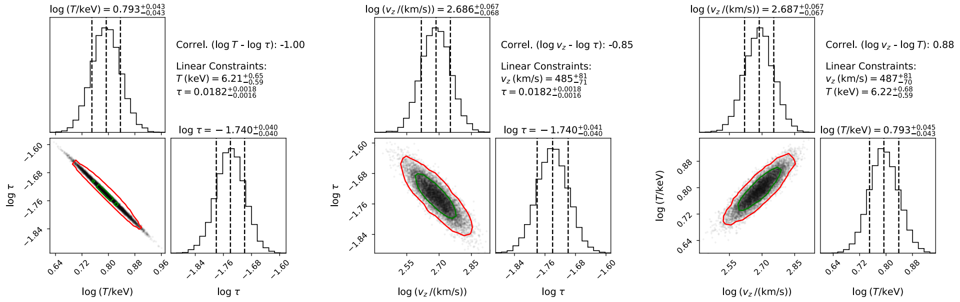

(a) 10% prior on T_e

Figure 4.2: Corner plots showing recovered parameter uncertainties in T_e, τ, and v_z with a 10% prior on the gas temperature for an example cluster with $T_e \approx 6$ keV, $v_z \approx 500$ km/s and $\tau \approx 0.02$. With the degeneracies (Figure 4.1a) broken, the parameters are distributed nearly log-normally and have substantially reduced uncertainties: $\sim$ 15% on v_z and $\sim$ 10% on τ. Moreover, this case demonstrates that the recovery of v_z and τ is not significantly biased.

4.1.3 Markov-Chain Monte Carlo Simulation

To improve the accuracy of the uncertainty estimation, it is likely possible to instead use a Markov-Chain Monte Carlo (MCMC) simulation in lieu of the bootstrapping approach described above. MCMC simulation is a Bayesian technique to sample high-dimensional probability distributions. Compared to the bootstrapping approach, MCMC has the advantage that it can reliably estimate uncertainties independent of the convergence criteria of a least-squares fitter. In addition, MCMC provides a more natural and statistically rigorous method of incorporating prior knowledge of the SZ parameters, especially of the gas temperature T_e. Several codes to perform MCMC simulation are available, such as Mahdavi (2014).

Rather than minimizing a χ^2 as above, MCMC seeks to sample the posterior PDF $P(\boldsymbol{\theta}|\boldsymbol{m})$, where $\boldsymbol{\theta}$ is the vector of cluster model parameters and $\boldsymbol{m}$ is the map data. We can calculate the posterior PDF as the product of the prior probability of $P(\boldsymbol{\theta})$ and the likelihood $\mathcal{L}(\boldsymbol{m}|\boldsymbol{\theta})$. In practice, one operates on the logarithms of these quantities, $\log P$ and $\log \mathcal{L}$, for numerical stability. The likelihood calculation is mechanically similar to the χ^2 calculation above.

However, robust uncertainty estimation with MCMC requires drawing many samples from the posterior PDF. If the log-likelihood is computationally expensive to calculate, this procedure can become intractable. For the test cases with instrument noise alone, it is sufficient to calculate the log-likelihood in terms of the cluster model. With the optimizations described in Section 2.2, it may be tractable to perform a robust MCMC with high-performance computing. However, for the test cases that include contaminants, one should also vary the contaminant models as nuisance parameters. Marginalizing over all CIB sources is particularly difficult, although recent work (Feder et al., 2020) may provide a tractable approach. It would likely require significant effort to adapt our pipeline to vary over all model parameters. In view of the above difficulties and the limited computation time, we rely exclusively on the bootstrapping technique to generate the results in this work. Incorporating an MCMC simulation into our pipeline remains a topic for future work.

4.1.4 Pipeline Validation

To confirm that our pipeline produces realistic outputs, we generated mock observations and calculated a v_z constraint for a cluster in the analysis of Sayers et al. (2019), which used data from a combination of Bolocam and *Herschel*/SPIRE.

We present this comparison in Appendix A.1.1. We obtained a σ_v within a factor of 2 of the value found by the original analysis, and we believe that the differences are likely attributable to complexities in the original analysis that we did not model fully.

4.2 Beam-Scale Constraints

In addition to cluster-scale constraints, it would be useful to place constraints on SZ parameters at the beam scale. Doing so would enable resolving the velocity structure of the ICM within the cluster. We have not had time to calculate any beam-scale constraints for our results, but we have considered how to adapt the pipeline to generate them as a suject for future work. We envisioned a method that makes use of the fitting machinery of Section 4.1: one could simply fit a GNFW model with fixed cluster shape and position while setting the field of view to a small, square region with the same angular scale as the beam. Varying the center of the field of view would enable producing a map of v_z and σ_v.

Chapter 5

RELEVANT EXAMPLES

In this chapter, we present estimates of the line-of-sight velocity precision σ_v from runs of the mock observation and analysis pipeline described in Chapters 2, 3, and 4. We examine the effects of incrementally adding backgrounds and adjusting the noise levels in the maps in Section 5.1. In addition, we explore the constraints achievable with different choices of instrumentation in Section 5.2. We summarize all these velocity constraints in Section 5.3, including reports of the constraints from different galaxy clusters.

5.1 Effects of Backgrounds and Noise Levels

We expect that the precision of the SZ constraints will be chiefly limited by two factors: the noise of the instrument, and the confusion noise. The noise level can be reduced by increasing the number of detectors (or increasing the integration time), while the confusion noise is fundamentally limited by the aperture diameter of the telescope. We list confusion limits for our choice of instrument diameters in Table 5.1, along with estimates of the integration times required to reach each confusion limit for a given diameter. Thus, we are interested in characterizing the effects of our assumptions about noise and the CIB on the resulting SZ constraints.

In this investigation, we explored four different scenarios, which we refer to with the numbers (1) through (4), or with the following shorthand:

1. “NoBkg”: confusion-limited instrument noise, no backgrounds;
2. “CIB”: confusion-limited instrument noise + CIB;
3. “LowNoise”: 10% of confusion-limited instrument noise, no backgrounds;
4. “LowNoiseCIB”: 10% of confusion-limited instrument noise + CIB.

Case (1) represents a roughly current-generation instrument, where the noise levels correspond to the confusion limits in the sense of Section 2.3.3, but it includes only instrument noise without astrophysical contaminants. Case (2) is a more realistic version of case (1) that includes the non-Gaussian CIB component. We were also

Frequency Band (GHz)	5σ Confusion Limit (mJy)			Required Integration Time (s)		
	10m	30m	50m	10m*	30m	50m
90	0.4	0.12	0.06	4262	684	355
150	1.1	0.24	0.09	1038	315	290
220	2.1	0.38	0.14	455	201	192
270	3.0	0.47	0.17	469	276	274
350	4.0	0.62	0.20	241	145	181
400	4.6	0.70	0.22	626	391	512

Table 5.1: Comparison of confusion limits for the instrument configurations. These values represent the 5σ detection threshold for CIB sources. These confusion limits were calculated using SIDES (Béthermin et al., 2017) with the formalism described in Zmuidzinas (2018, private communication). Confusion limits may be converted to map-space RMS values, with units of mJy/beam, by dividing by 5. We also list estimates of the integration times required to reach these confusion limits in practice, based on sensitivities at a high-altitude site such as the Chajnantor Plateau. The integration times assume a focal plane with 0.5 $(F/\#)\,\lambda$ spacing at 350 and 400 GHz and $(F/\#)\,\lambda$ spacing at lower frequencies; appropriate penalty factors have been taken for the lower frequencies to ensure sufficiently dense sampling of the sky. *The integration times listed under 10m were in fact calculated for a diameter of 10.4 m.

interested in exploring a longer-term scenario in case (3), where the instruments are assumed to have noise levels well below the confusion limit; in particular, we assume an improvement by a factor of 10 relative to case (1). Case (4) is the same as case (3) but with a CIB component added. While cases (1) and (3) are less realistic than cases (2) and (4), they provide a baseline for the behavior of the parameter constraints. In addition, the factor-of-10 noise improvement of cases (3) and (4) may not be achievable in practice (a factor of 3 may be more realistic), but we include it to show the implications of a CIB-dominated scenario.

The mock observations to produce the constraints in this section are derived from a cluster model based on the cluster MCXC J1056.9-0337 (also known as MS 1054), which has a mass of $M_{500} = 8.5 \times 10^{14} M.$ and a redshift $z = 0.83$. We provide a comprehensive set of corner plots for different cluster models in Appendix A.2.1. Additionally, we assume a fractional prior of 10% on the temperature T (see Section 4.1.2).

Figure 5.1 shows the constraints from all observational scenarios for this cluster model. Results for other cluster models are shown in Appendix A.2.1 and summarized in Section 5.3.

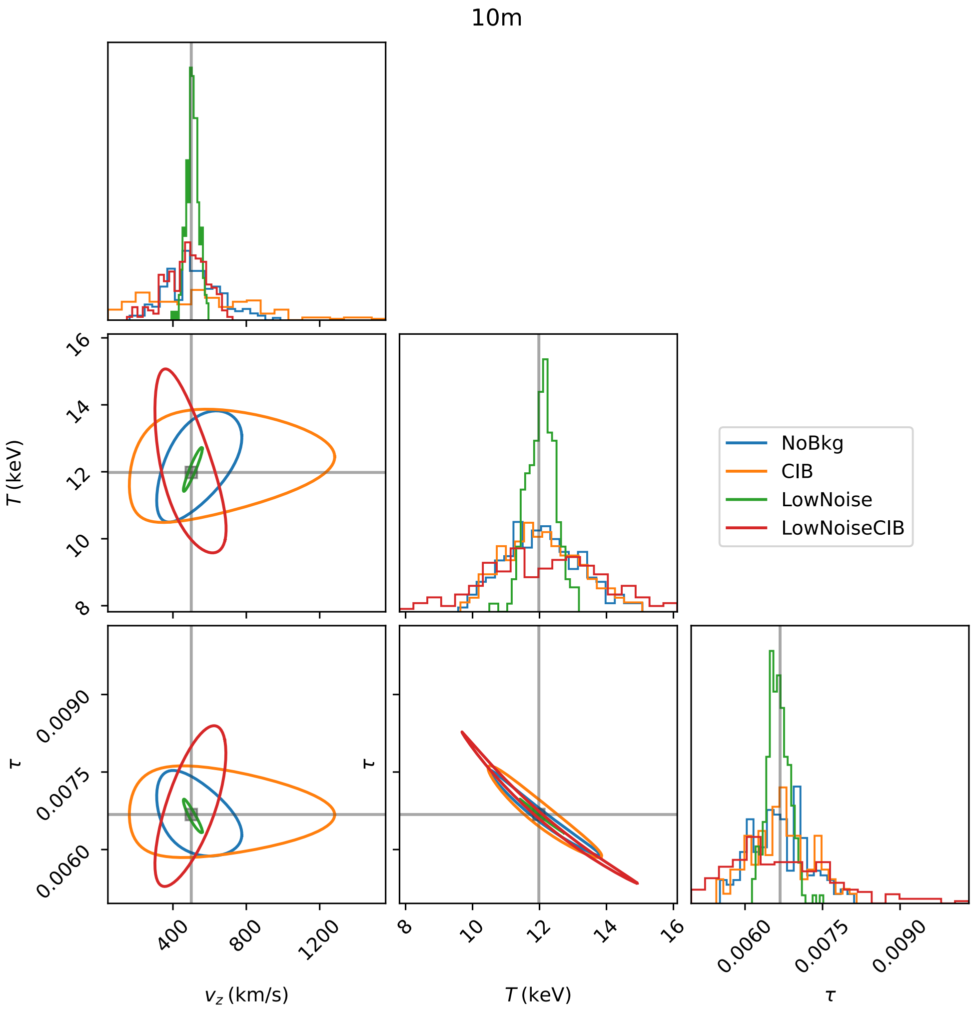

(a) 10m Parameter Constraints

Figure 5.1: 1D histograms and 2D contours showing SZ parameter constraints with different levels of noise and CIB contamination. The 1D histograms comprise the best-fit parameter values for each noise realization, while the 2D contours are 68% confidence regions based on curve fits to this distribution of optimal points for ease of visualization. We consider instruments with aperture diameters of 10m (Figure a), 30m (b), and 50m (c). For each aperture diameter, we show the following scenarios, corresponding to cases (1) through (4) in the text: instrument noise only, with noise at confusion limit ("NoBkg," blue); instrument noise + CIB, with noise at confusion limit ("CIB," orange); instrument noise only, with noise at 10% of the confusion limit (green); and instrument noise + CIB, with noise at 10% of the confusion limit (red). Ground-truth values are indicated with gray lines.

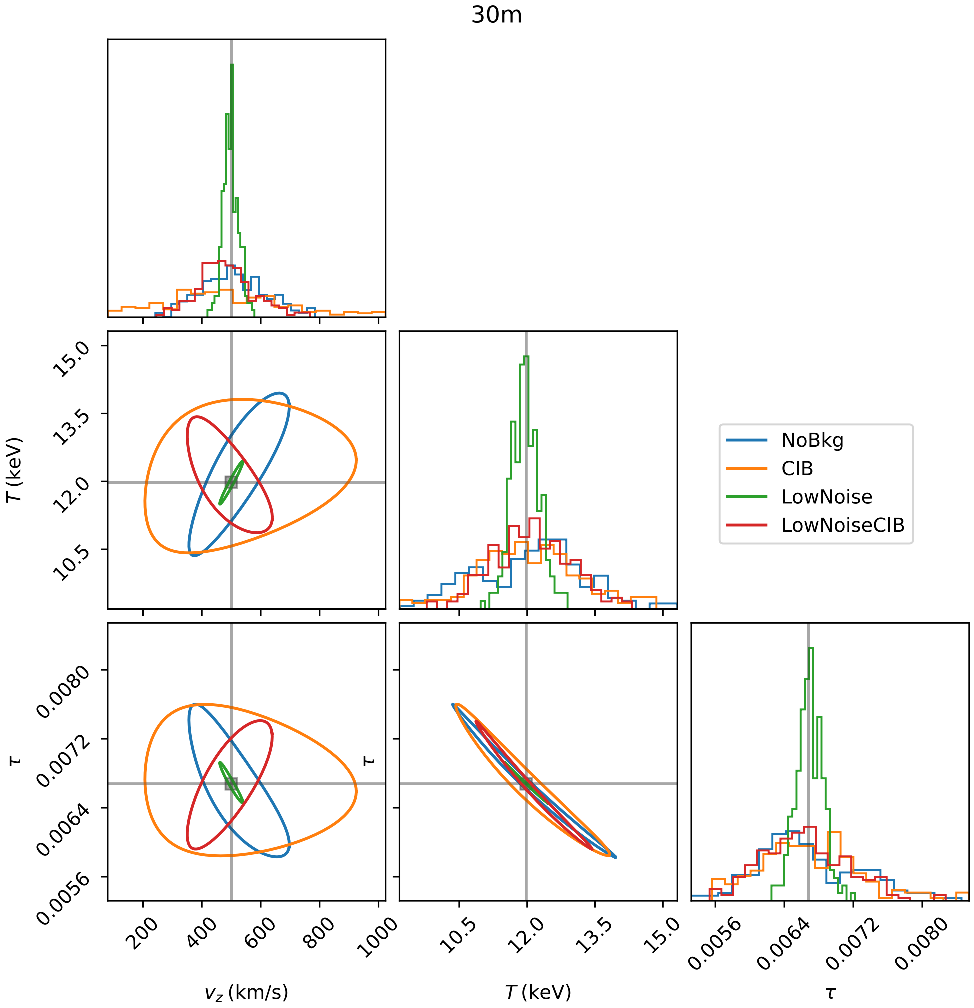

(b) 30m Parameter Constraints

In general, none of the observational scenarios 1-4 shows a large bias in the recovered parameters: all of the true parameter values (gray lines in Figure 5.1) fall within the 68% contours. This suggests that the source subtraction and fitting procedures are valid on at least a basic level.

We compare the constraints achieved by the different scenarios for each instrument class below. Many of these constraints behave similarly for the different instrument classes; the main differences appear to be due to differences in the CIB removal.

5.1.1 10m Diameter

We first address the cases without CIB: cases (1) and (3). The constraints scale in a straightforward way with the noise level: reducing the noise by a factor of 10

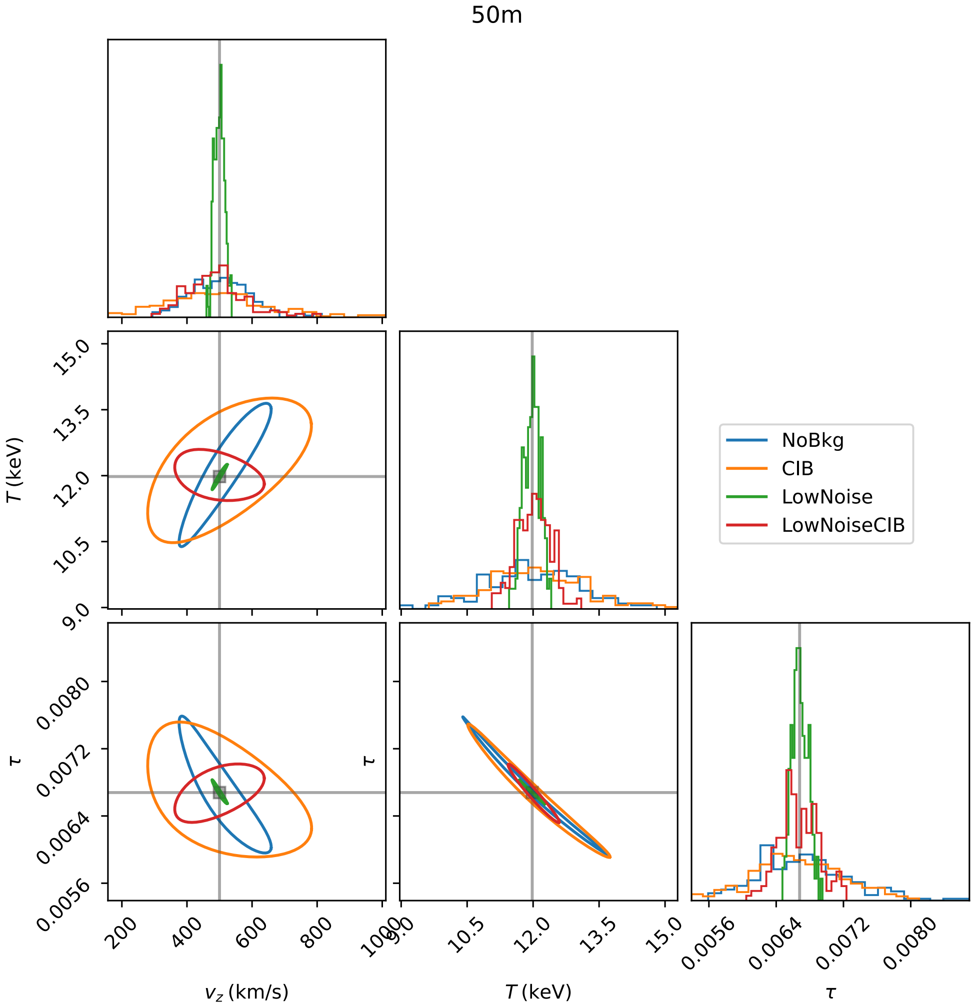

(c) 50m Parameter Constraints

simply shrinks the areas of the constraint regions while roughly maintaining their shapes. Accordingly, the velocity constraint improves with reduced noise, although the strength of this effect depends on the mass and redshift of the cluster as well as the telescope diameter; see Table 5.2 for precise σ_v ratios. Case (1) does not add significant constraining power on T beyond the 10% prior, suggesting that the data are insufficient to constrain the rSZ component. Case (3) also improves upon the rSZ constraint.

The inclusion of the CIB in case (2) significantly degrades the quality of the v_z constraint relative to case (1). This degradation is likely due to the degeneracy between the CIB and the SZ signals. The level of this effect demonstrates the importance of carefully considering the CIB contamination even when the instrument noise is confusion-limited.

It is surprising that the temperature constraint degrades in case (4) compared to case (2) considering the lower noise in case (4). Indeed, the T constraint in case (4) appears to be less precise than the 10% temperature prior. A likely explanation for this behavior is as follows. First, compared to the 30m and 50m cases, the 10m case lacks the resolving power to enable deep CIB cleaning towards the SZ peak. The residual CIB is degenerate with the SZ signals, so a given CIB realization can be fit with a T value that deviates from the prior. Finally, because of the low noise level, the uncertainty estimate from the least-squares fitter is interpreted as having greater precision than the 10% T prior, so the fitter converges to the deviant T value. We have compared the spread of T values for the realizations with the σ_T estimated by the fitter, and we have found that the empirical T spread is roughly 2 times as great, which is consistent with the above explanation. However, rigorously confirming the cause of this behavior is a subject for future investigation. In particular, it is not known with certainty whether the behavior is a fundamental limitation or a deficiency of the CIB removal algorithm.

Despite that case (4) yields a relatively poor T constraint, it still constrains v_z with significantly better precision than in case (2). This may be because a typical dusty galaxy SED more closely resembles the rSZ spectrum than the kSZ spectrum. In particular, the rSZ effect represents a larger fraction of the total SZ signal in the highest frequency bands, from 270 to 400 GHz, while the kSZ effect is fractionally strongest in the middle bands around 220 GHz; see Figure 3.1.

We note that the performance of case (4) is sensitive to the choice of the detection threshold supplied to StarFinder in the source subtraction algorithm. The StarFinder documentation indicates that the detection threshold should be set as the noise RMS in the map. We have found this choice to be valid for the confusion limited case (2), which was the context in which we developed the multiband detection and subtraction algorithm. However, when the instrument noise is reduced, the effective noise level becomes dominated by source confusion, and a threshold based on instrument noise alone becomes too aggressive, resulting in spurious detections. We varied the value of the threshold in case (4), trying factors of 1, 3, 5, and 10 of the instrument noise. We found that the optimal threshold, as determined by the SZ constraints, varies as a function of telescope diameter. However, a factor of 5 is close to optimal for each case, so we use it in the reported constraints for case (4) for consistency. These results may not be fully general, and refining this threshold is a subject for future work.

5.1.2 30m Diameter

As in the 10m case, the constraints from the noise-only cases (1) and (3) simply scale with the noise level. The constraints still degrade when the CIB is added, though the effect is less pronounced than in the 10m diameter case. Cases (2) and (4) improve more significantly due to the greater resolving power. Case (4) can now constrain T to a precision better than the prior's, presumably due to the improved CIB removal.

5.1.3 50m Diameter

The 50m case is qualitatively similar to the 30m case. This suggests that a 30m telescope provides sufficient data to capture much of the behavior due to CIB. The degeneracy shape in case (2) is slightly modified, such that its v_z constraint is only slightly degraded relative to case (1). The improvement in the T constraint is greater, which seems to be the primary benefit of the 50m telescope.

5.2 Effects of Instrumentation Choice

We consider three instrument classes, each with a characteristic diameter: 10m, 30m, and 50m. The primary benefit of large-diameter telescopes for SZ observation, at least in the context of cosmology, is their greater ability to remove point source contamination. At the 50m scale in particular, this mainly seems to improve the T constraint, which makes sense because the T constraint is driven more by high-frequency data than the v_z constraint. These telescopes can also better constrain internal cluster dynamics, though investigating these benefits is a subject for future work. In practice, however, a larger telescope diameter implies a higher construction cost. Thus, it is worthwhile to quantify the benefits of the increased resolving power.

In Figure 5.2, we revisit the SZ constraints of the previous section but instead show all instrument classes on the same axes for each observational scenario. This alternative visualization highlights the incremental impact of each increase in telescope diameter.

The behavior in the CIB-free cases (1) and (3) is not surprising. Increasing the telescope diameter in these cases simply lowers the instrument noise since we scale the instrument noise with the expected confusion noise, were CIB present, for the given telescope diameter. The variation among the diameters in case (3) (Figure 5.2c) is purely a rescaling of elliptical constraint regions. This is also nearly true in

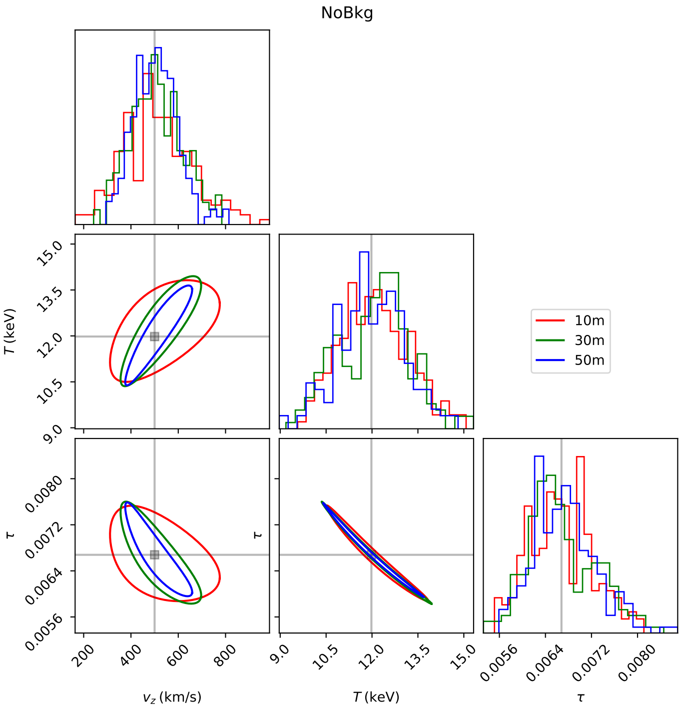

(a) Case 1

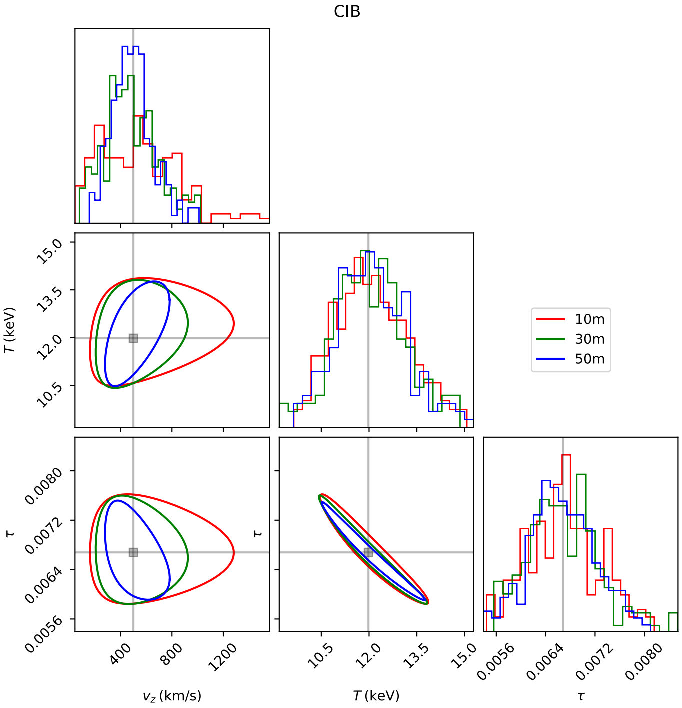

(b) Case 2

Figure 5.2: Corner plots for cases 1-4, showing the difference in constraints between telescope diameters. Shown: case 1 (a), case 2 (b), case 3 (c), and case 4 (d).

case (1) (Figure 5.2a), though the constraint is less elliptical for the 10m diameter.

In the more realistic case (2) (Figure 5.2b), we see a more pronounced improvement in the v_z constraint from increasing the aperture size, especially from 10m to 30m. None of the instrument choices can significantly constrain T, but the added resolving power seems to enable better CIB subtraction in the lower bands, which in turn enables a better kSZ constraint.

In case (4), σ_v surprisingly does not improve significantly from 30m to 50m (Figure 5.2d). This behavior may not be correct, though it may be at least partially explained by statistical fluctuations of order $\sigma_v/\sqrt{2N}$, where $N = 200$ is the number of noise realizations. Investigating this behavior further is a subject for future work.

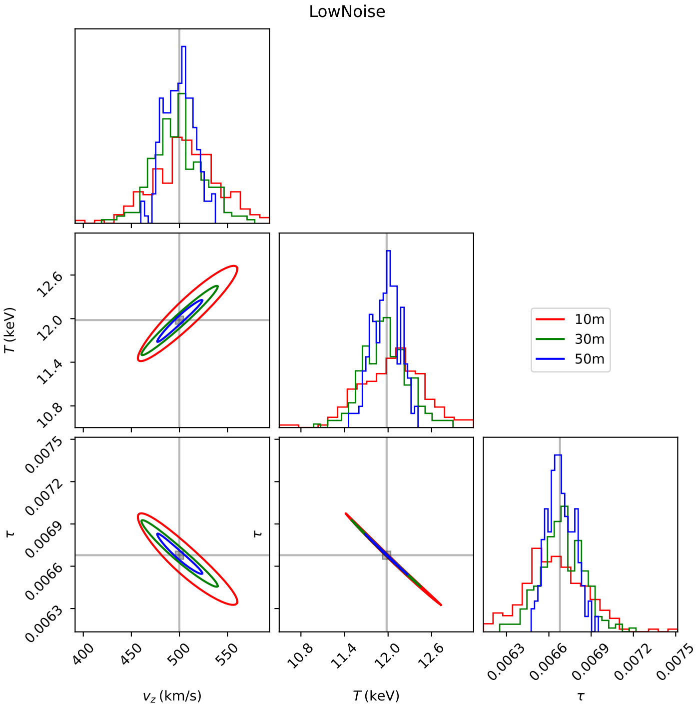

(c) Case 3

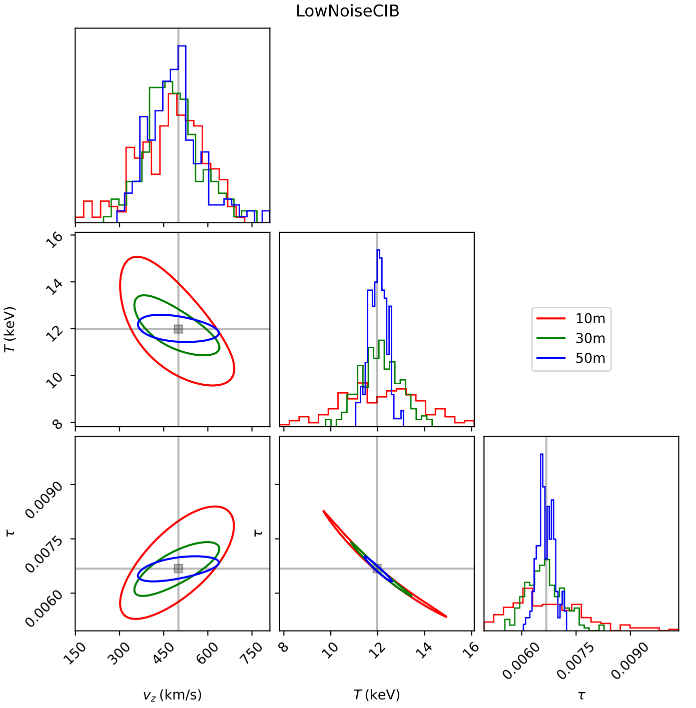

(d) Case 4

		σ_v			
	$M_{500}/(10^{14}M_\odot)$	3.7	3.0	10.9	8.5
	z	0.49	0.89	0.54	0.83
Scenario	Diameter				
(1) NoBkg	10m	81 ± 4	155 ± 8	94 ± 5	148 ± 7
	30m	62 ± 3	89 ± 4	73 ± 4	110 ± 6
	50m	66 ± 3	81 ± 4	59 ± 3	94 ± 5
(2) CIB	10m	170 ± 8	349 ± 17	135 ± 7	346 ± 17
	30m	113 ± 6	185 ± 9	93 ± 5	202 ± 10
	50m	83 ± 4	132 ± 7	79 ± 4	151 ± 8
(3) LowNoise	10m	42 ± 2	63 ± 3	18 ± 1	32 ± 2
	30m	23 ± 1	40 ± 2	12 ± 1	25 ± 1
	50m	16 ± 1	32 ± 2	7 ± 0	17 ± 1
(4) LowNoiseCIB	10m	60 ± 3	185 ± 9	36 ± 2	118 ± 6
	30m	51 ± 3	97 ± 5	29 ± 1	86 ± 4
	50m	55 ± 3	97 ± 5	32 ± 2	81 ± 4

Table 5.2: Predictions of recovered velocity precision σ_v for all combinations of observational scenario, telescope diameter, and cluster parameters. Figure 5.3 gives a graphical representation of these values. The uncertainties given here correspond to the estimated 1σ error bars given in Figure 5.3; in all cases, σ_v is either flat or monotonically decreasing with diameter within these errors.

5.3 Summary of Velocity Constraints

For each instrumentation case, we consider a realistic range of cluster parameters, as it is useful to understand which observing targets are best suited for each instrument type. We vary both the cluster mass, expressed as M_{500}, and the redshift z. More massive clusters have stronger SZ signals, but lower-mass clusters are more numerous, so it may be advantageous to explore both options. Thus, we consider clusters of masses $\sim 3\times10^{14}M_\odot$ and $\sim 10^{15}M_\odot$. We also vary the redshift, considering $z = 0.5$ and $z = 1$. While the SZ signal strength does not depend on redshift, the cluster's angular diameter does, so the contaminants affect our ability to reconstruct the SZ signal differently at different redshifts. We illustrate the dependence of σ_v on cluster mass and size in Figure 5.3. We also include numerical values of σ_v in Table 5.2.[1]

There are a few obvious trends in the data. First, the lower-redshift clusters generally have better constraining power on v_z: because of their larger angular diameter, these clusters' SZ signals occupy more pixels, yielding a higher total S/N.

---

[1] See also Appendix A.2.2 for tabulated values of σ_T and σ_τ.

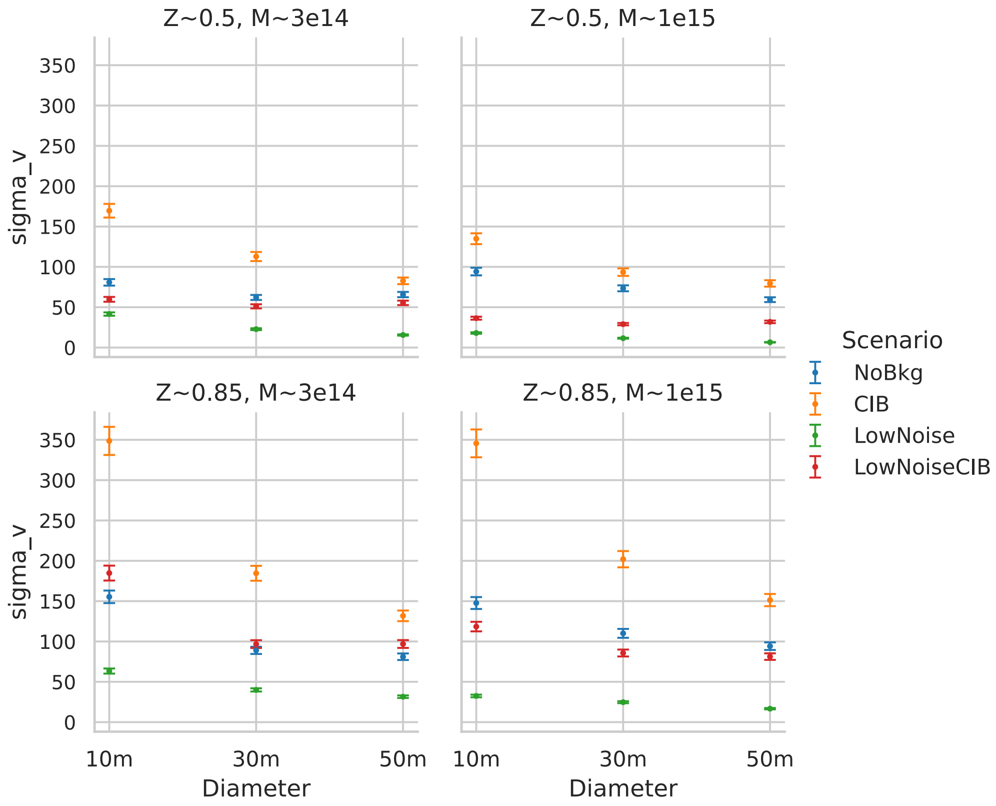

Figure 5.3: Predictions of recovered velocity precision σ_v for all combinations of observational scenario, telescope diameter, and cluster parameters. Labels for cluster masses are rounded to $3 \times 10^{14} M_\odot$ and $10^{15} M_\odot$, and redshift labels are rounded to 0.5 and 0.85. Error bars indicate 1σ uncertainties estimated as $\sigma_v/\sqrt{2N}$, where $N = 200$ is the number of noise realizations used to calculate σ_v. Numerical values and uncertainties of σ_v for these cases are shown in Table 5.2.

The higher-mass clusters also yield moderately improved constraints on v_z, likely for two reasons. For one, they have larger optical depth τ, which increases the normalization of the kSZ signal. They also tend to have higher temperatures, which may enable some constraining power on the rSZ signal. Even without an rSZ constraint, the assumption of a 10% fractional T prior together with a higher T implies a more precise T constraint in absolute terms, which in turn helps to constrain τ and therefore the kSZ signal.

Beyond these trends, these constraints provide additional confirmation of the impact of telescope diameter and noise levels. In case (2) (confusion-limited noise and CIB), the σ_v precision improves with telescope diameter for all the clusters. In case (4), σ_v does not improve from 30m to 50m in three of the clusters, though it does not degrade if the estimated uncertainties are accounted for. As noted above,

Frequency Band (GHz)	Sub-Confusion RMS Fraction 10m	30m	50m
90	0.66	0.31	0.18
150	0.59	0.38	0.30
220	0.60	0.47	0.40

Table 5.3: Ratios of map-space RMS per beam at the low-frequency bands between (a) sources that are below the 400 GHz confusion limit and (b) residuals after source removal. For the 30m and 50m telescopes, these ratios are less than $\frac{1}{2}$, indicating that the sub-confusion sources are subdominant to the residuals on subtracting the detectable sources in the low-frequency bands.

this behavior may be explained by the fact that these results are based on a limited sample size ($N = 200$).

Finally, we characterized the residual noise in the cleaned maps in the low-frequency bands, which are most relevant for SZ fitting. In particular, we compared (a) the RMS of the sources below the 400 GHz confusion limit to (b) the residual map-space RMS after source cleaning. We list ratios of (a) to (b) for the low-frequency bands (90 to 220 GHz) in Table 5.3. The sub-confusion sources contribute $\sim$ 60% to the residuals for the 10m telescope but are subdominant for the larger diameters. These results suggest that the residuals in the low-frequency bands are more strongly affected by modeling uncertainties on the detectable sources than by intrinsic fluctuations in the sources below the confusion limit.

Chapter 6

DISCUSSION

In this chapter, we consider the implications of the results presented in Chapter 5. We also discuss the limitations of this work and possible future investigations.

6.1 Broader Implications

We return to the cosmological questions of Chapter 1. In particular, given the σ_v values of Chapter 5, how well can we hope to constrain deviations from GR with a kSZ galaxy cluster survey? One can distinguish between models with constraints of the cosmic growth index γ (e.g., Gil-Marín et al., 2016). Figure 1 of Kosowsky et al. (2009) offers a prediction of the γ precision in terms of σ_v assuming a survey of 4000 galaxy clusters. As a simplistic forecast, we translate our σ_v values directly into $\sigma(\gamma)$ using that study's mapping in Figure 6.1. Improving the noise and aperture diameter yields only a modest improvement in the γ constraint, from a maximum of $\sigma(\gamma) \sim 0.07$ to a minimum of $\sigma(\gamma) \sim 0.047$.

We can make a more accurate forecast by accounting for the number of detectable clusters. As a concrete example, we consider the constraint on γ that could be attained by a wide-area survey with a 30m telescope such as CSST (Golwala, 2018). Given the relatively weak dependence of the σ_v precision on the instrument sensitivity, we assume confusion-limited noise. The γ constraint from such a survey depends on both (a) the mapping speed required to reach the assumed depth and (b) the number of detectable clusters in the survey.

To find the required mapping speed, we use prior calculations for the 25m CCAT observatory as a starting point. The CCAT noise levels are calculated in Morandi et al. (2013) for a targeted observation. Based on a personal communication with Jack Sayers, an instrument like CCAT could scan at a rate of 75 deg^2 yr^{-1} with the same noise RMS after extrapolating from a targeted observation to a dedicated survey mode and after applying a correction for observing efficiency. To translate this scanning speed to a CSST-like survey meeting our noise assumptions, we can scale by both the squared noise RMS and the collecting area. We scale the noise based on the 400 GHz band, for which Morandi et al. (2013) calculate an RMS of 75 μJy beam^{-1}, including both instrument noise and CIB confusion, or

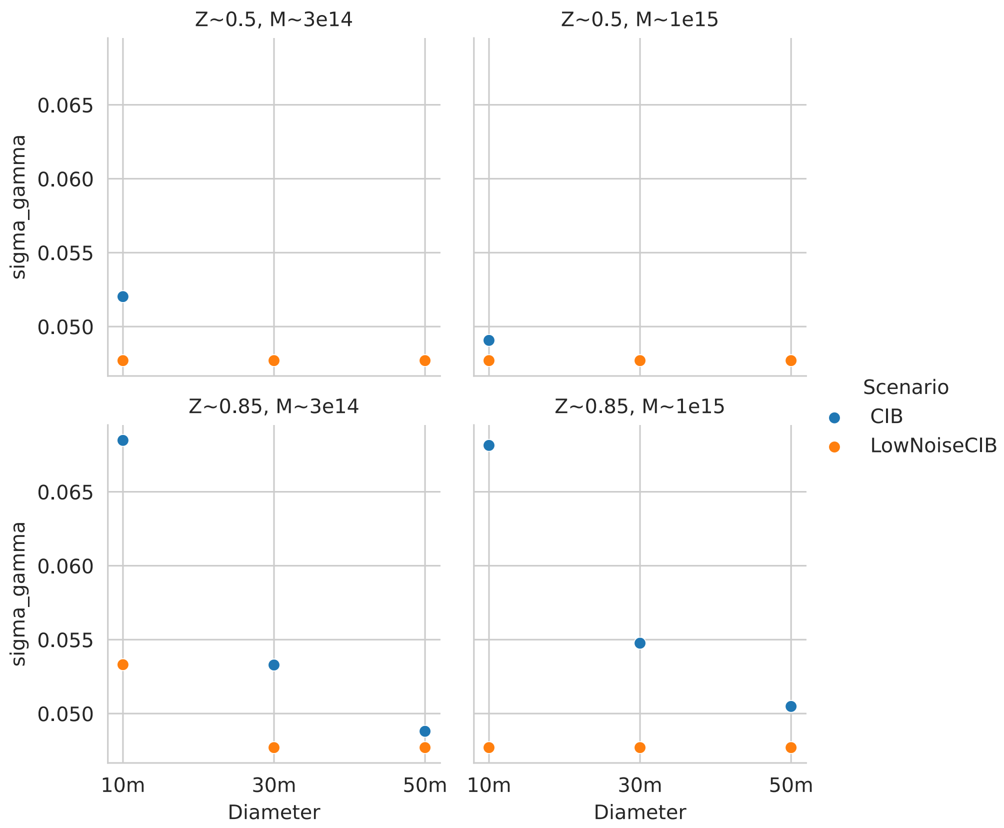

Figure 6.1: Predictions of $\sigma(\gamma)$ for a survey of 4000 clusters, generated by combining the velocity estimates of Section 5.3 with the scaling of Kosowsky et al. (2009).

$75/\sqrt{2}$ μJy beam^{-1} for instrument noise alone. Scaling to our shallower RMS of $\sim$ 140 μJy beam^{-1} and larger collecting area, we find that the mapping speed increases by the factor

$$\left(\frac{75}{140\sqrt{2}}\right)^2\left(\frac{30}{25}\right)^2 \approx 10, \tag{6.1}$$

which implies a scan rate of 750 deg^2 yr^{-1}.

To estimate the number of available clusters, we look to the forecasts of Raghunathan et al. (2022), which include estimates of cumulative tSZ-selected cluster counts as a function of redshift for several planned surveys. We use the predicted counts for the CMB-S4 wide-area survey as a match to the conservative mass threshold of $2\times10^{14}M_\odot$ for $z \lesssim 1$ in their Figure 3. In a full analysis, it would be necessary to consider counts for each mass bin, but our σ_v constraint depends only weakly on mass, so we assume this single effective threshold. We can scale the forecast of Raghunathan et al. (2022) in the regime to predict 2.5 detectable tSZ clusters per square degree in regions free from Galactic foregrounds.

Combining these cluster counts and the scanning rate above, we find that the CSST-like survey could conservatively place σ_v constraints on 1900 clusters per year. For a five-year survey, this translates to roughly $n = 10^4$ clusters. The $\sigma(\gamma)$ relation of Kosowsky et al. (2009) relation scales as $n^{-\frac{1}{2}}$. Thus, scaling the worst-case confusion-limited 30m case from Figure 6.1, we obtain $\sigma(\gamma) = 0.035$ for the wide-area survey.

To put this value in context in its ability to constrain modified gravity models, we can compare to γ forecasts for RSD measurements and pairwise kSZ surveys. The most competitive current RSD survey is DESI, which is projected to achieve $\sigma(\gamma) = 0.02 - 0.04$ (A. G. Kim et al., 2020; DESI Collaboration et al., 2016). This constraint is comparable to the constraint for the dedicated kSZ survey described above, and kSZ constraint can be brought closer to 0.02 if we assume that clusters can be detected with a decreased mass threshold.

We can also compare to the γ constraint achievable with a pairwise kSZ survey. With a survey like CMB-S4, Mueller et al. (2015a) conservatively predict a 5% fractional uncertainty on γ, which translates to $\sigma(\gamma) \sim 0.027$. The dedicated CSST-like 30m survey is quite competitive with this precision, and it probes complementary mass scales.

6.2 Limitations and Future work

There are a number of features that could be included in the pipeline to make the mock observations more realistic. Some of these have been mentioned earlier in the text, but we summarize them here for convenience.

In some cases, we have been able to model these features in the mock observations, but we have not fully explored how to treat them in the analysis stage of the pipeline. One such case is that of the primary CMB anisotropies, which may significantly impact the bulk SZ velocity reconstruction. We have described a CMB removal procedure in the text (Section 3.2), but future work should test the procedure in the context of the full analysis pipeline, especially the kSZ reconstruction via inpainting. One such feature is using hydrodynamical cluster simulations to generate more accurate SZ maps and mass distributions for the lensing calculation. Modeling the cluster morphology in this way is likely of secondary importance for predicting cosmological SZ constraints, which require only a measurement of the bulk velocity for each cluster, but it is likely important for usefully predicting measurements of the internal dynamics of the cluster. Future work should focus on tuning the least-squares fitting algorithm to converge properly in these more complicated maps.

There are other contaminants that we have not fully explored how to accurately include in the mock observations. One such contaminant is synchrotron emission from the brightest cluster galaxy (BCG), discussed in Section 2.3.1, and from field radio galaxies. The spectra of these galaxies are well modeled as a powerlaw at our wavelengths, and they can be cleaned from the maps with an algorithm analogous to that of Section 3.1. For maximum accuracy, however, it may be worth accounting for the correlation between radio and submm emission at the level of individual galaxies. We have also neglected fluctuations in the emissivity of Earth's atmosphere at the observing site. While we have included a model of the transfer function, which is used in practice to remove these fluctuations, there is still likely to be some residual correlated noise in the maps that may degrade the SZ reconstruction. Future work could also consider secondary kSZ and tSZ anisotropies, discussed in Section 2.3.2. The kSZ anisotropies could be treated in the analysis as simply a part of the CMB signal due to the degenerate spectra. The secondary tSZ signal and the gravitational lensing of the secondary kSZ signal are less straightforward to model and constrain. However, given their small amplitudes, they are likely subdominant to other sources of contamination for reconstructing the cluster signal.

Finally, our pipeline could be further improved by accounting for calibration systematics that may be relevant for practical observations. For one, future work could characterize the impact of flux calibration uncertainties, which limit the recovery of the overall SZ signal normalization. In addition, one could characterize the effect of a non-Gaussian PSF model on interpreting the cluster morphology.

There are also some natural follow-up studies that could be performed to improve the generality of these results. For one, we assume in this work that all clusters had a velocity of $v_z = +500$ km s^{-1}, but it is likely that the precision σ_v depends to some extent on the sign and magnitude of v_z.

In addition, one could explore the impact of the choice of frequency bands on the SZ constraints. Several upcoming surveys, kSZ-optimized or otherwise, will use different subsets of the mm/submm atmospheric windows. Some notable examples, both planned and under construction, include LCT (Vial et al., 2020) and CMB-S4 (K. Abazajian et al., 2019) (10m); CSST (30m) (Golwala, 2018); and LMT/TolTEC (Bryan, 2018) and AtLAST (Bertoldi, 2018) (50m). It would be informative to understand the extent to which additional bands can improve the constraints beyond the increased sensitivity. We anticipate that having at least some high-frequency bands is worthwhile to separate CIB contamination. As evidence, consider the improvement in the σ_v constraint from 10m to 30m: the precision increases more in case (2) than in case (1).

Future work could also investigate the constraints possible at the beam scale as mentioned in Section 4.2. Finally, it would be desirable to more thoroughly investigate how the kSZ constraints affect cosmological constraints.

Part II

Photolithographically Textured Silicon Optics for Millimeter and Submillimeter Wavelengths

Chapter 7

A 6-LAYER ANTIREFLECTIVE STRUCTURE FOR SILICON OPTICS

7.1 Introduction

In the first part of this thesis, I gave predictions for the ability of next-generation millimeter- and submillimeter-wave observatories to measure the Sunyaev-Zel'dovich effect. As I described before, these instruments will need broad frequency coverage to properly separate contaminants and reconstruct the SZ signal; recall, e.g., that the nominal instrument configuration has bands ranging from 90 to 400 GHz. Instruments can achieve such broad frequency coverage by either (1) using multiple receivers and multiple focal planes, with each optimized for a narrow frequency band or (2) combining all the detectors in one multifrequency focal plane and coupling to a single receiver. Both avenues are used in practice, but option (2) can significantly lower construction costs and facilitate deployment to space platforms. Pursuing option (2) can be difficult, however, as there are several components of an instrument's optical chain that can limit its frequency coverage. In this chapter, I will focus on the task of improving the bandwidth of two optical components in particular: windows and lenses.

7.1.1 Additional Scientific Background

Broadband silicon optics can simplify some other significant measurements in astrophysics besides the SZ effect. I will briefly motivate two such measurements: the polarization of the cosmic microwave background (CMB) and spectroscopy of high-redshift galaxies.

The CMB is one of the most powerful probes of cosmology in general. The polarization pattern of the CMB is particularly useful to study, as it can be used as a direct probe of even the earliest moments of the universe's existence. Models predict that an inflationary epoch in the early universe would produce a cosmic gravitational wave background (CGB), which would eventually leave its imprint as B-mode (divergence-free) polarization patterns in the CMB (Kamionkowski et al., 1998). A detection of the CGB would provide strong evidence for inflation's existence and would also be a direct probe of its energy scale. Combining information from this energy scale with measurements of the scalar spectral index n_s would yield tight constraints on the class of possible inflationary models, thus revolutionizing our understanding of the physics of the early universe. However, detecting these primordial B-modes has proven to be a significant observational challenge, as their observed pattern is dominated by foregrounds, especially by galactic dust emission and, to a lesser extent, synchrotron emission. Indeed, the claimed detection of cosmic B-modes by BICEP2 in 2014 proved to be completely attributable to dust foregrounds, as concluded by the joint analysis with Planck (Ade et al., 2015). To disentangle these foregrounds, a future polarization study will need broad spectral coverage to leverage the differing shapes of the CMB, synchrotron, and dust spectra. Accordingly, instruments for detecting the primordial B-mode signature will likely require large-format optics that can accommodate a wide frequency range from around 40 to 300 GHz.

In the 0.1–2 THz range, the gas in high-redshift galaxies exhibits many spectral lines that can be used to better understand both the star formation process and cosmology. Molecular rotation lines, such as those of CO and HCN, trace the mass of the cold molecular gas which is available for star formation. Atomic fine structure lines–[CII], [NII], [OI], and [OIII]—can be used to measure the properties of the actively star-forming ISM, including radiative cooling, density, temperature, and the ionizing radiation field. We can also perform cosmological measurements of baryon acoustic oscillations (BAO) and reshift-space distortions (RSD) by using these galaxies' spectral lines to measure redshifts. These BAO and RSD measurements are analogous to optical measurements by the likes of the Dark Energy Spectroscopic Instrument (DESI; DESI Collaboration et al. (2016)) and the Subaru Prime Focus Spectrograph (PFS; Takada et al. (2014)) but can probe much higher redshifts.

With any of these spectroscopic measurements, it is most efficient to measure multiple spectral lines in many galaxies in a range of redshifts at once. This procedure demands instrumentation with broad spectral coverage. Previously, it has only been feasible to perform such THz spectroscopy in a few individual galaxies, since current spectroscopic instruments are either not sensitive enough or have too small a field of view to efficiently survey a wide area. Although such spectrometers have only a few pixels, wideband optics would be useful because they would enable coverage of a wide frequency range at one time. Implementing such a scheme for integral-field-unit systems like SuperSpec and µSpec would enable mapping spectroscopy over a similarly wide frequency range. However, as with the CMB, as described below, there is an economic tradeoff between a single focal plane unit (FPU) covering a very wide frequency range versus multiple FPUs covering narrower frequency ranges, ~ 1 octave, and broadband optics are preferable in the limit of a larger, more expensive primary mirror.

7.1.2 Lenses vs. Mirrors

Why is it advantageous for mm/submm optical designs to include lenses, as opposed to just mirrors? To answer this question, we will first describe the state of the art, especially in the context of CMB polarization measurements, and then explain the advantages provided by wide-bandwidth lenses.

Technological advances in millimeter-wave observing have been driven primarily by the search for a gravitational-wave B-mode polarization signal in the CMB, as described above. The power of the B-mode measurement is commonly described by the so-called tensor-to-scalar ratio r, which is because tensor perturbations from primordial gravitational waves produce B-modes in the polarization signal. Improving the observational constraint on r is a matter of integrating to lower noise levels, or equivalently, mapping the sky to the same depth more quickly. In practice, one can integrate faster by observing with as many detectors as possible in a telescope. In other words, the quality of the constraint on r scales with detector count per focal plane.

Both ground-based and space-based observatories have made measurements to constrain r in recent years, but they have taken different approaches to maximizing the detector count. These approaches ultimately dictate the type of optics used, so we will take a moment to explore them.

On the ground, where the size and weight of a telescope's components are only secondary considerations, many instrument teams have favored modular optical designs. Such designs use multiple optics tubes, each of which contains a separate monochromatic focal plane for each frequency band. Some current observatories that use this design approach are ACTPol and the Simons Array (Henderson et al., 2016; Arnold et al., 2014). Several planned observatories have also proposed to use modular optics, including CMB-S4's large-aperture telescope (LAT) design (Niemack, 2016) in the intermediate term and AtLAST (Klaassen et al., 2019) and CMB-HD (Sehgal et al., 2019) in the longer term.

With these modular optics tubes, it is convenient to use lenses as the so-called reimaging optics, which couple light from the telescope to the focal plane, acting as the final stage of focusing in the optics chain. Since each optics tube only covers a single frequency band, these lenses only need to perform well over a relatively narrow range of frequencies. Thus, a single-layer AR coating is likely to be sufficient for such configurations.

In space, observatories are constrained in terms of payload size and weight, so their designs must be compact. Thus, most upcoming CMB space mission concepts have tried to maximize the detector count within a single multichroic focal plane. Some concepts that use this strategy are EPIC-IM (Bock et al., 2009), COrE (Collaboration et al., 2011), and PICO (Hanany et al., 2019). The EPIC-CS concept (Bock et al., 2008) is one exception, which uses lenses within a modular optical design.

In these cases, any reimaging optics would need to couple light from the telescope to the entire focal plane. To illuminate the entire focal plane area and cover all the detector frequencies, these designs would need a large-diameter lens with a broadband AR coating. Producing such a lens has proved to be a substantial design and fabrication challenge that has not yet been solved. While the required size of the optics could be reduced by using an array of lenslets (e.g., Westbrook et al., 2022), the problem of broadband AR-coating remains. Thus, the above non-modular concepts have eschewed reimaging optics in their designs. Accordingly, in these designs, the focal plane is situated directly at the focus of the secondary mirror.

However, this choice comes at a cost. In particular, in designs without reimaging optics (e.g., Bock et al., 2009), the image quality typically degrades away from the center of the focal plane. Thus, where possible, it is desirable to use lenses to improve the image quality over the whole focal plane (e.g., Niemack, 2016). The improved image quality increases the potential mapping speed, which translates to a shorter time required to obtain a given constraint on r.

In addition, the satellites with lens-free designs must include several absorbing baffles to mitigate the spillover of light from the primary mirror. These baffles can be heavy, and they must be cooled to mitigate optical loading and photon noise (Niemack, 2016). In a design with reimaging optics, such baffling could be replaced, or at least reduced, with a cold Lyot stop.

Thus, for both space-based and ground-based observatories, broadband AR coatings provide valuable flexibility in optical designs. For example, designs such as EPIC-LC and EPIC-CS (Bock et al., 2008) would be possible if advanced broadband

ARCs were available. A concept like EPIC-CS promises faster mapping speed than its lens-free counterparts. A concept like EPIC-LC takes advantage of simplified focal plane design to save on construction costs. Ground-based observatories can similarly benefit from the ability to use different optical configurations, including those that further increase detector coverage in a given focal plane. This is particularly true for telescopes at scales of 30m to 50m, as the telescope costs increase much more quickly with diameter than focal plane unit (FPU) costs scale with focal plane area. The CMB community at large has recognized these potential benefits, with NASA calling for broadband lenses as part of its Program Annual Technology report in both the PCOS and COR themes (*PCOS PATR* 2017; *COR PATR* 2017).

7.1.3 Vacuum Windows

In addition to lenses, vacuum windows are another important component of mm/submm optical chains. Vacuum windows are necessary to transmit light to a cryogenic focal plane while preserving the insulating vacuum of the dewar. Given that they transmit light, such windows are subject to the same optical requirements as the lenses discussed above. In addition, low loss in vacuum windows is important for minimizing optical loading: with the window at a temperature of 300 K, even 1% loss gives more loading than the CMB signal itself. For example, where silicon is not feasible, other materials are used, and the loss can reach, e.g., 1% at 150 GHz (Zotefoam; Yoon et al. (2006)) and 5% at 220 GHz (high-density polyethylene (HDPE); Sobrin et al. (2021)). The loss degrades further at higher frequencies (e.g., Barkats et al., 2018). Thus, materials such as silicon are highly desirable to minimize loss and therefore optical loading. The necessary AR treatments must also have low loss to maintain these advantages, and so broadband AR coatings on windows are advantageous in the same situations as on lenses. We note that the designs given in this work may be directly used as AR treatments for vacuum windows.

7.1.4 Antireflective Coatings for Silicon Optics

There are several possible choices of substrate material for mm/submm optics, including silicon, alumina, and sapphire. Plastics, such as high-density polyethylene (HDPE) have been used in these applications historically, but the field is moving to favor the aforementioned alternatives, chiefly for their lower dielectric loss. This work will focus on high-resistivity silicon, which has several properties that make it advantageous for such uses compared to conventional alternatives: in addition to low dielectric loss, it also has high physical strength, achromaticity, high thermal conductivity, and a high refractive index of 3.42. While silicon's high refractive index enables thinner optics with less curvature, it is problematic in that each interface reflects away much of the incident light (approximately 30% reflection at normal incidence). Silicon optics—both vacuum windows and lenses—must therefore be given AR treatments to be effective.

The usual approach to AR coating is to apply a layer of dielectric material to the surface of the optic to reduce reflections due to the mismatched indices of the optic and the external medium. It is a well-known result that the optimal choice for a single-layer dielectric AR coating has a thickness of $\lambda/4$. However, such a single-layer AR coating has limited bandwidth, so it is not suitable for our design requirements, which demand broad spectral coverage.

To increase the bandwidth, it is necessary to add more layers to the AR coating: as a rule of thumb, one needs $n+1$ layers to achieve $n:1$ fractional bandwidth with low reflection. To be concrete, our design covers the range 80 to 420 GHz, equal to a 5:25:1 fractional bandwidth, so we are targeting a design with six layers. However, it is difficult to find materials that have the required indices while also maintaining the advantages of using silicon, especially low loss, although some approaches to varying the index of laminated dielectric layers have been explored in the literature, e.g., Rosen et al. (2013), Jeong et al. (2016), Zhang et al. (2009), and Moseley et al. (2017).

An alternative to using conventional dielectrics is to reduce silicon's effective index of refraction by applying a texture of sub-wavelength features to its surface. Such an integral AR coating also has the advantage that it will not delaminate from the surface of the optic under thermal cycling. This technique has been demonstrated at mm wavelengths in silicon (as well as alumina and sapphire) by cutting features into the substrate using a dicing saw (Datta et al., 2013; Young et al., 2017) or a laser (Nitta et al., 2014; Matsumura et al., 2016; Drouet d'Aubigny et al., 2001; Westbrook et al., 2022; Takaku et al., 2020; Takaku et al., 2021). Extending to submm wavelengths and increasing the bandwidth requires finer features than such techniques can produce, which has led us to pursue using deep reactive ion etching (DRIE) to fabricate the AR structures. There have been a few demonstrations using DRIE of flat single-layer coatings at THz frequencies (Gallardo et al., 2017; Wheeler et al., 2014; Wagner-Gentner et al., 2006) A multi-depth DRIE technique (Jung-Kubiak et al., 2016) can be used to stack layers of different indices to form a gradient with depth, and multiple wafers etched in this fashion can be bonded together to create the thick, high layer-count structures needed for very wide-bandwidth AR coatings.

A limitation of DRIE is that it has not been adapted to curved surfaces such as conventional lenses. Some authors have mentioned an approach for slumping a DRIE-etched wafer into a curved shape (e.g., Wheeler et al., 2014), but this technique has not been demonstrated in practice. Thus, instead of curved lenses, we plan to use gradient-index (GRIN) lenses, which will themselves be realized using a DRIE-based technique. A flat cylindrical optic provides the same focusing as a parabolic lens if its refractive index follows a radial gradient:

$$n(r) = n_0 - \frac{r^2}{2 f t_0}, \tag{7.1}$$

where n_0 is the bulk index, t_0 is the center thickness, and f is the focal length. We can vary the index radially in a single silicon wafer by varying the DRIE pattern, and, as with the AR coating, we can bond such wafers together to form a focusing optic of the desired thickness. The AR structure is thus integrated into the outer layers of the optic, including the variation of the AR structure with radius.

7.1.5 Previous Work

Our group has previously demonstrated a wide-bandwidth 2-layer AR coating, and we have demonstrated wafer bonding with $\lesssim 1\%$ loss per interface (Defrance et al., 2018). Both examples were intended as intermediate demonstrations of a DRIE-based ARC application technique, with the goal of progressing towards an even wider-bandwith AR structure. We summarize the results of that work below.

2-Layer Antireflective Structures

The first design of Defrance et al. (2018) was intended to demonstrate that a DRIE-based technique can produce an effective 2-layer AR coating. The design was targeted to the 190–310 GHz band, which matches a wide atmospheric transmission window. To determine the characteristics of the design, a multi-step design process was used. First, an idealized model with uniform layers was used to calculate optimal refractive indices and thicknesses for the two layers, with the criterion of minimizing the peak reflection over the design band. This optimization was performed with a standard formalism based on Chebyshev polynomials (Baumeister, 1986).

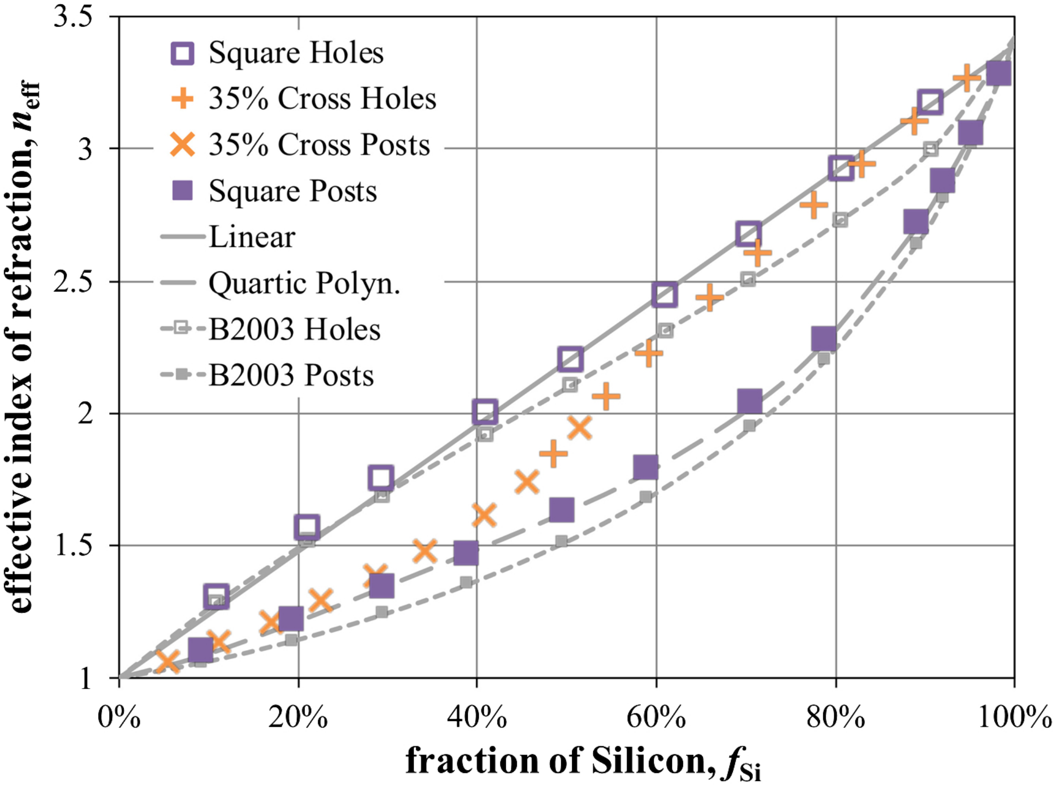

Figure 7.1: Effective index n_{eff} for various single-layer geometries as a function of fill factor f_{Si}. The discrete markers indicate results from HFSS simulations, while the curves indicate models that interpolate over the simulated data. The dashed curves (B2003) are predictions of the performance of both holes and posts from the effective capacitor model of Biber et al. (2003). From Defrance et al. (2018).

Next, the effective indices and thicknesses of the optimal model were converted into a set of microstructure dimensions, or equivalently, the fill factor f_{Si} denoting the fractional area of each layer that is occupied by silicon. The two layers used microstructures consisting of square holes (inner layer) and square posts (outer layer). Other geometries, such as crosses or hexagonal grids, did not demonstrate any additional design flexibility, so they were not used. An inverse mapping of fill factors to effective indices was calculated by simulating 1-layer structures with the finite-element software HFSS (Figure 7.1). These curves were interpolated to find dimensions matching the desired effective indices.

Finally, the performance of the full structure was verified by simulation with HFSS. This step was necessary to account for any deviations from the assumption of achromaticity in the effective index model. DRIE fabrication nonidealities, discussed in more detail later, were also included in these simulations. This design strategy formed the starting point for the one used in the present work, discussed in

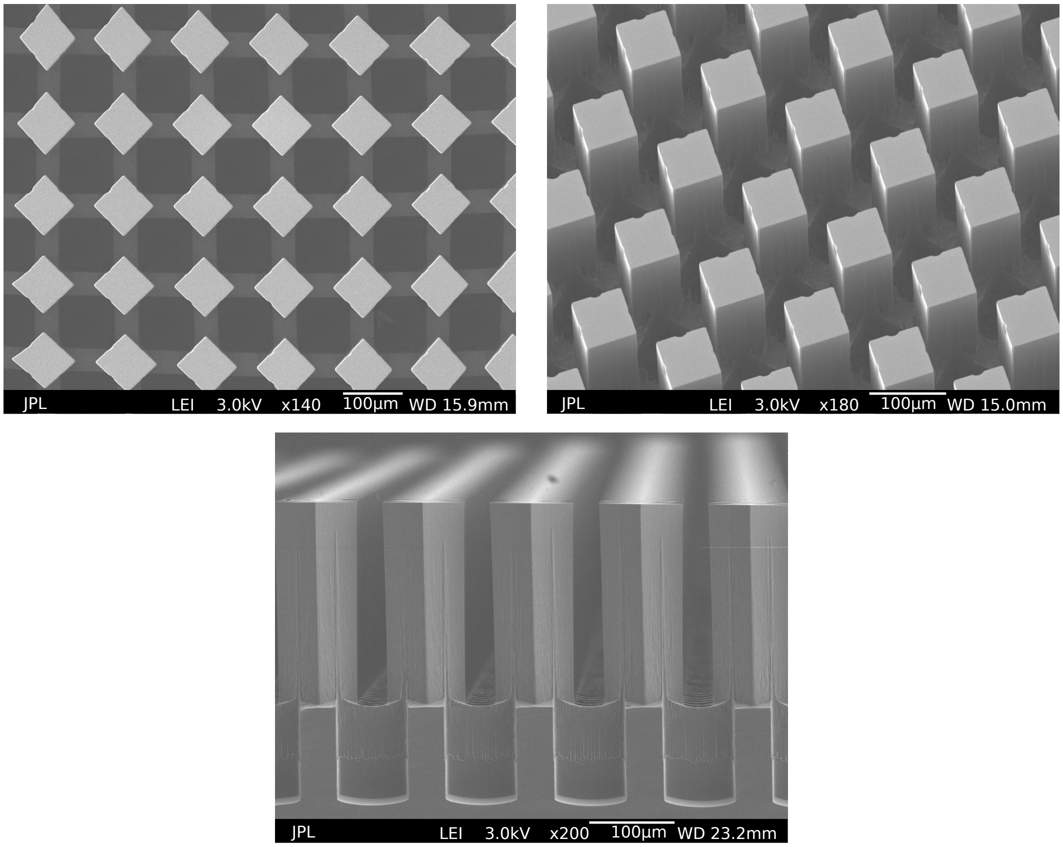

Figure 7.2: SEM images of the AR microstructures in the cleaved 2-layer sample, showing top-down (upper left), 30° (upper right), and cross-sectional views (bottom). From Defrance et al. (2018).

Section 7.2.

This design was fabricated on a high-resistivity float-zone silicon wafer with 1 mm thickness and 100 mm (4 in.) diameter. The optics used a single silicon wafer per sample, which was etched on both sides with the multidepth technique of Jung-Kubiak et al. (2016). To confirm that the as-fabricated dimensions matched the as-designed dimensions, the wafers were cleaved and imaged with scanning electron microscopy (SEM); see Figure 7.2.

Finally, to test the performance of the fabricated structures, the reflection and transmission of the structures were measured. Measurements were taken at 15° incidence with a quasi-optical test setup and confirmed with an alternative measurement technique at normal incidence. These measurement techniques are described in detail in Defrance et al. (2018). The results of these measurements are shown in Figure 7.3. The reflection and transmission were found to agree with expectations to a high degree of accuracy, especially when the dimensions used in the simulation

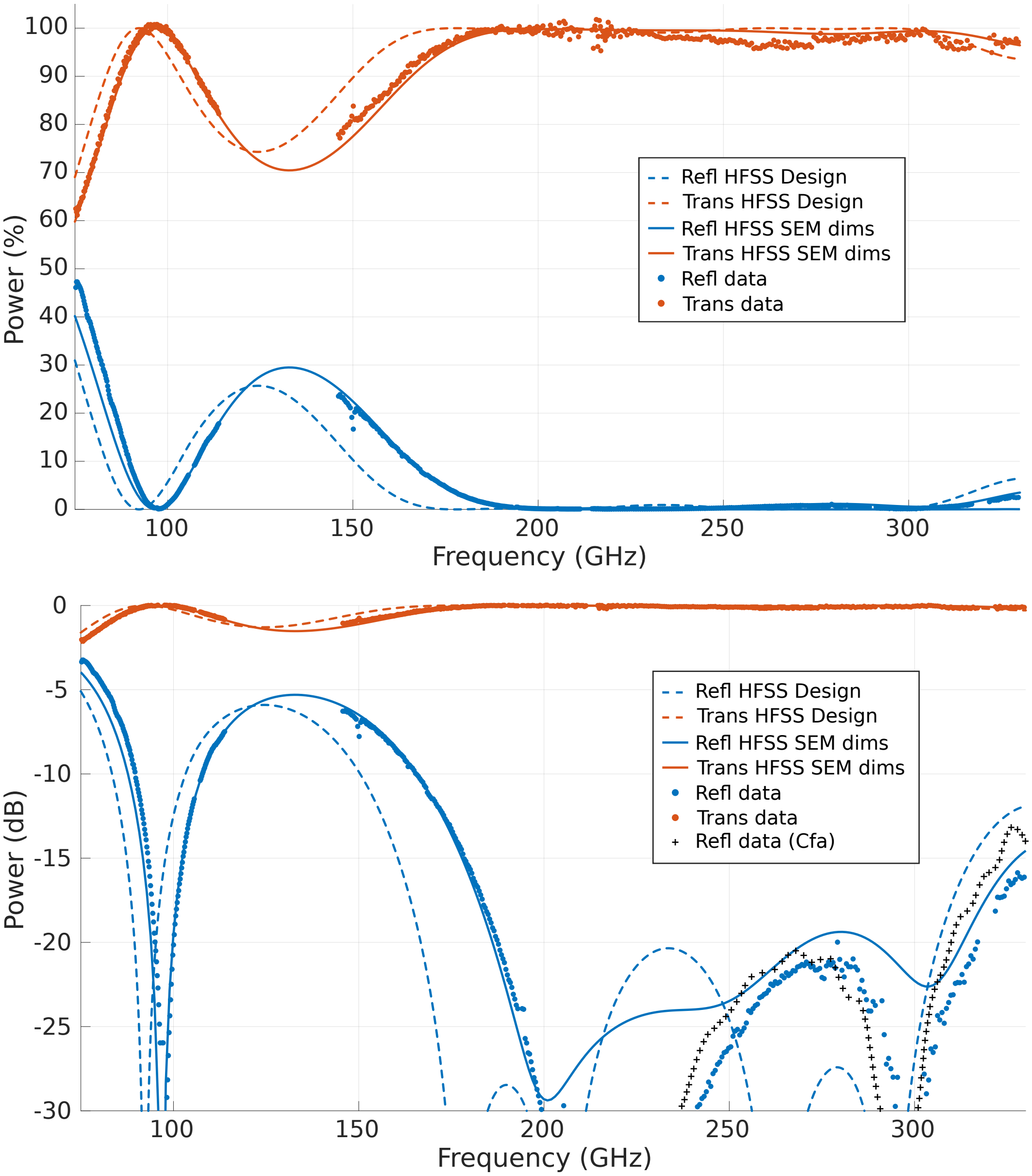

Figure 7.3: Reflection and transmission of the 2-layer sample, with linear scale (top) and logarithmic scale (bottom). The dashed lines show HFSS simulations of the design; the dots and crosses show the measured optical performance of the sample (dots measured at 15°; crosses measured at normal incidence using a different testbed); and the solid lines show HFSS simulations with microstructure dimensions adjusted to the measured values. From Defrance et al. (2018).

were adjusted to match the measured dimensions of the fabricated wafer. In addition, these results imply an upper limit of $1 - -2\%$ on the dielectric loss in the optic, as the sum of the reflected and transmitted power is equal to unity to that precision.

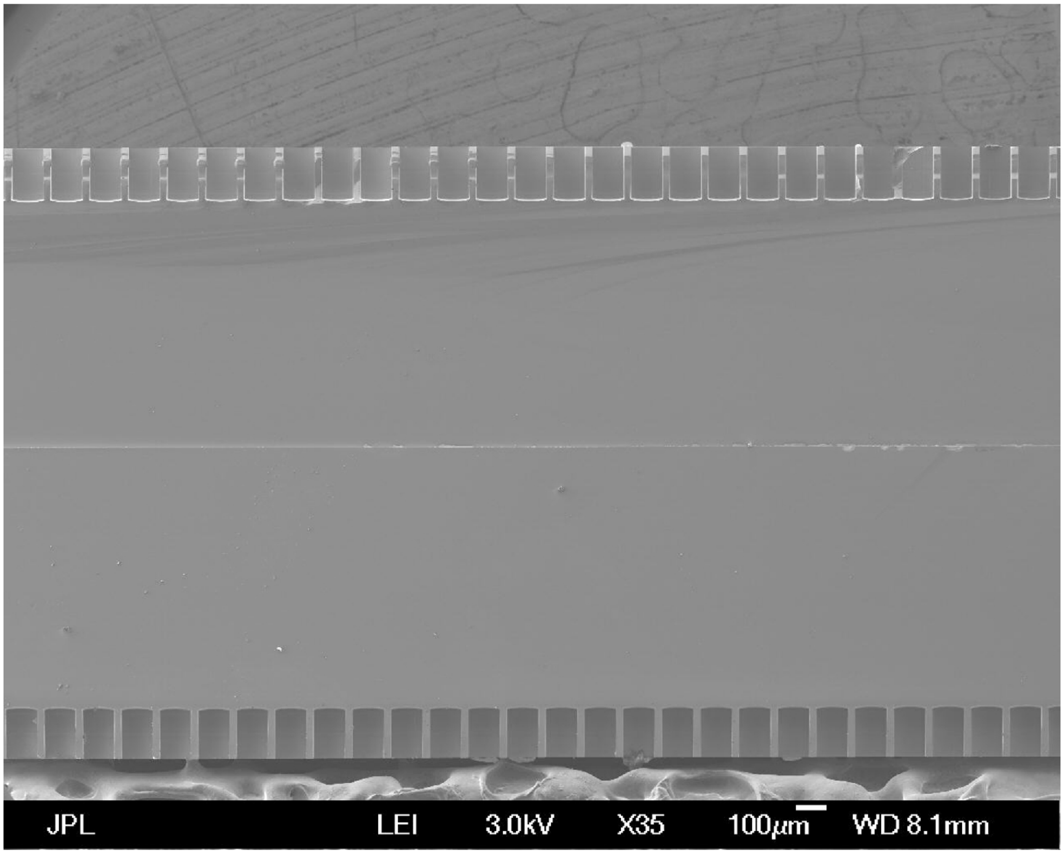

Figure 7.4: SEM image of the wafer bond in the 1-layer sample. There are no apparent gaps, indicating a successful bond. From Defrance et al. (2018).

Bonded Wafers With 1-Layer Antireflective Structure

The Jung-Kubiak et al. (2016) technique has two limitations that make it difficult to scale to thick multi-layer structures. The first limitation, as stated above, is that DRIE cannot etch at an aspect ratio $\gtrsim 20 : 1$. In addition, some of the etched layers in a multi-layer design require removing a significant fraction of the silicon, which contributes to the DRIE loading effect (e.g., Laermer et al., 2015). This effect makes it impractical to control the uniformity of a deep etch. Thus, extending to GRIN lenses and multi-layer ARCs will require stacking multiple wafers together. A convenient, and perhaps necessary, way to accomplish this stacking is by bonding together multiple wafers. To this end, Defrance et al. (2018) tested a wafer-bonded sample to determine whether the bond introduces any measurable artifacts.

The design of this sample consists simply of two wafers, each etched with a quarter-wave ARC on one side and bonded together on the unetched surface. The wafers used were of the same type and dimensions as with the two-layer design.

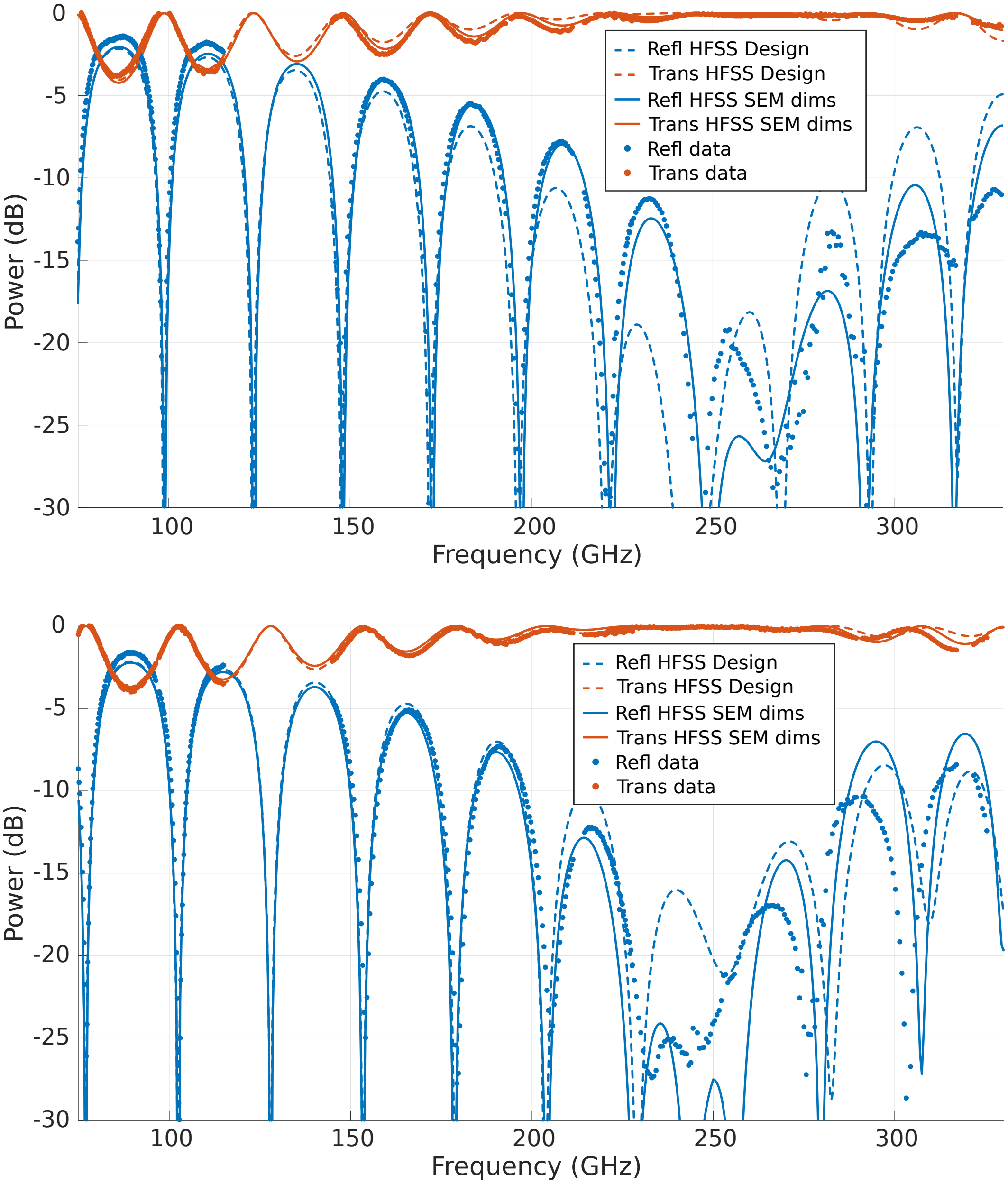

Figure 7.5: Reflection and transmission of the wafer-bonded 1-layer samples, with square posts (top) and square holes (bottom). The dashed lines show HFSS simulations of the design; the dots show the measured optical performance of the sample; and the solid lines show HFSS simulations with microstructure dimensions adjusted to the measured values. From Defrance et al. (2018).

For the geometry of the ARC, both square posts and square holes were tested. The dimensions of the geometry were chosen from the effective index model in the same manner as for the two-layer design. As with the two-layer structures, these structures were cleaved and imaged with SEM after the optical tests (Figure 7.4).

Measurements agree well with finite-element analysis (Figure 7.5), although the agreement is better for the square hole structures than for the square posts. Defrance et al. (2018) concluded that the discrepancy in the latter case was not due to the wafer bond but to nonuniformity in the etch. Given the single-layer structure of the AR coating, this optic has a lower expected bandwidth than the two-layer version. In addition, these measurements place limits on the reflection and transmission due to the wafer bond, as measured in the frequency range where the full structure has $\lesssim 1\%$ reflection. In the version with square posts, the transmission is $> 95\%$ and reflection is $< 1.2\%$ in this region; in the version with square holes, the transmission is $> 97\%$ and the reflection is $< 1\%$. Together, these values imply a conservative upper limit of 4% transmission loss due to the bond.

7.1.6 4-Layer Antireflective Structure Design

As an intermediate step towards a 6-layer AR structure, we are currently in the process of fabricating a 4-layer AR structure. The full 4-layer design (Figure 7.6) comprises a stack of four silicon wafers, where the two outer wafers are required to overcome the aspect ratio limitations of DRIE. There are two versions of this design, labeled A and B; the outer wafers in version A consist of post structures alone, while in version B, the outer wafers include a connected third layer etched with holes, which allows the wafers to hold together on their own. These designs are intended to test the wafer bonding procedure on etched wafers. In addition, the 6-layer optimization procedure, described in Section 7.2, was based on the optimization procedure for these 4-layer designs.

The details of the 4-layer fabrication process are still in development at JPL. A few preliminary samples with version B of the 4-layer ARC have been fabricated using 50 mm wafers, which can be accommodated by the wafer bonder at JPL and are less susceptible to bowing than larger wafers. Testing by Fabien Defrance has shown that these optics can achieve 87% transmission when stacked and clamped together and 95% transmission when bonded. A sample using 80 mm wafers is currently in development.

7.1.7 Chapter Outline

In the remainder of this chapter, we first discuss the method we used to design and optimize a 6-layer AR structure (Section 7.2). We then present the results of HFSS simulations of the reflection and transmissions of the optimized designs in Section 7.3. Finally, we discuss implications of this work and potential future work

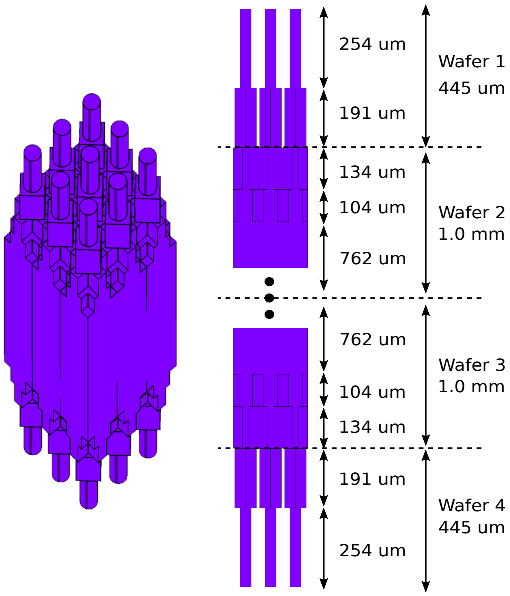

(a) Version A

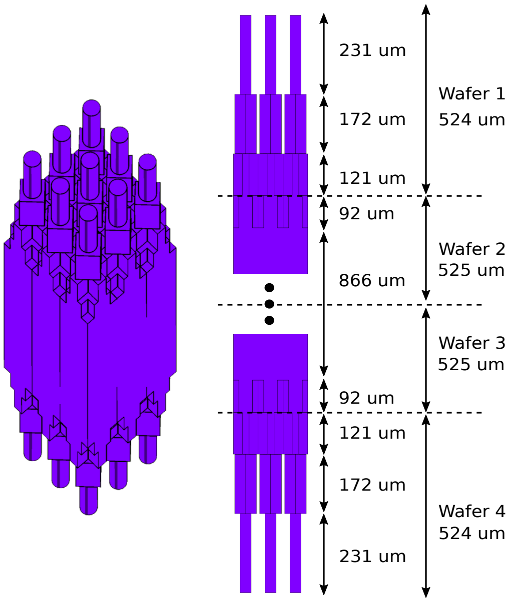

(b) Version B

Figure 7.6: Diagrams showing the dimensions of the preliminary 4-layer ARC structure design. (a) variant with post structures in the outer wafers 1 and 4; (b) alternative variant with self-supporting outer wafers.

in Section 7.4.

7.2 AR Structure Design

7.2.1 Design Description

Our ARC design consists of six layers of microstructures etched into silicon wafers 4 inches (100 mm) in diameter. The six layers are necessary to achieve the design frequency range of 80 to 420 GHz, which covers a fractional bandwidth of 5.25:1.

The basis for our design is a periodic square grid of microstructures with a pitch (i.e., grid spacing) of 75 μm. We chose the value of the pitch based on the heuristic that the scale of any etched features should be well below the maximum designed wavelength. In particular, our maximum design frequency of 420 GHz implies a minimum wavelength of 720μm, and 75μm is smaller by roughly a factor of 10. For comparison, Defrance et al. (2018) used a 125μm grid spacing for a maximum design frequency of 320 GHz. We chose a periodic grid for computational tractability, as periodic boundary conditions enable us to simulate the ARC's performance in a single unit cell instead of a full grid of $> 10^6$ microstructures, which would be intractable. For application to an optic such as a GRIN lens, where the effective refractive index of the uncoated optic varies with the radius, the choice of a periodic grid is no longer optimal, as the optimal AR coating in that case would itself need to vary with radius to match the structure beneath it. Designing a radially varying coating is outside the scope of this work, which focuses on an unpowered optic as a prototype. However, it is possible to approximate the performance for radially varying optics by simulating the microstructures within multiple annuli (e.g., Defrance et al., 2020). We are also in the midst of adapting the technique of Byrnes et al. (2016) to approach full electromagnetic simulation of optics with radial variation.

Given this grid layout, the next choice in the AR structure design is that of the microstructure geometry for each layer. When etching with our DRIE technique, there are two categories of possible geometries: posts and holes. Two factors constrain the choice of geometry. First, any walls and posts in the final structure must be thick enough to be structurally stable with a 75 μm pitch. Past experience of our JPL collaborators indicates that 10 μm wall thickness would be an aggressive but possibly achievable goal. Second, DRIE is limited to a maximum aspect ratio of roughly 20:1, which is the ratio of the etch depth to the width of the etched hole or groove. These constraints set the minimum and maximum fill factors achievable with a given geometry. For a low refractive index, then, circular posts are generally the best choice because they provide the largest minimum width for a given desired fill factor. For a high refractive index, square holes tend to perform better, as they have the largest minimum wall thickness for a given fill factor. We note our choices of geometry for each layer in Table 7.1.

The next consideration in the design is how to combine multiple layers together. The technique of Jung-Kubiak et al. (2016) enables multiple layers to be etched into a single substrate. However, this technique is limited by the maximum DRIE aspect ratio of $\sim 20:1$. Thus, to etch deeper structures, it is necessary to take two measures: (1) to etch each wafer from both sides and (2) to combine multiple wafers in the axial direction by wafer bonding. These two measures imply two constraints on the microstructure design. First, the full structure must be contiguous, otherwise it will fall apart after fabrication. Second, there must be good contact between layers at the boundary of wafers.

Based on our requirements for refractive index and layer thickness (discussed in detail in Section 7.2.2), we opted for a full structure design consisting of three silicon wafers. The middle wafer consists of 4 mm of silicon substrate, etched with three AR layers on each surface. Each of the two identical outer wafers consists of three layers, with two etched from the outside and one from the inside. A cross section of the full design is depicted in Figure 7.7.

A GRIN lens produced with this technique would require additional wafers. Specifically, in order to overcome the DRIE aspect ratio limitation, the single middle wafer etched on two sides would be replaced by a stack of wafers etched with the lens hole pattern sandwiched between two wafers etched with the three highest-index AR layers. See Section 7.4 for more detail on this preliminary GRIN lens design.

We modeled and simulated three variants of the geometry for the final design, which we compare in Section 7.3.1. In the "nominal" design, layer 3 (see Figure 7.7) consists of square posts. The nominal design has good simulated performance, but it may prove difficult to fabricate in practice. In particular, the outer wafers (wafers 1 and 3) consist entirely of posts, so they cannot be etched on their own, or else the post structures will fall apart. Thus, the nominal design requires a sequence of several fabrication steps: etch layer 3 in both outer wafers, etch layers 4 through 6 in Wafer 2, bond all the wafers together, then etch the outermost layers 1 and 2. With this sequence, it is difficult to achieve good alignment of the posts in layers

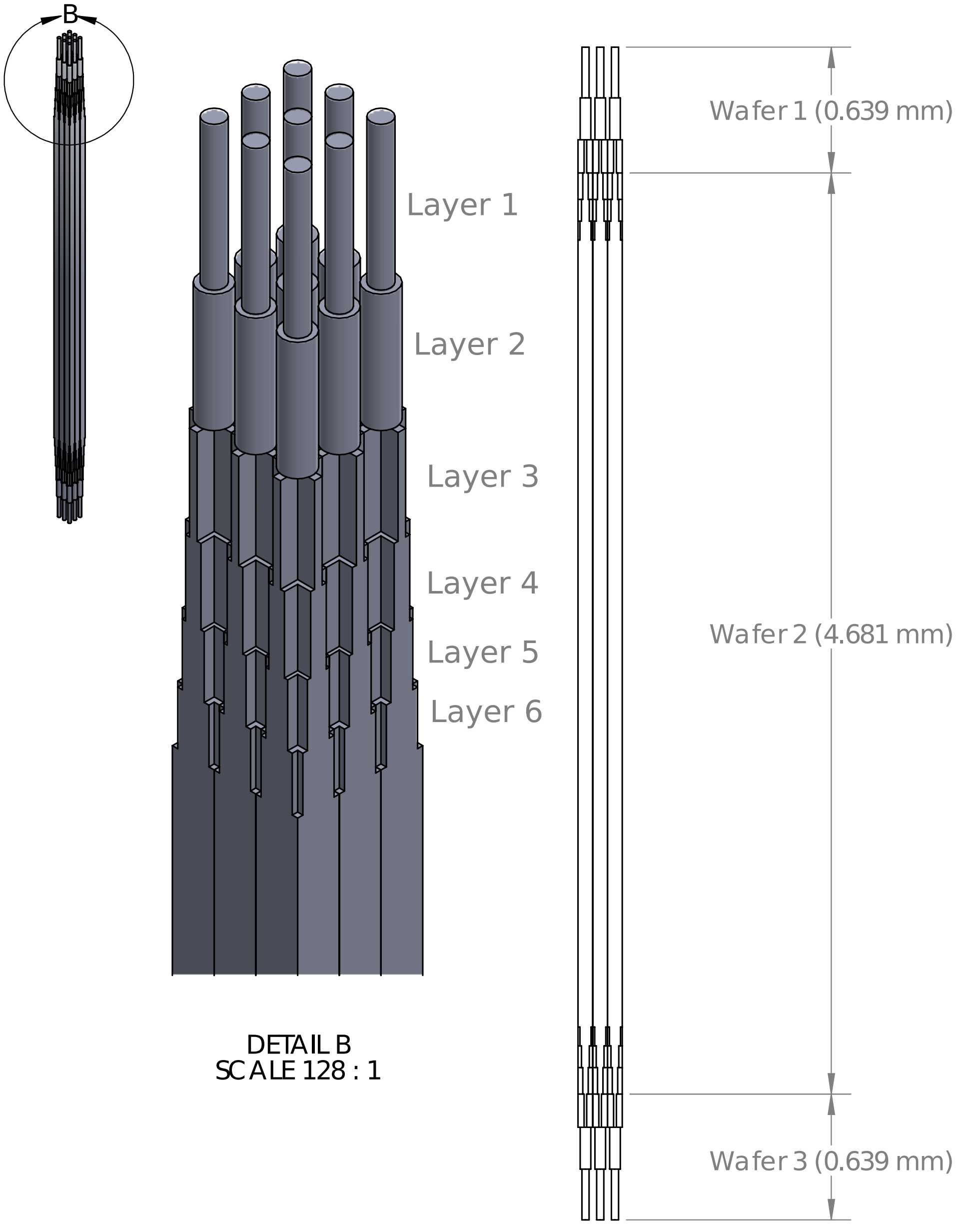

Figure 7.7: Isometric and cross-sectional views of the six-layer design showing nine unit cells with wafer boundaries. In particular, this is the design variation where Layer 3 (i.e., the innermost layer of the outer wafers) consists of square holes.

3 and 4, which can result in poor bond quality. Indeed, we found in a test of the 4-layer process that one of the samples split apart during the final etch step due to inadequate bonding during the previous step.

The two “alternative” designs aim to simplify the nominal design’s fabrication process by using a structure of holes for layer 3. This ensures that the outer wafers are contiguous on their own, so all three wafers can be fully etched before bonding. The “aggressive” version performs very well in simulations—better, in fact, than the nominal optimum; see Section 7.3.1—but the walls of layer 3 are only 10.5 μm thick as designed, so it is not yet certain whether they will be structurally sound. The “conservative” version sacrifices some performance for more structural integrity by using thicker walls, with a minimum of 13.5 μm.

We note that it would also be possible to use circular posts in Layer 3 in the nominal design. We have not simulated this case, but we briefly investigated whether it could improve the integrity of the structure by increasing the bonded area between layers 3 and 4. To do this, we estimated the contact area between layers 3 and 4 for both square and circular posts. In this comparison, the square posts have the dimensions of the optimized nominal design, and the circular posts have the dimensions implied by the slab model optimum; all other dimensions match the fully optimized nominal design. As a fraction of cell area, the square posts have 36% contact area, while the circular posts have 43% contact area. As a fraction of post area, the square posts have 61% contact area, while the circular posts have 72% contact area. We concluded that the improvement in contact area for circular posts is sufficiently modest that it does not yet warrant further investigation.

DRIE Nonidealities

In practice, the DRIE process introduces some fabrication nonidealities whereby the final fabricated structure deviates from the as-designed geometry. Such nonidealities fall into three categories: scalloping, tapered walls, and filleted edges. Scalloping refers to the concave profile of the bottom of any etched hole or groove, which arises even when the bottom is designed to be flat. Tapered walls occur because the transverse dimension of the etch increases weakly with depth. Finally, sharp edges in the design will come out filleted (i.e, rounded). We have previously found that these nonidealities occur at a noticeable level in the 2-layer ARC design, shown in Figure 7.8a.

Given that Defrance et al. (2018) found that nonidealities can affect the simulated

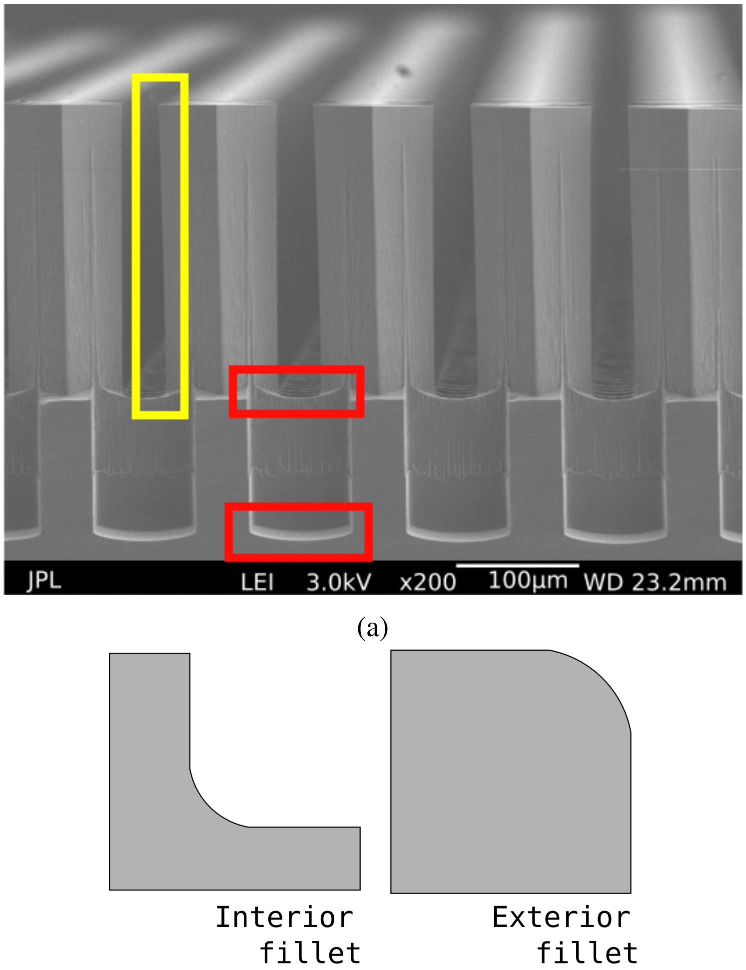

(a)

(b)

Figure 7.8: Illustrations of fabrication nonidealities. a SEM showing a cleaved sample of a previously fabricated 2-layer AR structure (Defrance et al., 2018), showing fabrication nonidealities. One can observe both the scalloping and tapering effects: scalloping (red outline) is visible at the bottom of the etched hole and groove structures, and tapering (yellow outline) can be seen in the upper layer, where the gap between the walls becomes wider at the bottom of the structure. b Illustration of the filleting effect, showing example interior and exterior fillets. The fillets are too small to be easily seen in a.

performance of the design by as much as a few dB, we also included them in these simulations. We modeled the nonidealities with dimensions estimated from measurements of previously fabricated structures. For the walls, we assumed a taper of 0.6° from the vertical, such that the walls are slightly thinner at the base than at the top. We modeled the scalloping in the square hole features as the intersection of two circular arches whose axes are orthogonal; we assumed a 6 μm depth for the scalloping. Finally, we modeled fillets around the interior corners of the bases of posts and holes; these had the same arc-shaped profile and 6 μm depth as the scalloping. We did not model filleted exterior corners, which were shown to have the smallest effect of all the nonidealities on reflections in previous simulations. Defrance et al. (2018) showed that similar models of the nonideal geometries can reproduce the measured optical performance of the fabricated structures to high accuracy.

7.2.2 Optimization Procedure

We now turn to the question of how to optimize the design described in Section 7.2.1. Loosely speaking, the goal of the optimization procedure is to minimize the total power reflected from the optic across the 80–420 GHz band. In terms of the S matrix, this is equivalent to minimizing $|S_{11}|^2$. Our criterion for this minimization is that $|S_{11}|^2$ should stay below the level of -20 dB for the whole band. We have chosen this -20 dB criterion to limit optical loading in addition to the "ghosting" effect (e.g., Aikin et al., 2010), in which multiple reflected images arrive at the focal plane. In practice, we have found it difficult to achieve this exact criterion, so we have chosen a slightly more lenient condition based on atmospheric observing windows, which we will describe in detail below. A space-optimized design with similar fractional bandwidths for the individual bands should be achievable with the same number of layers via reoptimization. A space-optimized design that endeavors to meet the -20 dB criterion over the entire window would likely require an additional layer. Both of these space-optimized designs are topics for future work.

To optimize the ARC design, we divided the procedure into a few steps, as follows: optimizing a slab model, mapping the slab model to structures, performing a grid search over the structure dimensions, and confirming the convergence of the grid search by 1-dimensional parameter sweeps. The steps are chosen to make the optimization process as tractable as possible, with each step aiming to successively improve the estimation of the optimal design parameters.

We note that the optimization process may be made more tractable with additional computing power. We performed our optimization—most importantly, the grid search—using up to 12 CPU cores on a shared 24-core machine, which enabled optimizing the design in a time on the order of two weeks. Since HFSS can parallelize its computations for multiple frequencies and different design variations, additional CPU cores—in the context of, e.g., high-performance computing—would speed up the grid search by a linear factor.[1] Such a speedup would enable additional grid resolution and more accurate sampling in the same time, and it could also enable simultaneously varying the layer widths and thicknesses.

Slab Model Optimization

The first step is to construct an analytical model of the entire AR-coated lens. This analytical model, hereafter called the "slab model," consists of a pure silicon substrate ($n = 3.42$), which has six symmetric AR layers on each side and is surrounded by vacuum ($n = 1$). The model has twelve free parameters, with two for each AR layer: the thickness t_i and the refractive index n_i for $1 \leq i \leq 6$. We compute the S parameters for this slab model analytically using the well-established theory of optical thin films (e.g., Born et al., 1999), which is equivalent to the theory of transmission-line impedance transformers (e.g., Pozar, 2012).

It is possible to optimize the slab model parameters t_i and n_i by using a formalism based on Chebyshev polynomials (e.g., Baumeister, 1986). This procedure minimizes the ripple within the passband, and we use its results as a starting point for further optimization. However, to bring the design into better agreement with our -20 dB criterion, we improve the model further using an assortment of least-squares minimization algorithms. We choose a cost function that strongly penalizes excess reflections over $P_{\max} = -18.2$ dB and weakly penalizes those below $P_{\min} = -21$ dB in the 80–420 GHz range. In particular, if we define G as the reflection in dB:

$$G = 20 \log_{10} |S_{11}|, \tag{7.2}$$

then the cost function is defined as

$$G_{\text{opt}} = \begin{cases} 0 & G < P_{\min} \\ \min(|P_{\min} - G|/3, 6) & P_{\min} \leq G \leq P_{\max} \\ \min(2|P_{\max} - G|, 6) & P_{\max} < G \end{cases} . \tag{7.3}$$

---

[1] To take full advantage of the speedup from distributed computing, we note that our optimization script may need to be modified to use the builtin optimetrics feature of HFSS.

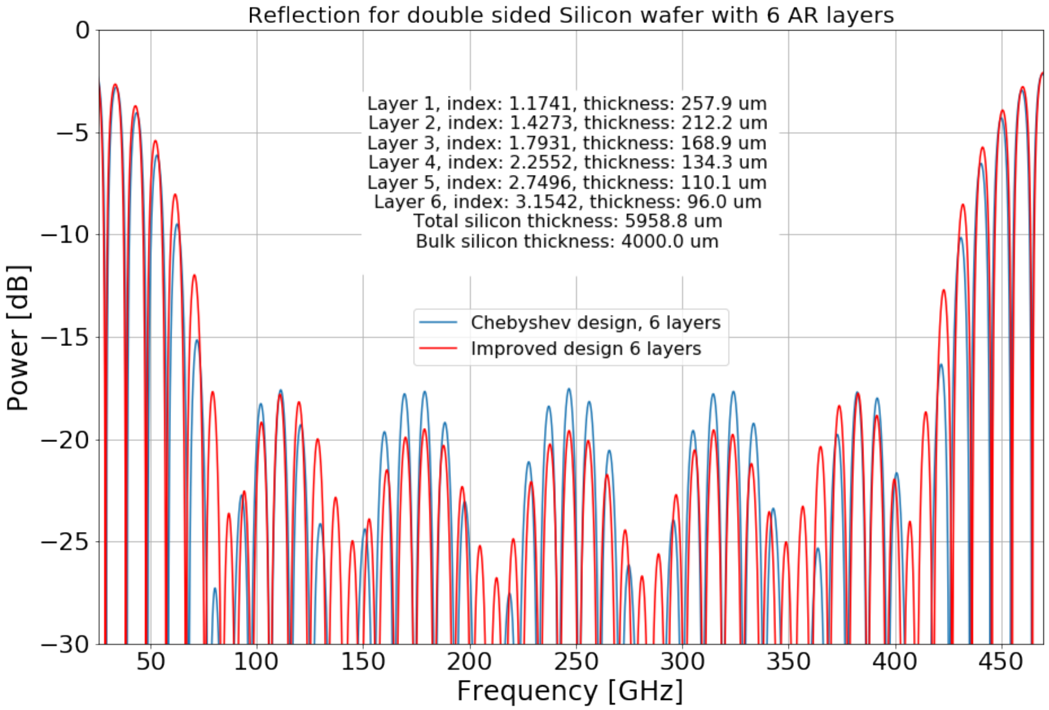

Figure 7.9: Optimized slab model performance for the six-layer design, showing both the Chebyshev-optimized design and the improved design.

We sample this cost function at 200 frequencies within the passband as the input to the least-squares minimizers. The results of the slab model optimization are shown in Figure 7.9.

From Slab Model to Structure

From this optimized slab-model design, we proceed to map the refractive indices n_i to the layer geometries chosen as in Section 7.2.1. We first calculate the inverse mapping of the effective index n_{eff} as a function of f_{Si} for a single AR layer. For the inverse mapping, we rely on the existing HFSS simulations of Defrance et al. (2018), as described in Section 7.1.5. These simulations explored a variety of structure geometries, including square posts, square holes, cross-shaped posts, and cross-shaped holes. Defrance et al. (2018) summarized their simulation results by computing n_{eff} from the simulated S parameters using the Fresnel formulas and then fitting linear and quartic polynomial models to n_{eff} as a function of f_{Si}. We use only their models for square posts and square posts, as follows:

$$n_{\text{eff}} = 1 + f_{\text{Si}}(n_{\text{Si}} - 1) \tag{7.4}$$

for holes and

$$n_{\text{eff}} = 4.9f_{\text{Si}}^4 - 6.28f_{\text{Si}}^3 + 3.11f_{\text{Si}}^2 + 0.66f_{\text{Si}} + 1 \tag{7.5}$$

for posts. Finally, we invert the polynomials of Equations 7.4 and 7.5 numerically to give f_{Si}, and thus the structure dimensions, as a function of n_{eff}. This inversion is valid because both polynomials are monotonic over the interval $[0, 1]$. By evaluating the inverted polynomials at the optimal n_i described above, we arrive at a first-pass model of the entire AR structure. We list the first-pass layer dimensions for several choices of geometry in Table 7.1.

We note a few caveats to this method. First, these models and their corresponding polynomial fits are not perfectly accurate for circular geometries, e.g., circular posts. Second, for a given microstructure geometry, the refractive index n_{eff} varies weakly as a function of frequency. Thus, the structure whose n_{eff} best matches n_i on average will not perform perfectly in agreement with the slab model across a range of frequencies. Despite these caveats, Equations 7.4 and 7.5 are suitable as a first-pass estimate. We verify the optical performance of the structures by simulating the entire AR structure in HFSS, which yields S parameter values roughly in agreement with the slab model predictions. We then optimize these structures as described below.

Layer Num.	t_i (μm)	n_i	Width (μm) (Sq. Posts)	Width (μm) (Sq. Holes)	Diameter (μm) (Cir. Posts)	Diameter (μm) (Cir. Holes)
1	257.9	1.17	30.8	72.3	34.8	-
2	212.2	1.43	44.9	68.1	50.6	-
3	168.9	1.79	58.1	61.5	65.5	69.4
4	134.3	2.26	66.4	52.0	75.0	58.7
5	110.1	2.75	71.1	39.5	-	44.5
6	96.0	3.15	73.8	24.9	-	28.0

Table 7.1: Slab model parameters t_i and n_i with corresponding approximations of the best feature dimensions for each feature geometry: square posts, square holes, circular posts, and circular holes. Missing entries indicate unrealizable dimensions, i.e., those whose dimensions exceed the size of the 75 μm cell.

HFSS Grid Search

Using the dimensions in Table 7.1 as a starting point, we performed a grid search to minimize the reflection $|S_{11}|^2$ over realizable values of the layer dimensions. We parameterized this grid search in terms of the width w_i of the features in each layer; i.e., w_i is the width of the square posts and holes as well as the diameter of circular posts. Each point of the grid search consists of calculating the S parameters for the full six-layer AR structure, with nonidealities modeled as described in Section 7.2.1.[2] The optimization criterion is described in detail below, but roughly speaking, the goal is to minimize the mean reflected power R across the 80–420 GHz band.

To perform the grid search, we vary each of the w_i in steps of ± 3 μm about the starting point. With 6 parameters to vary, this initial phase of the grid search contains $3^6 = 729$ points. Of these grid points, we consider the one that results in the lowest value of R. If the minimum-R point is the starting point, the 3μm grid search is complete, and we shrink the grid to a $1 - \mu$m parameter spacing and repeat the procedure. Otherwise, we extend the grid to include $\pm 3\mu$m steps about the minimum-R point until a local minimum is found.

This procedure has some limitations, but we argue that the obvious remedies are neither feasible nor necessary. For one, it is computationally intractable to simultaneously vary both the feature widths w_i and the layer thicknesses t_i due to the 12-dimensional parameter space combined with expensive HFSS simulations of the full six-layer AR structure, so we did not vary the layer thicknesses t_i in this grid search. We show below, however, that the optimization criterion depends only weakly on the values of t_i, so it is acceptable to omit t_i from the grid search. Additionally, the grid search offers limited precision on constraining the parameter values w_i, but the DRIE technique offers only ~ 1 μm manufacturing tolerance, further confounded by imperfectly known nonidealities, so optimizing to greater precision is unnecessary. Finally, we tried optimizing using a gradient descent algorithm, but we found that it was not numerically stable when run with reasonable accuracy parameters.

We now turn to the precise definition of the optimization criterion. First, we define the mean reflected power across a band $[\nu_0, \nu_1]$:

$$R(\nu_0, \nu_1) = \int_{\nu_0}^{\nu_1} \frac{|S_{11}|^2}{\nu_1 - \nu_0}\, d\nu. \tag{7.6}$$

In the context of space based missions, it is sensible to simply define the optimization criterion as $R(80\text{ GHz}, 420\text{ GHz})$. However, for ground-based observing, atmospheric transmission by water vapor limits observations to a handful of windows in the submm (e.g., Pardo et al., 2001). Thus, it is possible to optimize more aggressively, allowing the reflection to decrease within the windows at the expense

---

[2] We used a relatively relaxed set of simulation parameters for the grid search, including a frequency spacing of 4 GHz, $\Delta S = 0.1$, and a mesh refinement threshold of 0.1λ.

Band Number	1	2	3	4	5	6
Center Frequency (GHz)	90	150	225	285	350	400
Bandwidth (Wide) (GHz)	35	47	45	50	34	30
Bandwidth (Narrow) (GHz)	23.3	31.3	30.0	33.3	22.6	20.0

Table 7.2: Band definitions used to perform the optimizations and frequency scans.

of the reflection outside the windows. We model the observing windows as square bandpasses for simplicity. For this work, then, we minimize the "max-of-means" criterion M:

$$M = \max_b R(\nu_{b,0}, \nu_{b,1}), \tag{7.7}$$

where $\nu_{b,0}$ and $\nu_{b,1}$ are the edges of band b. We take these bands to be the ones centered on 90, 150, 220, 270, 350, and 400 GHz, as used in the first part of this thesis. Because the precise values of the atmospheric observing windows for a given observatory are not known in advance, we performed each calculation for two different sets of band definitions (Table 7.2). We refer to these definitions as the "wide" and "narrow" bands, with the "narrow" bands having $2/3$ the bandwidth of the "wide" bands . We show the results of the optimization in Section 7.3.1.

Alternative Optimization Method Using Transfer Matrices

Having recognized that the optimization procedure described above is computationally expensive, we also explored a cheaper alternative. Our strategy was to predict the multi-layer S matrix by combining the single-layer simulated S matrices S_i, converting to transfer matrices M_i, then multiplying:

$$M_{\text{total}} = M_1 M_2 \cdots M_n, \tag{7.8}$$

and finally converting this product back to an S matrix. This is a standard and correct calculation for a slab model, but we needed to ensure its accuracy in the regime of subwavelength structures with effective indices. If this prediction were accurate, it would enable us to tune each layer to the required effective index and thickness to optimize the multi-layer S parameters while eschewing the costly operation of simulating and modeling the entire structure in HFSS.

For the single-layer case, we succeeded in replicating the simulated S parameters to numerical precision for the full 80–420 GHz frequency range by using a model where both the effective refractive index n_{eff} and the effective thickness t_{eff} are allowed to vary as functions of frequency. However, we found that this approach did

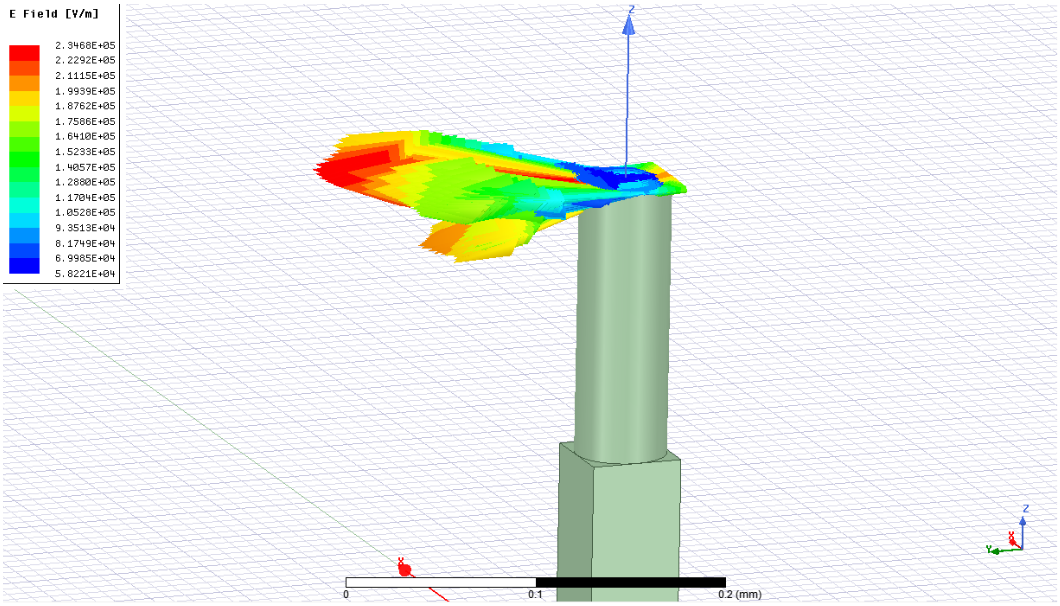

Figure 7.10: Illustration of E-field calculated in HFSS simulations at the top of the posts in a 2-layer structure. The field contains a component that is not tangential to the surface, contrary to the boundary conditions assumed by the transfer matrix method.

not scale accurately to multiple layers. We performed a simple test with two layers of square posts, both in periodic grids in the XY plane, to show that this approach cannot be accurate in general. In particular, we compared the S parameters of two different cases, where (1) the features' Z axes are perfectly aligned and (2) the Z axes are offset in the XY plane. We found that these two cases differ at a maximum level of $\sim 10\%$ over the design frequency range. To attempt to explain this discrepancy, we inspected the E-field calculated for an example structure by HFSS at the upper boundary of the structure, shown in Figure 7.10. We found that the E-field contains a non-zero component perpendicular to the layer boundary, which violates the boundary conditions of the transfer matrix method. Thus, we concluded that even a frequency-dependent S matrix does not have sufficient degrees of freedom to describe the behavior of a single AR layer when coupled to another AR layer. Further efforts to implement this transfer matrix-based optimization method are outside the scope of this work.

Parameter Scans to Confirm Optimization

Finally, to confirm that the grid search has converged to a local optimum, we perform additional HFSS simulations that sweep over each relevant parameter in the design.

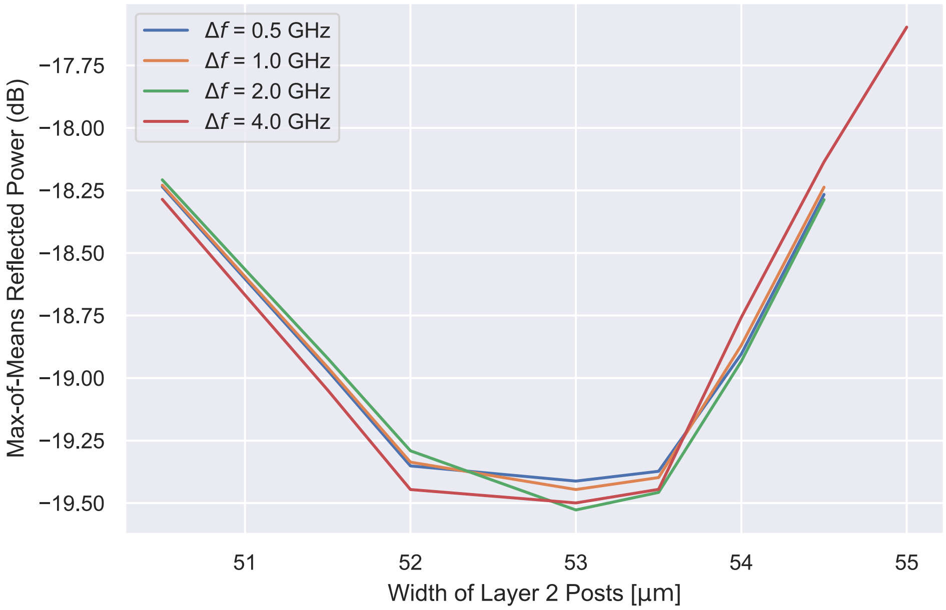

Figure 7.11: Example 1-D parameter scan showing variations of w_2 about the optimum for the nominal design. See Appendix B.1 for the full set of parameter scans.

That is, we individually vary the thickness t_i of each layer and the width w_i of each feature to calculate and show the max-of-means criterion as a function of these parameters. For these simulations, we use a rigorous set of simulation parameters, including a frequency spacing of 0.25 GHz, a mesh refinement threshold of 0.1λ, and a ΔS of 0.01 (cf. $\Delta\nu = 4$ GHz and $\Delta S = 0.1$ for the grid search). Each scan yields the “max-of-means” value as a function of a dimensional parameter. To confirm that these parameters are sufficient for convergence, we plot the 1D scan curves for increasingly coarse frequency spacing, ranging from the nominal 0.5 GHz to 4 GHz. We show an example in Figure 7.11. For the full set of parameter scan plots, refer to Appendix B.1.

7.3 Simulation Results

Below, we give the optimized dimensions of each design we considered along with the performance for each case. We consider the three variants of the six-layer design (Section 7.3.1) in addition to the single case of the five-layer design that we attempted (Section 7.3.2).

Name	Layer	Geometry	Width [μm]	Thickness [μm]
Nominal	1	Circular Posts	31	258
	2	Circular Posts	51	212
	3	Square Posts	56	169
	4	Square Holes	51	134
	5	Square Holes	40.5	110
	6	Square Holes	21.5	96
Aggressive	1	Circular Posts	39	258
	2	Circular Posts	55.5	212
	3	Square Holes	63.5	169
	4	Square Holes	49	134
	5	Square Holes	37.5	110
	6	Square Holes	21	96
Conservative	1	Circular Posts	38	258
	2	Circular Posts	54.5	212
	3	Square Holes	61.5	169
	4	Square Holes	49	134
	5	Square Holes	39.5	110
	6	Square Holes	22	96

Table 7.3: Optimized 6-layer AR structure design dimensions with fabrication nonidealities taken into account. All structures have a 75-μm pitch and are simulated with 4 mm bulk thickness. The performance of each design is given in Table 7.4.

Name	Mean In-Band Reflection (dB)					
	90	150	220	270	350	400
Nominal (wide bands)	-19.1	-19.2	-19.8	-22.2	-21.4	-22.1
Nominal (narrow bands)	-19.9	-19.8	-19.5	-21.9	-21.2	-23.8
Aggressive (wide bands)	-22.0	-26.0	-23.0	-25.6	-22.1	-21.3
Aggressive (narrow bands)	-22.5	-28.4	-22.8	-25.5	-21.8	-22.4
Conservative (wide bands)	-18.6	-19.4	-19.7	-22.6	-23.2	-18.4
Conservative (narrow bands)	-19.1	-20.2	-19.6	-22.9	-23.5	-18.2

Table 7.4: Optimized 6-layer AR structure design performance with fabrication nonidealities taken into account. Reflection and transmission are calculated assuming normal incidence. See Table 7.2 for the definitions of wide and narrow bands. Dimensions of each design are given in Table 7.3.

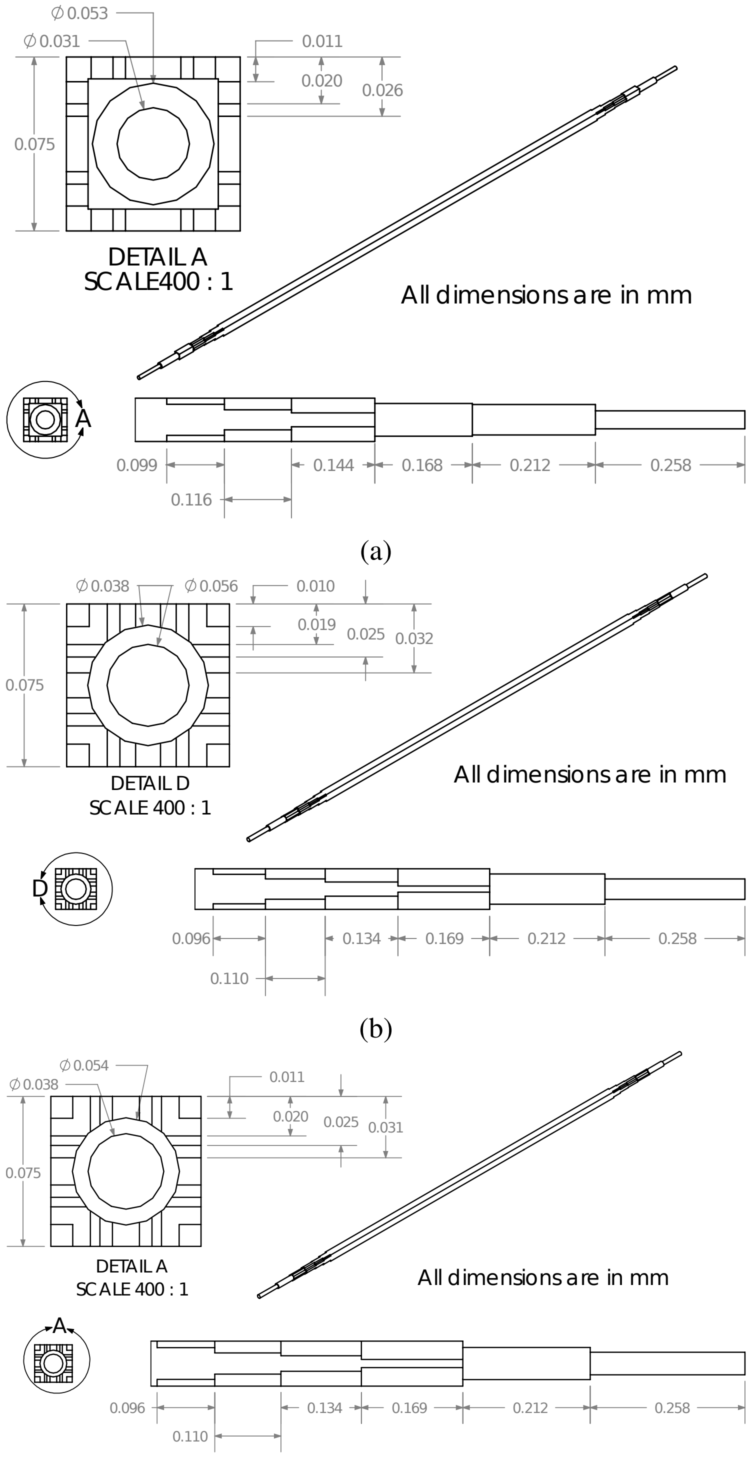

(a)

(b)

(c)

Figure 7.12: Variants of the six-layer ARC design, illustrating as-designed dimensions: nominal design (a), aggressive alternative design (b), and conservative alternative design (c). In all cases, the uppermost layers are circular; the segmented appearance is simply an artifact.

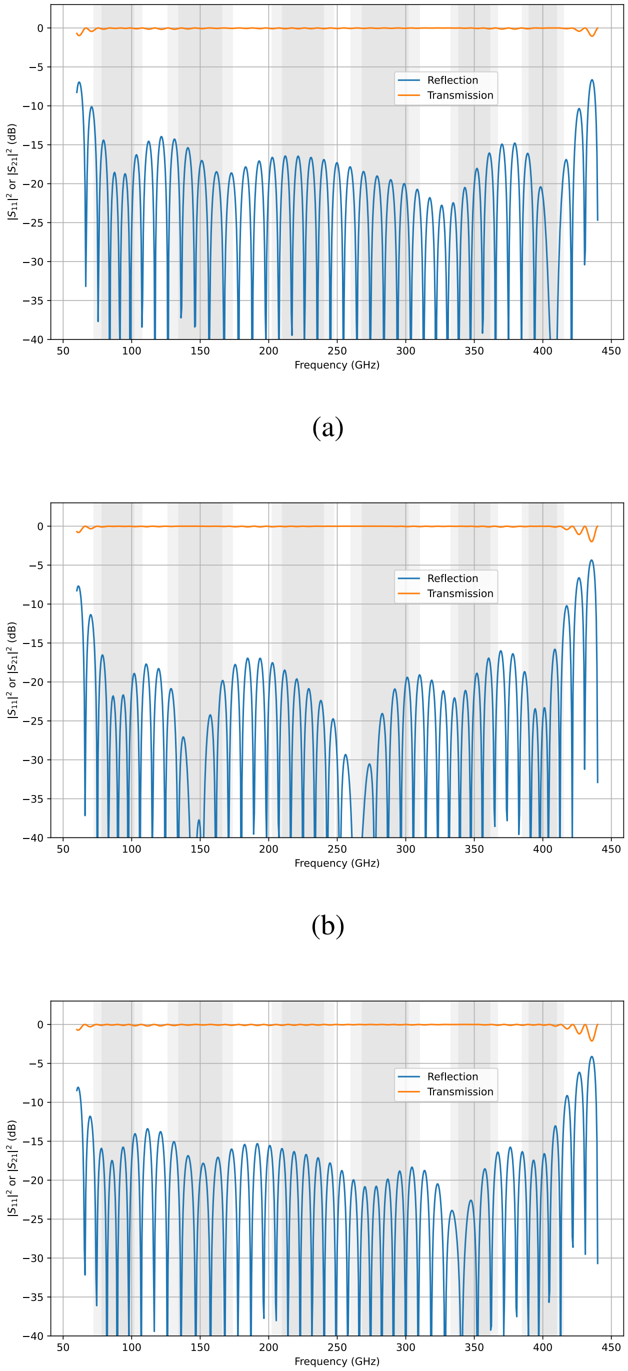

(a)

(b)

(c)

Figure 7.13: Reflection and transmission for variants of the six-layer ARC design, assuming as-designed dimensions: nominal design (a), aggressive alternative design (b), and conservative alternative design (c). The gray shadings denote the observing bands corresponding to the atmospheric transmission windows (Table 7.2), with the wide bands in lighter shading and the narrow bands in darker shading.

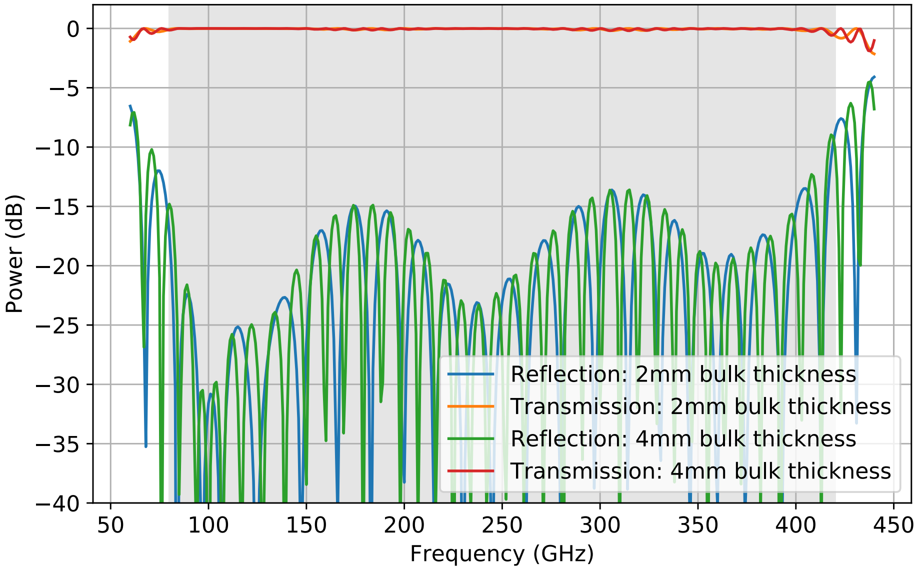

Figure 7.14: HFSS simulations showing reflection and transmission of designs with 2 mm and 4 mm bulk silicon thickness but with identical ARC dimensions. The fringe spacing becomes tighter as the bulk thickness increases, but both versions follow the same envelope.

7.3.1 Six-Layer Design

Here, we present optimization results for each of the nominal, aggressive alternative, and conservative alternative designs. Table 7.3 indicates the geometries and dimensions of each layer in the optimized designs. Figure 7.12 shows drawings of each version based on the optimal dimensions. Figure 7.13 shows the optimal reflection and transmission for each version of the design. Finally, Table 7.4 summarizes the maximum in-band reflection for each design based on the band definitions of Table 7.2. The dimensions were optimized according to the “wide” band definitions, but results are shown for both the wide and narrow band definitions.

The full designs are simulated and optimized under the assumption that the middle wafer contains a 4-mm thick layer of bulk silicon. This bulk silicon thickness primarily dictates the number and positions of the Fabry-Pérot fringes, while the AR structure dictates the envelope of the fringes. See Figure 7.14 for a demonstration of the effect of changing the bulk silicon thickness.

In addition, we examined how significantly nonidealities affected the performance in simulations. In Figure 7.15, we compare three scenarios: (1) the optimal version of the design without nonidealities, (2) a version with nonidealites with the

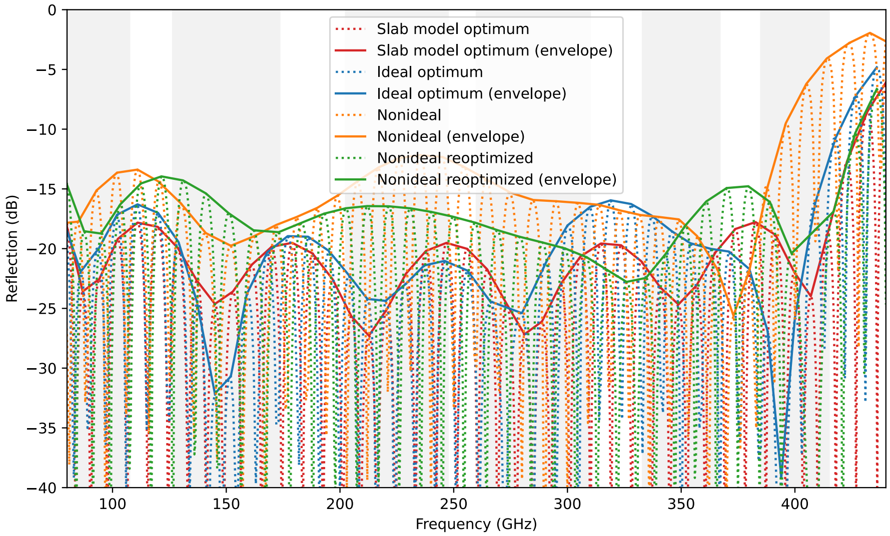

Figure 7.15: HFSS simulations showing optimal reflection of designs with and without nonidealities. The ideal optimum is shown in blue; of the cases that include nonidealities, the first (orange) has the same nominal dimensions as the optimized ideal version, while the second (green) has had its dimensions retuned to minimize reflections. For comparison, we also include the reflection of the optimized slab model (red). For legibility, we show the envelopes in each case (solid curves), along with the full simulated data including Fabry-Pérot fringes (dotted curves).

Name	Mean In-Band Reflection (dB)					
	90	150	220	270	350	400
Ideal nominal (wide bands)	-21.6	-25.6	-25.2	-23.7	-21.4	-23.0
Ideal nominal (narrow bands)	-22.3	-28.7	-25.5	-24.3	-22.3	-23.2
Nominal (wide bands)	-19.1	-19.2	-19.8	-22.2	-21.4	-22.1
Nominal (narrow bands)	-19.9	-19.8	-19.5	-21.9	-21.2	-23.8

Table 7.5: Comparison of optimized 6-layer AR structure design performance with and without fabrication nonidealities. Each version is optimized separately: the “ideal nominal” cases correspond to case (1) in the text, while the “nominal” cases correspond to case (3) in the text. Reflection and transmission are calculated assuming normal incidence. See Table 7.2 for the definitions of wide and narrow bands.

same nominal dimensions as case (1), and (3) the design with nonidealities but reoptimized to minimize in-band reflections. The third case is identical to the reflection in Figure 7.13a. It is apparent that the presence of nonidealities changes the reflection spectrum significantly, especially in band 6 in this case. However, reoptimizing the design with nonidealities taken into account reduces the in-band reflection back to an acceptable level. The band-by-band difference in mean reflection between cases (1) and (3) is given in Table 7.5.

We note that these simulations were performed under the assumption of normal incidence. Our previous measurements of two-layer structures (Defrance et al., 2018) show only a modest difference in performance between normal and 15° incidence, so we expect these optima to generalize well to slightly off-axis measurements. In practice, it would be prudent to verify the performance of any fabricated optics over the range of incidence angles that the application requires.

7.3.2 Five Layer Design

We also considered a five-layer design as an alternative that may be simpler to fabricate. We attempted to design such an alternative using the same methodology as for the six-layer design, except that we did not consider fabrication nonidealities. At the final step, we optimized separately for the wide-band and narrow-band max-of-means reflections. The performance of these optimized designs is shown in Figure 7.16. The wide-band optimized version (Figure 7.16a) has a maximum in-band reflection of -17.3 dB, while narrow-band optimized version (Figure 7.16b) has a maximum in-band reflection of -18.4 dB.

These values are a few dB higher than in the ideal version of the six-layer design. Given that adding nonidealites tends to worsen the reflections, we expect that a version of the five-layer design with nonidealities included would have unacceptably high reflections for the bandwidths considered. Thus, we did not investigate the five-layer case further.

7.4 Discussion and Future Work

With these six-layer designs, we have come close to the useful performance goal of -20 dB reflection silicon optics covering the 80–420 GHz range. These results are promising for the as-designed application of silicon vacuum windows.

We remind the reader of two important limitations in applying the ARC designs to focusing optics. First, the DRIE procedure cannot yet be used on curved lenses

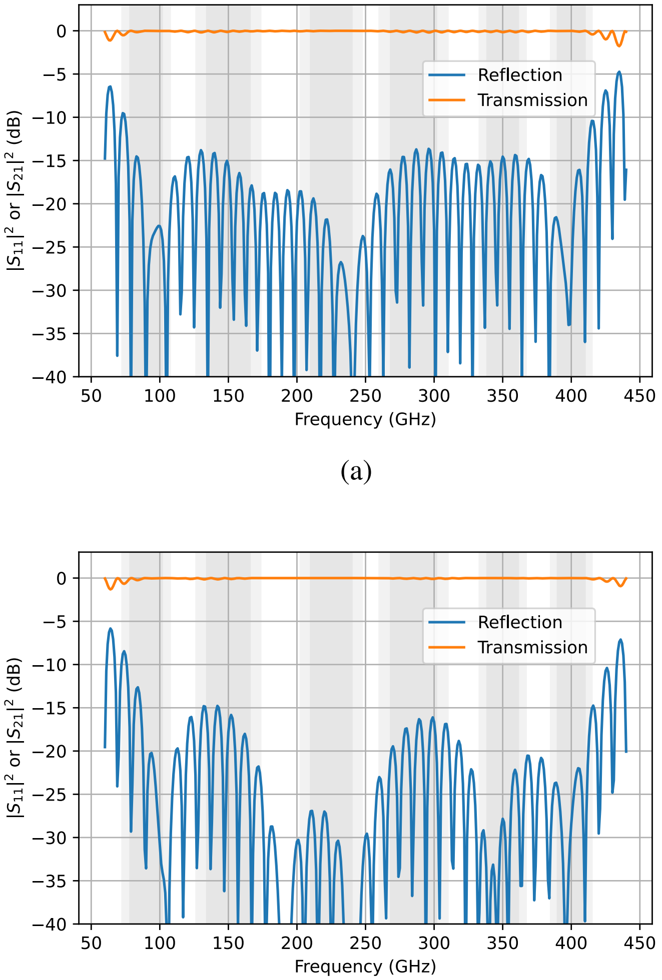

(a)

(b)

Figure 7.16: Reflection and transmission of the optimized ideal five-layer ARC design. (a) shows the performance when optimized for wide bands, and (b) shows the performance optimized for narrow bands.

(Section 7.1), so these ARC designs are not applicable to curved lenses. Second, even for a flat GRIN lens design (see Section 7.2.1), these ARC designs will no longer have optimal performance, as they do not account for the radial variation of the refractive index.

Future work may focus on fabricating and testing the designs presented in this work. Another useful possibility would be to reoptimize these designs for the GRIN lens scenario. To do so, one possible approach would be to extend the design strategy of Defrance et al. (2020), which is based on discrete annuli in the plane perpendicular to the optical axis. Simulating the ARC within each annulus would be possible under the assumption that the features are locally periodic. It would likely be intractable, however, to simultaneously vary each AR parameter over all annuli in a joint optimization. As an alternative, a simple intermediate step would be to optimize the reflection within each annulus individually by assuming that the substrate has an effective refractive index $n_{\mathrm{eff,GRIN}}$ instead of n_{Si}.

It may also be satisfactory to apply a radially uniform AR coating to a GRIN lens structure, which would simplify the design process. Indeed, our group has already designed, fabricated, and tested a prototype GRIN lens with such a relatively simple AR coating. The prototype consists of a stack of 5 GRIN-etched wafers and a 3-layer AR coating. No wafer bonding was used in fabricating this prototype; instead, the wafers of the structure were clamped together for testing. In addition, keys were etched into the wafers to ensure good and reproducible alignment.

Fabien Defrance has measured the prototype's focusing performance from 220 to 330 GHz by illuminating the sample with a corrugated feedhorn and mapping out the phase and magnitude with an XYZ scanning stage and a vector network analyzer. The test results indicate very good focusing performance: the focused beam is Gaussian and has a flat phase front near the focus. As an example, at 275 GHz (Figure 7.17), the beam waist size was measured to be 3.6mm (x axis) by 3.8mm (z axis), compared to the predicted waist size of 3.5mm. In addition, the measured focal length was 229 mm, which differs from the design focal length of 238 mm by only 0.4%. Future work will include characterization of the effects of any gaps between wafers, which may include scattering or imperfect reflection.

We must also note that the planned technique for fabricating the nominal design of the AR coatings depends on wafer bonding, which may introduce dielectric loss. We found in Defrance et al. (2018) that transmission losses from a single wafer bond in a 2-wafer sample were below 1% (see again Figure 7.5). However,

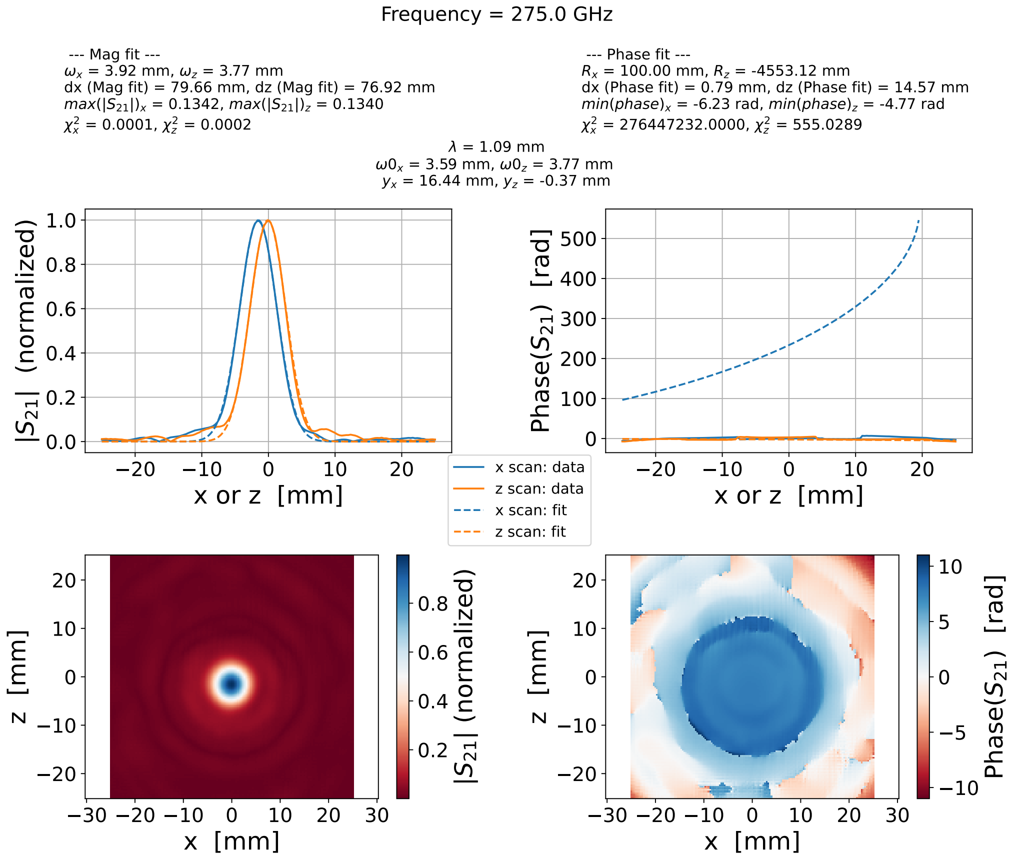

Figure 7.17: Example scans of the GRIN lens prototype at 275 GHz with 3-layer AR structure. The bottom row shows 2-D maps of the focused beam, and the top row shows 1-D profiles of these maps. The left hand column shows the magnitude, and the right column shows the phase front. Parametric fits to the beam profiles are also shown, confirming Gaussianity. The point ($x = 0, z = 0$) corresponds to the design focus. Credit: Fabien Defrance.

we explored variations of the bonding process that can reliably produce a robust bond, including bonding technologies provided by the third-party vendor Cactus Materials ("Cactus"). We determined that the thermal oxidation typically required for wafer bonding can introduce noticeable (>1%) loss and that the Cactus bonding process, which uses chemical activation to obtain a bond at lower temperature than conventional bonding processes, seems to result in higher loss than those conventional processes.

This level of loss may be acceptable for AR structures. For example, the structure described in this work consists of three wafers, so it would require only two wafer bonds in total (one bond for each interface). But such losses would be unacceptable for GRIN lenses that contain ten to tens of wafers. However, the GRIN structures are sufficiently physically robust that clamping, without any bonding, should be sufficient to hold the structure together. In the future, we plan to pursue a higher-temperature bonding process, which may enable a good-quality, low-loss bond, using a new wafer bonder at JPL. The new wafer bonder offers improved alignment capabilities, which may enable fabrication of version A of the 4-layer design (Section 7.1.6; akin to the nominal 6-layer design), which seems to be less fragile than version B, provided that a strong bond is possible.

BIBLIOGRAPHY

Abazajian, Kevork et al. (July 2019). "CMB-S4 Science Case, Reference Design, and Project Plan". In: *arXiv:1907.04473 [astro-ph, physics:hep-ex]*. arXiv: `1907.04473 [astro-ph, physics:hep-ex]`.

Abazajian, Kevork N. et al. (Oct. 2016). "CMB-S4 Science Book, First Edition". In: *arXiv:1610.02743 [astro-ph, physics:gr-qc, physics:hep-ph, physics:hep-th]*. arXiv: `1610.02743 [astro-ph, physics:gr-qc, physics:hep-ph, physics:hep-th]`.

Abitbol, Maximilian H. et al. (June 2017). "CMB-S4 Technology Book, First Edition". In: *arXiv:1706.02464 [astro-ph]*. arXiv: `1706.02464 [astro-ph]`.

Adam, R. et al. (Feb. 2017). "Mapping the Kinetic Sunyaev-Zel'dovich Effect toward MACS J0717.5+3745 with NIKA". In: *A&A* 598, A115. ISSN: 0004-6361, 1432-0746. DOI: `10.1051/0004-6361/201629182`.

Ade, P. A. R. et al. (Mar. 9, 2015). "Joint Analysis of BICEP2/ *Keck Array* and *Planck* Data". In: *Physical Review Letters* 114.10, p. 101301. ISSN: 0031-9007, 1079-7114. DOI: `10.1103/PhysRevLett.114.101301`. URL: `https://link.aps.org/doi/10.1103/PhysRevLett.114.101301` (visited on 06/22/2022).

Aikin, Randol W. et al. (July 16, 2010). "Optical Performance of the BICEP2 Telescope at the South Pole". In: SPIE Astronomical Telescopes + Instrumentation. Ed. by Wayne S. Holland et al. San Diego, California, USA, p. 77410V. DOI: `10.1117/12.857868`. URL: `http://proceedings.spiedigitallibrary.org/proceeding.aspx?doi=10.1117/12.857868` (visited on 04/02/2023).

Alberts, Stacey et al. (Jan. 2014). "The Evolution of Dust-Obscured Star Formation Activity in Galaxy Clusters Relative to the Field over the Last 9 Billion Years". In: *Monthly Notices of the Royal Astronomical Society* 437.1, pp. 437–457. ISSN: 0035-8711, 1365-2966. DOI: `10.1093/mnras/stt1897`.

Alberts, Stacey et al. (June 2016). "STAR FORMATION AND AGN ACTIVITY IN GALAXY CLUSTERS FROM $z = 1$–2: A MULTI-WAVELENGTH ANALYSIS FEATURING *HERSCHEL* /PACS". In: *ApJ* 825.1, p. 72. ISSN: 1538-4357. DOI: `10.3847/0004-637X/825/1/72`.

Alonso, David et al. (Aug. 2016). "Reconstructing Cosmic Growth with Kinetic Sunyaev-Zel'dovich Observations in the Era of Stage IV Experiments". In: *Phys. Rev. D* 94.4, p. 043522. ISSN: 2470-0010, 2470-0029. DOI: `10.1103/PhysRevD.94.043522`.

Antonucci, Robert (1993). "Unified Models for Active Galactic Nuclei and Quasars." In: *Annual Review of Astronomy and Astrophysics* 31, pp. 473–521. ISSN: 0066-4146. DOI: `10.1146/annurev.aa.31.090193.002353`.

Arnaud, M. et al. (July 2010). "The Universal Galaxy Cluster Pressure Profile from a Representative Sample of Nearby Systems (REXCESS) and the $Y_{\rm SZ} - M_{500}$ Relation". In: *A&A* 517, A92. ISSN: 0004-6361, 1432-0746. DOI: `10.1051/0004-6361/200913416`.

Arnold, K. et al. (Aug. 19, 2014). "The Simons Array: Expanding POLARBEAR to Three Multi-Chroic Telescopes". In: *Millimeter, Submillimeter, and Far-Infrared Detectors and Instrumentation for Astronomy VII*. Millimeter, Submillimeter, and Far-Infrared Detectors and Instrumentation for Astronomy VII. Vol. 9153. SPIE, pp. 466–473. DOI: `10.1117/12.2057332`. URL: `https://www.spiedigitallibrary.org/conference-proceedings-of-spie/9153/91531F/The-Simons-Array--expanding-POLARBEAR-to-three-multi-chroic/10.1117/12.2057332.full` (visited on 12/20/2022).

Barkats, Denis et al. (Aug. 2018). *Ultra-Thin Large-Aperture Vacuum Windows for Millimeter Wavelengths Receivers*. arXiv: `arXiv:1808.00570`.

Barret, Didier et al. (Feb. 2020). "The Athena Space X-ray Observatory and the Astrophysics of Hot Plasma". In: *Astron. Nachr* 341.2, pp. 224–235. ISSN: 0004-6337, 1521-3994. DOI: `10.1002/asna.202023782`. arXiv: `1912.04615`.

Bartelmann, Matthias (Feb. 1996). "Arcs from a Universal Dark-Matter Halo Profile". In: *arXiv:astro-ph/9602053*. arXiv: `astro-ph/9602053`.

Battaglia, N. et al. (Oct. 2013). "REIONIZATION ON LARGE SCALES. III. PREDICTIONS FOR LOW-ℓ COSMIC MICROWAVE BACKGROUND POLARIZATION AND HIGH-ℓ KINETIC SUNYAEV-ZEL'DOVICH OBSERVABLES". In: *ApJ* 776.2, p. 83. ISSN: 0004-637X, 1538-4357. DOI: `10.1088/0004-637X/776/2/83`.

Baumeister, Philip (Dec. 15, 1986). "Antireflection Coatings with Chebyshev or Butterworth Response: Design". In: *Applied Optics* 25.24, p. 4568. ISSN: 0003-6935, 1539-4522. DOI: `10.1364/AO.25.004568`. URL: `https://opg.optica.org/abstract.cfm?URI=ao-25-24-4568` (visited on 07/21/2022).

Bender, Amy Nicole (Jan. 2011). "Galaxy Cluster Scaling Relations with APEX-SZ". PhD thesis.

Benitez-Llambay, Alejandro (July 2015). *Py-Sphviewer: Py-Sphviewer V1.0.0*. Zenodo. DOI: `10.5281/ZENODO.21703`.

Benoit-Lévy, A. et al. (July 2013). "Full-Sky CMB Lensing Reconstruction in Presence of Sky-Cuts". In: *A&A* 555, A37. ISSN: 0004-6361, 1432-0746. DOI: `10.1051/0004-6361/201321048`.

Bertoldi, Frank (Jan. 2018). "The Atacama Large Aperture Submm/Mm Telescope (Atlast) Project". In: DOI: `10.5281/ZENODO.1158842`.

Béthermin, Matthieu et al. (Nov. 2017). "The Impact of Clustering and Angular Resolution on Far-Infrared and Millimeter Continuum Observations". In: *A&A* 607, A89. ISSN: 0004-6361, 1432-0746. DOI: `10.1051/0004-6361/201730866`.

Beutler, Florian et al. (Sept. 2014). “The Clustering of Galaxies in the SDSS-III Baryon Oscillation Spectroscopic Survey: Testing Gravity with Redshift-Space Distortions Using the Power Spectrum Multipoles”. In: *Monthly Notices of the Royal Astronomical Society* 443.2, pp. 1065–1089. ISSN: 1365-2966, 0035-8711. DOI: `10.1093/mnras/stu1051`. arXiv: `1312.4611 [astro-ph]`.

Bhattacharya, Suman et al. (Apr. 2008). “Dark Energy Constraints from Galaxy Cluster Peculiar Velocities”. In: *Phys. Rev. D* 77.8, p. 083004. ISSN: 1550-7998, 1550-2368. DOI: `10.1103/PhysRevD.77.083004`.

Biber, S. et al. (Oct. 2003). “Design of Artificial Dielectrics for Anti-Reflection-Coatings”. In: *33rd European Microwave Conference Proceedings (IEEE Cat. No.03EX723C)*. 33rd European Microwave Conference Proceedings (IEEE Cat. No.03EX723C). Vol. 3, 1115–1118 Vol.3. DOI: `10.1109/EUMC.2003.177679`.

Biffi, V. et al. (Mar. 2014). “The MUSIC of Galaxy Clusters – II. X-ray Global Properties and Scaling Relations”. In: *Monthly Notices of the Royal Astronomical Society* 439.1, pp. 588–603. ISSN: 0035-8711. DOI: `10.1093/mnras/stu018`.

Birkinshaw, M (Mar. 1999). “The Sunyaev–Zel’dovich Effect”. In: *Physics Reports* 310.2-3, pp. 97–195. ISSN: 03701573. DOI: `10.1016/S0370-1573(98)00080-5`.

Blain, A. W. (Sept. 1997). “Gravitational Lensing by Clusters of Galaxies in the Millimetre/Submillimetre Waveband”. In: *Monthly Notices of the Royal Astronomical Society* 290.3, pp. 553–565. ISSN: 0035-8711, 1365-2966. DOI: `10.1093/mnras/290.3.553`.

– (Feb. 2002). “Exploiting Magnification Bias in Ultradeep Submillimetre-Wave Surveys Using ALMA”. In: *Monthly Notices of the Royal Astronomical Society* 330.1, pp. 219–224. ISSN: 0035-8711, 1365-2966. DOI: `10.1046/j.1365-8711.2002.05058.x`.

Blandford, R. D. et al. (Sept. 1992). “Cosmological Applications of Gravitational Lensing”. In: *Annu. Rev. Astron. Astrophys.* 30.1, pp. 311–358. ISSN: 0066-4146, 1545-4282. DOI: `10.1146/annurev.aa.30.090192.001523`.

Bock, James et al. (May 27, 2008). “The Experimental Probe of Inflationary Cosmology (EPIC): A Mission Concept Study for NASA’s Einstein Inflation Probe”. URL: `http://arxiv.org/abs/0805.4207` (visited on 04/13/2021).

Bock, James et al. (June 5, 2009). “Study of the Experimental Probe of Inflationary Cosmology (EPIC)-Intemediate Mission for NASA’s Einstein Inflation Probe”. URL: `http://arxiv.org/abs/0906.1188` (visited on 04/13/2021).

Born, Max et al. (Oct. 13, 1999). *Principles of Optics: Electromagnetic Theory of Propagation, Interference and Diffraction of Light*. 7th ed. Cambridge University Press. ISBN: 978-0-521-64222-4 978-0-521-78449-8 978-1-139-64418-1. DOI: `10.1017/CBO9781139644181`. URL: `https://www.cambridge.org/core/product/identifier/9781139644181/type/book` (visited on 07/21/2022).

Bracco, A. et al. (Apr. 2011). "Herschel-ATLAS: Statistical Properties of Galactic Cirrus in the GAMA-9 Hour Science Demonstration Phase Field". In: *Monthly Notices of the Royal Astronomical Society* 412.2, pp. 1151–1161. ISSN: 0035-8711. DOI: `10.1111/j.1365-2966.2010.17971.x`.

Bryan, Sean (Jan. 2018). "The Toltec Camera For The Lmt Telescope". In: DOI: `10.5281/ZENODO.1159073`.

Butler, Victoria L. et al. (June 2022). "Measurement of the Relativistic Sunyaev–Zeldovich Correction in RX J1347.5-1145". In: *ApJ* 932.1, p. 55. ISSN: 0004-637X. DOI: `10.3847/1538-4357/ac6c04`.

Byrnes, Steven J. et al. (Mar. 7, 2016). "Designing Large, High-Efficiency, High-Numerical-Aperture, Transmissive Meta-Lenses for Visible Light". In: *Optics Express* 24.5, pp. 5110–5124. ISSN: 1094-4087. DOI: `10.1364/OE.24.005110`. URL: `https://opg.optica.org/oe/abstract.cfm?uri=oe-24-5-5110` (visited on 01/14/2023).

Cai, Zhen-Yi et al. (Apr. 2013). "A HYBRID MODEL FOR THE EVOLUTION OF GALAXIES AND ACTIVE GALACTIC NUCLEI IN THE INFRARED". In: *ApJ* 768.1, p. 21. ISSN: 0004-637X, 1538-4357. DOI: `10.1088/0004-637X/768/1/21`.

Calabrese, Erminia et al. (Aug. 2014). "Precision Epoch of Reionization Studies with Next-Generation CMB Experiments". In: *J. Cosmol. Astropart. Phys.* 2014.08, pp. 010–010. ISSN: 1475-7516. DOI: `10.1088/1475-7516/2014/08/010`.

Carlstrom, John E. et al. (Sept. 2002). "Cosmology with the Sunyaev-Zel'dovich Effect". In: *Annu. Rev. Astron. Astrophys.* 40.1, pp. 643–680. ISSN: 0066-4146, 1545-4282. DOI: `10.1146/annurev.astro.40.060401.093803`.

Casey, Caitlin M. et al. (Aug. 2014). "Dusty Star-Forming Galaxies at High Redshift". In: *Physics Reports* 541.2, pp. 45–161. ISSN: 03701573. DOI: `10.1016/j.physrep.2014.02.009`.

CCAT-Prime Collaboration et al. (Dec. 2022). "CCAT-prime Collaboration: Science Goals and Forecasts with Prime-Cam on the Fred Young Submillimeter Telescope". In: *ApJS* 264.1, p. 7. ISSN: 0067-0049. DOI: `10.3847/1538-4365/ac9838`.

Child, Hillary L. et al. (May 2018). "Halo Profiles and the Concentration–Mass Relation for a ΛCDM Universe". In: *ApJ* 859.1, p. 55. ISSN: 1538-4357. DOI: `10.3847/1538-4357/aabf95`.

Chluba, J. et al. (Jan. 2014). "Multiple Scattering Sunyaev–Zeldovich Signal – I. Lowest Order Effect". In: *Monthly Notices of the Royal Astronomical Society* 437.1, pp. 67–76. ISSN: 0035-8711, 1365-2966. DOI: `10.1093/mnras/stt1861`.

Chluba, Jens et al. (Oct. 2012). “A Fast and Accurate Method for Computing the Sunyaev-Zel’dovich Signal of Hot Galaxy Clusters: Computation of SZ Signal”. In: *Monthly Notices of the Royal Astronomical Society* 426.1, pp. 510–530. ISSN: 00358711. DOI: `10.1111/j.1365-2966.2012.21741.x`.

Coble, K. et al. (June 2007). “Radio Sources toward Galaxy Clusters at 30 GHz”. In: *AJ* 134.3, p. 897. ISSN: 1538-3881. DOI: `10.1086/519973`.

Collaboration, The COrE et al. (Apr. 29, 2011). “COrE (Cosmic Origins Explorer) A White Paper”. URL: `http://arxiv.org/abs/1102.2181` (visited on 04/23/2021).

Cooray, Asantha R. et al. (Apr. 1998). “Radio Sources in Galaxy Clusters at 28.5 GHz”. In: *AJ* 115.4, p. 1388. ISSN: 1538-3881. DOI: `10.1086/300310`.

COR PATR (2017). *Cosmic Origins (COR) Program Annual Technology Report*. URL: `https://cor.gsfc.nasa.gov/docs/CORPATR092817Finalweb.pdf` (visited on 07/14/2022).

Crawford, T. M. et al. (July 2010). “A METHOD FOR INDIVIDUAL SOURCE BRIGHTNESS ESTIMATION IN SINGLE- AND MULTI-BAND DATA”. In: *ApJ* 718.1, pp. 513–521. ISSN: 0004-637X, 1538-4357. DOI: `10.1088/0004-637X/718/1/513`.

Czakon, N. G. et al. (June 2015). “GALAXY CLUSTER SCALING RELATIONS BETWEEN BOLOCAM SUNYAEV–ZEL’DOVICH EFFECT AND *CHANDRA* X-RAY MEASUREMENTS”. In: *ApJ* 806.1, p. 18. ISSN: 1538-4357. DOI: `10.1088/0004-637X/806/1/18`.

Datta, R. et al. (Dec. 20, 2013). “Large-Aperture Wide-Bandwidth Antireflection-Coated Silicon Lenses for Millimeter Wavelengths”. In: *Applied Optics* 52.36, p. 8747. ISSN: 1559-128X, 2155-3165. DOI: `10.1364/AO.52.008747`. URL: `https://www.osapublishing.org/abstract.cfm?URI=ao-52-36-8747` (visited on 08/19/2019).

Davidzon, I. et al. (Sept. 2017). “The COSMOS2015 Galaxy Stellar Mass Function: Thirteen Billion Years of Stellar Mass Assembly in Ten Snapshots”. In: *A&A* 605, A70. ISSN: 0004-6361, 1432-0746. DOI: `10.1051/0004-6361/201730419`.

Davis, M. et al. (May 1985). “The Evolution of Large-Scale Structure in a Universe Dominated by Cold Dark Matter”. In: *The Astrophysical Journal* 292, pp. 371–394. ISSN: 0004-637X. DOI: `10.1086/163168`.

De Bernardis, Francesco et al. (Mar. 2017). “Detection of the Pairwise Kinematic Sunyaev-Zel’dovich Effect with BOSS DR11 and the Atacama Cosmology Telescope”. In: *J. Cosmol. Astropart. Phys.* 2017.03, pp. 008–008. ISSN: 1475-7516. DOI: `10.1088/1475-7516/2017/03/008`.

Defrance, F. et al. (Apr. 2020). “Flat Low-Loss Silicon Gradient Index Lens for Millimeter and Submillimeter Wavelengths”. In: *Journal of Low Temperature Physics* 199.1-2, pp. 376–383. ISSN: 0022-2291, 1573-7357. DOI: `10.1007/s10909-019-02255-x`. URL: `http://link.springer.com/10.1007/s10909-019-02255-x` (visited on 09/08/2022).

Defrance, Fabien et al. (June 20, 2018). “16:1 Bandwidth Two-Layer Antireflection Structure for Silicon Matched to the 190–310 GHz Atmospheric Window”. In: *Applied Optics* 57.18, p. 5196. ISSN: 1559-128X, 2155-3165. DOI: `10.1364/AO.57.005196`. URL: `https://www.osapublishing.org/abstract.cfm?URI=ao-57-18-5196` (visited on 08/19/2019).

Delabrouille, J. et al. (Dec. 2003). “Multidetector Multicomponent Spectral Matching and Applications for Cosmic Microwave Background Data Analysis”. In: *Monthly Notices of the Royal Astronomical Society* 346, pp. 1089–1102. ISSN: 0035-8711. DOI: `10.1111/j.1365-2966.2003.07069.x`.

Delabrouille, J. et al. (Jan. 2009a). “A Full Sky, Low Foreground, High Resolution CMB Map from WMAP”. In: *A&A* 493.3, pp. 835–857. ISSN: 0004-6361, 1432-0746. DOI: `10.1051/0004-6361:200810514`.

Delabrouille, J. et al. (2009b). “Diffuse Source Separation in CMB Observations”. In: *Data Analysis in Cosmology*. Ed. by Vicent J. Martinez et al. Lecture Notes in Physics. Berlin, Heidelberg: Springer, pp. 159–205. ISBN: 978-3-540-44767-2. DOI: `10.1007/978-3-540-44767-2_6`.

Deshev, Boris et al. (June 2020). “Mapping the Working of Environmental Effects in A963”. In: *Astronomy and Astrophysics* 638, A126. ISSN: 0004-6361. DOI: `10.1051/0004-6361/202037803`.

DESI Collaboration et al. (Dec. 2016). *The DESI Experiment Part I: Science,Targeting, and Survey Design*. arXiv: `arXiv:1611.00036`.

Diolaiti, Emiliano et al. (July 2000). “StarFinder: An IDL GUI-based Code to Analyze Crowded Fields with Isoplanatic Correcting PSF Fitting”. In: *Astronomical Telescopes and Instrumentation*. Ed. by Peter L. Wizinowich. Munich, Germany, pp. 879–888. DOI: `10.1117/12.390377`.

Drouet d’Aubigny, Christian Y. et al. (Sept. 28, 2001). “Laser Microchemical Etching of Waveguides and Quasi-Optical Components”. In: Micromachining and Microfabrication. Ed. by Jean Michel Karam et al. San Francisco, CA, pp. 101–110. DOI: `10.1117/12.442932`. URL: `http://proceedings.spiedigitallibrary.org/proceeding.aspx?articleid=899694` (visited on 08/19/2019).

Eckert, D. et al. (Jan. 2019). “Non-Thermal Pressure Support in X-COP Galaxy Clusters”. In: *Astronomy & Astrophysics, Volume 621, id.A40, <NUMPAGES>11</NUMPAGES> pp.* 621, A40. ISSN: 0004-6361. DOI: `10.1051/0004-6361/201833324`.

Eriksen, H. K. et al. (Sept. 2004). "On Foreground Removal from the Wilkinson Microwave Anisotropy Probe Data by an Internal Linear Combination Method: Limitations and Implications". In: *ApJ* 612.2, p. 633. ISSN: 0004-637X. DOI: `10.1086/422807`.

Erler, Jens et al. (May 2018). "Planck's View on the Spectrum of the Sunyaev–Zeldovich Effect". In: *Monthly Notices of the Royal Astronomical Society* 476.3, pp. 3360–3381. ISSN: 0035-8711, 1365-2966. DOI: `10.1093/mnras/sty327`.

Feder, Richard M. et al. (Mar. 2020). "Multiband Probabilistic Cataloging: A Joint Fitting Approach to Point-source Detection and Deblending". In: *AJ* 159.4, p. 163. ISSN: 1538-3881. DOI: `10.3847/1538-3881/ab74cf`.

Forni, Olivier et al. (Dec. 2005). "Adapted Method for Separating Kinetic SZ Signal from Primary CMB Fluctuations". In: *EURASIP J. Adv. Signal Process.* 2005.15, pp. 1–13. ISSN: 1687-6180. DOI: `10.1155/ASP.2005.2413`.

Gallardo, Patricio A. et al. (Apr. 1, 2017). "Deep Reactive Ion Etched Anti-Reflection Coatings for Sub-Millimeter Silicon Optics". In: *Applied Optics* 56.10, p. 2796. ISSN: 0003-6935, 1539-4522. DOI: `10.1364/AO.56.002796`. URL: `https://www.osapublishing.org/abstract.cfm?URI=ao-56-10-2796` (visited on 08/19/2019).

Gaskin, Jessica A. et al. (July 2018). "The Lynx X-ray Observatory: Concept Study Overview and Status". In: *Space Telescopes and Instrumentation 2018: Ultraviolet to Gamma Ray*. Vol. 10699. SPIE, pp. 120–129. DOI: `10.1117/12.2314149`.

Gianfagna, Giulia et al. (Mar. 2021). "Exploring the Hydrostatic Mass Bias in MUSIC Clusters: Application to the NIKA2 Mock Sample". In: *Monthly Notices of the Royal Astronomical Society* 502.4, pp. 5115–5133. ISSN: 0035-8711, 1365-2966. DOI: `10.1093/mnras/stab308`.

Gil-Marín, Héctor et al. (Aug. 2016). "The Clustering of Galaxies in the SDSS-III Baryon Oscillation Spectroscopic Survey: RSD Measurement from the LOS-dependent Power Spectrum of DR12 BOSS Galaxies". In: *Monthly Notices of the Royal Astronomical Society* 460, pp. 4188–4209. ISSN: 0035-8711. DOI: `10.1093/mnras/stw1096`.

Golse, G. et al. (Aug. 2002). "Pseudo Elliptical Lensing Mass Model: Application to the NFW Mass Distribution". In: *A&A* 390.3, pp. 821–827. ISSN: 0004-6361, 1432-0746. DOI: `10.1051/0004-6361:20020639`.

Golwala, Sunil (Jan. 2018). "The Chajnantor Sub/Millimeter Survey Telescope". In: DOI: `10.5281/ZENODO.1159094`.

Grazian, A. et al. (Mar. 2015). "The Galaxy Stellar Mass Function at $3.5 \leq z \leq 7.5$ in the CANDELS/UDS, GOODS-South, and HUDF Fields". In: *A&A* 575, A96. ISSN: 0004-6361, 1432-0746. DOI: `10.1051/0004-6361/201424750`.

Gruzinov, Andrei et al. (Dec. 1998). "Secondary Cosmic Microwave Background Anisotropies in a Universe Reionized in Patches". In: *ApJ* 508.2, pp. 435–439. ISSN: 0004-637X, 1538-4357. DOI: `10.1086/306432`.

Hanany, S. et al. (Aug. 20, 2019). "PICO: Probe of Inflation and Cosmic Origins". URL: `http://arxiv.org/abs/1908.07495` (visited on 04/23/2021).

Hand, Nick et al. (July 2012). "Evidence of Galaxy Cluster Motions with the Kinematic Sunyaev-Zel'dovich Effect". In: *Physical Review Letters* 109, p. 041101. ISSN: 0031-9007. DOI: `10.1103/PhysRevLett.109.041101`.

Henderson, S. W. et al. (Aug. 1, 2016). "Advanced ACTPol Cryogenic Detector Arrays and Readout". In: *Journal of Low Temperature Physics* 184.3, pp. 772–779. ISSN: 1573-7357. DOI: `10.1007/s10909-016-1575-z`. URL: `https://doi.org/10.1007/s10909-016-1575-z` (visited on 12/20/2022).

Hitomi Collaboration (July 2016). "The Quiescent Intracluster Medium in the Core of the Perseus Cluster". In: *Nature* 535.7610, pp. 117–121. ISSN: 0028-0836, 1476-4687. DOI: `10.1038/nature18627`.

Hitomi Collaboration et al. (Mar. 2018). "Atmospheric Gas Dynamics in the Perseus Cluster Observed with Hitomi*". In: *Publications of the Astronomical Society of Japan* 70.2. ISSN: 0004-6264, 2053-051X. DOI: `10.1093/pasj/psx138`.

Hoffman, Yehuda et al. (Oct. 1991). "Constrained Realizations of Gaussian Fields: A Simple Algorithm". In: *The Astrophysical Journal* 380, p. L5. ISSN: 0004-637X. DOI: `10.1086/186160`.

Huchra, J. P. et al. (June 1982). "Groups of Galaxies. I. Nearby Groups". In: *The Astrophysical Journal* 257, pp. 423–437. ISSN: 0004-637X. DOI: `10.1086/160000`.

Itoh, N. et al. (Apr. 2004). "Relativistic Corrections to the Sunyaev-Zeldovich Effect for Extremely Hot Clusters of Galaxies". In: *A&A* 417.3, pp. 827–832. ISSN: 0004-6361, 1432-0746. DOI: `10.1051/0004-6361:20034236`.

Itoh, Naoki et al. (July 1998). "Relativistic Corrections to the Sunyaev-Zeldovich Effect for Clusters of Galaxies". In: *ApJ* 502.1, pp. 7–15. ISSN: 0004-637X, 1538-4357. DOI: `10.1086/305876`.

Jeong, O. et al. (Aug. 2016). "Broadband Plasma-Sprayed Anti-reflection Coating for Millimeter-Wave Astrophysics Experiments". In: *Journal of Low Temperature Physics* 184.3-4, pp. 621–626. ISSN: 0022-2291, 1573-7357. DOI: `10.1007/s10909-015-1442-3`. URL: `http://link.springer.com/10.1007/s10909-015-1442-3` (visited on 01/06/2021).

Jung-Kubiak, Cecile et al. (2016). "A Multistep DRIE Process for Complex Terahertz Waveguide Components". In: *IEEE Transactions on Terahertz Science and Technology*, pp. 1–6. ISSN: 2156-342X, 2156-3446. DOI: `10.1109/TTHZ.2016.2593793`. URL: `http://ieeexplore.ieee.org/document/7534863/` (visited on 08/19/2019).

Kamionkowski, Marc et al. (Jan. 15, 1998). “Detectability of Inflationary Gravitational Waves with Microwave Background Polarization”. In: *Physical Review D* 57.2, pp. 685–691. ISSN: 0556-2821, 1089-4918. DOI: `10.1103/PhysRevD.57.685`. URL: `https://link.aps.org/doi/10.1103/PhysRevD.57.685` (visited on 06/22/2022).

Kelvin, Lee S. et al. (Oct. 2014). “Galaxy And Mass Assembly (GAMA): Stellar Mass Functions by Hubble Type”. In: *Monthly Notices of the Royal Astronomical Society* 444.2, pp. 1647–1659. ISSN: 0035-8711, 1365-2966. DOI: `10.1093/mnras/stu1507`.

Kennicutt, Robert C. (Sept. 1998). “STAR FORMATION IN GALAXIES ALONG THE HUBBLE SEQUENCE”. In: *Annu. Rev. Astron. Astrophys.* 36.1, pp. 189–231. ISSN: 0066-4146, 1545-4282. DOI: `10.1146/annurev.astro.36.1.189`.

Kim, Alex G. et al. (Jan. 2020). “Complementarity of Peculiar Velocity Surveys and Redshift Space Distortions for Testing Gravity”. In: *Phys. Rev. D* 101.2, p. 023516. ISSN: 2470-0010, 2470-0029. DOI: `10.1103/PhysRevD.101.023516`.

Kim, Junhan (May 2020). Private communication. URL: `http://mmtel.pbworks.com/w/file/fetch/140224611/200527KimkSZInpaintingLPF.pdf`.

Klaassen, Pamela et al. (July 2019). “The Atacama Large Aperture Submillimeter Telescope (AtLAST)”. In: *arXiv:1907.04756 [astro-ph]*. arXiv: `1907.04756 [astro-ph]`.

Knox, Lloyd et al. (Sept. 1998). “Impact of Inhomogeneous Reionization on Cosmic Microwave Background Anisotropy”. In: *Phys. Rev. Lett.* 81.10, pp. 2004–2007. ISSN: 0031-9007, 1079-7114. DOI: `10.1103/PhysRevLett.81.2004`.

Kosowsky, Arthur et al. (Sept. 2009). “A Future Test of Gravitation Using Galaxy Cluster Velocities”. In: *Phys. Rev. D* 80.6, p. 062003. ISSN: 1550-7998, 1550-2368. DOI: `10.1103/PhysRevD.80.062003`.

Laermer, Franz et al. (2015). “Deep Reactive Ion Etching”. In: *Handbook of Silicon Based MEMS Materials and Technologies*. Elsevier, pp. 444–469. ISBN: 978-0-323-29965-7. DOI: `10.1016/B978-0-323-29965-7.00021-X`. URL: `https://linkinghub.elsevier.com/retrieve/pii/B978032329965700021X` (visited on 08/19/2019).

Lau, Erwin T. et al. (Nov. 2009). “Residual Gas Motions in the Intracluster Medium and Bias in Hydrostatic Measurements of Mass Profiles of Clusters”. In: *The Astrophysical Journal* 705, pp. 1129–1138. ISSN: 0004-637X. DOI: `10.1088/0004-637X/705/2/1129`.

Leach, S. M. et al. (Nov. 2008). “Component Separation Methods for the PLANCK Mission”. In: *A&A* 491.2, pp. 597–615. ISSN: 0004-6361, 1432-0746. DOI: `10.1051/0004-6361:200810116`.

Lee, Elizabeth et al. (Dec. 2022). “A Multisimulation Study of Relativistic SZ Temperature Scalings in Galaxy Clusters and Groups”. In: *Monthly Notices of the Royal Astronomical Society* 517.4, pp. 5303–5324. ISSN: 0035-8711. DOI: `10.1093/mnras/stac2781`.

Levenberg, Kenneth (July 1944). “A Method for the Solution of Certain Non-Linear Problems in Least Squares”. In: *Quart. Appl. Math.* 2.2, pp. 164–168. ISSN: 0033-569X, 1552-4485. DOI: `10.1090/qam/10666`.

Levi, Michael et al. (Aug. 2013). “The DESI Experiment, a Whitepaper for Snowmass 2013”. In: *arXiv:1308.0847 [astro-ph]*. arXiv: `1308.0847 [astro-ph]`.

Lewis, Antony et al. (Aug. 2000). “Efficient Computation of Cosmic Microwave Background Anisotropies in Closed Friedmann-Robertson-Walker Models”. In: *The Astrophysical Journal* 538, pp. 473–476. ISSN: 0004-637X. DOI: `10.1086/309179`.

Li, Yi-Chao et al. (Jan. 2018). “Measurement of the Pairwise Kinematic Sunyaev-Zeldovich Effect with Planck and BOSS Data”. In: *Physical Review D* 97, p. 023514. ISSN: 1550-79980556-2821. DOI: `10.1103/PhysRevD.97.023514`.

Lima, Marcos et al. (Aug. 2010). “Lensing Magnification: Implications for Counts of Submillimetre Galaxies and SZ Clusters: Lensing Magnification: SMGs and SZ Clusters”. In: *Monthly Notices of the Royal Astronomical Society* 406.4, pp. 2352–2372. ISSN: 00358711. DOI: `10.1111/j.1365-2966.2010.16884.x`.

Lindner, Robert R. et al. (Apr. 2015). “THE ATACAMA COSMOLOGY TELESCOPE: THE LABOCA/ACT SURVEY OF CLUSTERS AT ALL REDSHIFTS”. In: *ApJ* 803.2, p. 79. ISSN: 1538-4357. DOI: `10.1088/0004-637X/803/2/79`.

Magdis, Georgios E. et al. (Nov. 2012). “THE EVOLVING INTERSTELLAR MEDIUM OF STAR-FORMING GALAXIES SINCE $z = 2$ AS PROBED BY THEIR INFRARED SPECTRAL ENERGY DISTRIBUTIONS”. In: *ApJ* 760.1, p. 6. ISSN: 0004-637X, 1538-4357. DOI: `10.1088/0004-637X/760/1/6`.

Mahdavi, Andisheh (Dec. 2014). “Hrothgar: MCMC Model Fitting Toolkit”. In: *Astrophysics Source Code Library*, ascl:1412.008.

Marinacci, Federico et al. (Aug. 2018). “First Results from the IllustrisTNG Simulations: Radio Haloes and Magnetic Fields”. In: *Monthly Notices of the Royal Astronomical Society*. ISSN: 0035-8711, 1365-2966. DOI: `10.1093/mnras/sty2206`.

Marquardt, Donald W. (June 1963). “An Algorithm for Least-Squares Estimation of Nonlinear Parameters”. In: *Journal of the Society for Industrial and Applied Mathematics* 11.2, pp. 431–441. ISSN: 0368-4245, 2168-3484. DOI: `10.1137/0111030`.

Matsumura, Tomotake et al. (May 1, 2016). “Millimeter-Wave Broadband Antireflection Coatings Using Laser Ablation of Subwavelength Structures”. In: *Applied Optics* 55.13, p. 3502. ISSN: 0003-6935, 1539-4522. DOI: `10.1364/AO.55.003502`.

URL: `https://www.osapublishing.org/abstract.cfm?URI=ao-55-13-3502` (visited on 08/19/2019).

Melin, J.-B. et al. (Sept. 2018). “Dust in Galaxy Clusters: Modeling at Millimeter Wavelengths and Impact on *Planck* Cluster Cosmology”. In: *A&A* 617, A75. ISSN: 0004-6361, 1432-0746. DOI: `10.1051/0004-6361/201732292`.

Meneghetti, Massimo et al. (Sept. 2020). “An Excess of Small-Scale Gravitational Lenses Observed in Galaxy Clusters”. In: *Science* 369.6509, pp. 1347–1351. ISSN: 0036-8075, 1095-9203. DOI: `10.1126/science.aax5164`.

Mittal, Avirukt et al. (Feb. 2018). “Optimizing Measurements of Cluster Velocities and Temperatures for CCAT-prime and Future Surveys”. In: *J. Cosmol. Astropart. Phys.* 2018.02, pp. 032–032. ISSN: 1475-7516. DOI: `10.1088/1475-7516/2018/02/032`.

Morandi, Andrea et al. (Sept. 2012). “X-Ray, Lensing and Sunyaev-Zel’dovich Triaxial Analysis of Abell 1835 out to R200”. In: *Monthly Notices of the Royal Astronomical Society* 425, pp. 2069–2082. ISSN: 0035-8711. DOI: `10.1111/j.1365-2966.2012.21196.x`.

Morandi, Andrea et al. (May 2013). “Reconstructing Three-Dimensional Parameters of Galaxy Clusters via Multifrequency Sunyaev–Zeldovich Observations”. In: *Monthly Notices of the Royal Astronomical Society* 431.2, pp. 1240–1251. ISSN: 1365-2966, 0035-8711. DOI: `10.1093/mnras/stt252`.

Moseley, Paul et al. (Oct. 16, 2017). “Dual Focus Polarisation Splitting Lens”. In: *Optics Express* 25.21, p. 25363. ISSN: 1094-4087. DOI: `10.1364/OE.25.025363`. URL: `https://www.osapublishing.org/abstract.cfm?URI=oe-25-21-25363` (visited on 01/06/2021).

Moutard, T. et al. (June 2016). “The VIPERS Multi-Lambda Survey: II. Diving with Massive Galaxies in 22 Square Degrees since $z = 1.5$”. In: *A&A* 590, A103. ISSN: 0004-6361, 1432-0746. DOI: `10.1051/0004-6361/201527294`.

Mroczkowski, Tony et al. (Feb. 2019). “Astrophysics with the Spatially and Spectrally Resolved Sunyaev-Zeldovich Effects. A Millimetre/Submillimetre Probe of the Warm and Hot Universe”. In: *Space Science Reviews* 215.1, p. 17. ISSN: 0038-6308. DOI: `10.1007/s11214-019-0581-2`.

Mueller, Eva-Maria et al. (July 2015a). “CONSTRAINTS ON GRAVITY AND DARK ENERGY FROM THE PAIRWISE KINEMATIC SUNYAEV–ZEL’DOVICH EFFECT”. In: *ApJ* 808.1, p. 47. ISSN: 1538-4357. DOI: `10.1088/0004-637X/808/1/47`.

– (Sept. 2015b). “Constraints on Massive Neutrinos from the Pairwise Kinematic Sunyaev-Zel’dovich Effect”. In: *Phys. Rev. D* 92.6, p. 063501. ISSN: 1550-7998, 1550-2368. DOI: `10.1103/PhysRevD.92.063501`.

Nagai, Daisuke et al. (Oct. 2007). "Effects of Galaxy Formation on Thermodynamics of the Intracluster Medium". In: *ApJ* 668.1, pp. 1–14. ISSN: 0004-637X, 1538-4357. DOI: `10.1086/521328`.

Nagai, Daisuke et al. (Nov. 2013). "Predicting Merger-induced Gas Motions in ΛCDM Galaxy Clusters". In: *The Astrophysical Journal* 777, p. 137. ISSN: 0004-637X. DOI: `10.1088/0004-637X/777/2/137`.

Naiman, Jill P et al. (June 2018). "First Results from the IllustrisTNG Simulations: A Tale of Two Elements – Chemical Evolution of Magnesium and Europium". In: *Monthly Notices of the Royal Astronomical Society* 477.1, pp. 1206–1224. ISSN: 0035-8711, 1365-2966. DOI: `10.1093/mnras/sty618`.

Navarro, Julio F. et al. (May 1996). "The Structure of Cold Dark Matter Halos". In: *ApJ* 462, p. 563. ISSN: 0004-637X, 1538-4357. DOI: `10.1086/177173`. arXiv: `astro-ph/9508025`.

– (Dec. 1997). "A Universal Density Profile from Hierarchical Clustering". In: *ApJ* 490.2, pp. 493–508. ISSN: 0004-637X, 1538-4357. DOI: `10.1086/304888`.

Nelder, J. A. et al. (Jan. 1965). "A Simplex Method for Function Minimization". In: *The Computer Journal* 7.4, pp. 308–313. ISSN: 0010-4620, 1460-2067. DOI: `10.1093/comjnl/7.4.308`.

Nelson, Dylan et al. (Mar. 2018). "First Results from the IllustrisTNG Simulations: The Galaxy Colour Bimodality". In: *Monthly Notices of the Royal Astronomical Society* 475.1, pp. 624–647. ISSN: 0035-8711, 1365-2966. DOI: `10.1093/mnras/stx3040`.

Nelson, Dylan et al. (Apr. 2019). "The IllustrisTNG Simulations: Public Data Release". In: *arXiv:1812.05609 [astro-ph]*. arXiv: `1812.05609 [astro-ph]`.

Nelson, Kaylea et al. (Sept. 2014). "Hydrodynamic Simulation of Non-thermal Pressure Profiles of Galaxy Clusters". In: *The Astrophysical Journal* 792, p. 25. ISSN: 0004-637X. DOI: `10.1088/0004-637X/792/1/25`.

Niemack, Michael D. (Mar. 1, 2016). "Designs for a Large-Aperture Telescope to Map the CMB 10× Faster". In: *Applied Optics* 55.7, p. 1688. ISSN: 0003-6935, 1539-4522. DOI: `10.1364/AO.55.001688`. URL: `https://www.osapublishing.org/abstract.cfm?URI=ao-55-7-1688` (visited on 04/23/2021).

Nitta, Tom et al. (Sept. 2014). "Anti-Reflection Coating for Cryogenic Silicon and Alumina Lenses in Millimeter-Wave Bands". In: *Journal of Low Temperature Physics* 176.5-6, pp. 677–683. ISSN: 0022-2291, 1573-7357. DOI: `10.1007/s10909-013-1059-3`. URL: `http://link.springer.com/10.1007/s10909-013-1059-3` (visited on 08/19/2019).

Nozawa, Satoshi et al. (Nov. 1998a). "Relativistic Corrections to the Sunyaev-Zeldovich Effect for Clusters of Galaxies. II. Inclusion of Peculiar Velocities". In: *ApJ* 508.1, pp. 17–24. ISSN: 0004-637X, 1538-4357. DOI: `10.1086/306401`.

Nozawa, Satoshi et al. (Nov. 1998b). “Relativistic Thermal Bremsstrahlung Gaunt Factor for the Intracluster Plasma”. In: *ApJ* 507.2, pp. 530–557. ISSN: 0004-637X, 1538-4357. DOI: `10.1086/306352`.

Pardo, J. R. et al. (Feb. 1, 2001). “Submillimeter Atmospheric Transmission Measurements on Mauna Kea during Extremely Dry El Nino Conditions: Implications for Broadband Opacity Contributions”. In: *Journal of Quantitative Spectroscopy and Radiative Transfer* 68, pp. 419–433. ISSN: 0022-4073. DOI: `10.1016/S0022-4073(00)00034-0`. URL: `https://ui.adsabs.harvard.edu/abs/2001JQSRT..68..419P` (visited on 08/12/2022).

Parrish, Ian J. et al. (Jan. 2012). “Turbulent Pressure Support in the Outer Parts of Galaxy Clusters: Turbulent Pressure Support in Galaxy Clusters”. In: *Monthly Notices of the Royal Astronomical Society: Letters* 419.1, pp. L29–L33. ISSN: 17453925. DOI: `10.1111/j.1745-3933.2011.01171.x`.

PCOS PATR (2017). *Physics of the Cosmos (PCOS) Program Annual Technology Report.* URL: `https://pcos.gsfc.nasa.gov/docs/PCOSPATR092817Finalweb.pdf` (visited on 07/14/2022).

Pillepich, Annalisa et al. (Mar. 2018a). “First Results from the IllustrisTNG Simulations: The Stellar Mass Content of Groups and Clusters of Galaxies”. In: *Monthly Notices of the Royal Astronomical Society* 475.1, pp. 648–675. ISSN: 0035-8711, 1365-2966. DOI: `10.1093/mnras/stx3112`.

Pillepich, Annalisa et al. (Jan. 2018b). “Simulating Galaxy Formation with the IllustrisTNG Model”. In: *Monthly Notices of the Royal Astronomical Society* 473.3, pp. 4077–4106. ISSN: 0035-8711, 1365-2966. DOI: `10.1093/mnras/stx2656`.

Planck Collaboration et al. (Oct. 2016a). “*Planck* 2015 Results: XIII. Cosmological Parameters”. In: *A&A* 594, A13. ISSN: 0004-6361, 1432-0746. DOI: `10.1051/0004-6361/201525830`.

Planck Collaboration et al. (Feb. 2016b). “*Planck* Intermediate Results: XXXVII. Evidence of Unbound Gas from the Kinetic Sunyaev-Zeldovich Effect”. In: *A&A* 586, A140. ISSN: 0004-6361, 1432-0746. DOI: `10.1051/0004-6361/201526328`.

Planck Collaboration et al. (Sept. 2018). “Planck Intermediate Results. LIII. Detection of Velocity Dispersion from the Kinetic Sunyaev-Zeldovich Effect”. In: *Astronomy and Astrophysics* 617, A48. ISSN: 0004-6361. DOI: `10.1051/0004-6361/201731489`.

Planck Collaboration et al. (Sept. 2020). “*Planck* 2018 Results: V. CMB Power Spectra and Likelihoods”. In: *A&A* 641, A5. ISSN: 0004-6361, 1432-0746. DOI: `10.1051/0004-6361/201936386`.

Plazas, A A et al. (Jan. 2019). “Image Simulations for Gravitational Lensing with SKYLENS”. In: *Monthly Notices of the Royal Astronomical Society* 482.2, pp. 2823–2832. ISSN: 0035-8711, 1365-2966. DOI: `10.1093/mnras/sty2737`.

Pozar, David M (2012). *Microwave Engineering*. Fourth edition. Hoboken, NJ : Wiley, [2012] ©2012. URL: `https://search.library.wisc.edu/catalog/9910153599402121`.

Raghunathan, Srinivasan et al. (Nov. 2019). “An Inpainting Approach to Tackle the Kinematic and Thermal SZ Induced Biases in CMB-cluster Lensing Estimators”. In: *Journal of Cosmology and Astroparticle Physics* 2019, p. 037. ISSN: 1475-7516. DOI: `10.1088/1475-7516/2019/11/037`.

Raghunathan, Srinivasan et al. (Feb. 2022). “Constraining Cluster Virialization Mechanism and Cosmology Using Thermal-SZ-selected Clusters from Future CMB Surveys”. In: *ApJ* 926.2, p. 172. ISSN: 0004-637X. DOI: `10.3847/1538-4357/ac4712`.

Reichardt, C. L. et al. (Feb. 2021). “An Improved Measurement of the Secondary Cosmic Microwave Background Anisotropies from the SPT-SZ + SPTpol Surveys”. In: *ApJ* 908.2, p. 199. ISSN: 1538-4357. DOI: `10.3847/1538-4357/abd407`. arXiv: `2002.06197`.

Remazeilles, Mathieu et al. (Feb. 2011). “CMB and SZ Effect Separation with Constrained Internal Linear Combinations: CMB and SZ Separation with Constrained ILC”. In: *Monthly Notices of the Royal Astronomical Society* 410.4, pp. 2481–2487. ISSN: 00358711. DOI: `10.1111/j.1365-2966.2010.17624.x`.

Rephaeli, Yoel (Sept. 1995a). “Comptonization of the Cosmic Microwave Background: The Sunyaev-Zeldovich Effect”. In: *Annu. Rev. Astron. Astrophys.* 33.1, pp. 541–579. ISSN: 0066-4146, 1545-4282. DOI: `10.1146/annurev.aa.33.090195.002545`.

– (May 1995b). “Cosmic Microwave Background Comptonization by Hot Intracluster Gas”. In: *ApJ* 445, p. 33. ISSN: 0004-637X, 1538-4357. DOI: `10.1086/175669`.

Robitaille, Thomas P. et al. (Jan. 2010). “THE PRESENT-DAY STAR FORMATION RATE OF THE MILKY WAY DETERMINED FROM SPITZER -DETECTED YOUNG STELLAR OBJECTS”. In: *ApJL* 710.1, pp. L11–L15. ISSN: 2041-8205. DOI: `10.1088/2041-8205/710/1/L11`.

Rodighiero, G. et al. (Oct. 2011). “The Lesser Role of Starbursts in Star Formation at z = 2”. In: *The Astrophysical Journal Letters, Volume 739, Issue 2, article id. L40, <NUMPAGES>6</NUMPAGES> pp. (2011).* 739.2, p. L40. ISSN: 0004-637X. DOI: `10.1088/2041-8205/739/2/L40`.

Rodríguez-Puebla, Aldo et al. (Oct. 2016). “Halo and Subhalo Demographics with Planck Cosmological Parameters: Bolshoi–Planck and MultiDark–Planck Simulations”. In: *Mon. Not. R. Astron. Soc.* 462.1, pp. 893–916. ISSN: 0035-8711, 1365-2966. DOI: `10.1093/mnras/stw1705`.

Romero, Charles E. et al. (Mar. 2017). “Galaxy Cluster Pressure Profiles as Determined by Sunyaev Zel’dovich Effect Observations with MUSTANG and Bolocam. II. Joint Analysis of 14 Clusters”. In: *ApJ* 838.2, p. 86. ISSN: 0004-637X. DOI: `10.3847/1538-4357/aa643f`.

Romero, Charles E. et al. (Mar. 2020). “Pressure Profiles and Mass Estimates Using High-resolution Sunyaev–Zel’dovich Effect Observations of Zwicky 3146 with MUSTANG-2”. In: *ApJ* 891.1, p. 90. ISSN: 0004-637X. DOI: `10.3847/1538-4357/ab6d70`.

Rosen, Darin et al. (Nov. 20, 2013). “Epoxy-Based Broadband Antireflection Coating for Millimeter-Wave Optics”. In: *Applied Optics* 52.33, p. 8102. ISSN: 1559-128X, 2155-3165. DOI: `10.1364/AO.52.008102`. URL: `https://www.osapublishing.org/abstract.cfm?URI=ao-52-33-8102` (visited on 01/06/2021).

Ruppin, F. et al. (July 2018). “First Sunyaev–Zel’dovich Mapping with the NIKA2 Camera: Implication of Cluster Substructures for the Pressure Profile and Mass Estimate”. In: *A&A* 615, A112. ISSN: 0004-6361, 1432-0746. DOI: `10.1051/0004-6361/201732558`.

Rybicki, George B. et al. (June 1986). *Radiative Processes in Astrophysics*.

Sayers, J. et al. (Feb. 2011). “Cluster Morphologies and Model-independent Y SZ Estimates from Bolocam Sunyaev-Zel’dovich Images”. In: *The Astrophysical Journal* 728, p. 39. ISSN: 0004-637X. DOI: `10.1088/0004-637X/728/1/39`.

Sayers, J. et al. (Nov. 2013). “A MEASUREMENT OF THE KINETIC SUNYAEV-ZEL’DOVICH SIGNAL TOWARD MACS J0717.5+3745”. In: *ApJ* 778.1, p. 52. ISSN: 0004-637X, 1538-4357. DOI: `10.1088/0004-637X/778/1/52`.

Sayers, Jack et al. (July 2019). “Imaging the Thermal and Kinematic Sunyaev–Zel’dovich Effect Signals in a Sample of 10 Massive Galaxy Clusters: Constraints on Internal Velocity Structures and Bulk Velocities”. In: *ApJ* 880.1, p. 45. ISSN: 1538-4357. DOI: `10.3847/1538-4357/ab29ef`.

Sazonov, S. Y. et al. (Nov. 1998). “Cosmic Microwave Background Radiation in the Direction of a Moving Cluster of Galaxies with Hot Gas: Relativistic Corrections”. In: *ApJ* 508.1, pp. 1–5. ISSN: 0004-637X, 1538-4357. DOI: `10.1086/306406`.

Schaan, Emmanuel et al. (Apr. 2016). “Evidence for the Kinematic Sunyaev-Zel’dovich Effect with the Atacama Cosmology Telescope and Velocity Reconstruction from the Baryon Oscillation Spectroscopic Survey”. In: *Physical Review D* 93, p. 082002. ISSN: 1550-79980556-2821. DOI: `10.1103/PhysRevD.93.082002`.

Schaffer, K. K. et al. (Nov. 2011). “THE FIRST PUBLIC RELEASE OF SOUTH POLE TELESCOPE DATA: MAPS OF A 95 Deg2 FIELD FROM 2008 OBSERVATIONS”. In: *ApJ* 743.1, p. 90. ISSN: 0004-637X. DOI: `10.1088/0004-637X/743/1/90`.

Schellenberger, G. et al. (Mar. 2015). “XMM-Newton and Chandra Cross-Calibration Using HIFLUGCS Galaxy Clusters - Systematic Temperature Differences and Cosmological Impact”. In: *A&A* 575, A30. ISSN: 0004-6361, 1432-0746. DOI: `10.1051/0004-6361/201424085`.

Sehgal, Neelima et al. (June 2019). “CMB-HD: An Ultra-Deep, High-Resolution Millimeter-Wave Survey Over Half the Sky”. In: *arXiv:1906.10134 [astro-ph, physics:hep-ph]*. arXiv: `1906.10134 [astro-ph, physics:hep-ph]`.

Siegel, Seth R. et al. (July 2018). “Constraints on the Mass, Concentration, and Nonthermal Pressure Support of Six CLASH Clusters from a Joint Analysis of X-Ray, SZ, and Lensing Data”. In: *The Astrophysical Journal* 861, p. 71. ISSN: 0004-637X. DOI: `10.3847/1538-4357/aac5f8`.

Sobrin, J. A. et al. (June 2021). “The Design and Integrated Performance of SPT-3G”. In: *eprint arXiv:2106.11202*, arXiv:2106.11202. arXiv: `2106.11202`.

Soergel, B. et al. (Sept. 2016). “Detection of the Kinematic Sunyaev–Zel’dovich Effect with DES Year 1 and SPT”. In: *Mon. Not. R. Astron. Soc.* 461.3, pp. 3172–3193. ISSN: 0035-8711, 1365-2966. DOI: `10.1093/mnras/stw1455`.

Springel, Volker (Jan. 2010). “*E Pur Si Muove:* Galilean-invariant Cosmological Hydrodynamical Simulations on a Moving Mesh”. In: *Monthly Notices of the Royal Astronomical Society* 401.2, pp. 791–851. ISSN: 00358711, 13652966. DOI: `10.1111/j.1365-2966.2009.15715.x`.

Springel, Volker et al. (Mar. 2018). “First Results from the IllustrisTNG Simulations: Matter and Galaxy Clustering”. In: *Monthly Notices of the Royal Astronomical Society* 475.1, pp. 676–698. ISSN: 0035-8711, 1365-2966. DOI: `10.1093/mnras/stx3304`.

Sugiyama, Naonori S. et al. (Apr. 2018). “A Direct Measure of Free Electron Gas via the Kinematic Sunyaev-Zel’dovich Effect in Fourier-space Analysis”. In: *Monthly Notices of the Royal Astronomical Society* 475, pp. 3764–3785. ISSN: 0035-8711. DOI: `10.1093/mnras/stx3362`.

Sunyaev, R. A. et al. (Nov. 1972). “The Observations of Relic Radiation as a Test of the Nature of X-Ray Radiation from the Clusters of Galaxies”. In: *Comments on Astrophysics and Space Physics* 4, p. 173. ISSN: 0010-26790146-2970.

– (Mar. 1980). “The Velocity of Clusters of Galaxies Relative to the Microwave Background. The Possibility of Its Measurement”. In: *Monthly Notices of the Royal Astronomical Society* 190.3, pp. 413–420. ISSN: 0035-8711, 1365-2966. DOI: `10.1093/mnras/190.3.413`.

Takada, Masahiro et al. (Feb. 1, 2014). “Extragalactic Science, Cosmology, and Galactic Archaeology with the Subaru Prime Focus Spectrograph”. In: *Publications of the Astronomical Society of Japan* 66.1, R1. ISSN: 0004-6264. DOI: `10.1093/pasj/pst019`. URL: `https://doi.org/10.1093/pasj/pst019` (visited on 12/20/2022).

Takaku, Ryota et al. (Dec. 16, 2020). “Demonstration of Anti-Reflective Structures over a Large Area for CMB Polarization Experiments”. In: *Millimeter, Submillimeter, and Far-Infrared Detectors and Instrumentation for Astronomy X*. Millimeter, Submillimeter, and Far-Infrared Detectors and Instrumentation for Astronomy X. Vol. 11453. SPIE, pp. 236–247. DOI: `10.1117/12.2562028`. URL:

https://www.spiedigitallibrary.org/conference-proceedings-of-spie/11453/114531A/Demonstration-of-anti-reflective-structures-over-a-large-area-for/10.1117/12.2562028.full (visited on 11/10/2022).

Takaku, Ryota et al. (Dec. 6, 2021). "Large Diameter Millimeter-Wave Low-Pass Filter Made of Alumina with Laser Ablated Anti-Reflection Coating". In: *Optics Express* 29.25, pp. 41745–41765. ISSN: 1094-4087. DOI: 10.1364/OE.444848. URL: https://opg.optica.org/oe/abstract.cfm?uri=oe-29-25-41745 (visited on 11/10/2022).

Turner, E. L. (Dec. 1980). "The Effect of Undetected Gravitational Lenses on Statistical Measures of Quasar Evolution". In: *ApJ* 242, p. L135. ISSN: 0004-637X, 1538-4357. DOI: 10.1086/183418.

Vazza, F. et al. (Jan. 2017). "Turbulence and Vorticity in Galaxy Clusters Generated by Structure Formation". In: *Mon. Not. R. Astron. Soc.* 464.1, pp. 210–230. ISSN: 0035-8711, 1365-2966. DOI: 10.1093/mnras/stw2351.

Vial, José et al. (Dec. 2020). "The Leighton Chajnantor Telescope: Project Update and Mechanical Structural Analysis in Preparations for New Deployment in Chajnantor, Chile". In: *Proc.SPIE*. Vol. 11445.

Vikhlinin, A. et al. (Apr. 2006). "*Chandra* Sample of Nearby Relaxed Galaxy Clusters: Mass, Gas Fraction, and Mass-Temperature Relation". In: *ApJ* 640.2, pp. 691–709. ISSN: 0004-637X, 1538-4357. DOI: 10.1086/500288.

– (Jan. 2015). "ERRATUM: " *CHANDRA* SAMPLE OF NEARBY RELAXED GALAXY CLUSTERS: MASS, GAS FRACTION, AND MASS-TEMPERATURE RELATION" (2006, ApJ, 640, 691)". In: *ApJ* 799.1, p. 113. ISSN: 1538-4357. DOI: 10.1088/0004-637X/799/1/113.

Voit, G. Mark (Apr. 2005). "Tracing Cosmic Evolution with Clusters of Galaxies". In: *Rev. Mod. Phys.* 77.1, pp. 207–258. ISSN: 0034-6861, 1539-0756. DOI: 10.1103/RevModPhys.77.207.

Wagner-Gentner, A. et al. (Aug. 2006). "Low Loss THz Window". In: *Infrared Physics & Technology* 48.3, pp. 249–253. ISSN: 13504495. DOI: 10.1016/j.infrared.2006.01.004. URL: https://linkinghub.elsevier.com/retrieve/pii/S1350449506000053 (visited on 08/19/2019).

Wang, Wei-Hao et al. (Nov. 2017). "SCUBA-2 Ultra Deep Imaging EAO Survey (STUDIES): Faint-end Counts at 450 *M*m". In: *ApJ* 850.1, p. 37. ISSN: 0004-637X. DOI: 10.3847/1538-4357/aa911b.

Westbrook, B. et al. (Aug. 31, 2022). "Development of the Low Frequency Telescope Focal Plane Detector Modules for LiteBIRD". In: *Millimeter, Submillimeter, and Far-Infrared Detectors and Instrumentation for Astronomy XI*. Millimeter, Submillimeter, and Far-Infrared Detectors and Instrumentation for Astronomy XI. Vol. 12190. SPIE, pp. 274–290. DOI: 10.1117/12.2630574. URL: https:

//www.spiedigitallibrary.org/conference-proceedings-of-spie/12190/121900I/Development-of-the-low-frequency-telescope-focal-plane-detector-modules/10.1117/12.2630574.full (visited on 11/10/2022).

Wheeler, Jordan D. et al. (July 23, 2014). "Antireflection Coatings for Submillimeter Silicon Lenses". In: SPIE Astronomical Telescopes + Instrumentation. Ed. by Wayne S. Holland et al. Montréal, Quebec, Canada, 91532Z. DOI: 10.1117/12.2057011. URL: http://proceedings.spiedigitallibrary.org/proceeding.aspx?doi=10.1117/12.2057011 (visited on 08/19/2019).

XRISM Science Team (Mar. 2020). "Science with the X-ray Imaging and Spectroscopy Mission (XRISM)". In: *arXiv e-prints*, arXiv:2003.04962.

Yoon, K. W. et al. (June 2006). "The Robinson Gravitational Wave Background Telescope (BICEP): A Bolometric Large Angular Scale CMB Polarimeter". In: 62751K. DOI: 10.1117/12.672652. arXiv: astro-ph/0606278.

Young, Karl et al. (June 7, 2017). "Broadband Millimeter-Wave Anti-Reflection Coatings on Silicon Using Pyramidal Sub-Wavelength Structures". In: *Journal of Applied Physics* 121.21, p. 213103. ISSN: 0021-8979, 1089-7550. DOI: 10.1063/1.4984892. URL: http://aip.scitation.org/doi/10.1063/1.4984892 (visited on 08/19/2019).

Zavala, J. A. et al. (Jan. 2017). "The SCUBA-2 Cosmology Legacy Survey: The EGS Deep Field – I. Deep Number Counts and the Redshift Distribution of the Recovered Cosmic Infrared Background at 450 and 850 μ m". In: *Monthly Notices of the Royal Astronomical Society* 464.3, pp. 3369–3384. ISSN: 0035-8711. DOI: 10.1093/mnras/stw2630.

Zemcov, M. et al. (May 2013). "HerMES: A DEFICIT IN THE SURFACE BRIGHTNESS OF THE COSMIC INFRARED BACKGROUND DUE TO GALAXY CLUSTER GRAVITATIONAL LENSING". In: *ApJ* 769.2, p. L31. ISSN: 2041-8205, 2041-8213. DOI: 10.1088/2041-8205/769/2/L31.

Zemcov, Michael et al. (Dec. 2003). "Measurement of the Sunyaev-Zel'dovich Increment in Massive Galaxy Clusters". In: *Monthly Notices of the Royal Astronomical Society* 346.4, pp. 1179–1188. ISSN: 0035-8711. DOI: 10.1111/j.1365-2966.2003.07163.x.

Zemcov, Michael et al. (Apr. 2007). "A Study of the Sunyaev–Zel'dovich Increment Using Archival SCUBA Data". In: *Monthly Notices of the Royal Astronomical Society* 376.3, pp. 1073–1098. ISSN: 0035-8711. DOI: 10.1111/j.1365-2966.2007.11443.x.

Zhang, J. et al. (Dec. 10, 2009). "New Artificial Dielectric Metamaterial and Its Application as a Terahertz Antireflection Coating". In: *Applied Optics* 48.35, p. 6635. ISSN: 0003-6935, 1539-4522. DOI: 10.1364/AO.48.006635. URL: https://www.osapublishing.org/abstract.cfm?URI=ao-48-35-6635 (visited on 01/06/2021).

Zhao, Gong-Bo et al. (June 2021). “The Completed SDSS-IV Extended Baryon Oscillation Spectroscopic Survey: A Multitracer Analysis in Fourier Space for Measuring the Cosmic Structure Growth and Expansion Rate”. In: *Monthly Notices of the Royal Astronomical Society* 504, pp. 33–52. ISSN: 0035-8711. DOI: `10.1093/mnras/stab849`.

Zmuidzinas, Jonas (2018). Private communication.

ZuHone, J. A. et al. (Feb. 2018). “What Do the Hitomi Observations Tell Us About the Turbulent Velocities in the Perseus Cluster? Probing the Velocity Field with Mock Observations”. In: *The Astrophysical Journal* 853, p. 180. ISSN: 0004-637X. DOI: `10.3847/1538-4357/aaa4b3`.

Appendix A

MOCK KSZ OBSERVATIONS: SUPPLEMENTAL MATERIALS

A.1 Mock Observation Pipeline Validation

A.1.1 Constraint Validation

To test our pipeline, we attempted to recreate the σ_v constraints published by Sayers et al. (2019) using measurements from Bolocam and *Herschel*/SPIRE. We selected the cluster RX J1347.5-1145 for the comparison because the SPIRE observations had relatively low noise. We generated mock observations with a GNFW model matching the fit to this cluster from Czakon et al. (2015) and including instrument noise, CIB, and a Bolocam-like transfer function. We assumed a noise RMS of 2 mJy/beam for the SPIRE bands based on Butler et al. (2022). In addition, we assumed a T prior of $\sim 11\%$ as a quadrature sum of the calibration uncertainty and statistical uncertainty of the T constraint used by Sayers et al. (2019).

We tried to match the assumptions of Sayers et al. (2019) as closely as possible; however, the original analysis used some functionality not present in our pipeline. In particular, the original observations had nonuniform noise in the map, had correlated residual atmospheric fluctuations in the Bolocam bands, and modeled an overall calibration uncertainty. We also neglected the CIB lensing for simplicity, although we expect this to primarily result in a bias on v_z rather than a degradation on σ_v. We attempted to correct for these shortcomings by degrading the Bolocam and AzTEC noise by a factor of $\sqrt{2}$ in each band to account for the non-uniform coverage in the observed map and by an additional factor of 1.1 in the 140 GHz band (Bolocam) and a factor of 1.4 in the 270 GHz band (AzTEC) to account for the non-flat noise power spectrum.

The constraints we obtained with our pipeline are shown in Figure A.1. Sayers et al. (2019) obtained a constraint of $v_z = 950^{+640}_{-680}$, while we find $v_z = 890^{+500}_{-390}$. Our uncertainty is somewhat lower than the Sayers et al. (2019) value, but the difference is likely attributable to differences between the real and mock observations and in the reconstruction procedures. Some possible sources of discrepancy include nontrivial velocity structure in the real images, the overall SZ calibration uncertainty, imperfection in our correction for nonuniform coverage and non-flat noise, and bright CIB sources towards the cluster signal in the real observation.

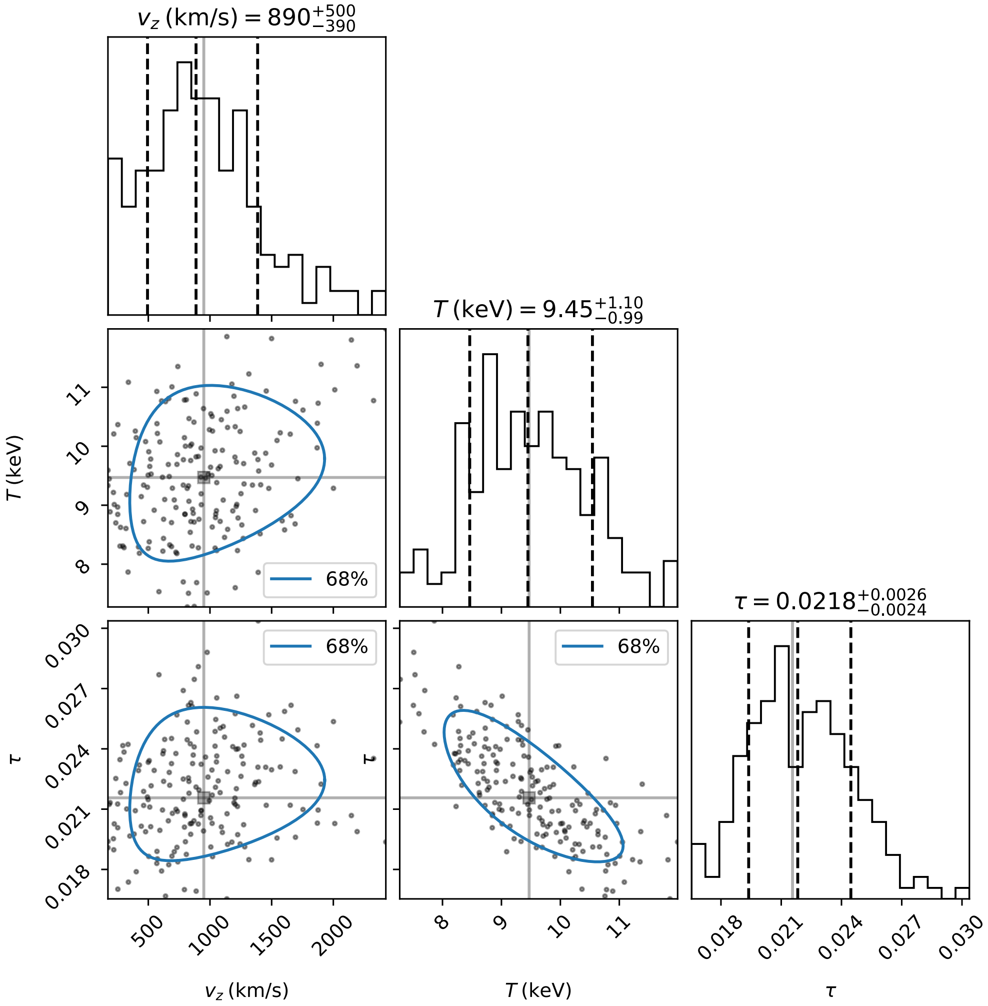

Figure A.1: Bulk motion constraint for the cluster RX J1347.5-1145 as generated with our pipeline based on the observations of Sayers et al. (2019). The 2D contours (blue) are fits to the collection of best-fitting parameters for each realization (black dots). Vertical and horizontal lines are the published best-fitting values from Sayers et al. (2019). We note that the τ values are not directly comparable to those in Sayers et al. (2019), as we calculate τ within an aperture of $1'$ rather than within r_{2500} as in the original analysis.

A.1.2 Validation of SED Fitting

We present a collection of modified blackbody fits to different galaxies from SIDES, as described in Section 3.1, in Figure A.2. We include sources that are best fit with both high and low values of the dust temperature T to demonstrate the performance of the model. All SED fits assume a value of the spectral index $\beta = 1.8$ (Equation 2.10), as the data are insufficient to constrain both β and T.

A.1.3 Validation of Cluster Member Galaxy Model

Here, we describe our model of the dust emission from cluster member galaxies, as introduced in Section 2.3.1. Cai et al. (2013) use a collection of infrared and submillimeter observations to provide IR luminosity functions and SEDs for four different types of sources: warm dusty galaxies, cool dusty galaxies, and active galactic nuclei (AGN) of types 1 and 2. The "cool" dusty galaxies are the most common type of galaxy, sometimes called late-type galaxies, which follow the galactic main sequence in the relation between star formation rate and total stellar mass (see, e.g., Rodighiero et al., 2011). The "warm" variety, which are known as starburst galaxies, are outliers from the main sequence, having significantly higher star formation rates per stellar mass. The two AGN types are distinguished by their level of dust obscuration; according to the standard unified AGN model (e.g., Antonucci, 1993), these types are in fact the same class of object as viewed from different angles relative to the dusty torus, with type 1 AGN being viewed through torus's axis (and thus having low dust obscuration) and type 2 AGN being viewed through the lobes (high dust obscuration).

To implement the cluster member dust model, we must scale the Cai et al. (2013) luminosity functions by the local matter overdensity within the cluster. To do this, we infer a mass profile for the cluster's total matter distribution based on the known mass (M_{500}) and redshift of the cluster. We assume that the mass density profile is described by an NFW model (Navarro et al., 1996; Navarro et al., 1997), and we calculate the model's scale radius from the concentration-mass scaling relation of Child et al. (2018). However, it is not sufficient to simply scale the field luminosity function by the overdensity: we must also adjust for the abundance of different types of galaxies relative to the field. Alberts et al. (2016) measured this "field-relative fraction" of galaxies within clusters using *Herschel*/PACS and Spitzer data, reporting abundance of each galaxy type as a function of radius and redshift. Thus, we scale the Cai et al. (2013) luminosity functions by the Alberts et al. (2016) field-relative fraction for each type. Finally, Alberts et al. (2014) found that the infrared

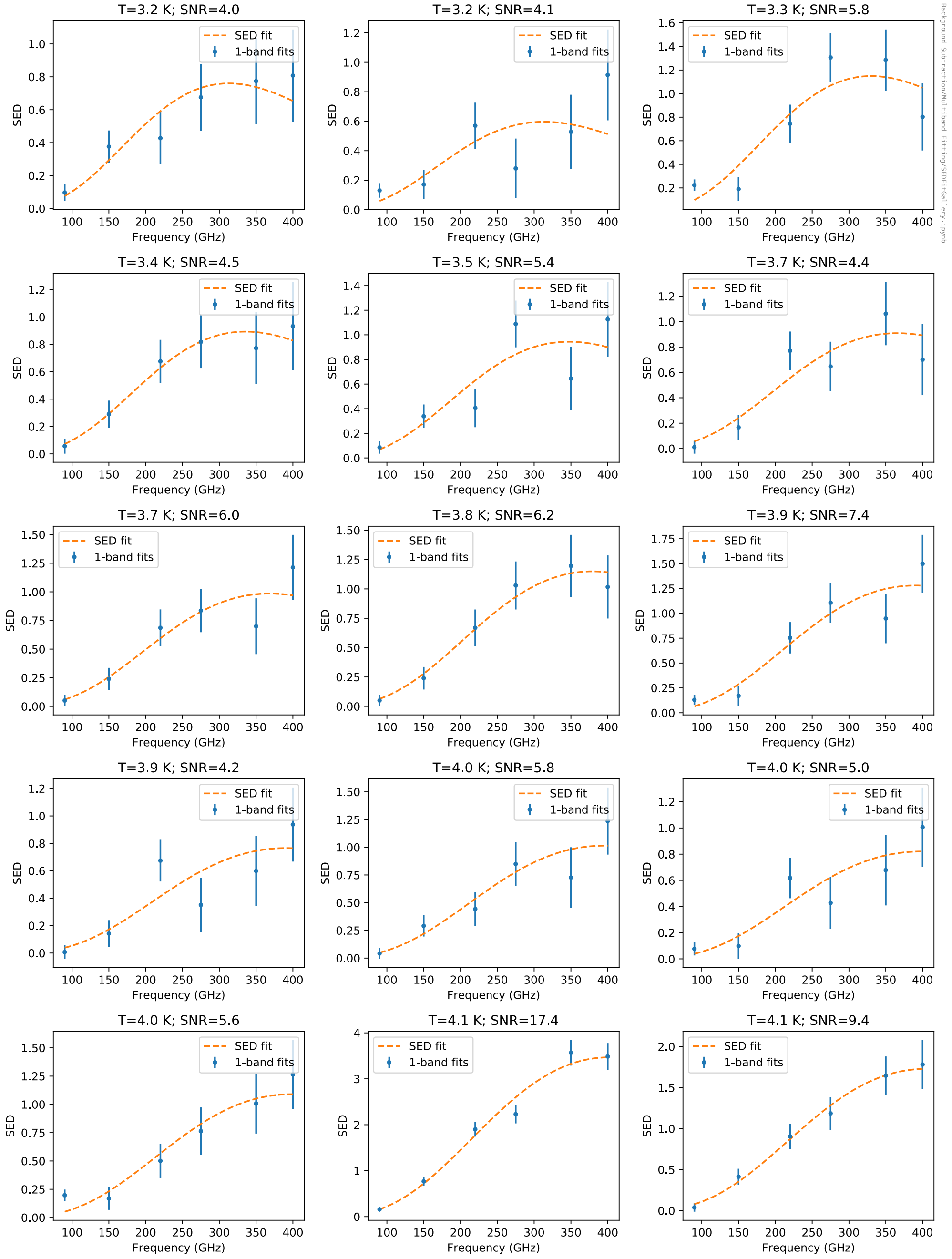

(a) Cold sources

Figure A.2: Fitted SEDs for a selection of 60 sources detected by the removal pipeline in a mock observation with the 30m telescope. A.2a and A.2b are the 30 sources with the lowest fitted values of $T/(1+z)$, while A.2c and A.2d were randomly chosen among the remaining sources. The orange dashed curves represent the SED fits, while the blue points represent photometry values for each bandpass with estimated uncertainties.

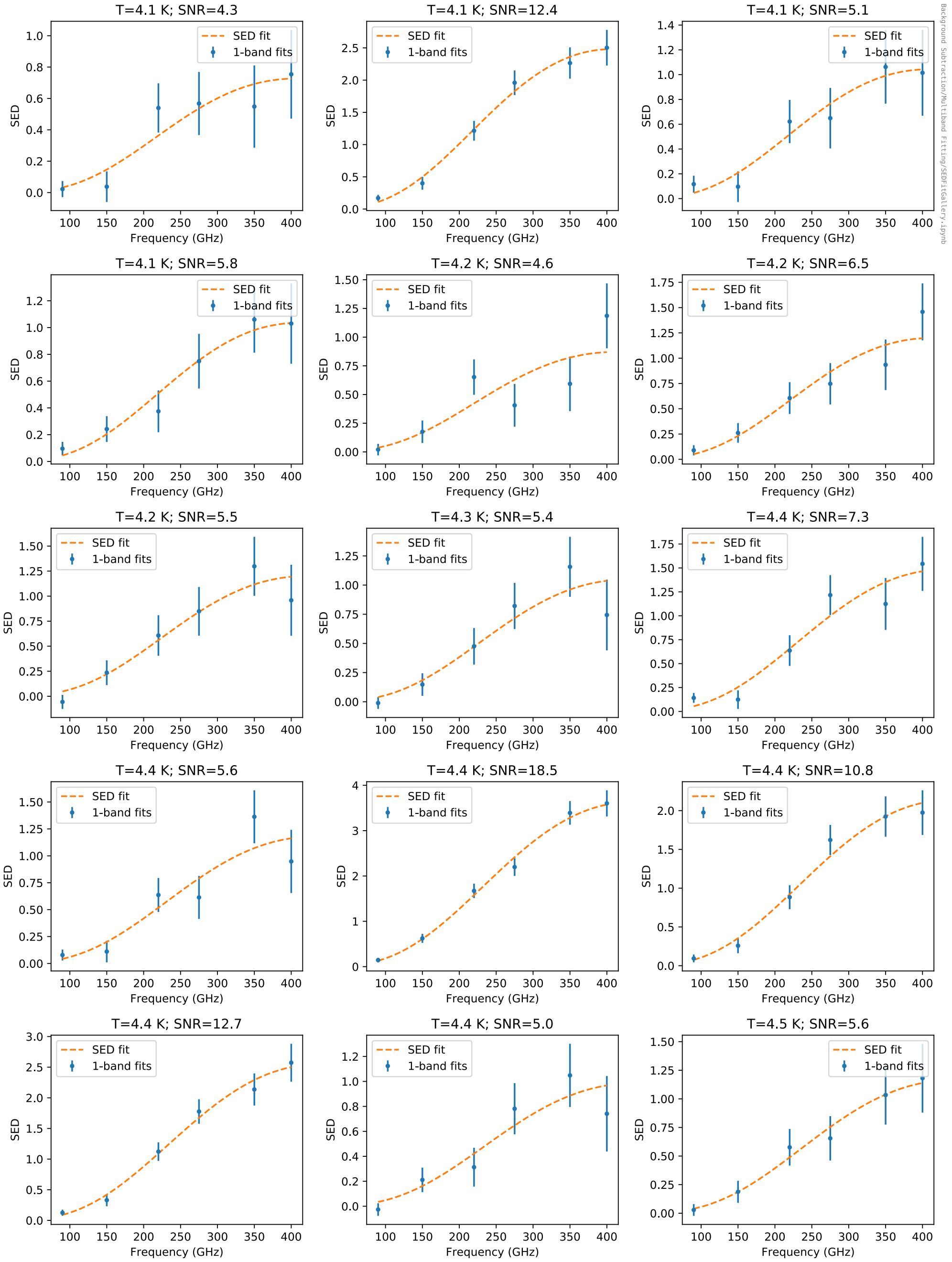

(b) Cold sources

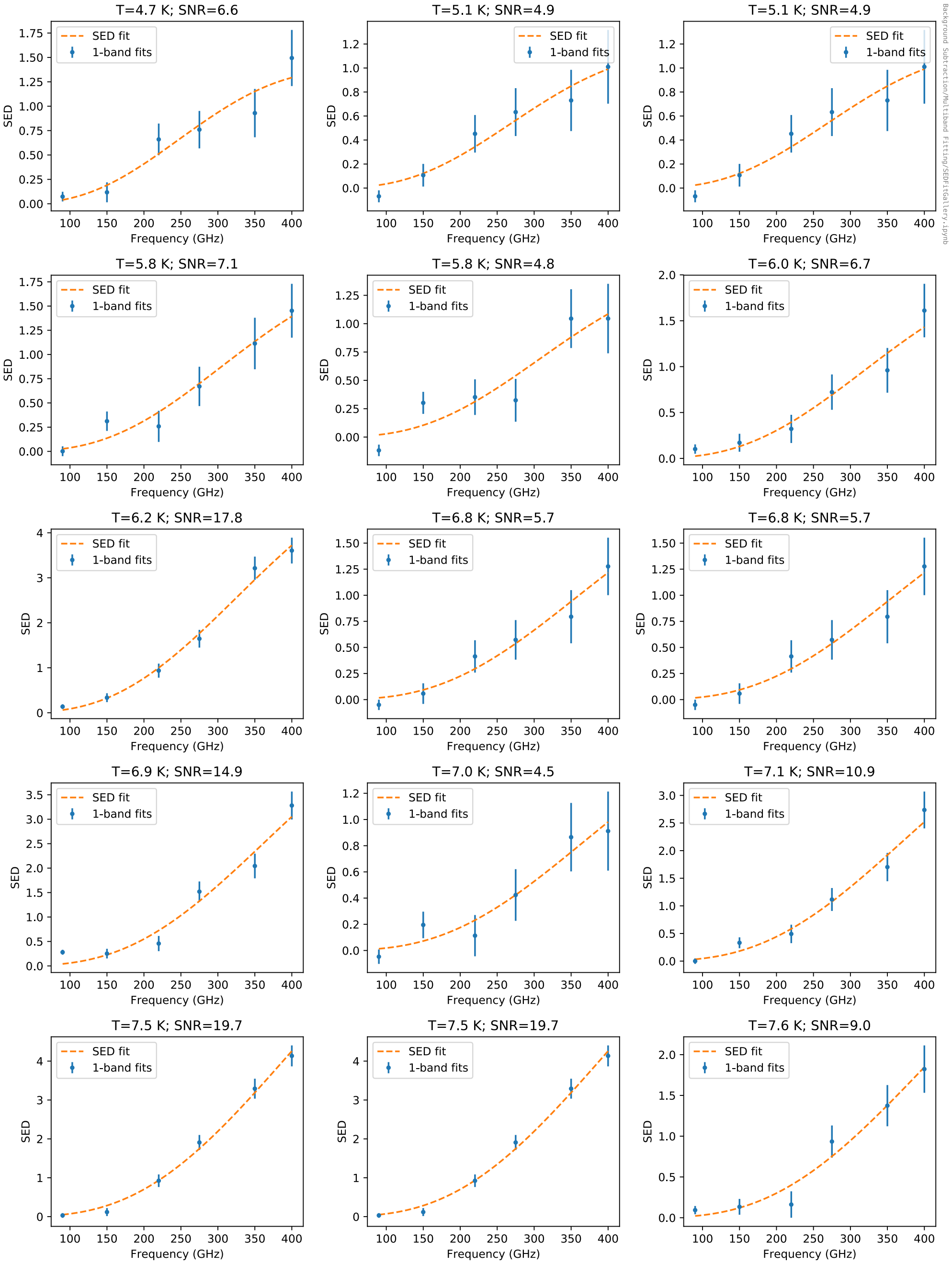

(c) Warm Sources

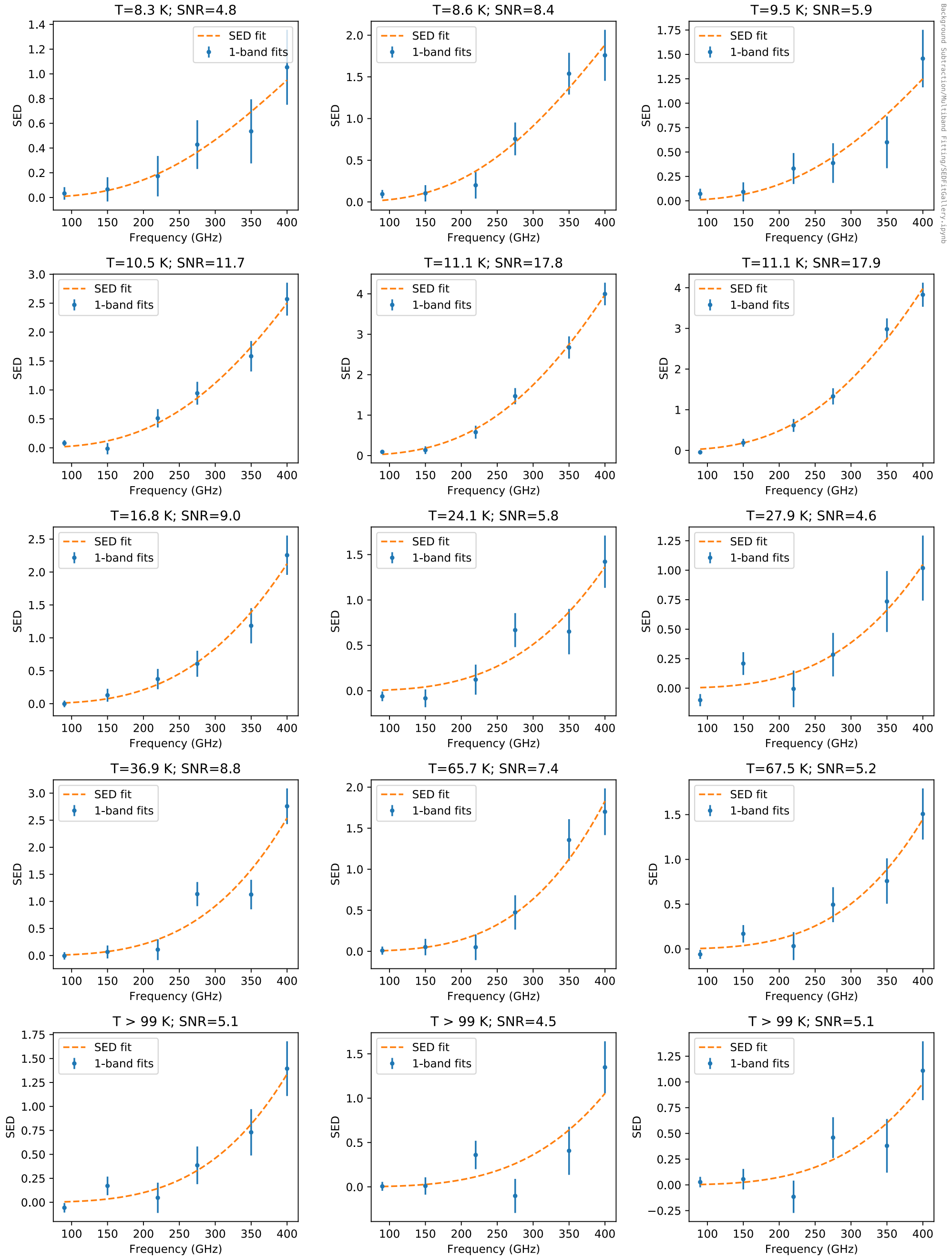

(d) Warm Sources

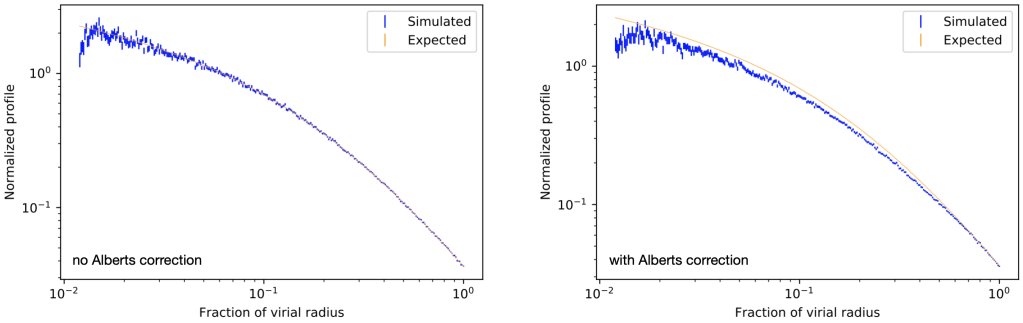

Figure A.3: Comparison of the normalized projected NFW profile with the mean normalized simulated cluster profiles with (*right*) and without the (*left*) Alberts et al. (2016) correction applied.

luminosity of cluster members differs from the field in a redshift-dependent way. We follow the Melin et al. (2018) interpretation of the Alberts et al. (2014) findings and rescale each galaxy's luminosity by the function

$$f(z) = 5.77\mathrm{e}^{-0.34 t_{\mathrm{Gyr}}(z)}, \tag{A.1}$$

where t_{Gyr} is the cosmic time at redshift z.

Below, we include a few validation checks of our cluster member galaxy model. As one caveat, these checks all depend on the assumption of azimuthal symmetry, which may not be fully valid (Deshev et al., 2020).

Check 1 (Figure A.3): Comparison of the expected normalized projected NFW profile to the mean normalized profile from the simulated cluster samples generated with and without Alberts et al. (2016) correction applied.

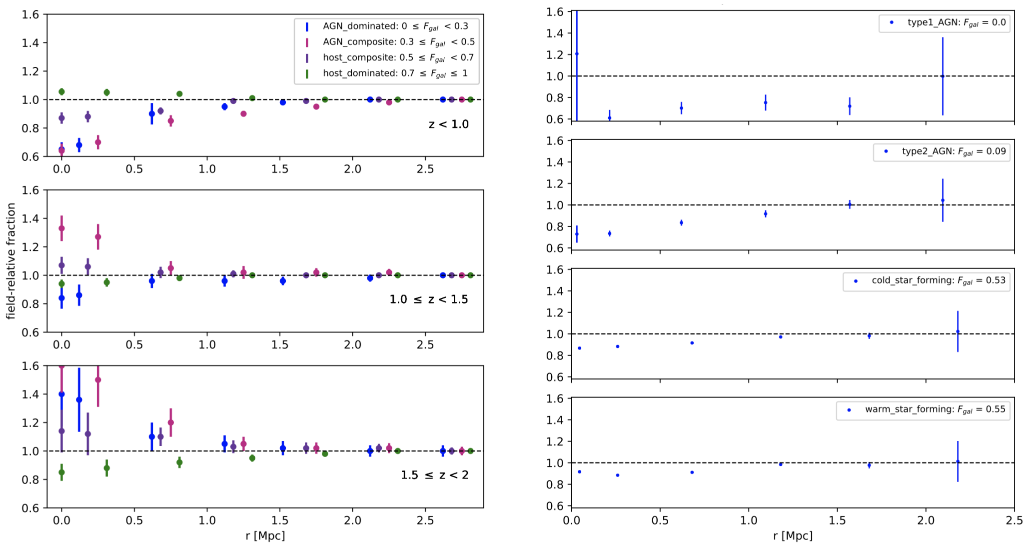

Figure A.4: Alberts et al. (2016) radial distribution corrections for each redshift range and galaxy type. The values at $r = 0$ are extrapolated from Figure 5 in Alberts et al. (2016). *Right:* Empirical values of the same radial distribution correction for our simulated clusters, calculated as the ratio (with Alberts et al. (2016) correction / without Alberts et al. (2016) correction) and sorted by galaxy type. Redshifts used in simulating clusters with and without the Alberts et al. (2016) correction applied are given in Figure A.5.

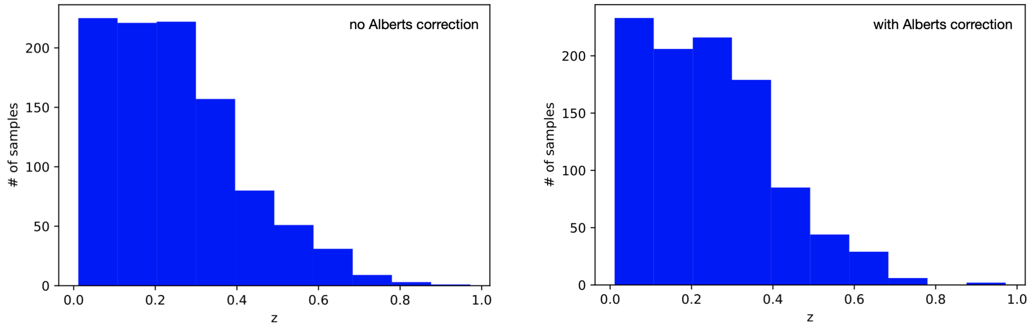

Figure A.5: Redshifts used for simulated cluster samples with (*right*) and without (*left*) Alberts et al. (2016) correction applied. In both cases, redshifts used in the simulated clusters are consistently at $z < 1$.

Check 2 (Figure A.4): Comparison of the ratio of normalized profiles for simulated clusters generated with and without Alberts et al. (2016) correction applied with the expected Alberts et al. (2016) radial distribution correction.

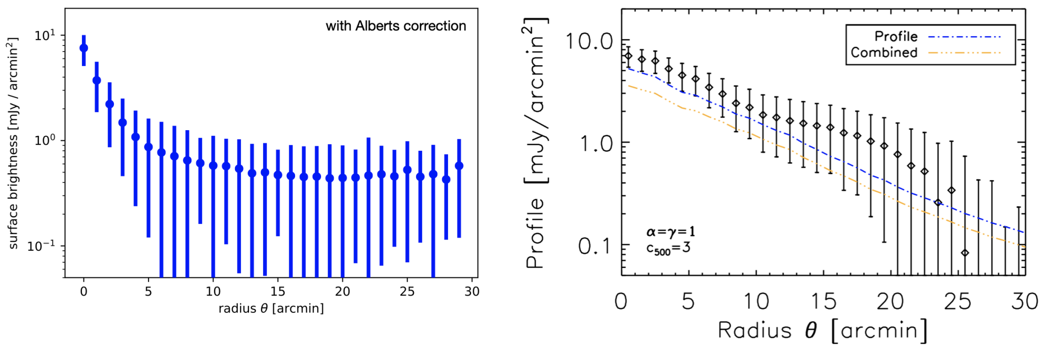

Figure A.6: 857 GHz surface brightness profile for the simulated cluster sample. *Right:* 857 GHz stacked PSZ2 profiles (Melin et al., 2018).

Check 3 (Figure A.6): 857 GHz simulated surface brightness profile comparison with Melin et al. (2018) stacked PSZ2 profiles in the 857 GHz *Planck* band. The simulated surface brightness profile is calculated using the SEDs from Cai et al. (2013) and evaluated in 1′ radial bins. While the overall normalization is consistent between our profile and that of Melin et al. (2018), their shapes are somewhat discrepant. There are are some differences between the algorithm of our work and the one used by Melin et al. (2018)—e.g., Melin et al. (2018) apply the Alberts et al. (2016) correction at the cluster level while we apply it as a function of radius—though we have not conclusively determined that the discrepancy is fully explained by algorithmic differences.

A.1.4 Accuracy of SZ Bandpass Calculation

As noted in Section 2.5, SZ effect photometry depends on the bandpass of the instrument. When calculating this band-averaged SZ signal using a numerical method such as SZpack, it is necessary to sample the bandpass and SZ signal at discrete values of frequency. This procedure can become computationally expensive, so it is worthwhile to examine how finely the frequency domain must be sampled to accurately estimate the band average. In what follows, we assume that each bandpass is a top-hat function of frequency.

We estimate the SZ signal $f(\nu)$ with varying numbers of samples n and take $n_{max} = 128$ samples as the "true" value of the signal. At each band and for each number of samples n, we choose a representative set of n sample frequencies as follows: (1) partition the frequency domain into n equal bins from $i = 0..n$, (2) calculate the average of $f(\nu)$ over each bin ($\equiv \langle f \rangle_{\nu,i}$) by numerical integration, and (3) numerically solve for the frequency ν_i within each bin such that $f(\nu_i) = \langle f \rangle_{\nu,i}$. The collection of ν_i is the set of frequency samples, and the SZ signal can be estimated for each n as

$$\hat{f}_n = \frac{1}{n} \sum_{i=1}^{n} f(\nu_i). \tag{A.2}$$

The above procedure can be used to optimize the reference frequencies ν_i for a particular spectral shape of $f(\nu)$, i.e., for particular values of the cluster temperature T and the velocity υ_z. We use optimize the reference frequencies using the values of $T = 5$ keV and $\nu_z = 0$, for which the estimate $\hat{f}$ correctly estimates $\langle f \rangle$ up to the numerical tolerance of the integration in step (2). However, the estimation is no longer perfect for other values of T and ν_z. It is for these values that we wish to characterize the accuracy of $\hat{f}_n$. To this end, we compare the fractional deviations

$$D_n = \frac{\hat{f}_n - \hat{f}_{128}}{\hat{f}_{128}} \tag{A.3}$$

in Figure A.7. We include estimates for both the tSZ signal (including relativistic corrections) and the kSZ signal with $\nu_z = 500$ km/s. We use values of T ranging from 2 keV to 30 keV and n ranging from 1 to 128. We set nominal accuracy goals of $D_n = 0.1\%$ for tSZ and $D_n = 1\%$ for kSZ so that the error in the theoretical SZ calculation is subdominant to the expected reconstruction errors. We mark each case that meets these requirements with a red dot.

In most cases, 2 samples are sufficient to reconstruct both the tSZ and signals for a wide range of temperatures. The few cases that exceed the accuracy threshold

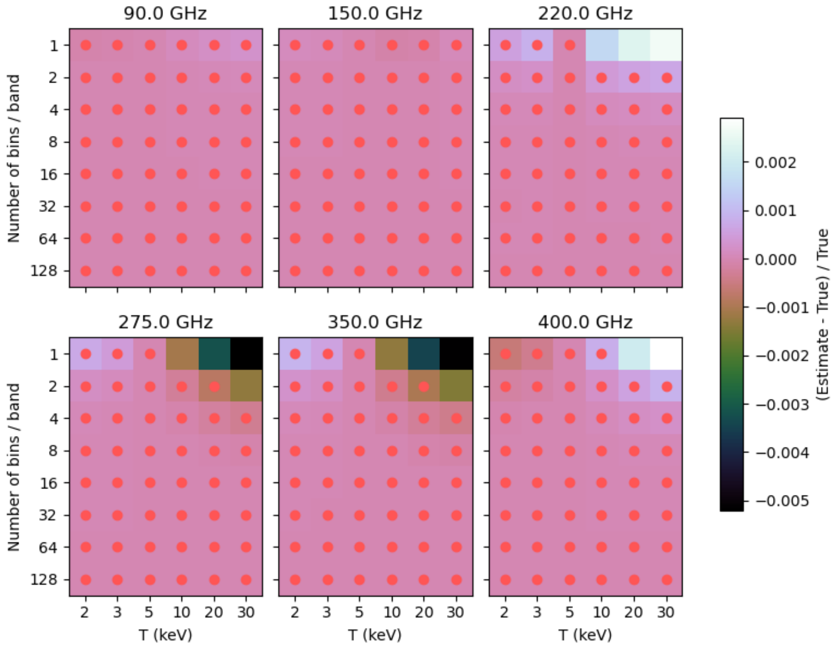

(a) tSZ

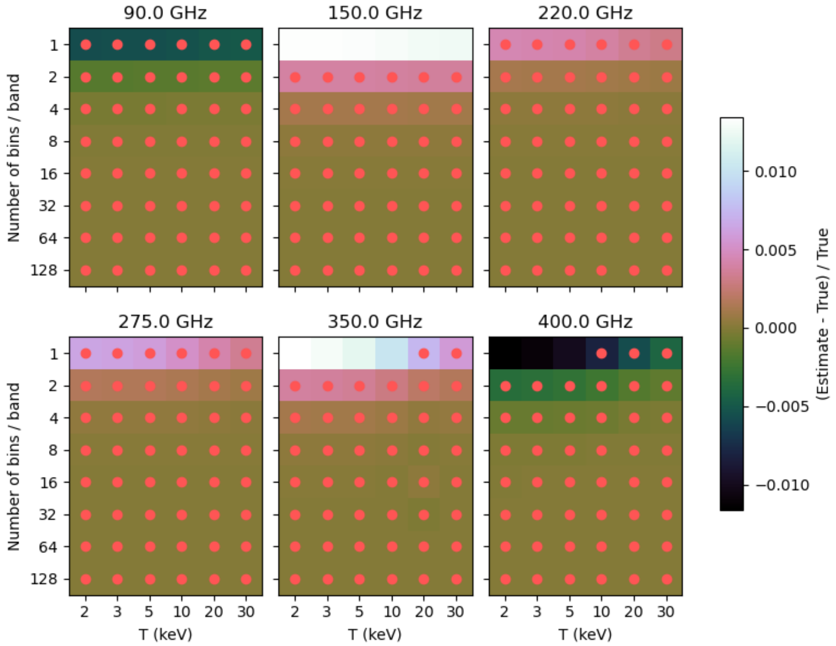

(b) kSZ

Figure A.7: Fractional deviation of band-averaged SZ estimate vs. the true value for the tSZ (a) and kSZ (b) signals. Each grid shows the deviations for a given frequency band, as defined in Table 7.2. The grid rows indicate the number of frequency samples used to calculate the estimate, while the columns represent different values of the ICM temperature T in keV. The red dots indicate scenarios that meet the accuracy goals of 0.1% (for tSZ) and 1% (for kSZ).

with 2 samples are at unusually high temperatures, where rSZ becomes important. The kSZ estimation works well in general despite that the reference frequencies are optimized for $v_z = 0$ (i.e., no kSZ signal), likely due to the kSZ signal's relatively smooth spectral shape. As the accuracy goals above are relatively stringent, it is not unreasonable to use just 1 sample, as we have done elsewhere in this work. To obtain greater accuracy without incurring high computational overhead, one could calculate a lookup table of reference frequencies based on estimates with $n = 1$ for a grid of T and v_z.

A.2 Additional SZ Constraints

A.2.1 kSZ Constraint Plots

In Figure A.8, we show corner plots of SZ parameter constraints from Chapter 5 for the cluster models that were not shown in Section 5.1.

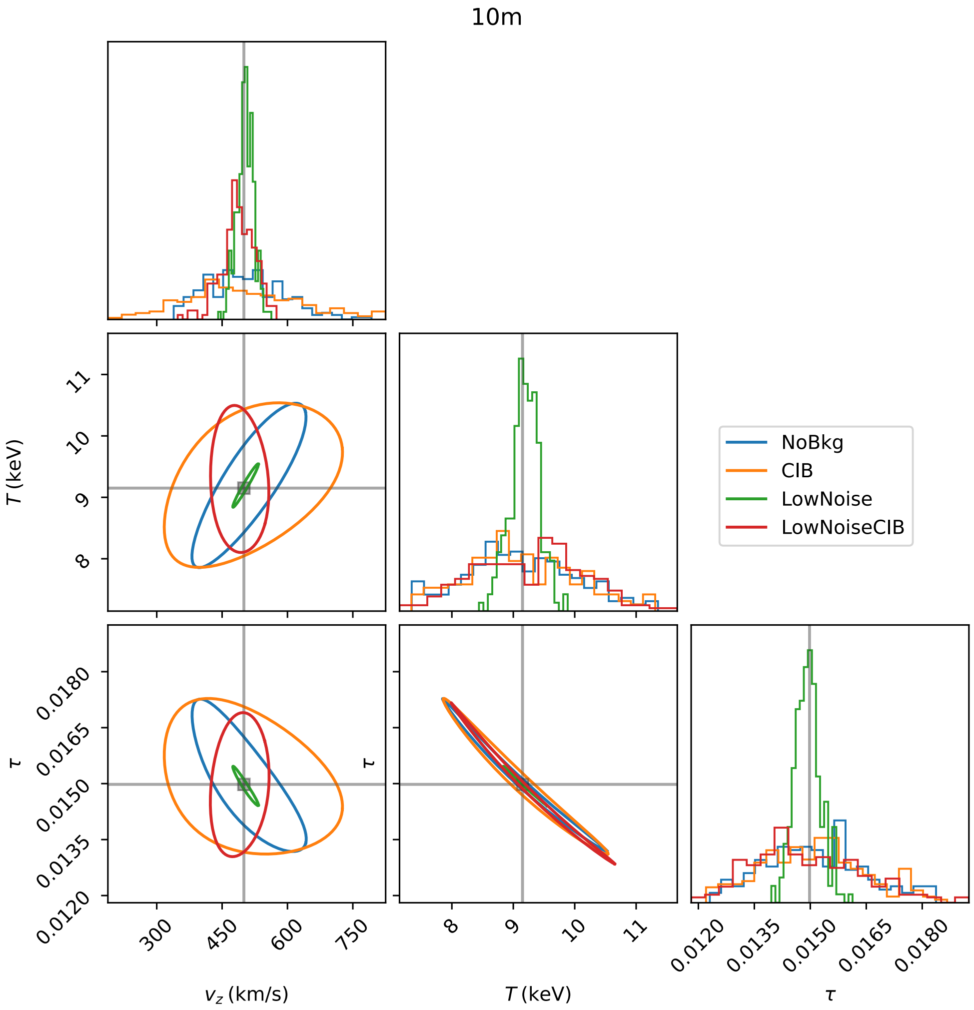

(a) $M_{500} \sim 8.5 \times 10^{14} M_{\odot}$, $z \sim 0.5$; 10m diameter

Figure A.8: 1D histograms and 2D contours for clusters not shown in Section 5.1. These include a cluster of $\sim 8.5{\times}10^{14} M_{\odot}$ at $z \sim 0.5$ (a,bc), a cluster of $\sim 3{\times}10^{14} M_{\odot}$ at $z \sim 0.5$ (d,e,f), and a cluster of $\sim 8.5 \times 10^{14} M_{\odot}$ at $z \sim 0.85$ (g,h,i). Observational scenarios are labeled as in Chapter 5.

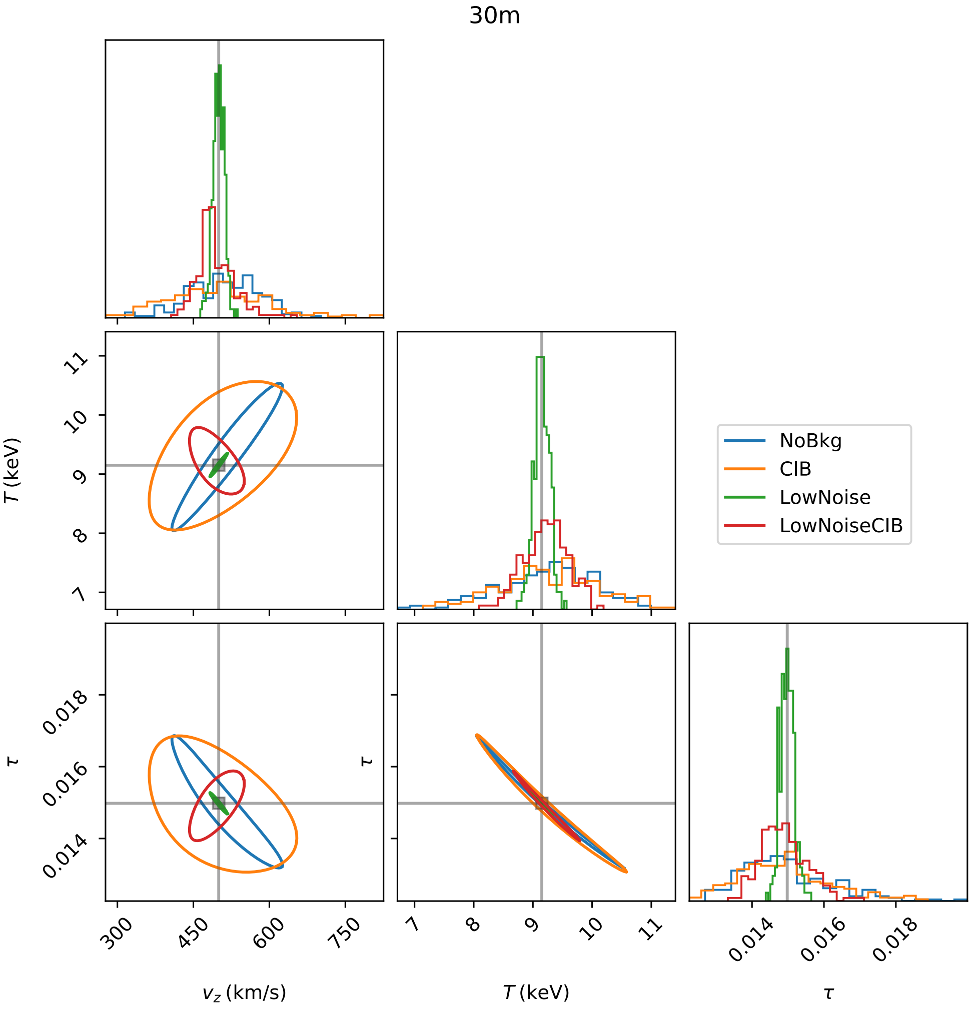

(b) $M_{500} \sim 8.5 \times 10^{14} M_{\odot}$, $z \sim 0.5$; 30m diameter

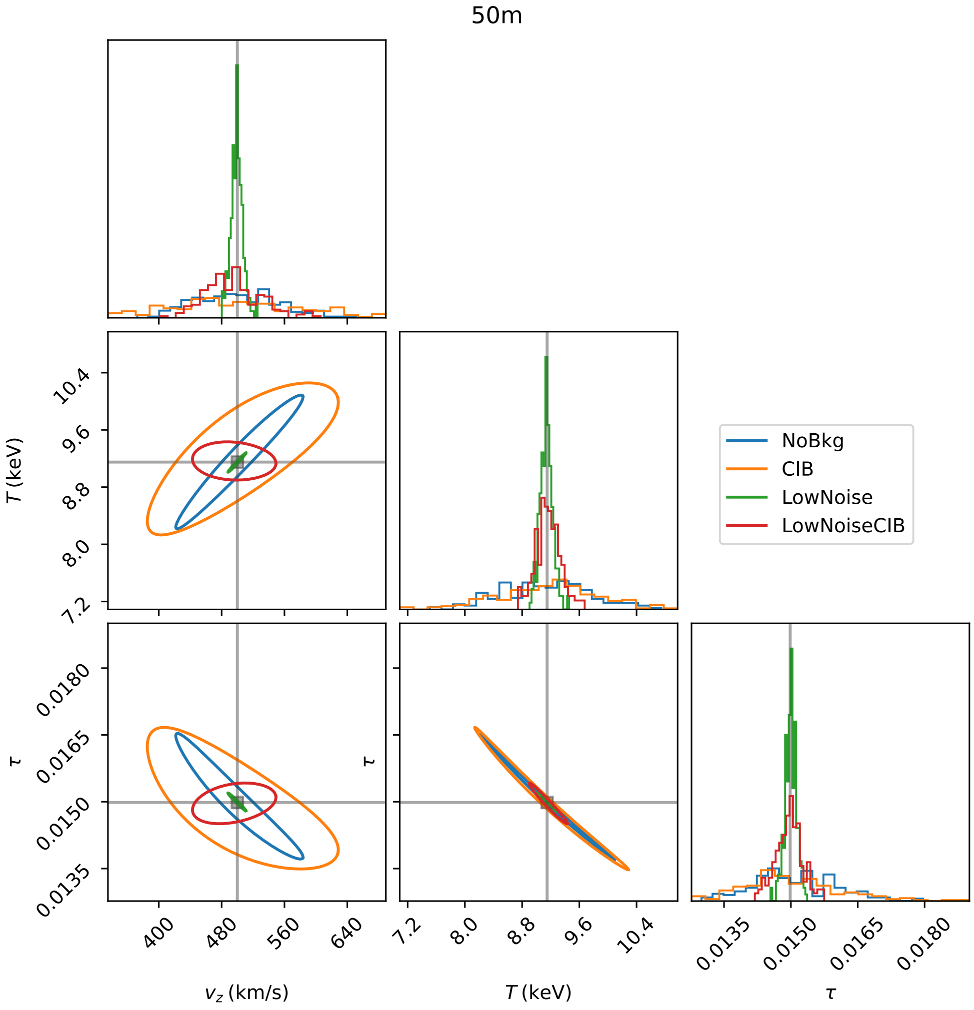

(c) $M_{500} \sim 8.5 \times 10^{14} M_{\odot}$, $z \sim 0.5$; 50m diameter

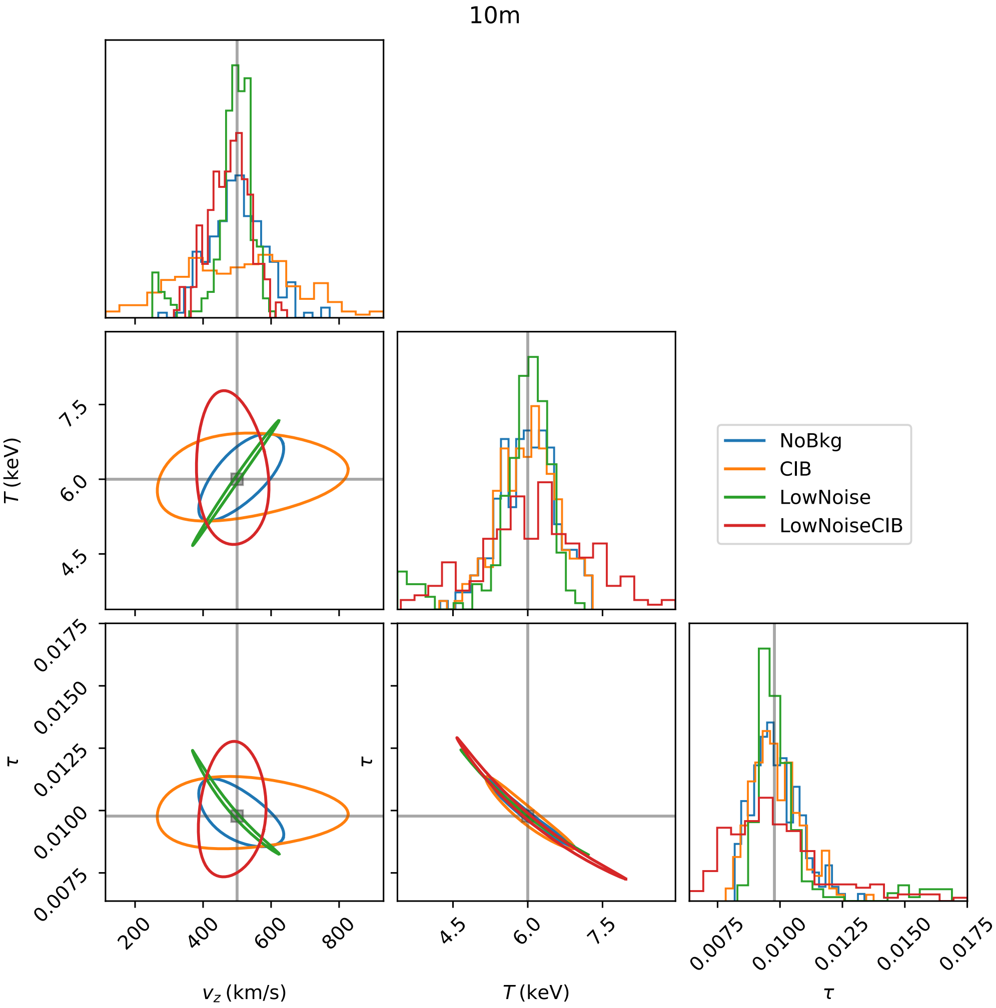

(d) $M_{500} \sim 3 \times 10^{14} M_{\odot}$, $z \sim 0.5$; 10m diameter

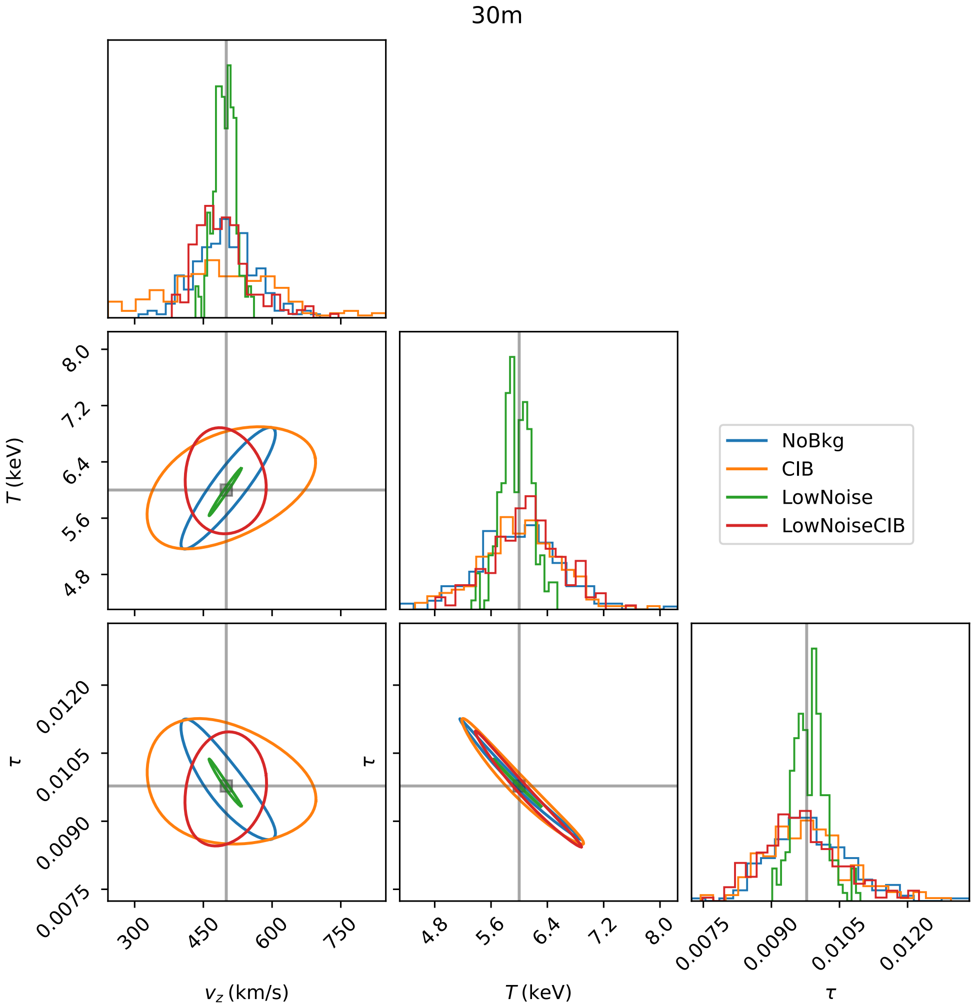

(e) $M_{500} \sim 3 \times 10^{14} M_{\odot}$, $z \sim 0.5$; 30m diameter

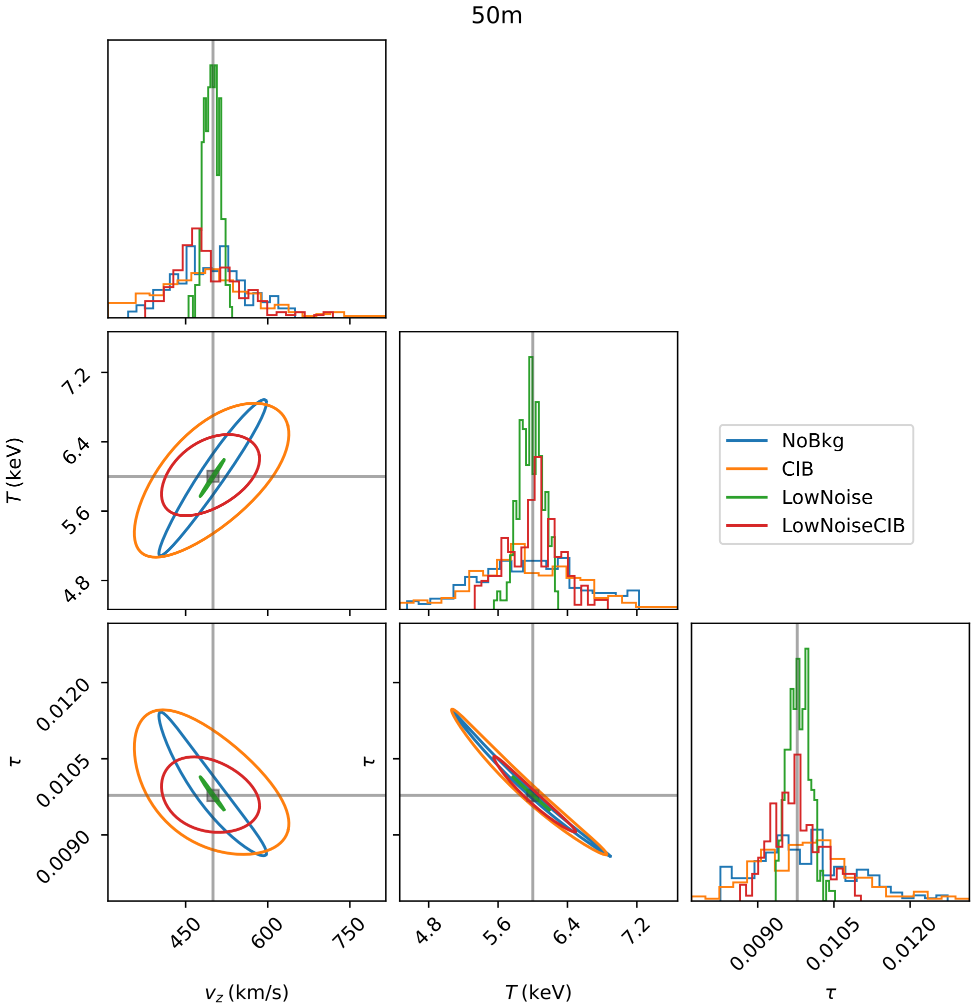

(f) $M_{500} \sim 3 \times 10^{14} M_{\odot}$, $z \sim 0.5$; 50m diameter

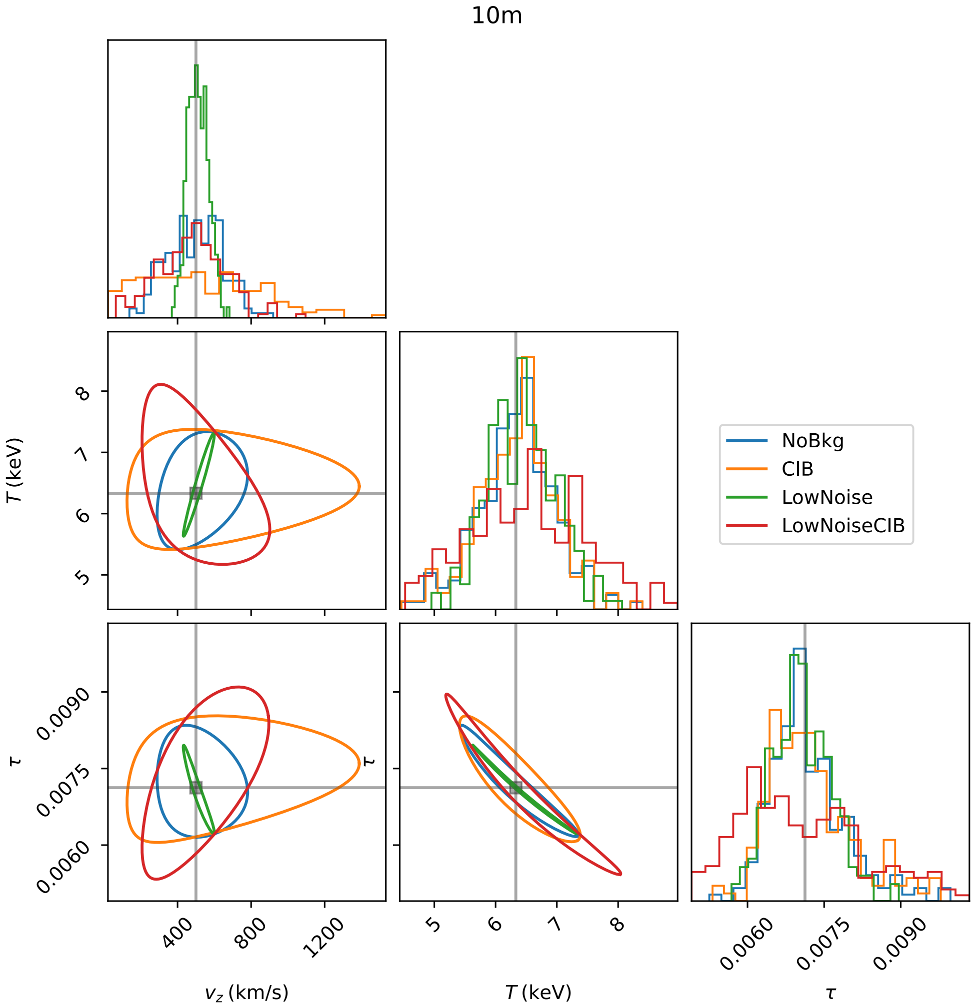

(g) $M_{500} \sim 3 \times 10^{14} M_{\odot}, z \sim 0.85$; 10m diameter

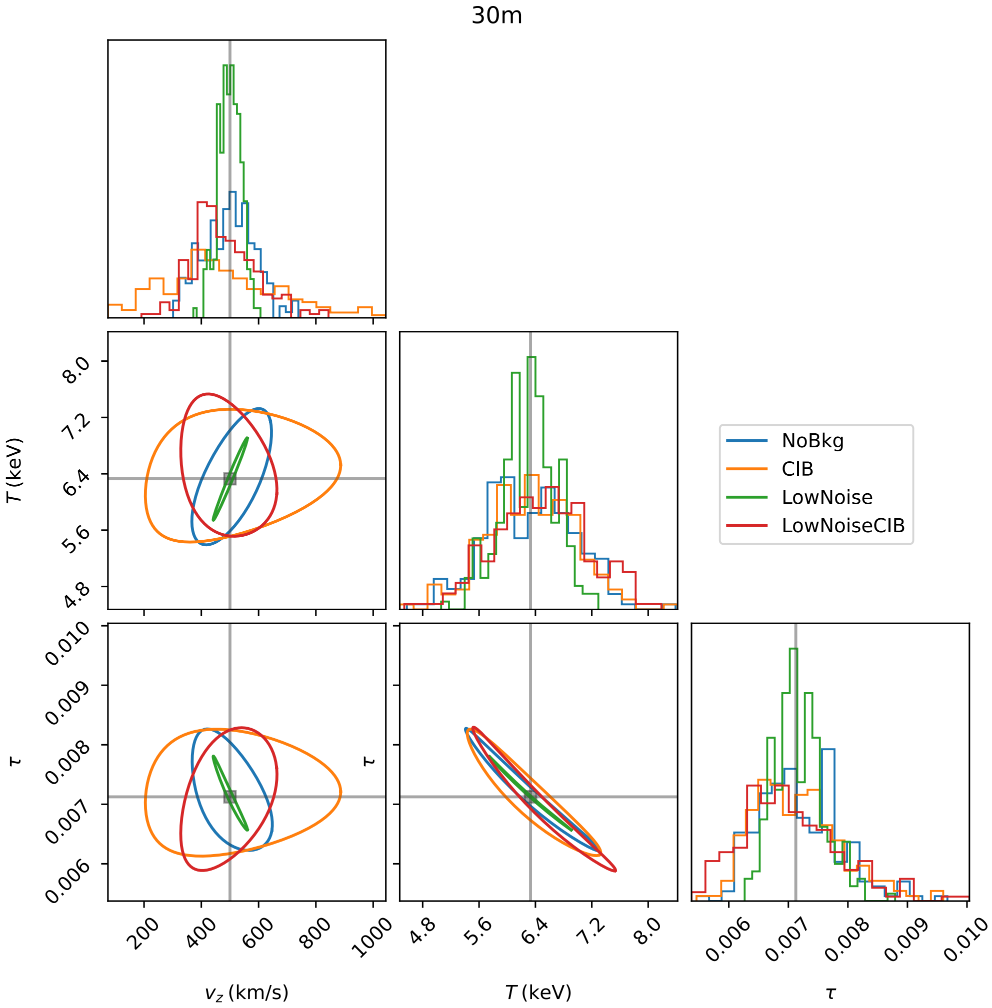

(h) $M_{500} \sim 3 \times 10^{14} M_{\odot}, z \sim 0.85$; 30m diameter

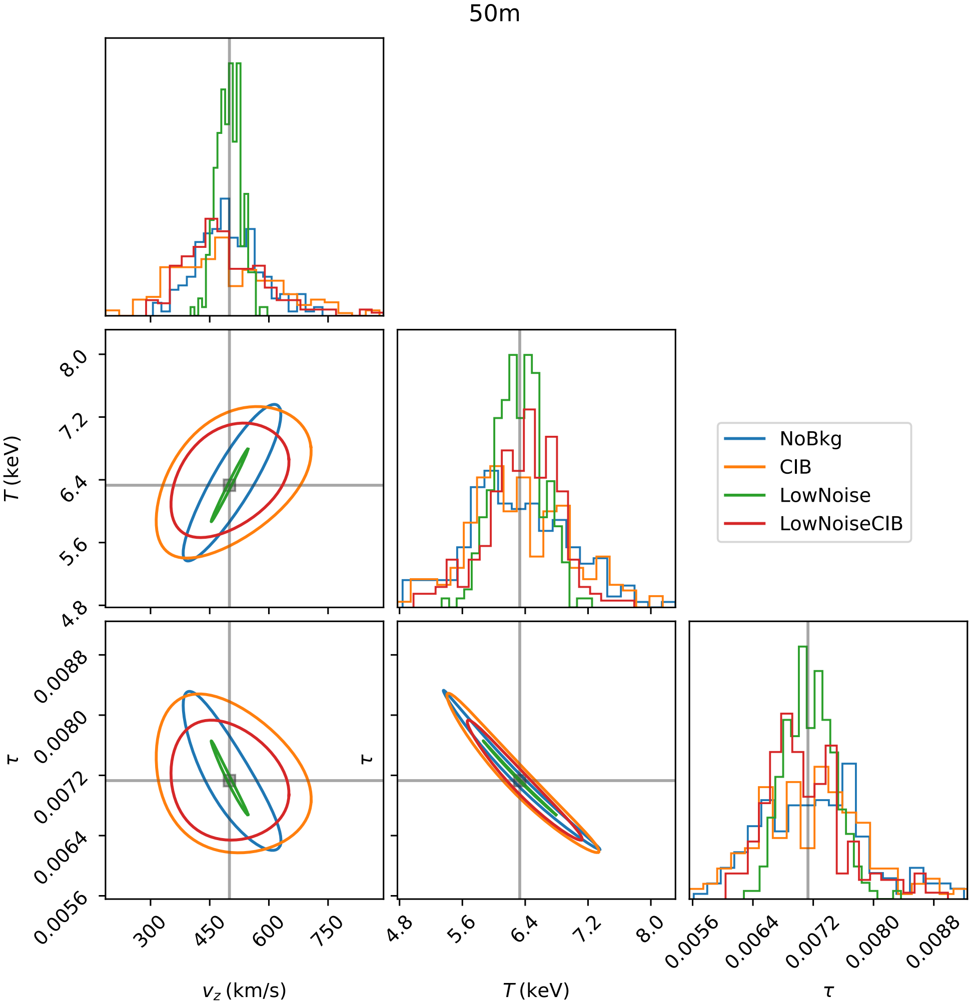

(i) $M_{500} \sim 3 \times 10^{14} M_{\odot}, z \sim 0.85$; 50m diameter

		$\sigma_T \times 10^2$			
	$M_{500}/(10^{14} M_{\odot})$	3.7	3.0	10.9	8.5
	z	0.49	0.89	0.54	0.83
Scenario	Diameter				
(1) NoBkg	10m	60 ± 3	55 ± 3	89 ± 4	115 ± 6
	30m	54 ± 3	66 ± 3	82 ± 4	112 ± 6
	50m	60 ± 3	65 ± 3	66 ± 3	109 ± 5
(2) CIB	10m	61 ± 3	58 ± 3	89 ± 4	121 ± 6
	30m	53 ± 3	62 ± 3	78 ± 4	107 ± 5
	50m	61 ± 3	64 ± 3	66 ± 3	108 ± 5
(3) LowNoise	10m	42 ± 2	56 ± 3	22 ± 1	43 ± 2
	30m	22 ± 1	37 ± 2	12 ± 1	31 ± 2
	50m	14 ± 1	32 ± 2	8 ± 0	21 ± 1
(4) LowNoiseCIB	10m	106 ± 5	100 ± 5	95 ± 5	185 ± 9
	30m	48 ± 2	69 ± 3	38 ± 2	85 ± 4
	50m	32 ± 2	44 ± 2	16 ± 1	44 ± 2

Table A.1: Predictions of recovered temperature precision σ_T in keV for all combinations of observational scenario, telescope diameter, and cluster parameters. The uncertainties represent estimated 1σ error bars as in Table 5.2. σ_T values are shown multiplied by a factor of 10^2 for brevity.

A.2.2 Summary of constraints on T and τ

In addition to the cluster velocity constraints presented in Table 5.2, we also calculated constraints on the gas temperature T and optical depth τ. These calculations were done in an analogous way from the same set of mock observations. We present these values in Tables A.1 and A.2.

		$\sigma_\tau \times 10^5$			
	$M_{500}/(10^{14} M_\odot)$	3.7	3.0	10.9	8.5
	z	0.49	0.89	0.54	0.83
Scenario	Diameter				
(1) NoBkg	10m	91 ± 5	64 ± 3	140 ± 7	60 ± 3
	30m	80 ± 4	74 ± 4	118 ± 6	55 ± 3
	50m	94 ± 5	72 ± 4	93 ± 5	56 ± 3
(2) CIB	10m	99 ± 5	72 ± 4	144 ± 7	64 ± 3
	30m	82 ± 4	70 ± 4	116 ± 6	59 ± 3
	50m	93 ± 5	69 ± 3	95 ± 5	56 ± 3
(3) LowNoise	10m	64 ± 3	61 ± 3	33 ± 2	21 ± 1
	30m	34 ± 2	39 ± 2	18 ± 1	15 ± 1
	50m	22 ± 1	34 ± 2	12 ± 1	10 ± 1
(4) LowNoiseCIB	10m	182 ± 9	126 ± 6	143 ± 7	95 ± 5
	30m	75 ± 4	78 ± 4	61 ± 3	48 ± 2
	50m	50 ± 2	49 ± 2	28 ± 1	24 ± 1

Table A.2: Predictions of recovered optical depth precision σ_τ for all combinations of observational scenario, telescope diameter, and cluster parameters. The uncertainties represent estimated 1σ error bars as in Table 5.2. σ_τ values are shown multiplied by a factor of 10^5 for brevity.

A.3 Mock Observation Pipeline Implementation Details

A.3.1 Weight Factors for Multiband Detection

Our goal is to devise an optimal weighting scheme to combine CIB maps from different bands to maximize the expected signal-to-noise ratio (S/N) on average, which should maximize the effectiveness of source-finding algorithms.

We begin with some definitions. In what follows, we work with discretized quantities where possible in order to match with the implementation. We consider maps M_ν in all 6 SZ bands: 90, 150, 220, 270, 350, and 400 GHz. We use j as an index over the map pixels, which have sky positions $\boldsymbol{\theta}_j$ and all have the same area Ω_{px} in units of solid angle, e.g. arcsec^2. The maps have units of flux density, in the sense that the value of each map pixel is the total flux density of all point sources within it (neglecting beam convolution, discussed below).

Each map M_ν can be written as the sum of its signal and noise components:

$$M_\nu = \mathrm{CIB}_\nu + N_\nu. \tag{A.4}$$

The RMS of each pixel in the noise map N_ν is given by σ_ν. The CIB is composed of point sources with sky positions $\boldsymbol{\vartheta}_i$ and spectral energy distributions (SEDs) $S_{\nu,i}$ with units of flux density (e.g., Jy). We can write down how much flux density a point source in pixel i contributes to a pixel j before beam convolution as

$$\mathrm{CIB}_{\nu,i,\mathrm{beamless}}[\boldsymbol{\theta}_j] = S_{\nu,i}\delta_i[\boldsymbol{\theta}_j],^{1} \tag{A.5}$$

where δ_i is akin to a dimensionless, discretized delta function centered at $\boldsymbol{\vartheta}_i$, defined such that $\delta_i[\boldsymbol{\theta}_j] = \delta_{ij}$, and δ_{ij} is the usual Kronecker delta:

$$\delta_{ij} = \begin{cases} 1 & \text{if } i = j \\ 0 & \text{if } i \neq j. \end{cases} \tag{A.6}$$

We now wish to convolve the point sources with the beam. The beam has a discretized response function $f_\nu[\boldsymbol{\theta}]$ for a pixel at position $\boldsymbol{\theta}$ in frequency band ν, normalized such that it is dimensionless and obeys

$$\sum_j f_\nu[\boldsymbol{\theta}_j] = 1. \tag{A.7}$$

---

[1] This assumes that a given source is perfectly centered within one of the map pixels; in practice, one must decide how fine a pixelization is needed to achieve sufficient positional accuracy. In our pipeline, we discretize source positions at 1/8 the nominal pixel size (nominal pixel size is 4″, 2″, and 1″ for 10m, 30m, and 50m telescopes, respectively) and then degrade the resolution after convolving with the beam.

We define the convolution $*$ as a fully discrete operator that preserves the units of the operands. E.g., for maps $m[\boldsymbol{\theta}]$ and $n[\boldsymbol{\theta}]$, we have

$$(m * n)[\boldsymbol{\theta}_j] = \sum_k m[\boldsymbol{\theta}_k] n[\boldsymbol{\theta}_k - \boldsymbol{\theta}_j], \tag{A.8}$$

where the sum runs over all map pixels k.[2] To calculate the value of the full CIB map, we convolve (A.5) with (A.7) and sum over all sources i:

$$\mathrm{CIB}_\nu[\boldsymbol{\theta}_j] = \sum_i \left(S_{\nu,i}\delta_i * f_\nu\right)[\boldsymbol{\theta}_j] = \sum_i S_{\nu,i} f_\nu[\boldsymbol{\theta}_j - \boldsymbol{\vartheta}_i]. \tag{A.9}$$

It can be seen that the sum over all the pixels of (A.9) gives the total flux density of all the sources in the map (neglecting edge effects).

We also note that the effective beam area Ω_ν can be expressed in terms of the peak value of $f_\nu[\boldsymbol{\theta}]$. To show this, we may introduce the analytic form of the beam response, $F_\nu(\boldsymbol{\theta})$, which has units of inverse solid angle (e.g., arcsec^{-2}) and is normalized such that it integrates to unity:

$$\int d^2\boldsymbol{\theta} F_\nu(\boldsymbol{\theta}) = 1. \tag{A.10}$$

The beam area Ω_ν is defined as the integral of the *peak*-normalized beam, i.e.:

$$\begin{aligned} \Omega_\nu &= \int d^2\boldsymbol{\theta} \left[\frac{F_\nu(\boldsymbol{\theta})}{\max_{\boldsymbol{\theta}'} F_\nu(\boldsymbol{\theta}')}\right] \\ &= \frac{1}{\max_{\boldsymbol{\theta}} F_\nu(\boldsymbol{\theta})} \int d^2\boldsymbol{\theta} F_\nu(\boldsymbol{\theta}) \\ &= \frac{1}{\max_{\boldsymbol{\theta}} F_\nu(\boldsymbol{\theta})}. \end{aligned} \tag{A.11}$$

If the discretized beam $f_\nu[\boldsymbol{\theta}]$ is well sampled, we can make the approximation

$$f_\nu[\boldsymbol{\theta}] \approx \Omega_{px} F_\nu(\boldsymbol{\theta}) \tag{A.12}$$

and find that

$$\Omega_\nu \approx \frac{\Omega_{px}}{\max_j f_\nu[\boldsymbol{\theta}_j]}. \tag{A.13}$$

The sources do not have identical SEDs in general, but we assume the SEDs have the approximate form of a modified blackbody, with units of flux density:

$$S_\nu \propto B_\nu(T)\nu^\beta \propto \frac{(\nu/\nu_0)^{3+\beta}}{e^{h\nu/k_B T} - 1}, \tag{A.14}$$

---

[2] The maps may be zero-padded and cropped if they do not have the same dimensions.

where T is the (redshifted) dust temperature, β is the spectral index, and ν_0 is an arbitrarily chosen reference frequency.

To find an appropriate weighting scheme, it is desirable to reframe our task in terms of a standard problem, namely, that of combining multiple measurements of a single value with different uncertainties. Assuming the uncertainties are independent, the standard approach to this problem is to weight the measurements by the inverses of their variances. The measurements we wish to combine are the signals within each map pixel in the six observing bands, which have uncertainties σ_ν. However, the signals in each band are not measurements of the same quantity, as the different bands scale by the SEDs. Thus, the combination we seek is a weighted average of the bands after rescaling by factors r_ν:

$$M_{\text{combined}} = \frac{\sum_\nu M_\nu r_\nu w_\nu}{\sum_\nu w_\nu}, \tag{A.15}$$

where the w_ν are the weight factors. If each source SED perfectly followed the same modified blackbody (A.14), it would be sufficient to set r_ν equal to the band-to-band ratios of signal values from (A.9), and weight the rescaled maps $M_\nu r_\nu$ by the rescaled per-pixel inverse variances $(\sigma_\nu r_\nu)^{-2}$. However, if the underlying source SED differs from the assumed template, the optimal weights vary with position due to the differing beam sizes in each band, so it is not possible to choose a single set of weights in this way.

Instead, we choose the weights and scale factors that maximize the total expected S/N within a beam, corresponding to the expected S/N of a given source's flux density. To select the appropriate weight factors w_ν, we consider the total RMS fluctuation of M_ν due to noise within a beam, $\sigma_{\nu,\text{tot}}$, which corresponds to the RMS uncertainty of the flux density of a point source. To derive $\sigma_{\nu,\text{tot}}$, we can write down a single-source model $\mathscr{M}_{\nu,j}$ for the value of the map $M_{\nu,j}$ at pixel index j in terms of the flux density S_ν of the source and the known beam response:

$$\mathscr{M}_{\nu,j} = S_\nu f_\nu[\boldsymbol{\theta}_j], \tag{A.16}$$

where we have assumed without loss of generality that the source lies at position $\vartheta = 0$. The value we seek, $\sigma_{\nu,\text{tot}}$, is the uncertainty on the model parameter S_ν given the noise in the map. To calculate this value, we can write down the χ^2 for the model over all pixels j as:

$$\chi^2 = \frac{\sum_j (M_{\nu,j} - \mathscr{M}_{\nu,j})^2}{\sigma_\nu^2} = \frac{\sum_j (M_{\nu,j} - S_\nu f_\nu[\boldsymbol{\theta}_j])^2}{\sigma_\nu^2}, \tag{A.17}$$

where the index j runs over the map pixels, and take the second derivative with respect to S_ν:

$$\frac{\partial^2\chi^2}{\partial S_\nu^2} = 2\frac{\sum_j (f_\nu[\boldsymbol{\theta}_j])^2}{\sigma_\nu^2}. \tag{A.18}$$

Since our model has only one parameter, we can express the standard relationship between the variance of S_ν and the second derivative (A.18) as follows:

$$\sigma_{\nu,\mathrm{tot}}^2 = 2\left(\frac{\partial^2\chi^2}{\partial S_\nu^2}\right)^{-1}. \tag{A.19}$$

Finally, taking the square root, this yields the desired uncertainty on S_ν:

$$\sigma_{\nu,\mathrm{tot}} = \frac{\sigma_\nu}{\sqrt{\sum_j \left(f_\nu[\boldsymbol{\theta}_j]\right)^2}}. \tag{A.20}$$

To simplify this expression, we may approximate $f_\nu[\boldsymbol{\theta}]$ by its continuous counterpart $F_\nu(\boldsymbol{\theta})$ (Equation A.12) and approximate the sum over pixels $\boldsymbol{\theta}_j$ in Equation A.20 as an integral over the full 2D plane:

$$\sigma_{\nu,\mathrm{tot}} \approx \frac{\sigma_\nu}{\sqrt{\int d^2\boldsymbol{\theta}(1/\Omega_{px})\left(F_\nu(\boldsymbol{\theta})\Omega_{px}\right)^2}}. \tag{A.21}$$

Assuming the beam is Gaussian, as is the case in our analysis, we can evaluate this integral and simplify to obtain the convenient approximation

$$\sigma_{\nu,\mathrm{tot}} \approx \sigma_\nu\sqrt{\frac{2\Omega_\nu}{\Omega_{px}}}, \tag{A.22}$$

which also holds approximately for nearly-Gaussian (e.g., Airy) beams.

Returning to the question of the weights, we wish to combine beam-scale quantities representing both the signal and the noise. The noise RMS per beam is simply (A.21). The summation property of (A.9) tells us that the signal per beam is $S_{\nu,i}$ for a particular source i, or simply S_ν (A.14) on average. Thus, to correctly rescale the signals, we use scale factors proportional to the inverse of S_ν in flux density units:

$$r_\nu = \frac{S_{\mathrm{ref}}}{S_\nu}, \tag{A.23}$$

where S_{ref} is the value of S_ν at an arbitrarily chosen reference band. Finally, by rescaling (A.21) with (A.23), we arrive at the appropriate factors for inverse variance weighting in (A.15):

$$w_\nu = \frac{1}{\left(r_\nu\sigma_{\nu,\mathrm{tot}}\right)^2} = \frac{1}{\sigma_\nu^2}\frac{S_\nu^2}{S_{\mathrm{ref}}^2}\frac{\Omega_{px}}{2\Omega_\nu}. \tag{A.24}$$

We can use these weights to determine the expected per-pixel noise of M_{combined} using the fact that the noise is rescaled by the same factors (A.23):

$$\text{Var}(M_{\text{combined}}) = \text{Var}\left(\frac{\sum_\nu M_\nu r_\nu w_\nu}{\sum_\nu w_\nu}\right) = \frac{\sum_\nu \sigma_\nu^2 r_\nu^2 w_\nu^2}{(\sum_\nu w_\nu)^2}; \tag{A.25}$$

$$\sigma_{\text{combined}} = \sqrt{\text{Var}(M_{\text{combined}})} = \frac{\sqrt{\sum_\nu (\sigma_\nu r_\nu w_\nu)^2}}{\sum_\nu w_\nu}; \tag{A.26}$$

$$\text{SNR}_{\text{combined}} = \frac{M_{\text{combined}}}{\sigma_{\text{combined}}} = \frac{\sum_\nu M_\nu r_\nu w_\nu}{\sqrt{\sum_\nu (\sigma_\nu r_\nu w_\nu)^2}}. \tag{A.27}$$

We can also use the weights (A.24) to form an effective multiband PSF:

$$f_{\text{combined}}[\boldsymbol{\theta}_j] = \frac{\sum_\nu w_\nu f_\nu[\boldsymbol{\theta}_j]}{\sum_\nu w_\nu}, \tag{A.28}$$

which remains area-normalized, i.e., it satisfies Equation A.7. This effective PSF can be used to detect sources in M_{combined}; its solid angle Ω_{combined} is calculated as in (**??**):

$$\frac{1}{\Omega_{\text{combined}}} = \frac{\max_j f_{\text{combined}}[\boldsymbol{\theta}_j]}{\Omega_{px}} = \frac{\sum_\nu (w_\nu/\Omega_\nu)}{\sum_\nu w_\nu}, \tag{A.29}$$

which is valid as long as the PSF peaks at the same location in each band. It is also desirable to form a combined catalog of sources, with effective flux densities S_{combined}, for the purpose of calculating the boost correction:

$$S_{\text{combined},i} = \frac{\sum_\nu S_{\nu,i} r_\nu w_\nu}{\sum_\nu w_\nu}. \tag{A.30}$$

In the case that the true source SEDs exactly follow the assumed modified blackbody, it can be shown that convolving the combined source catalog with $f_{\text{combined}}(\boldsymbol{\theta}_j)$ as in (A.9) reproduces M_{combined} in the absence of noise. In this case, $S_{\text{combined},i}$ reduces to the reference flux density $S_{\text{ref},i}$ for each source, and we have:

$$\begin{aligned}
\sum_i S_{\text{combined},i} f_{\text{combined}}[\boldsymbol{\theta} - \boldsymbol{\theta}_i] &= \sum_i \left(\frac{\sum_\nu S_{\text{ref},i} w_\nu f_\nu[\boldsymbol{\theta} - \boldsymbol{\theta}_i]}{\sum_\nu w_\nu}\right) \\
&= \frac{\sum_\nu r_\nu w_\nu \sum_i S_{\nu,i} f_\nu[\boldsymbol{\theta} - \boldsymbol{\theta}_i]}{\sum_\nu w_\nu} \\
&= \frac{\sum_\nu r_\nu w_\nu M_\nu}{\sum_\nu w_\nu} \\
&= M_{\text{combined}}.
\end{aligned} \tag{A.31}$$

A.3.2 Procedure for Estimating Uncertainties from Degeneracy Curves

Here, we describe our procedure for estimating the behavior of the SZ parameter degeneracies (Section 4.1.2) for a small collection of N map realizations. We initially tested the procedure for $N = 100$; we use $N = 200$ for the final results in Chapter 5.

We begin with the collection of best-fitting SZ parameters v_z, T, and τ for all n map realizations. Ideally, one would model the behavior of all three SZ parameters jointly in terms of a 3D region. However, it was not obvious how to parameterize such a region for fitting. Instead, we work in the three 2D planes specified by pairs of the SZ parameters.

We observe that the degeneracies between the parameters roughly follow a curve once the logarithms of the parameters are taken: see, e.g., Figure 4.1. However, while T and τ are positive by definition, v_z is not necessarily positive. For the examples in this work, we use an input value of $v_z = +500$ km s^{-1} and discard any realizations where the best-fitting $v_z < 0$. In the cases we have studied that have any useful constraining power on v_z, this procedure is sufficient to retain almost all of the data. In general, to enable analyzing cases where v_z is negative or close to 0, one may instead use coordinates that are linear in v_z and logarithmic in T and τ. Hereafter, we will assume that the logarithms have been taken, and we will refer to each parameter pair as (x, y), e.g., $(x, y) = (\log T, \log v_z)$.

Given that each pair of parameters roughly follows a degeneracy curve, our strategy is to characterize the degeneracy by fitting a curve and characterzing the distribution of the residuals. We considered a number of functional forms for these curves, but we settled on a polynomial curve $P_d(x)$ with variable degree d for simplicity and ease of fitting. In performing this fit, we minimize the residual R with respect to the n pairs of data points x_i, y_i, where $0 \leq i < n$:

$$R = \sum_{i=0}^{N-1} (P_d(x_i) - y_i)^2. \tag{A.32}$$

This procedure requires that y be a single-valued function of x; for the degeneracies we consider, this is always true. However, in some cases, y may be a steep function of x, so in practice we renormalize both coordinates by their sample RMS before fitting to give them similar units.[3] To choose the degree d, we run the full degeneracy-fitting procedure with polynomials of degrees 2 through 6. We discard any cases

---

[3] This renormalization is not necessary for the fit itself, but the remaining steps in the procedure can fail if the renormalization is not done.

where $P_d(x)$ has any extrema or inflection points within the range of the data. We also discard any cases where the quality of the final fit, as measured by the PTE (discussed below), is determined to be poor. From the remaining cases, we select the degree that minimizes the area of the 68% confidence region in the xy plane, which we calculate as described below.

Next, we wish to convert to a set of primed coordinates (x', y') in which the degeneracy is well behaved. To do this, for each point (x_i, y_i), we first calculate the point (x_c, y_c) on the fitted curve $P_d(x)$ that is closest to (x_i, y_i). That is, we numerically calculate the optimal value of x_c as

$$x_c = \arg\max_x \left((x - x_i)^2 + (P_d(x) - y_i)^2\right) \tag{A.33}$$

and plug in to P_d to obtain y_c:

$$y_c = P_d(x_c). \tag{A.34}$$

We then take x' to be the signed distance along the curve $(x, P_d(x))$ with respect to a reference point $(x_{\text{ref}}, y_{\text{ref}})$ on the curve and take y' to be the signed distance from (x_c, y_c) to (x_i, y_i). The signed distance along the curve is determined with the usual formula from calculus:

$$x'_i = \int_{x_{\text{ref}}}^{x_c} \sqrt{1 + P'_d(x)^2}\, dx, \tag{A.35}$$

where P'_d is the derivative of P_d. The distance to (x_i, y_i) can be given a sign with respect to the unit vector $\hat{\boldsymbol{N}}_i$ normal to the curve at (x_c, y_c):

$$\boldsymbol{N}_i = (-P'_d(x_c), 1), \tag{A.36}$$

and

$$\hat{\boldsymbol{N}}_i = \frac{\boldsymbol{N}_i}{|\boldsymbol{N}_i|}, \tag{A.37}$$

and so, writing the vector distance $\boldsymbol{D}_i = (x_i - x_c, y_i - y_c)$, we obtain

$$y'_i = \boldsymbol{D}_i \cdot \hat{\boldsymbol{N}}_i. \tag{A.38}$$

The reference point is arbitrary, but we use the value of P_d at the mean of the data:

$$x_{\text{ref}} = \langle x_i \rangle_i; \quad y_{\text{ref}} = P_d(x_{\text{ref}}). \tag{A.39}$$

The last step of the degeneracy fitting procedure is to fit a 2D Gaussian PDF to the data in the primed coordinate plane. Rather than using a full parametric fit, we

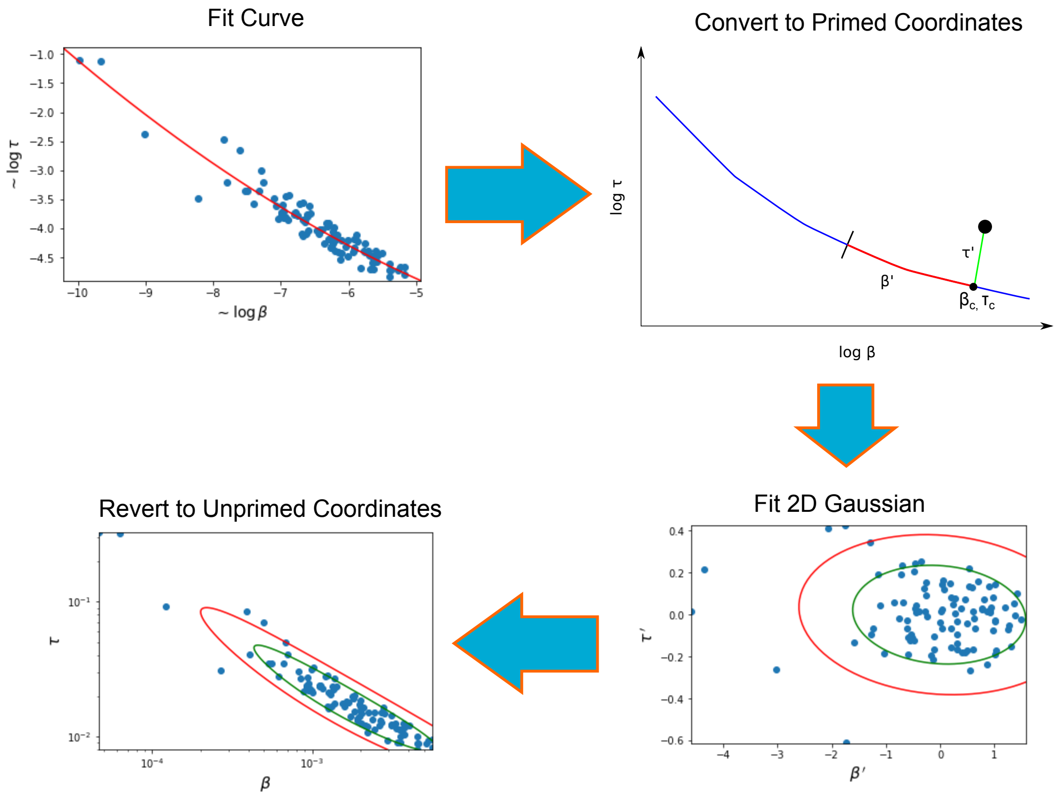

Figure A.9: Illustration of the procedure for fitting degeneracy curves for example parameters $x = \log\beta = \log\frac{v_z}{c}$ and $y = \log\tau$. We show the major steps: the best-fit curve P_d, the transformation to primed coordinates (x', y') (in this case (β', τ')), the 2D Gaussian fit in primed coordinates, and the contours returned to unprimed coordinates after inverting the transformation. The green and red contours are the 68% and 95% confidence regions, respectively.

approximate the best-fitting Gaussian as follows. We estimate the rotation angle θ of the Gaussian by fitting a line to the data (x_i', y_i') and taking $\theta = \arctan m$, where m is the slope. After rotating all the data by the angle $-\theta$, we determine the remaining parameters of the Gaussian as the sample means and sample RMSes of the rotated x_i' and y_i'. We illustrate the full procedure in Figure A.9.

To determine the quality of the fit, we use a Kolmogorov-Smirnov (KS) test. In general, the KS test measures how consistent the samples of a given variable are with a given theoretical probability distribution. To perform the KS test for a variable v, one calculates the KS statistic as

$$\max_{v} |\mathrm{CDF}(v) - \mathrm{EDF}(v)|, \tag{A.40}$$

where CDF denotes the theoretical cumulative distribution of v and EDF denotes the empirical cumulative distribution of the samples of v. In our case, we choose

$v = r^2$, where r^2 is the normalized squared radial distance[4] from the mean of the Gaussian $\boldsymbol{\mu} = (\mu_x, \mu_y)$ to the point $\boldsymbol{x}' = (x', y')$ in primed coordinates:

$$r^2 = (\boldsymbol{x}' - \boldsymbol{\mu})^T \mathbf{C}^{-1} (\boldsymbol{x}' - \boldsymbol{\mu}), \tag{A.41}$$

where $\mathbf{C}$ is the covariance matrix of the 2D Gaussian. The EDF is simply calculated as the cumulative distribution of r^2 values for all the points $\boldsymbol{x}'_i$; we calculate the KS statistic (Equation A.40) by comparing this to the theoretical CDF of a χ^2 distribution with 2 degrees of freedom, which describes the sum of two independent 1D Gaussians. Finally, we wish to calculate the probability to exceeed (PTE), i.e., the probability that a random realization drawn from a 2D Gaussian has a KS statistic higher than that of our data points $\boldsymbol{x}'_i$. To do this, we construct 10000 simulations consisting of n random samples drawn from a 2D Gaussian and calculate the KS statistic for each simulation[5,6]. We calculate the PTE as the quantile of our KS statistic among those of the simulations. The PTE lies in the interval $[0, 1]$, with a low value indicating a poor fit and a high value a good fit. As mentioned above, we use the PTE as one factor in selecting the degree d of the polynomial fit.

With a 2D Gaussian description of the degeneracies in the primed coordinates, it is straightforward to draw random samples or calculate contours corresponding to the desired confidence regions, e.g., the 68% region. To transform these degeneracy contours back to the xy plane, we must invert the transformation from (x, y) to (x', y'). To perform this inversion for a given point (x', y'), we invert Equation A.35 using a standard library ODE solver to recover the corresponding x_c and y_c (Equations A.33 and A.34). We then add the normal along the curve $\hat{\boldsymbol{N}}$ (as in Equation A.37) scaled by y' to recover the unprimed coordinates (x, y). The 2D contours in our results are the 68% contours generated in this manner.

---

[4] To be maximally rigorous, one could also apply an azimuthal variant of this KS test against a uniform expected distribution of angles, but we did not investigate this variant of the test.

[5] We performed additional simulations with fewer random samples for cases where we had to discard one or more outliers from the data.

[6] Such simulations are necessary except for a CDF that has a standard formula for the PTE, e.g., a 1D Gaussian.

Appendix B

SIX-LAYER AR COATINGS: SUPPLEMENTAL PLOTS

B.1 1D Parameter Scans

Below we give the full set of 1D parameter scans to confirm the results of the HFSS simulations described in Section 7.2.2. Each panel of each figure shows how the “max-of-means” value for a particular design varies as a function of one dimensional parameter (e.g., the width of the features layer 2.) We performed scans each parameter about the nominal design (Figures B.1, B.2), the aggressive alternative design (Figures B.3, B.4), and the conservative alternative design (Figures B.5, B.6). We also considered both the “wide” and “narrow” bandpass definitions for the atmospheric windows (Table 7.2). The wide bands are used in figures B.1, B.3, and B.5; the narrow bands are used in figures B.2, B.4, and B.6. In addition, to test convergence of the results, we varied the frequency resolution used to compute the max-of-means value. The values of the frequency resolution are indicated in the legend of each panel.

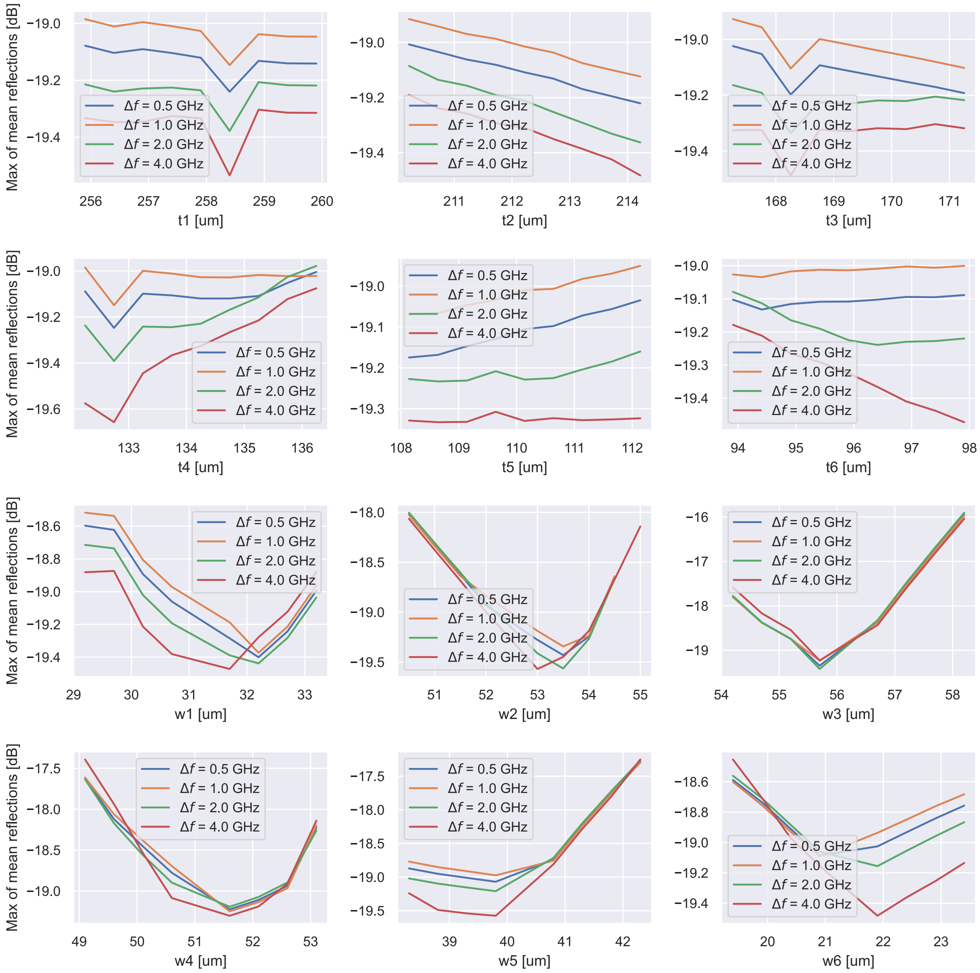

Figure B.1: Parameter scans for the nominal design, with wide bands.

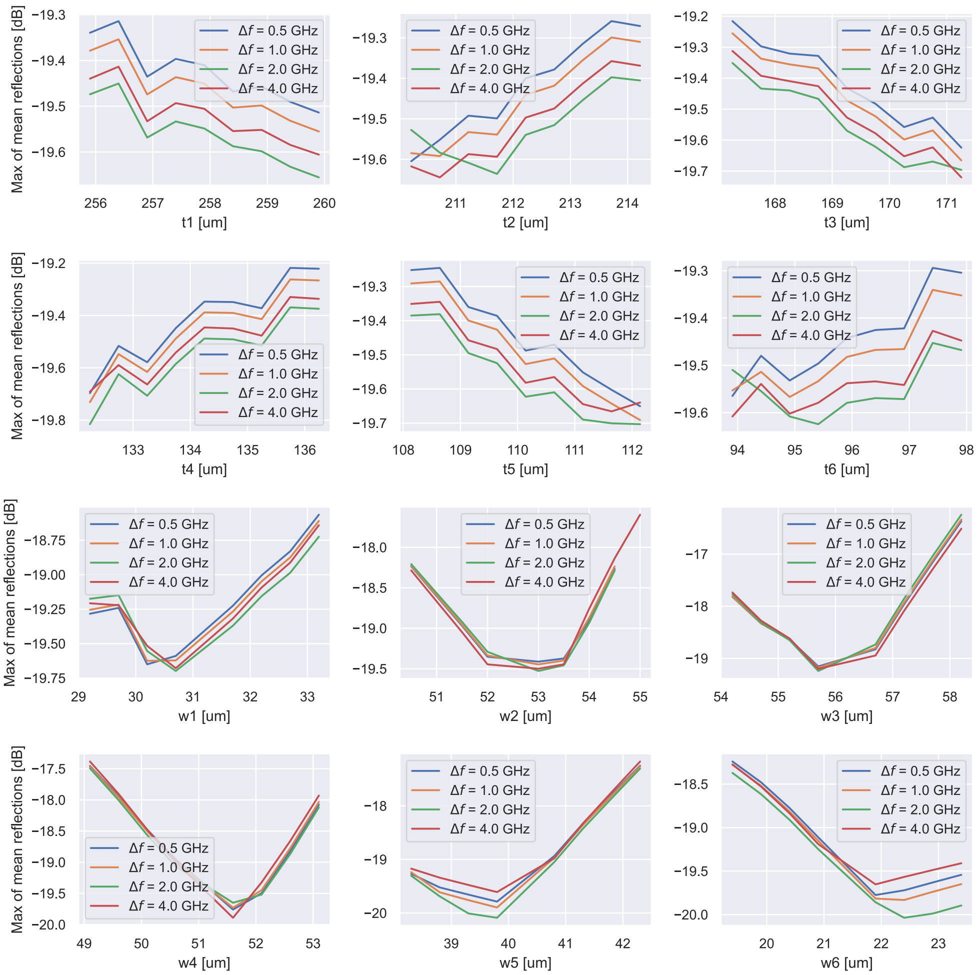

Figure B.2: Parameter scans for the nominal design, with narrow bands.

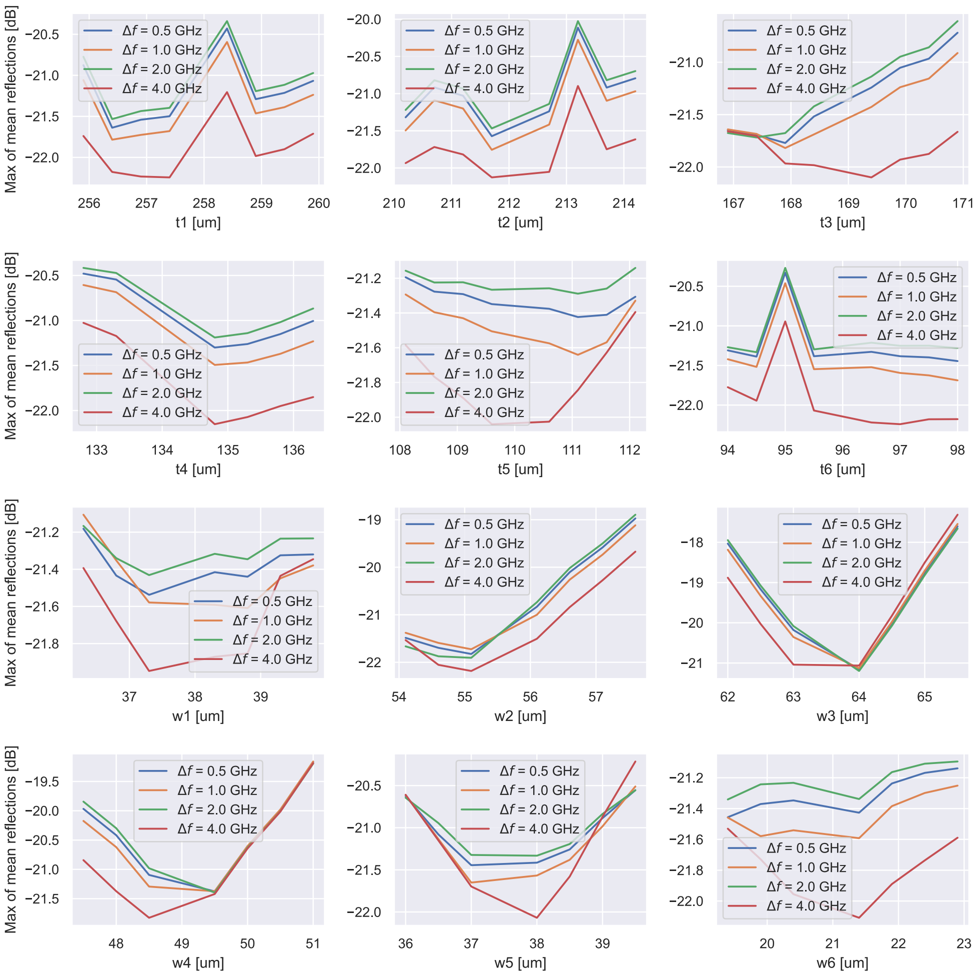

Figure B.3: Parameter scans for the aggressive design, with wide bands.

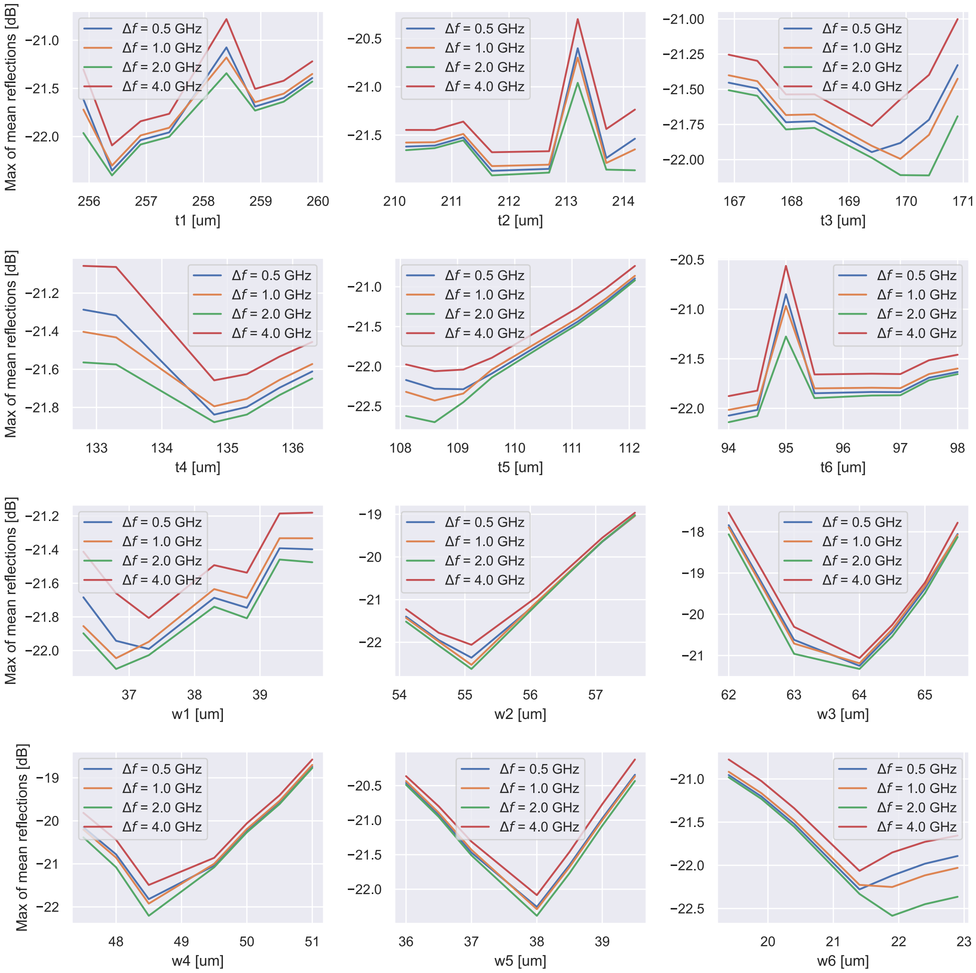

Figure B.4: Parameter scans for the aggressive design, with narrow bands.

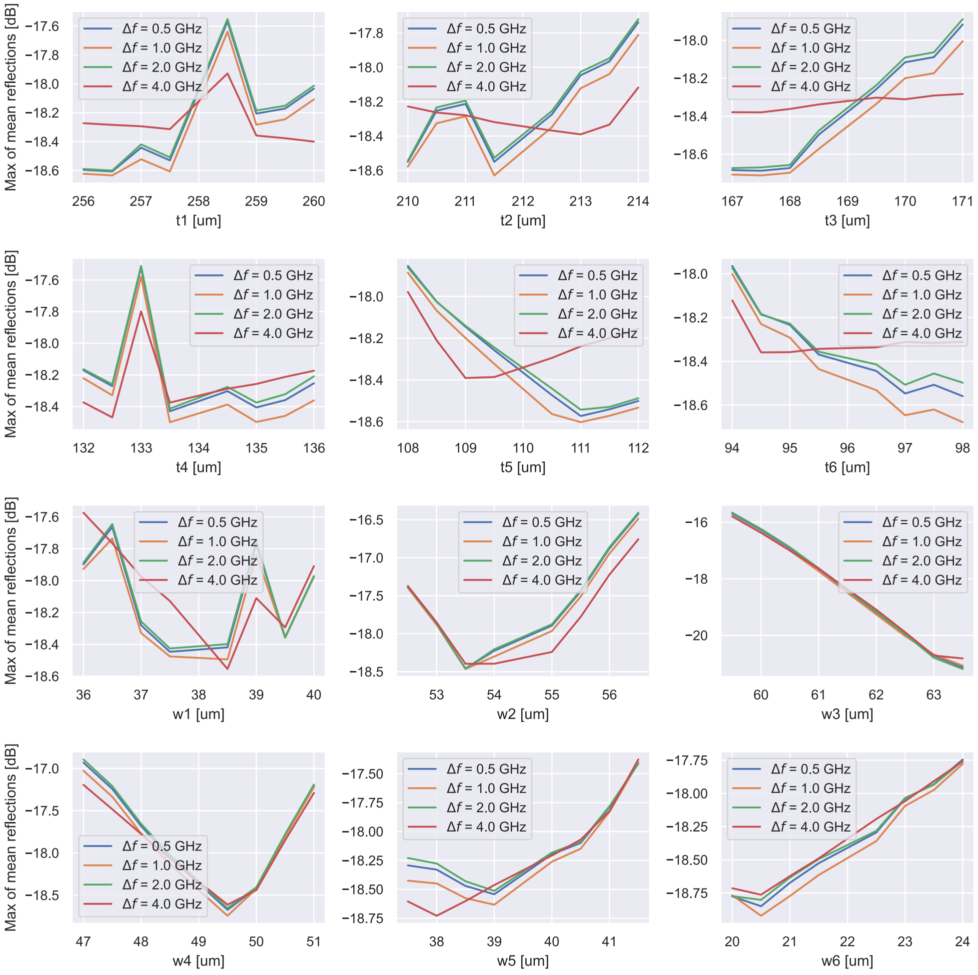

Figure B.5: Parameter scans for the conservative design, with wide bands.

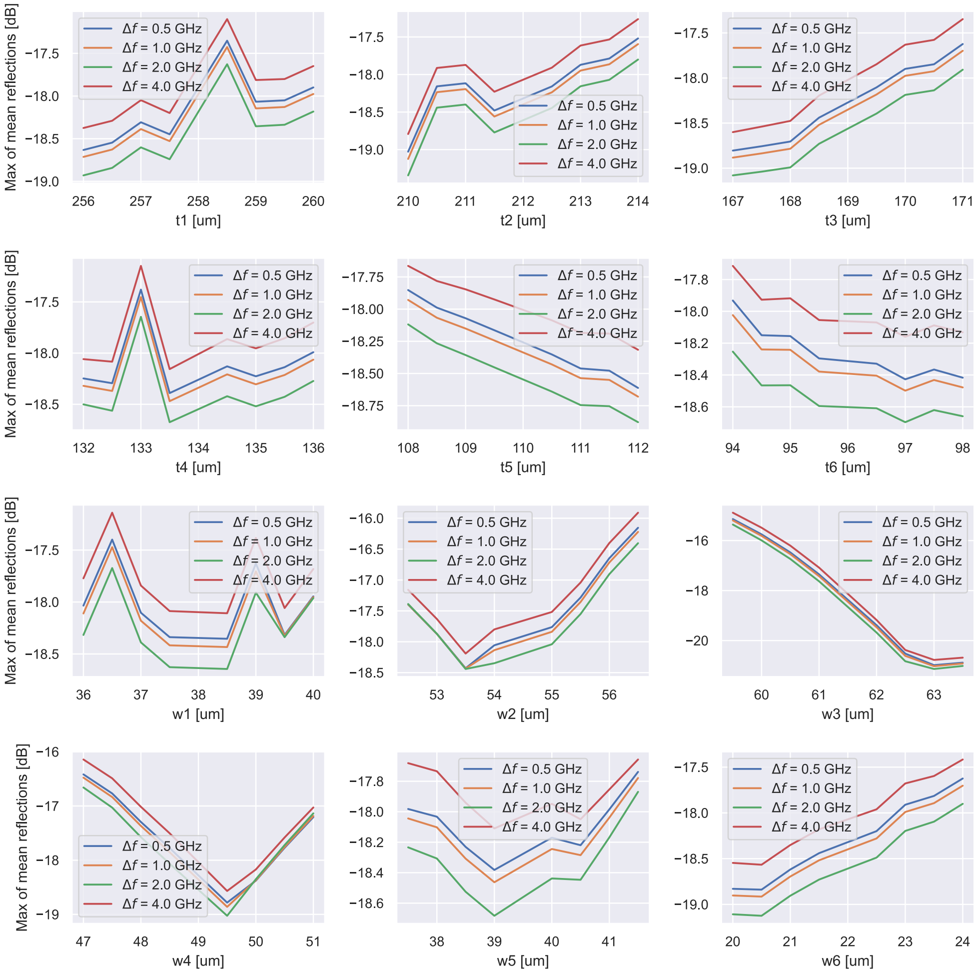

Figure B.6: Parameter scans for the conservative design, with narrow bands.